Dissertation

submitted to
the Combined Faculties of the Natural Sciences and Mathematics
of the Ruperto-Carola-University of Heidelberg, Germany,
for the degree of Doctor of Natural Sciences

Put forward by
Sebastian Lindemann
born in Freiburg im Breisgau, Germany
Oral examination on 13 November 2013

Intrinsic ^{85}Kr and ^{222}Rn Backgrounds in the XENON Dark Matter Search

Referees:
Prof. Dr. Wolfgang Hampel
Prof. Dr. Werner Aeschbach-Hertig

Intrinsic ^{85}Kr and ^{222}Rn Backgrounds in the XENON Dark Matter Search

The XENON Dark Matter search is aiming for the direct detection of Dark Matter in the form of weakly interacting massive particles (WIMPs) scattering off xenon nuclei. This process is expected to be extremely rare, if at all existing. To be detectable, competing background has to be suppressed to unprecedented level. This defines the framework for this thesis. First, the data analysis is sketched that resulted in todays strongest limit on the spin-independent WIMP-nucleon scattering for WIMP masses above 8 GeV/c^2 using an exposure of 225 live days × 34 kg collected by the XENON100 detector. For this analysis we develop a successfully employed consistency condition rejecting non-physical background. In the main part of this thesis, we investigate the intrinsic backgrounds ^{85}Kr and ^{222}Rn. To be sensitive to a potential WIMP signal, ultra-low concentrations have to be achieved in the liquid xenon target. We developed a method to determine krypton traces in xenon above a detection limit of only 6 parts per quadrillion (ppq) – two orders of magnitude below previous achievements. We prove that the cryogenic fractional distillation reaches a krypton level in xenon below 1 parts per tril (ppt). This represents a crucial proof-of-principle for the needs of the upcoming XENON1T detector. Moreover, we present a ^{222}Rn emanation assay of the XENON100 detector and apply our results to cast projections on the future background handling in XENON1T. Finally, we introduce two promising realizations of radon removal systems and argue for the utmost importance of ^{222}Rn emanation assays.

Intrinsischer ^{85}Kr und ^{222}Rn Untergrund im XENON Dunkle Materie Projekt

Das XENON Dunkle Materie Projekt hat zum Ziel Dunkle Materie in Form von schwachwechselwirkenden, massiven Teilchen (WIMPs) durch ihren Stoß mit Xenon-Atomkernen nachzuweisen. Falls es ihn überhaupt gibt, so ist dieser Prozess sehr selten. Um ihn dennoch beobachten zu können, muss der Untergrund auf ein zuvor unerreichtes Level minimiert werden. Die vorliegende Arbeit wurde unter diesem Aspekt verfasst. Zu Beginn soll die Datenanalyse beschrieben werden, die zum bis heute stärksten Limit für den Prozess der elastischen, spinunabhängigen Streuung eines WIMPs an einem Atomkern für WIMP Massen oberhalb von 8 GeV/c^2 lieferte. Dabei wurde ein Datensatz von 225 Tagen × 34 kg ausgewertet, der mit dem XENON100 Detektor aufgezeichnet wurde. Für diese Analyse wurde eine Konsistenzbedingung aufgestellt, um unphysikalische Untergrundereignisse auszusondern. Der Hauptteil dieser Arbeit widmet sich den intrinsischen Untergründen von ^{85}Kr und ^{222}Rn. Niedrigste Konzentrationen müssen im Target aus flüssigem Xenon erreicht werden, um ein mögliches WIMP Signal beobachten zu können. Hierzu wurde eine Methode entwickelt, die Spurenverunreinigungen von Krypton in Xenon mit einer Sensitivität von 6×10^{-15} (ppq) nachweisen kann – das stellt eine Verbesserung gegenüber herkömmlichen Methoden um zwei Größenordnungen dar. Es wird gezeigt, dass kryogene Destillation bereits ein Krypton-Level in Xenon von unter 10^{-12} (ppt) erreicht hat. Damit wird ein wichtiger Machbarkeitsnachweis für das Folgeexperiment XENON1T erbracht. Im Anschluss daran wird eine ^{222}Rn-Emanationsmessung des XENON100 Detektors präsentiert. Diese Ergebnisse werden dazu benutzt, eine Vorhersage für den Umgang mit diesem Untergrund in XENON1T zu treffen. Abschliessend werden zwei vielversprechende Systeme zur Radon-Entfernung präsentiert und die Wichtigkeit von ^{222}Rn-Emanationsmessungen betont.

Contents

1 Dark Matter and the direct detection experiment XENON **11**

1.1 Seeking the Dark 11
  1.1.1 The total energy density in our universe 12
  1.1.2 Cosmic microwave background 13
  1.1.3 Observational evidences for Dark Matter 14
  1.1.4 Candidates for particle-like Dark Matter 15
  1.1.5 Experimental WIMP detection strategies 16
1.2 XENON direct Dark Matter search 18
  1.2.1 The dual-phase LXe TPC 19
  1.2.2 The XENON100 detector 20
  1.2.3 The XENON1T detector 33

2 XENON100 data analysis: the ionization signal S2 and its pulse width **39**

2.1 A brief introduction to the XENON100 data analysis 39
  2.1.1 Data acquisition 39
  2.1.2 Data processing 40
  2.1.3 Calibration sources 43
  2.1.4 Energy scales 44
  2.1.5 Event selection 45
2.2 The secondary scintillation light S2 and its pulse width 49
  2.2.1 Electric field in gas gap 50
  2.2.2 Electron mobility and electron drift velocity in gaseous xenon . . . 52
  2.2.3 The S2 pulse width and its xy-dependence 52
  2.2.4 Mesh warping and gas gap determination 54
  2.2.5 S2 pulse width dependence on drift time in LXe 57
2.3 Correcting the S2 pulse width 59
  2.3.1 Data Selection 60
  2.3.2 Fitting energy and drift time dependence of the S2 pulse width . . 61

2.3.3 Fitting the S2 pulse width correction map and its drift time behavior 62
2.4 Longitudinal diffusion coefficient of electrons in LXe 64
2.5 Quantification of horizontal gas gap width dependence 67
2.6 Definition of a consistency cut on the S2 pulse width 67
2.6.1 Impact of the S2 pulse width cut on the 225 live days analysis . . 71

3 Krypton in XENON 75
3.1 Introduction 75
3.1.1 Krypton analytics 77
3.1.2 The ^{85}Kr/$^{\mathrm{nat}}$Kr ratio 79
3.2 The sector field mass spectrometer 81
3.2.1 The mass spectrometer 82
3.2.2 The gas chromatography system 83
3.2.3 Calibration and data analysis 85
3.3 Commercial gas chromatograph 96
3.3.1 Pulsed discharge detector 97
3.3.2 Customized setup 99
3.3.3 Calibration and data analysis 100
3.3.4 Sensitivity 101
3.4 Krypton assay 101
3.4.1 Drawing xenon samples 102
3.4.2 Krypton assay results 104
3.5 Summary and outlook 109

4 Radon in XENON 111
4.1 ^{222}Rn assay of the XENON100 detector 112
4.1.1 ^{222}Rn assay of the XENON100 cryostat 113
4.1.2 ^{222}Rn assay of the XENON100 gas system 114
4.1.3 Conclusions on the ^{222}Rn assay of XENON100 115
4.2 ^{222}Rn in XENON1T 116
4.2.1 Estimations on radon background of XENON1T 116
4.2.2 Impact of radon removal system 118
4.3 Single column adsorption 124
4.3.1 Henry's law and retention time predictions 124
4.3.2 Intrinsic radon emanation of single column radon removal system . 129
4.3.3 Static adsorbent selection 130

4.3.4 Dynamic adsorbent selection 133
4.3.5 Xenon adsorption 141
4.3.6 Conclusions on single column adsorption radon removal system . . 142
4.4 Alternatives to single column adsorption 144
4.4.1 Temperature swing adsorption 144
4.4.2 Cryogenic fractional distillation 149
4.5 Radon emanation assay studies 153
4.5.1 Principle of ^{222}Rn emanation measurements 154
4.5.2 General formula to evaluate ^{222}Rn emanation measurements 157
4.5.3 Excerpt ^{222}Rn screening results 160
4.6 Summary and outlook 165

Chapter 1

Dark Matter and the direct detection experiment XENON

A vast amount of experimental indications points towards the existence of a non-luminous, non-baryonic form of matter, the so-called Dark Matter. Even though the standard model of particle physics (SM) seems to bear even the closest examination, the astrophysical puzzle might still find its solution therein. Having excluded all so-far known dark objects from the biggest (MACHOS) to the point-like (neutrinos), astrophysics is fated to abandon Newton and Einstein, or provides the first evidence for physics beyond the standard model of particle physics.

The quest for Dark Matter also sets the (by far smaller) foundation of this thesis and we feel obliged to mention some of its highlights. Yet section 1.1 is intended to quicken the reader's interest more than to quench his thirst for answers. Section 1.2.1 is already of much more technical nature setting the framework for a direct Dark Matter detection experiment based on the target and detection material liquid xenon. Section 1.2.2 and 1.2.3 will introduce the reader to the direct Dark Matter detectors XENON100 and XENON1T, respectively. Currently the former is leading the field of direct Dark Matter search; the latter is supposed to take on this position in the near future.

1.1 Seeking the Dark

The hypothetical matter exploited to explain mass discrepancies of astronomical bodies is customary called Dark Matter (DM). Commonly, motions of other bodies around or within the object under study are used to directly determine its mass. Mass discrepancies, i.e. Dark Matter, in the past often arose comparing different methods to estimate masses in astronomy. Historically, two Dark Matter problems existed. The local Dark

Matter close to our Galaxy and the global Dark Matter surrounding galaxies and clusters of galaxies. Their intrinsic difference, however, was understood only later. In [1] a well written review of the concept of Dark Matter can be found, highlighting its historical origin as a minor observational puzzle developing to a major challenge of modern physics.

In the remainder of this introductory section we want to highlight the observational evidence classifying the global Dark Matter to be of cold (non-relativistic), non-baryonic nature (in opposition to the baryonic local Dark Matter being faint stars or jupiters [1]). However, we will start with a very short intersection rewriting the Friedmann equation in terms of the density parameter Ω. This parameter, or, to be more precise, its single constituents Ω_b (baryonic matter), Ω_c (cold DM), Ω_Λ (vacuum energy) with $\Omega = \sum \Omega_i \approx \Omega_b + \Omega_c + \Omega_\Lambda$, is accessible studying anisotropies in the cosmic microwave background (CMB). This results in today's strongest evidence for and most precise quantification of additional energy densities relegating ordinary matter to a mere 4 % of the total. For further reading we suggest the review article [2] and references therein.

1.1.1 The total energy density in our universe

Galaxy surveys find our universe to be homogeneous and isotropic at scales $\sim 100\,\mathrm{Mpc}$. Based on this, we can construct the so-called Friedmann-Lemaître-Robertson-Walker metric. This metric is characterized by a time dependent scale factor $a(t)$ and a constant $k \in \{-1, 0, 1\}$ describing the spatial curvature with $k = 0$ denoting a flat universe. Employing Einstein's equations of general relativity, the time evolution of the scale factor $a(t)$ is given in the analytical Friedmann equations. These lay the foundations of standard big bang cosmology including the ΛCDM model. The first of the set of two Friedmann equations reads:

$$\left(\frac{\dot{a}}{a}\right)^2 + \frac{kc^2}{a^2} = \frac{8\pi G_N}{3}\,\rho_{\mathrm{tot}}\,. \tag{1.1}$$

Therein, G_N is Newton's constant and $\rho_{\mathrm{tot}} \approx \rho_{\mathrm{matter}} + \rho_\Lambda$ the total energy density. Here we defined the energy density of the vacuum

$$\rho_\Lambda \equiv \frac{\Lambda c^2}{8\pi G_N}\,, \tag{1.2}$$

emerging from the constant term Λ in Einstein's equations on general relativity (he referred to once as his biggest blunder). Introducing the Hubble parameter, $H(t) = \dot{a}/a$, and the aforementioned density parameter

$$\Omega - 1 \equiv \frac{k}{H^2\, a^2}\,, \tag{1.3}$$

we immediately find $\Omega = 1$ in case of a flat universe of $k = 0$, and rewrite equation 1.1 solving for the density parameter:

$$\Omega = \frac{8\pi G_N}{3\,H^2}\,\rho_{\text{tot}} = \frac{\rho_{\text{tot}}}{\rho_{\text{crit}}} = \sum \Omega_i\,. \tag{1.4}$$

Here we introduced the critical density $\rho_{\text{crit}} = 3H^2/(8\pi G_N)$ causing the universe to be flat in case it equals the total energy density $\rho_{\text{crit}} = \rho_{\text{tot}}$.

1.1.2 Cosmic microwave background

Background radiation originating from the propagation of photons in the early universe, decoupled from matter, was postulated by George Gamow and his collaborators in 1948 and discovered by Arno Penzias and Robert Wilson in 1965. Decoupling of photons happened shortly after recombination, i.e. the epoch at which protons and electrons first became bound to form electrically neutral hydrogen atoms. This process drastically reduced the amount of charged particles that made the early universe – emerged from the big bang – practically opaque for electromagnetic radiation. The cosmic microwave background (CMB) follows a black body spectrum corresponding to a precisely determined temperature of $(2.725\,48 \pm 0.000\,57)\,\text{K}$ [3] and shows anisotropies at the level of $100\,\mu\text{K}$. These anisotropies, as they are observed in the sky, are usually expanded in spherical harmonics $Y_{lm}(\theta, \phi)$:

$$\frac{\delta T}{T}(\theta, \phi) = \sum_{l=2}^{+\infty} \sum_{m=-l}^{+l} a_{lm}\, Y_{lm}(\theta, \phi)\,. \tag{1.5}$$

Assuming the temperature fluctuations to be Gaussian, the information of the CMB is completely contained in the power spectrum. The latter essentially is the behavior of coefficients a_{lm} as function of the multipole moment l (to be more precise, the coefficients' variance $C_l \equiv \langle |a_{lm}|^2 \rangle \equiv (2l+1)^{-1} \sum_{m=-l}^{l} |a_{lm}|^2$ is plotted versus l usually in the form of $l(l+1)C_l/2\pi$). FIG. 1.1 shows both the fluctuations of the CMB over about 97 % of the sky (left) plus the precisely determined temperature angular power spectrum (right) measured by the Planck satellite [4]. Overlaid to the power spectrum is the best fit of a theoretical six-parameter ΛCDM model perfectly reproducing the data. From this the

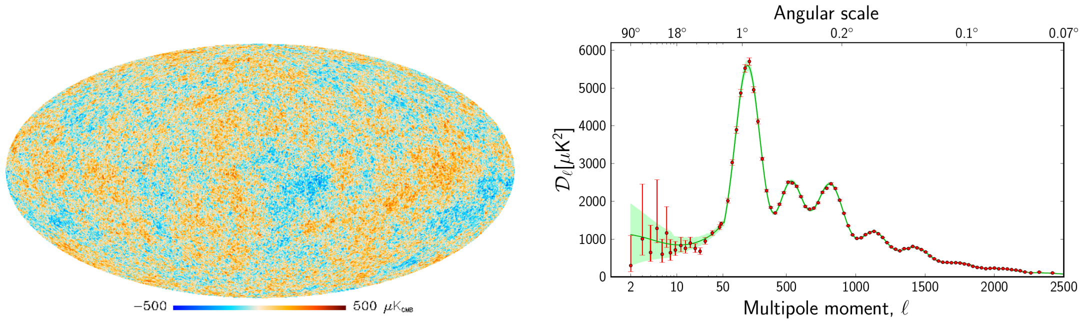

Figure 1.1: Planck 2013 results on the temperature fluctuations (±500 μK) of the CMB over about 97 % of the sky (left) and precise measurement of seven acoustic peaks plus the best fit of a theoretical six-parameter ΛCDM model to the temperature angular power spectrum (right). Figures from [4].

different density parameters are obtained to be [5]:

$$\begin{gathered}\Omega_b h^2 = 0.022\,07 \pm 0.000\,33 \qquad \Omega_c h^2 = 0.1196 \pm 0.0031 \qquad \Omega_\Lambda = 0.686 \pm 0.020 \\ H_0 = (67.4 \pm 1.4)\,\mathrm{km\,s^{-1}\,Mpc^{-1}}\end{gathered} \tag{1.6}$$

Therein $h = H_0/(100\,\mathrm{km\,s^{-1}\,Mpc^{-1}})$ and H_0 is the Hubble parameter as of today. Employing above results and assuming a flat universe (also this assumption is strongly supported by e.g. Planck 2013 data) we compute the universe's energy density to be composed of 68.6 % Dark Energy (Ω_Λ), 26.3 % Dark Matter (Ω_c) and only 4.9 % baryonic matter (Ω_b).

1.1.3 Observational evidences for Dark Matter

The standard model of cosmology (ΛCDM) relying on Cold Dark Matter as a key ingredient, precisely predicts the observed temperature fluctuations of the cosmic microwave background and is able to put stringent constraints on the abundances of baryons and Dark Matter in the universe. Still there exist an array of evidence for Dark Matter on the distance scales of the size of galaxies and galaxy clusters. We do not want to go into detail here and refer the interested reader again to [1, 2]. In a nutshell, extended flat rotation curves at large distances from the galactic center support the presence of massive dark halos surrounding galaxies. This was discovered independently by Vera Rubin and collaborators in 1978 [6] and Albert Bosma [7], also in 1978, both in optical and radio data. On the distance scale of galaxy clusters velocity dispersions and mass-to-light ratios are found to be substantially lower than expected [8]. X-ray observations, e.g.

from the Chandra X-ray Observatory, revealed the mass of hot X-ray emitting gas to be insufficient to gravitationally hold clusters together. Additional evidence is provided by (strong and weak) gravitational lensing both on subgalactic and inter-galactic distance scales with its most (visually) striking confirmation of Dark Matter, the "Bullet Cluster" [9]. The X-ray signature measured by the Chandra X-ray Observatory indicating the hot baryonic distribution is clearly (more than 8σ statistical evidence) separated from the Bullet Cluster's mass distribution as reconstructed from gravitational lensing.

1.1.4 Candidates for particle-like Dark Matter

In the previous section we sketched the compelling evidence for non-baryonic Dark Matter. Neutrinos have been considered natural candidates due to their "undisputed virtue of being known to exist" [10]. However, laboratory constraints on neutrino masses and stringent analyses of CMB data rule them out as viable Dark Matter candidates simply because they are not abundant enough. Furthermore, neutrinos are relativistic particles and consequently have a high free-streaming length that would have erased density fluctuations below a scale of $\sim 40\,\mathrm{Mpc}$ [11]. This implies big structures forming first (top-down formation) in the history of the universe what is in contradiction to the observed.

There exist many models beyond the standard model of particle physics, that were introduced to solve problems inherent to the SM like the hierarchy problem, and that contain particle candidates for Dark Matter. Supersymmetric (SUSY) models extend the SM relating bosons and fermions by a symmetry. It is beyond the scope of this work to review these models, but we want to highlight the neutralino as DM candidate. To avoid proton decay, R-parity was introduced to some SUSY models. In addition, R-parity also forbids the decay of the lightest SUSY particle into lighter SM particles. If this lightest SUSY particle happens as well to be neutral with respect to electromagnetic and strong interactions, a so called neutralino, it is also an appealing candidate for Dark Matter, while being motivated to solve problems related to the SM of particle physics.

Without specifying an underlying theory, we want to introduce the general class of weakly interacting massive particles (WIMPs): Weakly interacting particle DM candidates have just the right cross sections to produce the relic abundance observed today: In the early universe WIMPs were in thermal equilibrium with SM particles, i.e. they annihilated into and were being produced from SM particles at equal rates. Due to the expansion of the early universe, its temperature decreased and dropped below the WIMP mass. At this point the annihilation into SM particles dominated over the production of

WIMP particles. With the universe expanding and cooling further, the annihilation of WIMPs into SM particles stopped because of the tiny probability of two WIMP particles to meet and annihilate. This causes a relic WIMP density that is supposed to make up the bulk of Dark Matter. An order of magnitude estimate for today's relic density of WIMP particles, commonly denoted by χ, is [12]

$$\Omega_\chi h^2 \sim \frac{3 \times 10^{-27}\,\mathrm{cm}^3/\mathrm{s}}{\langle \sigma v \rangle}\,. \tag{1.7}$$

Therein $\langle \sigma v \rangle$ is the thermal average of the total annihilation cross section of a WIMP multiplied by its velocity. It seems to be an astonishing coincidence that a cross section typical for weak interactions causes our hypothetical WIMPs to be produced in the early universe at the correct amount observed today.

1.1.5 Experimental WIMP detection strategies

Following the above sketched cosmological reasoning, two obvious experimental strategies exist when aiming for a verification of the WIMP hypothesis: to look for annihilation into SM particles (indirect detection) or creation out of SM particles (accelerator based detection). Both routes are widely exploited but are out of the scope of this work. The interested reader is directed to the publications [13**?** –16] for the accelerator based search and to [2] for an overview of indirect detection approaches.

Direct detection A third route, though, exists if our galaxy is filled with Dark Matter in form of WIMPs, because then interactions with matter on the Earth might be detectable. A common approach of so-called direct detection experiments is to record the recoil energy of nuclei as WIMPs scatter off them [17–19]. This thesis has been prepared in the context of XENON100 and XENON1T, direct detection experiments looking for WIMPs recoiling off xenon nuclei, motivating us to present some important facts common for direct detection experiments.

The rate expected in a direct detection detector depends on the density and the velocity distribution of WIMPs at the Earth's position and the WIMP-nucleon scattering cross-section. In [12] a thorough discussion thereof is found, approximately stating the recoil rate on each target nuclei species to be proportional to the number of nuclei in the target, the local WIMP energy density divided by its mass and the WIMP-nucleon scattering cross-section averaged over the relative WIMP velocity with respect to the target nuclei. For the local WIMP energy density a value of $0.3\,\mathrm{GeV/cm^3}$ is commonly assumed [20] to be able to compare results of different direct detection experiments. This value, however, is accompanied by relatively large uncertainties. The type of scattering processes can be classified into elastic or inelastic scattering and spin-dependent or spin-independent scattering. In context of the XENON experiments the elastic spin-independent scattering is most important. Here the WIMP scatters off a nucleus as a whole, causing the cross-section to be roughly proportional to the square of the number of target nuclei. This fact makes xenon a well suited target material for direct detection experiments. The axial-vector mediated spin-dependent interaction is roughly proportional to $J(J+1)$, where J is the total angular momentum of the nucleus [13, 21]. Natural xenon contains two non-zero spin isotopes (^{129}Xe and ^{131}Xe) making xenon detectors also sensitive for this type of coupling.

The velocity distribution of WIMPs in a standard Dark Matter halo model is assumed to be Maxwellian with a mean velocity dispersion of $(220 \pm 20)\,\mathrm{km/s}$ [22]. This causes the number of expected recoils to a good approximation to decrease exponentially with deposited recoil energy. A low detection threshold on the order of a few keV only results as immediate consequence for direct detection experiments.

Direct Dark Matter detection experiments In the field of direct Dark Matter search there exists a multitude of different detection strategies. Generally speaking, energy deposited by a particle interaction can result in ionization, scintillation (at least in some materials) and heat (phonons). As of now, the most competitive direct Dark Matter detection experiments make use of two out of these three excitation modes. This is motivated by the advantageous fact that different particle interactions, depositing the same energy, have different shares in ionization, scintillation and heat. Being able to measure two of the excitation signals simultaneously, will allow us to distinguish between them. Recalling the roughly exponentially falling spectrum of recoil energies and the low interaction rates we expect from WIMPs, it is obvious that we have to avoid any background that could mimic such interactions especially for low energies. Electronic recoils (ER) induced by γ rays and β decays interacting with the target's shell electrons can be distinguished from nuclear recoils (NR) of neutrons scattering off the target's nuclei. The former displays in nearly all experiments the most abundant type of background while the latter can become the ultimate background as it is intrinsically indistinguishable from WIMP interactions. The last statement holds as long as recoil directions are not resolvable. Experiments overcoming this burden might be able to statistically tell interactions from fast neutrons and WIMPs apart, exploiting the expected anisotropy of WIMP interactions due to the earths movement through space, i.e. through the assumed

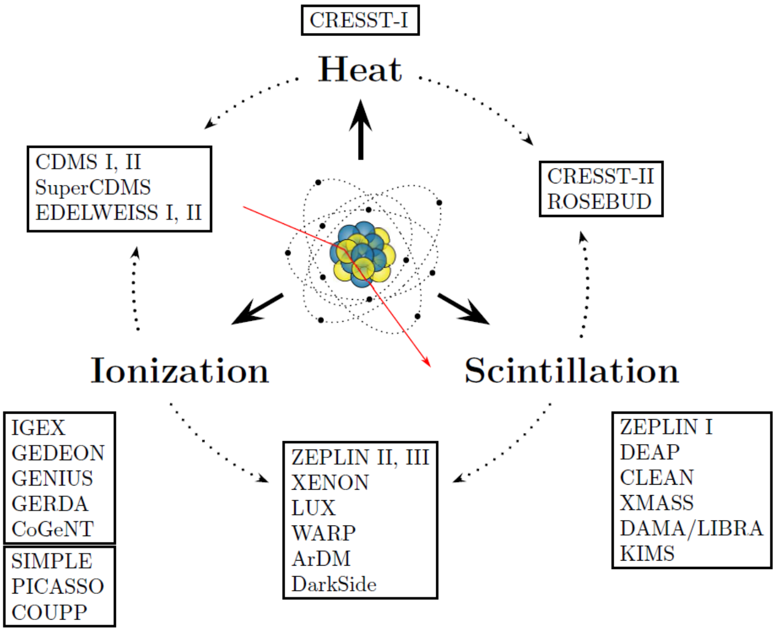

Figure 1.2: Direct Dark Matter detection experiments classified for the excitation channels exploited. Figure taken from [23].

WIMP halo. FIG. 1.2 lists past and present direct Dark Matter detection experiments and classifies them according to the excitation channels exploited.

1.2 XENON direct Dark Matter search

In a phased approach, the XENON Dark Matter search program employs liquid xenon (LXe) detectors with increasingly larger mass and lower background in the underground facilities of the INFN Laboratori Nazionali del Gran Sasso (LNGS[1]) in Italy. The LNGS underground facilities are shielded on average by $\sim 1400\,\mathrm{m}$ rock overburden ($3700\,\mathrm{m}$ water equivalent) reducing the atmospheric muon flux by about 6 orders of magnitude [24]. After a preceding phase demonstrating the detector concept, the first prototype detector in the XENON Dark Matter search program, XENON10, started scientific data taking in October 2006. XENON10 successfully competed [25] with the predominant ionization-phonon technology at the time [26].

XENON10's successor experiment, XENON100, is located as well at LNGS, using the same passive shielding of XENON10 and thereby demonstrating the potential of the liquid xenon technology being scalable with moderate effort. The XENON100 detector

---

[1] http://www.lngs.infn.it/

started science data taking in October 2009, only three years after XENON10, and has since then achieved unprecedented sensitivities [27, 28].

Inspired by XENON100's success, the assembly for the next phase detector XENON1T started. This detector will be hosted as well by LNGS. An large scale 9.6 m diameter water tank as shield and active Cherenkov muon veto with 4π coverage will replace the compact shield design of XENON100. In absence of a positive WIMP signal, XENON1T is designed to exclude cross-sections above $\sigma_{\mathrm{SI}}\sim 2\times 10^{-47}\,\mathrm{cm}^2$ at 90 % confidence level (CL) for a WIMP mass of $50\,\mathrm{GeV/c}^2$ [29].

1.2.1 The dual-phase LXe TPC

The principle of a dual-phase time-projection chamber (TPC) was introduced in 1989 [30] and initiated the use of liquid xenon in the search for Dark Matter. The dual-phase TPC is able to measure both scintillation and ionization signals from a particle interaction inside its liquid target. Photomultiplier tubes (PMTs) are employed to detect both the (primary) scintillation light (S1) and the secondary scintillation photons (S2), that are proportionally produced in the gaseous xenon from drifted ionization electrons. An electric field, E_d, across the liquid xenon target forces the ionization electrons from the interaction vertex to the gas phase. The secondary, proportional scintillation light S2 is locally produced in the gas phase above the liquid level. Therein a second electrical field E_g ($E_g > E_d$) is applied to convert the ionization electrons into a proportional amount of photons through the mechanism of electroluminescence [31]. By means of the different shares the PMTs observe the S2 signal (PMT hit-pattern), the position in the horizontal xy plane can be reconstructed (see section 2.1). The time difference between prompt S1 signal and drift time delayed S2 signal is used to reconstruct the z position of the interaction vertex. This three-dimensional vertex reconstruction enables LXe TPCs to fully exploit the high self shielding of liquid xenon. In the data analysis an inner fiducial volume is selected optimized for its signal to background ratio and, thus, sensitivity for WIMP interactions.

Moreover, measuring both scintillation photons and ionization electrons, the XENON detectors have the capability to distinguish electronic from nuclear recoils. An electron, produced via β^- disintegration or Compton scattering of a γ ray, will deposit energy along its trajectory and thereby imply comparably low ionisation density because of its rather large scattering length. A hypothetical WIMP, much heavier than an electron, will predominantly lose its energy in recoils with xenon nuclei of comparable mass. The resulting ionisation density caused by the recoiling nuclei (nuclear recoil NR) is greater

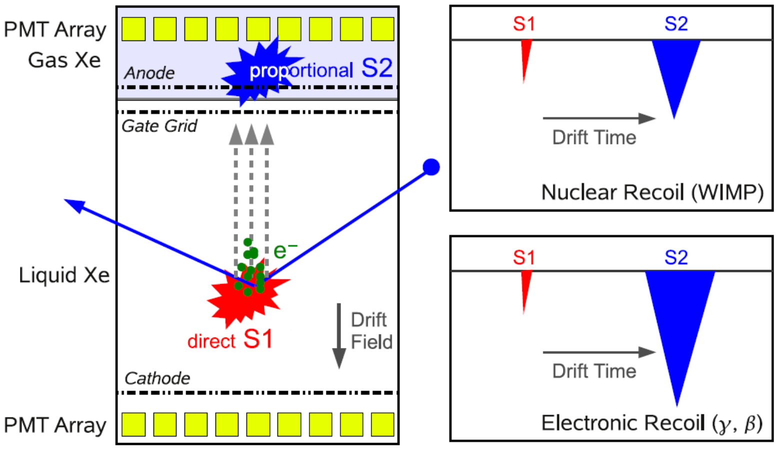

Figure 1.3: Working principle of a dual-phase liquid-xenon (LXe) time-projection chamber (TPC). (left) Vertical slice through a dual-phase LXe TPC illustrating generation of primary (S1) and secondary, proportional scintillation (S2) signals. (right) Sketch of two different waveforms showing nuclear (NR) and electronic (ER) recoils. The enhanced S2/S1 ratio of ERs can be exploited to discriminated them against WIMP-like NR signals. Figure from [34].

than the one by electrons (electronic recoil ER). As a consequence, the recombination probability of the ionized xenon atoms with their electrons differs along the trajectories of the ionizing particles. The lower recombination probability of electronic recoils leads to an enhanced ionization (S2) and a more strongly quenched scintillation (S1) signal. This anti-correlation of S1 and S2 light was first observed in [32]. The ratio of S2/S1 is therefore successfully employed to discriminate ER background from signal-like NR events. In [27] this discrimination technique, first proven in liquid xenon by [33], achieved an ER rejection of 99.75 % at an NR acceptance in the region of interest of roughly 40 %. FIG. 1.3 (left) illustrates the above explained working principle of a dual-phase LXe TPC. Sketched (right) are two waveforms illustrating the different S2/S1 ratios that are exploited to discriminate ER background, induced by β particles and γ rays, against NRs expected from WIMPs scattering off xenon nuclei.

1.2.2 The XENON100 detector

The Xenon collaboration prepared a detailed description of the Xenon100 detector in [34]. We want to redirect the interested reader to this comprehensive work for specific details. We still want to give a brief introduction to this "*amazing piece of hardware*" (Xenon100 detector; freely adopted from E. Aprile) that is supposed to be helpful in the further reading.

The actual TPC is made of 24 1/4 inch-thick polytetrafluorethylen (PTFE) panels enclosing an almost cylindrical volume of 30.5 cm height and 30.6 cm diameter. When filled, this TPC contains about 62 kg of LXe. FIG. 1.4 (left) shows a sketch of the TPC inside its cryostat. PTFE is chosen for its well-suited properties. It is known to be radio-pure, stands the temperature conditions in the cryostat, is non-conductive and a good reflector for vacuum ultra-violet (VUV) scintillation light of xenon [35]. At its top the TPC is closed by a diving bell design. This allows to precisely control the level of liquid-gas interface independently on the filling height of the surrounding LXe in the cryostat. This makes it possible to achieve a 4π coverage of the outer LXe veto equipped with 64 PMTs. The amount of LXe in the veto volume is about 99 kg. The height of the liquid-gas interface is controlled pressurizing the diving bell by a constant inflow of gaseous xenon from the purification recirculation loop that will be explained in the following.

The aforementioned drift field $E_d = 0.53\,\mathrm{kV/cm}$ inside the LXe of the TPC is created between a 75 µm cathode mesh at $-16\,\mathrm{kV}$ mounted at the bottom of the PTFE panels of the TPC and a grounded gate mesh (the lower of the three meshes labeled “Top Mesh Stack” in FIG. 1.4 (left)) mounted on top. 40 equidistant field-shaping electrodes made of copper are running on the inside and outside of the PTFE panels and guarantee homogeneous field lines. A screening mesh is mounted below the cathode to shield electrical fields generated by the bottom PMTs. The extraction field E_g in the gas phase responsible for the proportional scintillation light (electroluminescence) is established between the grounded gate mesh and a central anode grid (125 µm thick) put 5 mm above. The anode is set to about 4.5 kV creating a field of $E_g\sim 12\,\mathrm{kV/cm}$. A third grounded mesh, again shifted by 5 mm, is installed to shield electrical fields created by the top PMT array that would otherwise distort the extraction field.

As mentioned above, two PMT arrays (bottom and top) are installed to observe the primary (S1) and secondary (S2) scintillation photons. 80 Hamamatsu R8520-06-Al 1 inch square photomultiplier tubes (PMTs), selected for low radioactivity [37], are mounted as closely as possible in the bottom PMT array. The high internal reflection at the liquid-gas interface causes about 80 % of the S1 photons to be detected by the bottom PMT array [34]. Their close arrangement provides optimal coverage to efficiently detect S1 light that is used as an energy estimator in the data analysis (see section 2.1). The position in xy is reconstructed by the hit pattern of the S2 light produced just below the top PMT array. This array consists of 98 PMTs of same type arranged in concentric circles optimized for resolution in the xy position reconstruction.

The cryostat containing the LXe TPC is placed inside a passive shield. The cryogenics

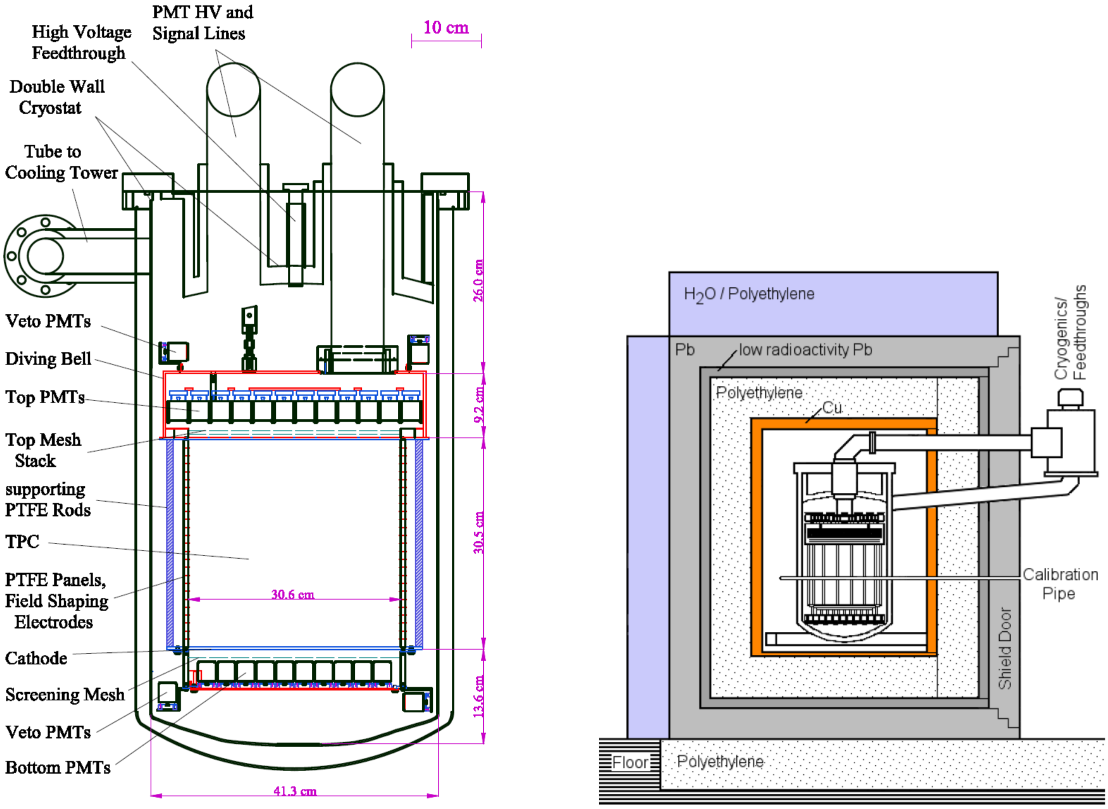

Figure 1.4: (left) Sketch of the XENON100 cryostat housing the TPC that contains up to 62 kg LXe. A diving bell structure enables the setup to maintain a gaseous xenon phase while the cryostat is filled to a height above the bell. About 99 kg of LXe surround the TPC (optically separated) implemented as active veto shielding against external radioactivity. (right) XENON100 cryostat placed in its compact shield design consisting of H_2O filled canisters and polyethylene to moderate neutrons (for their production mechanisms see [36]) and high purity copper and low radioactivity lead to shield environmental radiation. Figures taken from [34].

and electrical feedthroughs are placed outside of this shield and are connected to the cryostat by three stainless steel tubes. The passive shield is shown in FIG. 1.4 (right). It is composed of H_2O filled canisters and polyethylene to moderate and eventually stop neutrons and a combination of lead, low radioactivity lead and high purity copper to shield environmental radiation. The interior of the shield is flushed by boil-off nitrogen to mitigate air-borne radon. The background induced to XENON100 by neutrons is discussed in [36], the ER background inside the TPC is dominated by γ rays from (subsequent) decays of ^{238}U, ^{232}Th,^{40}K and ^{60}Co abundant in the detector materials [38].

The cryogenic system of Xenon100

The XENON100 detector is operated at a temperature of $-91\,^\circ\mathrm{C}$. The cooling power is supplied by a pulse tube refrigerator (PTR) [39] (model Iwatani PC150) driven by a 6.5 kW helium compressor that reaches a cooling power of 200 W at $-103\,^\circ\mathrm{C}$ [34]. A scheme of the cryogenic system is shown in FIG. 1.5. The PTR is coupled to a cold finger made of copper, i.e. the PTR itself does not belong to the cryostat's closed xenon system marked red in FIG. 1.5. Boil-off xenon from within the cryostat reaches the cold finger through a double walled stainless steel tube, liquefies at the cold finger and drops into a funnel mounted directly below. The funnel itself is connected to a pipe of smaller diameter directing the LXe back into the detector. To adjust the cooling power and avoid xenon ice forming at the cold finger, that in turn would drastically reduce the cooling power, electric heaters are mounted to the copper of the cold finger outside the closed xenon system. A proportional-integral-derivative (PID) controller adjusts the electrical power of the heater to compensate additional cooling power supplied by the PTR.

The gas handling and purification system of Xenon100

The primary scintillation signal as well as the charges of the ionization signal are adversely altered by impurities present in the liquid xenon. The main culprits are H_2O, that attenuates the mean free path of photons inside the LXe [40], and the electronegative O_2, removing charges while they are drifted from the interaction vertex towards the liquid-gas interface [41]. To achieve a reasonable light yield and drift length of electrons, impurities have to be eliminated. Xenon gas is constantly evaporated from the liquid target (green tube in FIG. 1.5 (left)) and purified by a high temperature getter at a flow rate of about 5 standard liters per minute (slpm). The purified gaseous xenon is subse-

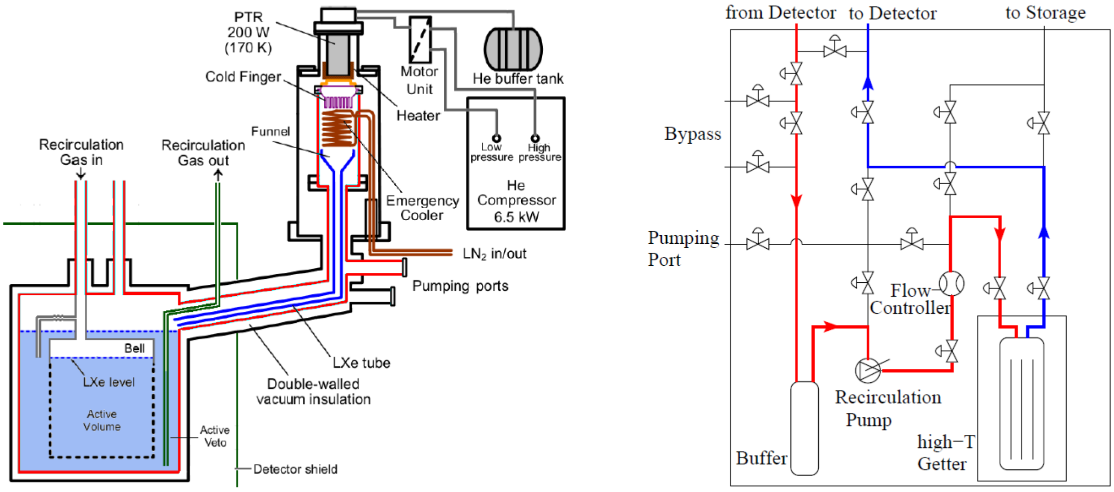

Figure 1.5: (left) Schematic of the XENON100 cryogenic system. Marked red are the parts in contact with the liquid/gaseous xenon target. In the following we will refer to these parts simply as *cryostat*. (right) Schematic of the XENON100 gas handling and purification loop (gas system). LXe is extracted from the liquid by means of a diaphragm pump, evaporates in the stainless steel gas lines and is passed through a hot getter (high-T Getter) at an operational temperature of about 400 °C for gas purification. A flow controller sets the gaseous xenon recirculation flow. The purified gas is put back to the diving bell. Figures taken from [34].

quently fed back to the diving bell structure where its mass-flow defines the level height of the liquid-gas interface. The 5 slpm are maintained by a diaphragm pump (KNF) and controlled by a mass flow controller. High temperature getter, diaphragm pump and mass flow controller are assembled in the gas handling and purification system shown in FIG. 1.5 (right). This system is fully constructed in stainless steel tubes employing fully metal sealed valves. Besides directing the recirculation loop during detector operation, the system allows to mount auxiliary equipment, for instance to draw gaseous xenon samples from the detector, as was done in this work (see chapter 3), or access the interior of the cryostat for ^{222}Rn emanation measurements (see chapter 4). Further the system is permanently connected to the xenon gas storage (4×75 l aluminum gas cylinders) in case the liquid xenon has to be recuperated from the cryostat. In this scenario, the xenon is extracted by the diaphragm pump and stored in the aluminum gas cylinders that are immersed in a liquid nitrogen (LN_2) cooling bath. After recuperation, the LN_2 can safely be removed.

The krypton distillation column

Before filling the gaseous xenon from the storage gas cylinders to the detector, the xenon gas is purified from krypton by means of cryogenic fractional distillation [42, 43]. Krypton contains the radioactive isotope ^{85}Kr that represents a serious source of background. Chapter 3 will be entirely devoted to this topic. XENON100 operates a distillation column similar to the one described in [44]. Exploiting the different vapor pressures P_i of xenon and krypton at the distillation column operation temperature ($P_{\mathrm{Kr}}/P_{\mathrm{Xe}} = 10.4$ [44]) it is possible to deplete the xenon in krypton at the bottom of the column and enrich its krypton content at the top of the column. While the depleted xenon from the bottom is fed to the detector, the krypton enriched part is removed at 1 % of the total purification flow and stored in a separate gas cylinder.

Commercially available xenon contains $^{\mathrm{nat}}$Kr at the parts per million (ppm) or, in case of high purity xenon, at the parts per billion (ppb) level. A krypton concentration level on the order of 10 parts per trillion (ppt) is needed to achieve the aimed XENON100 sensitivity. This goal has been achieved as will be shown in this work. A schematic drawing of the krypton distillation column is shown in FIG. 1.6. The column is designed to reach a reduction in the krypton level of 1000 in a single pass, at a purification speed of 0.6 kg/h. We will show in this work, that the distillation column of XENON100 reached a reduction in the krypton level by a factor of (390 ± 120) in a single pass. The same distillation column is shown to have reached the unprecedented krypton concentration of below 1 ppt (see chapter 3).

Timeline of events

FIG. 1.7 displays a timeline of events related to the XENON100 detector that are of importance for this work. Plotted by the thin black curve is the reading of a temperature sensor mounted at the bottom of the cryostat from the beginning of XENON100 science data taking until early 2013. While FIG. 1.7 (top) shows the full timeline, FIG. 1.7 (bottom) focuses ("zoom in") on the marked region between May 2012 and January 2013. After XENON100's commissioning, a first publication ("11 days") demonstrating the detector capabilities [45] was followed up by two benchmarking results [27, 46], analysing exposures of 100.9 live days ("100 days") and 224.6 live days ("225 days").

Air leak After the 11 live days science data were acquired, in December 2009 ambient air entered the system due to a leak in the diaphragm pump of the recirculation system. (10.0 ± 0.2) l of air were introduced as determined from the rapidly increasing ^{222}Rn

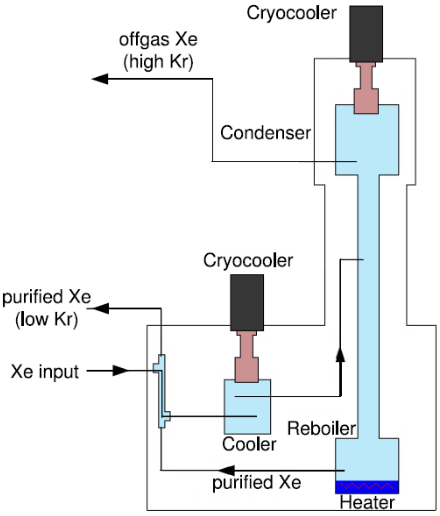

Figure 1.6: Sketch illustrating the krypton distillation column used in XENON100. The full column has a height of about 3 m. Two cryocooler are employed to maintain a purification speed of 0.6 kg/h. Figure taken from [34].

signal [47], if assuming a homogeneous distribution of ^{222}Rn in the full 161 kg LXe target. Anticipating later results, we measured the krypton concentration after this air leak with a mass spectroscopic setup (see chapter 3) to be (340 ± 60) ppt. There is no such data about the krypton level before the leak had appeared and we have to rely on a delayed coincidence method (more details in section 3.1.1) that results in $\left(143^{+130}_{-90}\right)$ ppt [45]. We want to use the updated[2] value of $^{85}\mathrm{Kr}/^{\mathrm{nat}}\mathrm{Kr} = 2 \times 10^{-11}$ that reduces the krypton concentration stated in [45] by a factor of two and consequently reads $\left(70^{+70}_{-50}\right)$ ppt. Combining both results, we compute for the amount of krypton introduced by the leak $\left(270^{+90}_{-80}\right)$ ppt. In section 3.1.2 we compute the number of krypton atoms in ambient air to be 5.1×10^{-5} mol/m^3 (see equation 3.1). At the time we drew the xenon sample from the XENON100 detector (SR8 in FIG. 1.7) the assumption of a homogeneous krypton mixture in the xenon target is supposed to be perfectly valid. 161 kg of xenon correspond to about 1226 mol (average xenon weight is 131.3 g/mol; see TAB. 3.1). Hence, 1 l of air equals ~ 42 ppt natural krypton homogeneously mixed in 161 kg xenon. Using this number, we estimate the amount of air entering in December 2009 from the increased krypton concentration to be $\left(6.4^{+2.1}_{-1.9}\right)$ l. Within 2σ both methods agree on the amount of air that entered the leak. The assumption of ^{222}Rn being homogeneously mixed in an instant, however, might not be valid. We explained above, that the xenon gas from the

---

[2] See section 3.1.2 motivating an updated ratio in comparison to the value of 1×10^{-11} that has been used in [28, 45].

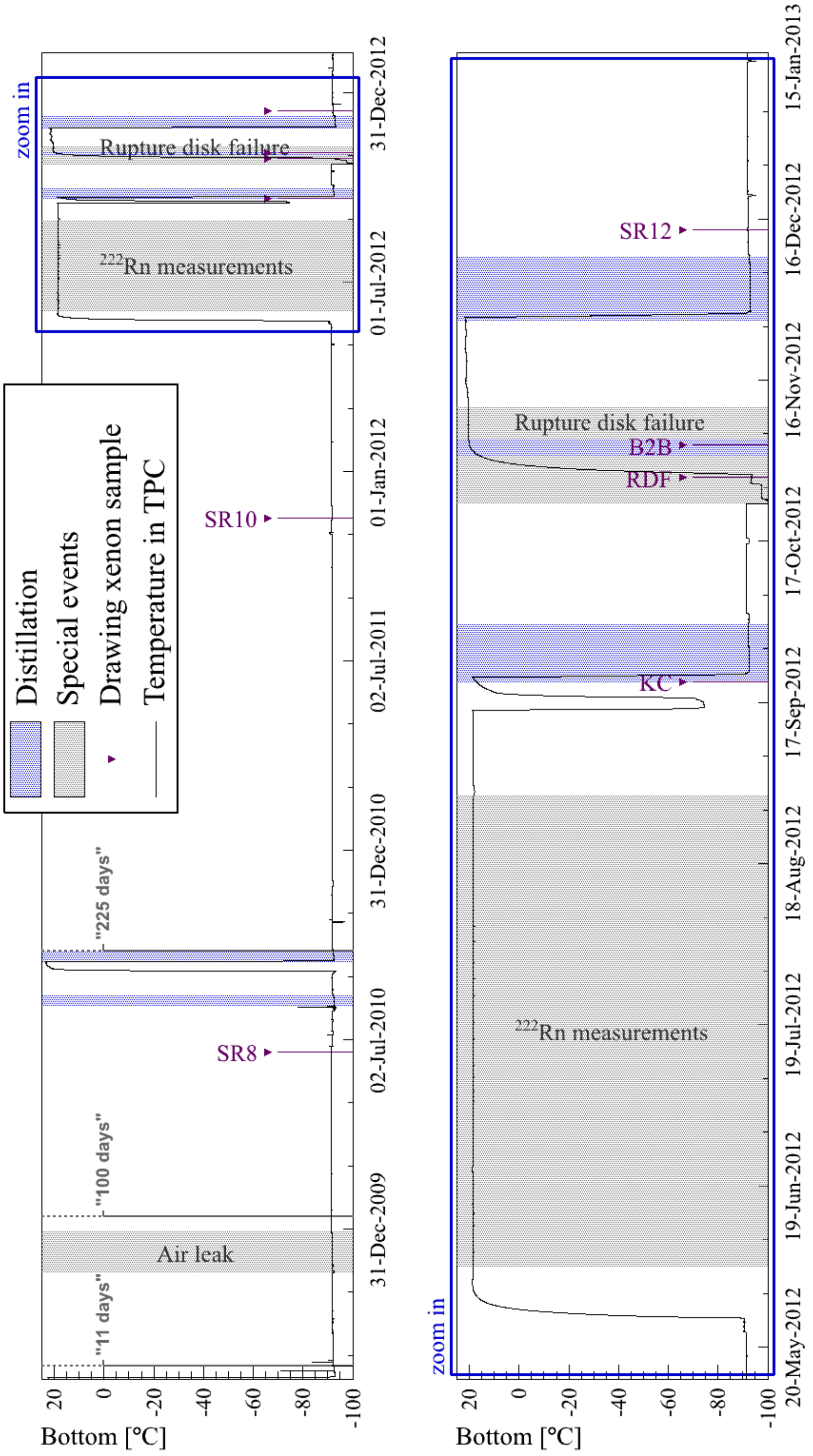

Figure 1.7: History of XENON100

diaphragm pump is directly fed to the diving bell. That is, the radon atoms have to pass the TPC first before entering the larger volume of the veto. At the recirculation flow of 5 slpm, that correspond to about 40 kg/d, it takes slightly longer than one full ^{222}Rn half-life to exchange once the full 161 kg xenon target. A somewhat enhanced ^{222}Rn signal inside the TPC thus is expected. A gradient of this type lowers the estimation on the actual amount of air that entered the system (see [47]) and, thus, the small discrepancy between both methods estimating the air leak would be reduced.

Distillation Shaded blue time periods indicate when the xenon target was first recuperated and afterwards filled again to the detector through the krypton distillation column. This sequence is nicely illustrated by the "Bottom" temperature reading increasing from its otherwise stable value of about $-91\,^{\circ}\mathrm{C}$ to ambient temperature. Once the distillation starts and the xenon is put back to the detector, the bottom temperature reading decreases again. The krypton distillations mitigated the krypton level as was observed both by a reduced background in the detector and through the assay of xenon samples drawn from the detector and analyzed in this work (see chapter 3).

Xenon samples Marked by magenta triangles, dates are indicated when xenon samples were drawn from the XENON100 detector or the krypton distillation column. Next to each magenta marker a tag is placed that identifies the sample. These identifiers will be used in the result section of chapter 3.

^{222}Rn measurement During summer 2012, the xenon target was recuperated and stored in the mentioned gas cylinders. Meanwhile ^{222}Rn emanation measurements of the cryostat and, separately, of the gas system were performed. Details on these measurements are found in chapter 4. In a nutshell, a total ^{222}Rn emanation of (11.9 ± 1.1) mBq is found at ambient temperature in this work. This number compares to (10.13 ± 0.13) mBq found by counting ^{222}Rn alpha decays [47]. Both rates agree reasonably well and we conclude that, to a good approximation, emanated ^{222}Rn is homogeneously admixed in the detector's LXe target.

A tendency of the alpha technique detecting slightly less radon, though, is observed. This supports the model we introduced to explain the different outcome of the two techniques, $^{\mathrm{nat}}$Kr and ^{222}Rn counting, that quantified the amount of air entering the leak in December 2009 (see above). We will see in chapter 4 that the total ^{222}Rn emanation can be attributed to emanation of the cryostat of (9.3 ± 1.0) mBq and of the gas recirculation-purification system of (2.6 ± 0.5) mBq. That is to say, the total emanation is dominated by the cryostat. However, the study on the air leak suggests the alpha counting technique to be particularly sensitive to ^{222}Rn entering through the purification-recirculation loop. This was attributed to the fact, that the gas from the recirculation-purification loop is directly fed into the diving bell right above the sensitive volume; while it takes about one ^{222}Rn half-life to recirculate the entire volume once. This reasoning, on the other hand, implies that ^{222}Rn atoms, that are emanated outside of the sensitive volume but inside the cryostat, will partially decay before contributing to the alpha signal. For the given shares between gas system and cryostat, the alpha technique consequently slightly underestimates the total ^{222}Rn emanation when a homogeneous concentration is assumed.

Still, we want to re-emphasize that the differences are marginal. We cannot conclude ^{222}Rn emanation in the cryostat to be suppressed by much with respect to its contribution to the overall background. Depending on their specific location, different ^{222}Rn sources inside the cryostat likely will contribute differently to the ER background. A precise forecast of this contribution based on an external ^{222}Rn emanation assay, as explained in chapter 4, likely will not surpass a systematic uncertainty of $\sim 50\,\%$ (note also the effect of an enhanced ^{222}Rn emanation to cryogenic liquids observed in [48] that we will discuss blow). Yet this technique is perfectly suited to guide material selection (see section 4.5) during construction of the next phase detector and unambiguously identifies ^{222}Rn as one of the most serious threats for the upcoming XENON1T experiment.

Rupture disk failure In late October 2012 a rupture disk failed due to insufficient cooling and a consequential pressure increase inside the detector. For some time the detector was unsealed and air was able to enter. Before this event we measured the xenon gas at the outlet of the krypton column (KC) to contain (1.0 ± 0.2) ppt. After the failure, a sample drawn from the detector (RDF) resulted in (1.8 ± 0.4) ppt. Employing again above numbers, we compute the amount of air that entered to be (19 ± 11) ml. This confirms the expectation that boil-off xenon from within the cryostat streaming out the leak mostly prevented ambient air from entering. Presumably the greatest fraction of air entered the system while the rupture disk was being dismounted and replaced.

Scientific results

The good reputation XENON100 has in the field of Dark Matter search is based on the benchmarking scientific data collected during the past three years. In the previous section we already introduced the two major science runs of 100 and 225 live days. At this point we want to give a short summary of the most noted 225 live days publication looking for the spin-independent elastic WIMP-nucleon scattering cross-section. Although not successful in discovery, the most stringent limit was set on this cross section for WIMP masses above $8\,\mathrm{GeV/c^2}$, with a minimum of $2 \times 10^{-45}\,\mathrm{cm^2}$ at $55\,\mathrm{GeV/c^2}$ and 90 % confidence level [27].

Prior to the science data taking, a distillation significantly lowered the krypton concentration introduced by the aforementioned air leak (see FIG. 1.7). A level of (14 ± 2) ppt was measured by the mass spectroscopic setup developed in this work (see SR10 in section 3.4.2). This is an improvement by a factor of ~ 25 compared to the previous science run (100 live days [28]) where a krypton level of (340 ± 60) ppt (SR8) was determined by the same method.

For the 225 live days science run a total ER background of (5.3 ± 0.6) mDRU is found inside a fiducial volume of 34 kg and the energy region of interest for the Dark Matter search [27]. Here we introduced the differential rate unit (DRU) defined as $1\,\mathrm{DRU} \equiv 1\,\mathrm{event/keV/kg/d}$. Employing the results given in [38], we can translate the krypton concentration (C_{Kr}) into an expected background index (R_{Kr}). For this simulation a ratio of $^{85}\mathrm{Kr}/^{\mathrm{nat}}\mathrm{Kr} = 1 \times 10^{-11}$ was used. Rescaling the given conversion by the updated ratio of $^{85}\mathrm{Kr}/^{\mathrm{nat}}\mathrm{Kr} = 2 \times 10^{-11}$ (see section 3.1.2), we find (see also [47]):

$$R_{\mathrm{Kr}} = 0.039 \times (C_{\mathrm{Kr}}/\mathrm{ppt})\ \mathrm{mDRU}\,. \tag{1.8}$$

Using equation 1.8 we immediately compute the ER background index created by ^{85}Kr to be (13 ± 2) mDRU and (0.55 ± 0.08) mDRU for the 100 and 225 live days science runs, respectively. Comparing these numbers to the total ER background of the 225 live days science run of $R_{\mathrm{tot}} = (5.3 \pm 0.6)\,\mathrm{mDRU}$, we observe that krypton has lost its role as dominant background source.

The Monte Carlo study presented in [38] also relates the ^{222}Rn activity concentration (C_{Rn}) in the liquid xenon to an expected background index (R_{Rn}). The following conversion is found (see also [47]):

$$R_{\mathrm{Rn}} = 0.029 \times (C_{\mathrm{Rn}}/(\mathrm{\mu Bq/kg}))\ \mathrm{mDRU}\,. \tag{1.9}$$

Anticipating again later results, we found the ^{222}Rn emanation at ambient temperature of the entire XENON100 detector to be (11.9 ± 1.1) mBq. Assuming this emanation to be unaffected by filling the cryostat with 161 kg liquid xenon, we compute a background index generated by ^{222}Rn of (2.14 ± 0.20) mDRU. [47] interpolates the external

γ radiation background indices originating from all outside materials, given in [38] for the two fiducial volumes of 40 kg and 30 kg, to the employed fiducial volume of 34 kg. A background index of $R_{\mathrm{ext}}^{34\,\mathrm{kg}} = 2.4\,\mathrm{mDRU}$ is found. Summing up the contributions of the internal backgrounds ^{85}Kr and ^{222}Rn and adding the interpolated value from the outside materials, we end up with:

$$R = R_{\mathrm{Kr}} + R_{\mathrm{Rn}} + R_{\mathrm{ext}}^{34\,\mathrm{kg}} = (5.1 \pm 0.2)\,\mathrm{mDRU}\,. \tag{1.10}$$

This value is in striking agreement with the measured value of $(5.3 \pm 0.6)\,\mathrm{mDRU}$ confirming the thorough background understanding achieved. We have to remain skeptic, though, as the equilibrium of the ^{222}Rn chain was shown to be broken inside the LXe TPC [47]. Within this chain the dominant contribution to the ER background index is generated by the low energy β continuum of ^{214}Pb disintegrations [49]. Consequently we might overestimate the radon background looking at ^{222}Rn emanation only. Also the external contribution based on a thorough material screening imply an uncertainty not specified in the results of [38]. Further we want to mention a result obtained for liquid argon (LAr) [48]. Therein, ^{222}Rn emanation was shown to increase in presence of LAr. The authors attribute their observation to stopping recoiling ^{222}Rn ions in the dense liquid; in contrast to re-implanting them into surrounding solid materials when the liquid is exchanged by a gas at the same temperature but of strongly reduced density. An increased emanation to the LAr of roughly 35 % is found. A similar effect in LXe is conceivable and would counteract the above mentioned depletion of ^{214}Po in the drift field of the LXe TPC [47]. We conclude that the achieved overall agreement is very satisfying, while there is only little room left for an additional background source not accounted for so far.

The science data of the 225 live days were acquired blinded in order to avoid any bias in the analysis, i.e. the region of interest for the WIMP analysis from 2 PE to 100 PE in S1 was not accessible below 90 % of the ER band until the data analysis was finalized and a background prediction defined. The data analysis itself will be sketched in section 2.1. The sum of neutron induced background and leakage of ERs into the NR region of interest was estimated to be (1.0 ± 0.2) events. After unblinding the full dataset, two events in the WIMP benchmark region were observed as shown in FIG. 1.8 (left). Their reconstructed spatial positions are shown in the same figure (right). The region of interest for the cut based analysis was set to range from $6.6\,\mathrm{keV_{nr}}$ to $30.5\,\mathrm{keV_{nr}}$ in energy (blue dashed and green dashed horizontal lines). In parallel to the cut-based analysis, a profile likelihood (PL) evaluation of the data was performed. The latter has

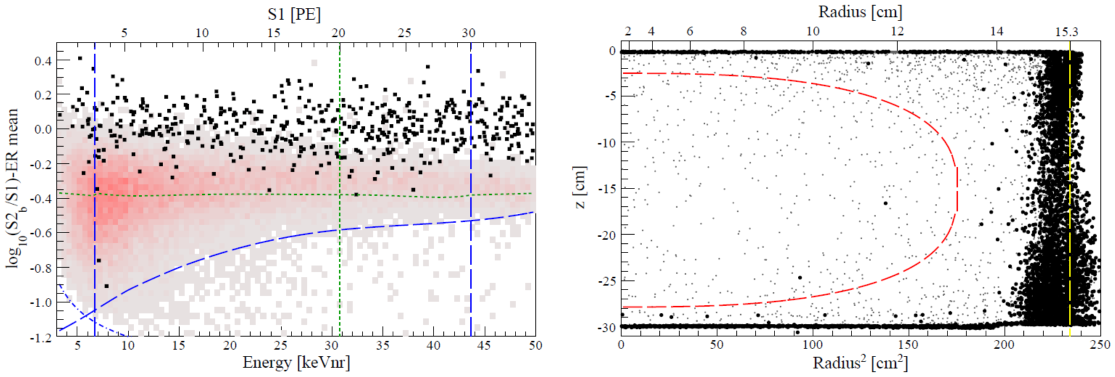

Figure 1.8: (left) Event distribution in the flattened discrimination parameter space $\log_{10}(S2_b/S1)$ observed after unblinding the 225 live days data set and applying all analysis cuts (see section 2.1) in a fiducial volume of 34 kg. Two events are visible in the WIMP benchmark region (PL analysis) in the energy range from 6.6 $\mathrm{keV_{nr}}$ to 30.5 $\mathrm{keV_{nr}}$ (dotted blue vertical lines). From above the region is confined by the 99.75 % ER rejection (green dotted horizontal line) and from below by the 99.7 % lower NR quantile (blue dashed curve). (right) Spatial event distribution of the events plotted on the left in the range from 6.6 $\mathrm{keV_{nr}}$ to 30.5 $\mathrm{keV_{nr}}$. Black circles are below the 99.75 % ER rejection line, gray points above. Indicated is the 34 kg fiducial volume (red dotted line) and the spatial appearance of the two observed events.

several advantages over the cut-based analysis as explained in [50]. The region of interest for the PL analysis was set from 6.6 $\mathrm{keV_{nr}}$ to 43.3 $\mathrm{keV_{nr}}$ (blue dashed horizontal lines). From above the region is confined by the 99.75 % ER rejection line (green dashed), from below by the 99.7 % lower NR quantile (blue dashed curve).

The two observed events are in good agreement with the background-only hypothesis resulting in an exclusion limit on the elastic spin-independent WIMP-nucleon cross-section as shown in FIG. 1.9. For a given WIMP mass assumed, the XENON100 data rejects the signal-hypothesis at 90 % confidence level for cross-sections equal or lower than indicated by the solid blue line. The expected sensitivity (yellow/green bands) and the observed exclusion limit (at 90 % confidence level, solid blue line) of FIG. 1.9 are computed from the PL technique. Still, the cut-based analysis provides a more intuitive understanding of the observation. In the cut based approach the maximum-gap method [51] is used to compute an exclusion limit that serves as cross check. Shown gray-shaded in FIG. 1.9 are theory predictions from SUSY models. Also shown in the figure are signal claims and exclusion limits from competing direct Dark Matter searches.

Besides the sketched physical reach of the XENON100 experiment for elastic scattering of WIMPs off xenon nuclei via a scalar (spin-independent) interaction, the collaboration

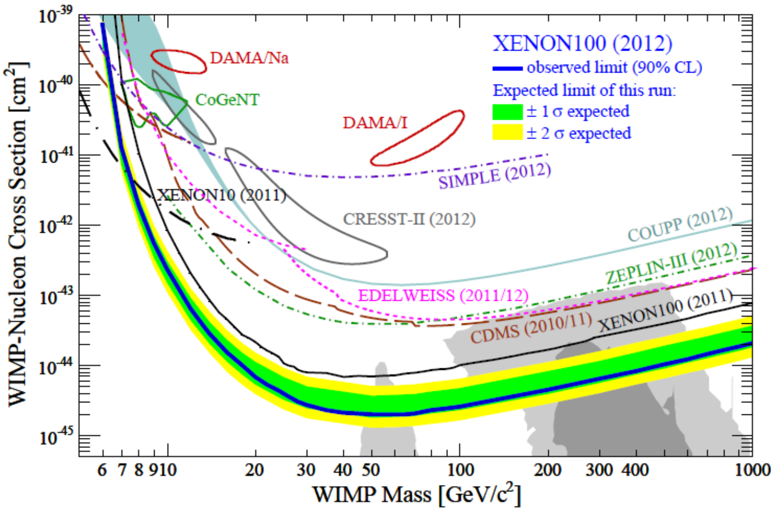

Figure 1.9: Exclusion limit on the elastic, spin-independent WIMP-nucleon scattering at 90 % confidence level (solid blue line) extracted from 225 live days (2012) acquired by the XENON100 detector. Shown are further the expected limit (green/yellow colored bands) of this science run as derived from a profile likelihood analysis. Shaded in gray are theory predictions on this cross-section. For comparison further exclusion limits and signal claims from competing direct Dark Matter search experiments are indicated. Figure taken from [27].

has performed further studies on spin-dependent scattering and inelastic Dark Matter models [21, 46].

1.2.3 The XENON1T detector

Assembly for XENON1T's water shield and active Cherenkov muon veto started in summer 2013. Succeeding the XENON100 experiment, this ton-scale experiment aims for equal success. The reader is directed to [29] where a thorough introduction to this next generation detector is given. We want to limit ourselves highlighting the main modifications that distinguishes XENON1T from the current detector generation.

Its probably most striking attribute is a 9.6 m diameter water tank (see FIG.1.10). The LXe TPC, sitting in a cryostat similar to the one of XENON100 (see FIG.1.11), will be placed in its center. Light sensitive PMTs inside the water tank will detect Cherenkov light and generate a logical veto to discriminate against high energetic muons. Muons are known to induce secondary neutrons, one of the remaining backgrounds in XENON1T. The detector will have a fiducial volume of ~ 1 t surrounded by an active LXe veto of about ~ 2 t. As in XENON100 two PMT arrays (top and bottom) will be instrumented

Figure 1.10: Artist's view of the XENON1T cryostat inside its 9.6 m diameter water shield and Cherenkov muon veto.

to detect primary (S1) and secondary (S2) scintillation light. XENON100's cubic 1 inch PMTs are going to be replaced by cylindrical 3 inch PMTs (Hamamatsu R11410). The greater spatial coverage of each single PMT will result in a total number of ∼ 300 PMTs similar to XENON100. Cooling power will be provided by two 200 W PTRs backed up by two identical spare units. A heat exchanger unit is employed to drastically reduce the cooling power necessary transferring the latent heat from the xenon taken in liquid phase from the detector to the gaseous xenon coming from the purification-recirculation loop [52, 53]. The electron drift field will be achieved biasing the cathode at 100 kV. A special low-radioactivity high voltage feedthrough was designed withstanding the high field strengths present.

To establish the electron drift over a distance of ∼ 1 m in the TPC a high purity of the liquid xenon target is mandatory. A gaseous purification-recirculation loop similar to the one of XENON100 is planned, increasing the recirculation flow from 5 slpm to 100 slpm [52, 53]. Such flow rates are achievable only by a parallelized gas purification system that is projected to contain three units consisting each of recirculation pump and high temperature getter. Other than in XENON100, the correlation between purification speed and level of liquid-gas interface is avoided. Purification loop and xenon gas stream to pressurize the diving bell will be separated. If the diving bell approach will be adopted for XENON1T is still under discussion.

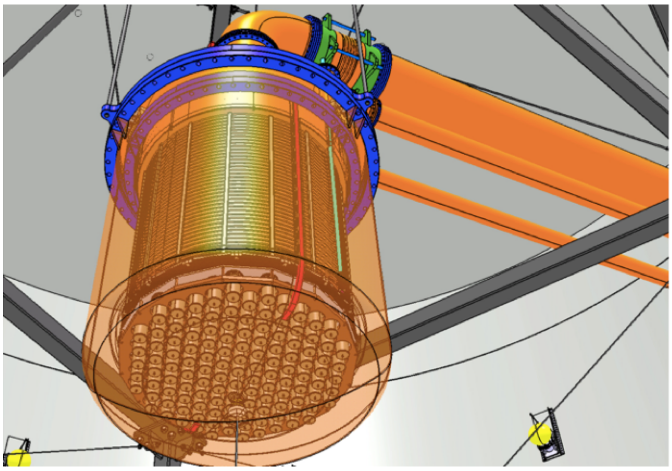

Figure 1.11: Artist's view of XENON1T's LXe TPC inside the cryostat. The bottom PMT array (cylindrical 3 inch Hamamatsu R11410 PMTs) and the long tubes connecting the cryostat to the gas system outside the water tank are shown.

Simulations showed that the water tank attenuation of fast neutrons and veto efficiency against high energetic muons is able to sufficiently suppress the NR background mandatory for XENON1T's projected sensitivity. We will show in chapter 3 that cryogenic fractional distillation has proven to reach a krypton level below 1 ppt. This was achieved using XENON100's "small" krypton distillation column. For XENON1T an improved version thereof is under construction and we are optimistic that the remaining factor of $\lesssim 10$ in the krypton level can be achieved.

The additional instrumentation needed to grant the required xenon purity for drifting electrons, create a serious problem for the electromagnetic (ER) background that originates from ^{222}Rn emanation. To avoid background from ^{222}Rn emanation in the ambient or even high temperature regions of the gas purification system, a radon mitigation system (radon removal system in the following) was proposed. This system is supposed to impede radon from entering the LXe target by the purification loop. Chapter 4 is entirely devoted to the ^{222}Rn emanation problem. We will construct a conservative projection on the ^{222}Rn emanation rate expected for XENON1T based on a ^{222}Rn assay of XENON100, discuss possible realizations of a radon removal system as well as point out its limitations. Reaching its design goal requires XENON1T to reduce the total ^{222}Rn emanation by a factor of ~ 20 compared to XENON100 (see chapter 4). If a radon removal system will prove feasible, its impact on ^{222}Rn emanation inside the cryostat is limited to roughly a factor of 2.5 (see section 4.2.2). We forecast 20 mBq ^{222}Rn emanation rate of the cryostat. The radon removal system diminishes this rate to 8 mBq. Its maximum allowed emanation rate (assuming a flat spatial concentration) is estimated in chapter 4 to be ~ 0.6 mBq. The remaining factor of ~ 10 reduction has to be achieved by other means.

One promising approach is to increase the efficiency of transporting ^{222}Rn atoms emanated inside the cryostat to the gas system. The operational radon removal system will then separate the ^{222}Rn atoms from the recirculation gas stream. A significant fraction of the ^{222}Rn atoms emanated inside the cryostat is supposed to origin from sources in contact with the gaseous xenon, e.g. the cabling and feedthroughs of the ~ 300 PMTs inside the stainless steel tube that connects the cryostat with the electronics outside the water muon shield. The largest part of the 100 slpm recirculation-purification loop will be evaporated directly from the liquid as done in XENON100 (see FIG. 1.5 (left)). A small fraction ($\sim$ 5slpm) of xenon gas will be used to push out the gas blanket formed above the LXe phase and inside the three tubes that connect the cryostat with the electronics and the gas purification-recirculation loop. Those parallelized gas streams will be merged again in the gas system and processed by the radon removal system.

Second, a possible reduction might be achieved by purging the TPC with radon-free LXe from the radon removal system. We concluded from the comparison of the estimates made on the amount of air entering the XENON100 detector in 2009, that the TPC is particularly sensitive to ^{222}Rn introduced from the gas recirculation loop. We attributed this to the fact that radon does not immediately mix in the LXe target but actually forms a gradient. Exploiting this fact should result in a reduction of the ^{222}Rn concentration inside the TPC.

A third, well established approach, realized since more than a 15 years at the Max-Planck-Institut für Kernphysik, Heidelberg (Germany), is a thorough material screening for ^{222}Rn emanation. To reach the required sensitivities ultra-low-background miniaturized proportional counters [54] are used in a sophisticated measurement procedure. We will introduce the reader to this technique in section 4.5 and present assay results relevant for this work in order to construct the XENON1T detector at a minimal ^{222}Rn emanation rate.

XENON1T is designed to be sensitive to WIMP-nucleon cross-sections (elastic, spin-independent scattering) of $\sim 2 \times 10^{-47}\,\mathrm{cm}^2$ at 90 % confidence level for a WIMP mass of 50 GeV/c^3. Compared to the passive shielding of the current generation detector XENON100, the large water tank assembled with light sensitive PMTs which turn it into a highly efficient active muon veto, represents a significant improvement. Its sensitive volume, being about a factor 20 larger than the corresponding volume of XENON100, makes the detector even more sensitive to NR multi-site events. This is an additional handle to discriminate neutron induced background from WIMP interactions (WIMPs are supposed to scatter only once). Further its sensitive volume can be adjusted (fiducial volume cut) to exploit the high self-shielding capacity of LXe. What we are left with is a fiducial volume in which the radio-purity is solely determined by the intrinsic backgrounds from ^{85}Kr and ^{222}Rn, the two isotopes investigated in this thesis.

Chapter 2

XENON100 data analysis: the ionization signal S2 and its pulse width

Seeking for Dark Matter the XENON100 experiment so far achieved unprecedented sensitivity for the spin-independent WIMP-nucleon cross section [27]. In this chapter we will outline the thorough data analysis performed that fully exploits the capabilities of the dual-phase liquid xenon TPC. In section 2.1 we give a very brief introduction to XENON100's standard data analysis (a detailed description thereof can be found in [34, 55]). Section 2.2 will recall the physical mechanisms of the secondary scintillation light (S2) focusing on its pulse width. In section 2.3 we will introduce a new method to correct the S2 pulse width for its position dependence. The longitudinal diffusion coefficient of electrons in liquid xenon and a quantification of the inhomogeneity in the distance between the field generating gate and anode grids will be given in section 2.4 and 2.5, respectively. Finally, in section 2.6, a consistency condition relating longitudinal electron diffusion (S2 pulse width) to the z coordinate of the particle interaction is defined and its impact on the Dark Matter analysis is outlined.

2.1 A brief introduction to the XENON100 data analysis

2.1.1 Data acquisition

FIG. 2.1 shows a simplified scheme of the XENON100 data acquisition (DAQ) system. The 242 PMTs are digitized by 31 Flash analog-digital-converters (ADCs) of 100 MHz sampling rate and 14 bit resolution at 2.25 V full scale. The ADCs are equipped with an on-board FPGA (field programmable gate array) that allows to digitize only parts of the total event waveform (zero-length-encoding) around signals above a predefined noise threshold. This technique reduces the file size by more than a factor of 10 (most

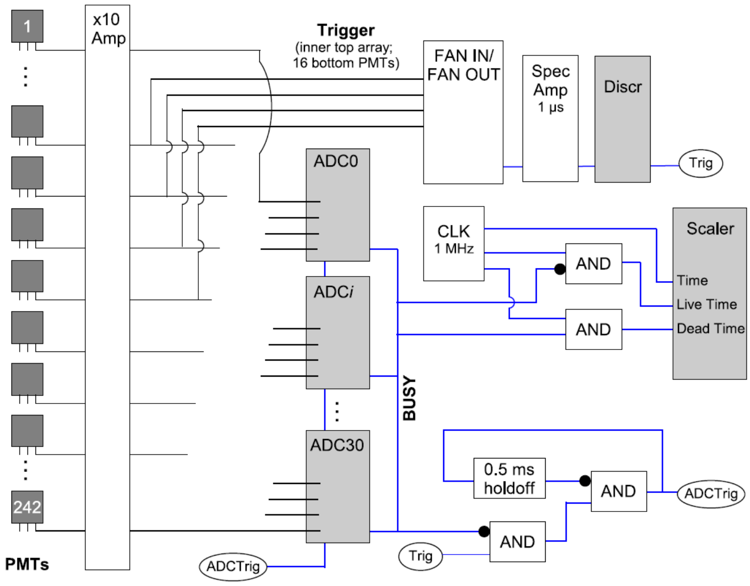

Figure 2.1: Schematics of the DAQ system employed in XENON100 with trigger configuration as used in the 100 live days publication [28]. The individual PMTs are digitized by 100 MHz, 14 bit Flash ADCs. Figure from [34].

parts of the waveforms is quiet baseline) and events can be recorded in a 400 µs wide time window centered around the triggering signal. By doing so, regardless whether a S1 or S2 triggered, the full event information is stored as the maximum electron drift time in the XENON100 TPC at 0.53 kV/cm is 176 µs. Under standard Dark Matter search conditions the background trigger rate is about 1 Hz, however, high energy γ-source calibration data of up to 30 Hz can be acquired by the DAQ system. The trigger generating logics, as sketched in FIG. 2.1 and used in the 100 live days publication [28], achieved a trigger efficiency $> 99\,\%$ for S2 signals above 300 PE. For the 225 live days publication [27] this logic was altered leading to a significantly improved trigger efficiency $> 99\,\%$ for S2 signals above 150 PE (details are found in [27, 34]).

A VME (Versa Module Eurocard) scaler, using an external 1 MHz clock and the BUSY output of the ADCs, determines the detector live time that is found to be about 99 % during Dark Matter data taking conditions.

2.1.2 Data processing

The XENON100 raw data processor, a ROOT based [56] program, is used to extract physical quantities from the raw waveforms of the 242 PMTs. Those quantities are stored event based in so called branches of the ROOT file tree. The processing of the data includes the following steps: peak identification, PMT gain correction, vertex reconstruction and position dependent signal correction.

Peak identification

The zero-length-encoded waveforms are reconstructed for every PMT and the baseline is computed and subtracted individually for each PMT and waveform fragment. For the peak finding algorithms the inner 178 PMTs (excluding ~ 5 PMTs with high dark count rates) are summed and filtered by a digital low pass filter to remove high frequencies (see section 2.2.4 and [23]). Then the algorithms recursively scan the derived waveforms for large S2 candidates. Due single electrons and afterpulses following larger S2 signals the localization of S1 candidates appearing after the main S2 signal is difficult. Hence, the raw data processor does not look for S1 signals after the largest identified S2 pulse exceeding 300 PE. This is unproblematic searching for single scatters events, as any valid S1 signal precedes its corresponding S2 pulse. The algorithm distinguishes between S1 and S2 signals by their pulse shape: the primary scintillation has a much shorter pulse width than the secondary scintillation signal that is created by electrons drifting through the gas gap (see section 2.2). For more details on the algorithms for peak finding we refer to [23, 34].

For each identified peak the raw data processor computes practical quantities such as position within the waveform, coincidence level, pulse area and width, et cetera. Monitoring the gain of each PMT on a regular basis and averaging the respective values over a few months, the peak area is converted into photoelectrons (PE). The gain itself is determined by single photoelectron emission from the photocathode using light pulses from a blue LED ($\lambda = 470\,\mathrm{nm}$) produced outside the XENON100 detector and coupled inside by means of optical fibres. The light level of the LED is chosen such that in $< 5\,\%$ of LED triggers a single photoelectron is seen by a PMT in the time window considered for the analysis. By doing so the probability for two coincident photoelectrons is sufficiently low to avoid any bias in determining the PMT gain.

Vertex reconstruction

The XENON100 LXe TPC detector design allows for a 3-dimensional vertex reconstruction on single event basis. We have to distinguish between the reconstruction in the horizontal xy plane and the reconstruction of the z component of an event in the liquid xenon. The latter is determined by the time difference $t_d \equiv t_{S1} - t_{S2}$ between the S1 and

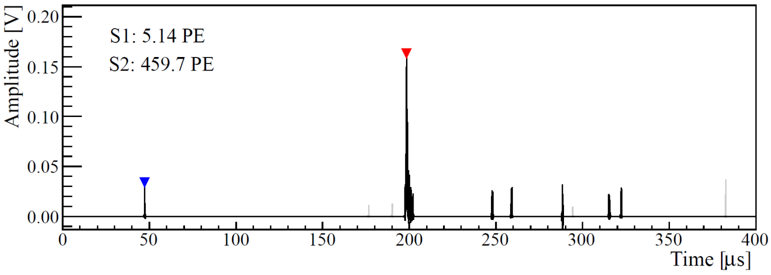

Figure 2.2: Low energetic single scatter event showing both a clear S1 (blue marker) and S2 (red marker) peak with a drift time delay of $t_d = 151\,\mu s$ used to reconstruct the z component of the interaction vertex. Figure adopted from [34].

S2 signal timestamps localized by the data processor in the waveform (by this definition the z coordinate is zero at the liquid-gas interface and < 0 in the liquid). Electrons from an ionization signal are drifted at a constant velocity v_d in the electrical field and the z component is related to the drift time t_d via the simple equation $z = v_d \cdot t_d$.

The reconstruction of the horizontal xy vertex component exploits the fact that the secondary scintillation light is produced locally in the gas gap between gate grid and anode grid (see also section 2.2) just below the top PMT array. The drift field – in a good approximation vertical (see section 2.1.2) – projects the electron cloud from the interaction vertex to the same xy coordinates in the gas gap where the secondary scintillation light results in a very clustered hit pattern on the top PMT array. Three different techniques to reconstruct the xy position have been developed (χ^2 minimization, support vector machine and neural network (abbreviated as Nn in the following)), all based on comparing a Monte Carlo generated hit pattern with the observed one. More details are found in [34] and references therein.

In a detailed study using background and ^{57}Co data, a resolution in z of 0.3 mm and in xy of < 3 mm is found, respectively. However, two coincident events in z can only be separated if they are more than 3 mm apart due to the S2 pulse width itself [34].

FIG. 2.2 shows a full 400 µs waveform summed over the inner 178 PMTs. A S1 signal (blue marker) of 5.14 PE is found at $\sim 47\,\mu s$, the corresponding S2 signal (red marker) of 459.7 PE is drift time delayed by $t_d = 151\,\mu s$ and located at $\sim 198\,\mu s$. This feature allows us to determine the z position of the interaction vertex. The S2 signal is followed by several small S2 signals from single electrons likely produced by photoionization of impurities in the xenon, triggered by the S2 light [57].

Position dependent signal corrections

To remove any position dependence in the standard WIMP analysis, these effects are corrected for on the event by event basis. Inhomogeneities of the electrostatic drift field affect the z component in the vertex reconstruction and are corrected by a detailed electrical field simulation. The size of the primary scintillation light depends on the event's vertex (x, y, z) as solid angle, reflectivity, quantum efficiency of the various PMTs, non functional PMTs, Rayleigh scattering length, transmission of the meshes, etc. affect the light collection on the PMT arrays. A 3-dimensional light collection map is constructed from calibration data to correct the S1 signals for these effects. Similar arguments hold for the light collection of the PMT arrays in xy for the secondary scintillation light where inhomogeneities in the proportional scintillation gas gap enhance the xy position dependence. 2-dimensional correction maps are derived from calibration data to correct the S2 light collection for top and bottom PMT array individually. Additionally, the S2 signal has a z dependence. Electronegative impurities present in the LXe diminish the number of ionization electrons during their drift towards the gas gap. The number of electrons lost per unit length is proportional to their absolute number and, hence, the secondary scintillation signal follows an exponential decay law (parameterized by the electron lifetime τ_e) with increasing drift time t_d. The electron lifetime is determined by weekly ^{137}Cs calibration. In section 2.3 we will describe in detail the additional correction of the S2 pulse width.

2.1.3 Calibration sources

The NR signal region, i.e. the region where a WIMP signal is expected, as well as the ER background region is determined by a variety of calibration sources applicable for XENON100. Events produced from these sources are further exploited to define above sketched position dependent corrections as well as the data quality cuts that will be depicted in section 2.1.5.

The response of the XENON100 detector to electronic recoils is studied by means of ^{137}Cs, ^{57}Co, ^{60}Co and ^{232}Th sources. While the cesium source is mainly used to determine the electron lifetime set by the level of electronegative impurities (see section 2.1.2), the flat low-energy Compton continuum spectrum of the cobalt and thorium sources define the electron recoil band.

To investigate the response to nuclear recoils, as they are expected from WIMPs scattering off Xe nuclei, an ^{241}AmBe (α, n) calibration source is used. The produced neutrons have a kinetic energy spectrum ranging roughly from 0.5 MeV to 12 MeV and induce an exponentially falling spectrum of nuclear recoils in the XENON100 detector that extends to about 250 keV. A detailed description of the source is found in [47]. The ^{241}AmBe source provides further gamma lines for electronic recoil calibration through inelastic scattering on xenon, ^{129}Xe (40 keV) and ^{131}Xe (80 keV), and neutron activation of both fluorine (abundant in the PTFE reflector) and xenon: ^{19}F (110 keV), $^{131\mathrm{m}}$Xe (164 keV), ^{19}F (197 keV) and $^{129\mathrm{m}}$Xe (236 keV).

2.1.4 Energy scales

Energy scales can be defined on the light signal (S1), the charge signal (S2) and the combination of both. Light and charge signal are known to be anti-correlated in LXe [58, 59] and a projection along the correlation axis leads to the optimal energy resolution achievable with a LXe TPC.

In section 1.2.1 we introduced the advantageous fact of different partitioning nuclear and electronic recoils have in scintillation (S1) and ionization signal (S2). This, however, results in two energy scales dependent on the type of interaction.

Electronic recoils

The energy of electronic recoils (E_{ee}) is given in electron-equivalent units (keV$_{ee}$). In XENON100 at 1 MeV the resolution is 1.9 % using the combined electronic energy scale [34], comparable with NaI(Tl) crystals. FIG. 2.3 shows the ^{241}AmBe calibration spectrum in combined energy scale (electronic recoil interactions only). While the γ-lines from the ^{241}AmBe calibration source (see section 2.1.3) are well suited to calibrate the response of the XENON100 detector to electronic recoils above 40 keV, the high self shielding capability of the XENON100 detector prevents any calibration with external gamma sources of lower energy. One possibility is the use of an internal calibration source, e.g. $^{83\mathrm{m}}$Kr [60], or to determine the scintillation yield of low energetic electrons in an external setup, for example done in [61], and interpret the result in terms of the specific features (like light yield and electric field) of XENON100.

Nuclear recoils

At the time of writing the energy scale for nuclear recoils (E_{nr}) is determined from the S1 signal only. However, recent results [47, 62] might change this for upcoming publications.

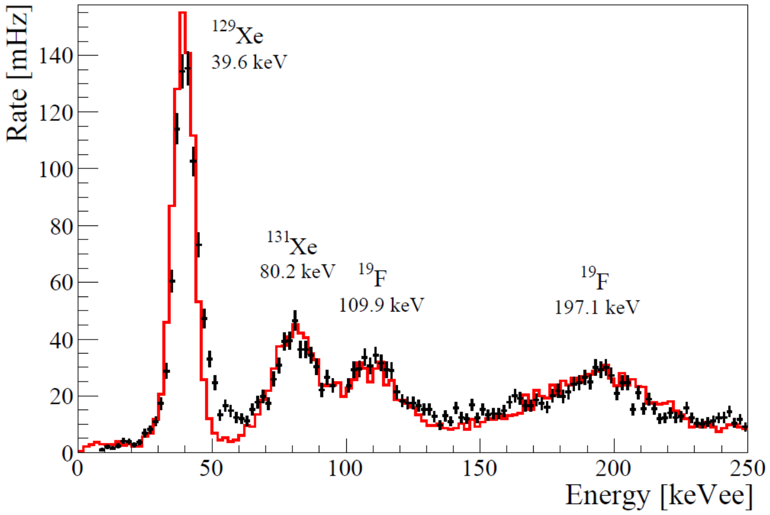

Figure 2.3: Spectrum in combined energy scale of ^{241}AmBe calibration source showing only electronic recoil interactions. Figure taken from [34].

The nuclear recoil energy is computed from the (corrected) S1 signal via:

$$E_{nr} = \frac{S1}{\mathcal{L}_{eff}(E_{nr}) \cdot L_y} \cdot \frac{S_e}{S_n}\,, \tag{2.1}$$

where L_y is the XENON100-averaged light yield (found to be $L_y = (2.28 \pm 0.04)$ PE/keV [27]), $\mathcal{L}_{eff}$ the relative scintillation yield of nuclear recoils with respect to a reference γ-line of 122 keV at zero field, and S_n and S_e are the reductions in light yield due to field quenching for nuclear and electronic recoils [55]. The relative scintillation yield of nuclear recoils $\mathcal{L}_{eff}$ is a quantity usually measured in external fixed target experiments, where the energy transfer to a xenon nucleon is determined by the scattering angle of the neutron produced in a monochromatic neutron source. A recent direct measurement of $\mathcal{L}_{eff}$ is found in [63], whereas in [62] an indirect determination of $\mathcal{L}_{eff}$ is presented extracted from the matching of Monte Carlo simulation data to ^{241}AmBe calibration data.

2.1.5 Event selection

In the standard Dark Matter analysis only data taken during stable detector operation conditions is considered. Removed are periods that exhibit increased electronic noise conditions or that show in the xy plane spiked light emission, as well as periods with xenon pressure and/or temperature values outside their nominal range. In the following we present criteria the data (on the event by event basis) has to obey in order to be accepted in the standard Dark Matter analysis. In the following we want to call these criteria *cuts*.

Data quality cuts

A 2-fold PMT time-coincidence in a 20 ns window is required for physical events in order to reject PMT dark current signals. A signal-to-noise condition requires most parts of the signal to be distributed among the main S1 and S2 peaks not the case for waveforms with a strongly variating baseline.

Single scatter selection

WIMPs are supposed to scatter (if at all) only once inside the XENON100 detector. A valid interaction therefore produces one S1 and one S2 and no coincident signal in the LXe veto. A waveform containing more S1 or S2 signals, hence, is likely to be background-induced and should be removed. However, the detector is known to produce small S2 pulses following the main S2 signal [55, 57] that could bias the single scatter selection when misidentified as second scatter. The rate of the small S2 pulses correlates with the amount of light produced by the S2 signal (photoionization of impurities [57]). The single scatter selection further requires all other S2 signals found in the trace to be below a certain threshold dependent on the main S2 signal.

Consistency cuts

Consistency cuts are conditions where additional information is available to localize an event in the LXe TPC. We introduced in section 2.1.2 the vertex reconstruction used in the standard XENON100 analysis. The position in xy is found by three algorithms comparing the PMT hit pattern from the locally produced secondary scintillation light S2 on the top PMT array. The reconstructed xy position from only one of those three algorithms is used. However, large differences in the reconstructed positions are a strong indicator for unresolved multiple scatters and such events are rejected. The two primary scintillation signals S1 from a multi scatter event are not resolved within the 10 ns wide binning of the XENON100 DAQ system. In case that the vertex of one of those two scatters happens to be in a part of the detector where no drift field is extracting the ionization electrons to the gas gap (e.g. between the bottom PMT array and the cathode) but the scintillation light is observed by the PMTs, the second S2 is missing in the waveform and the event is falsely interpreted as single scatter. As a consequence,

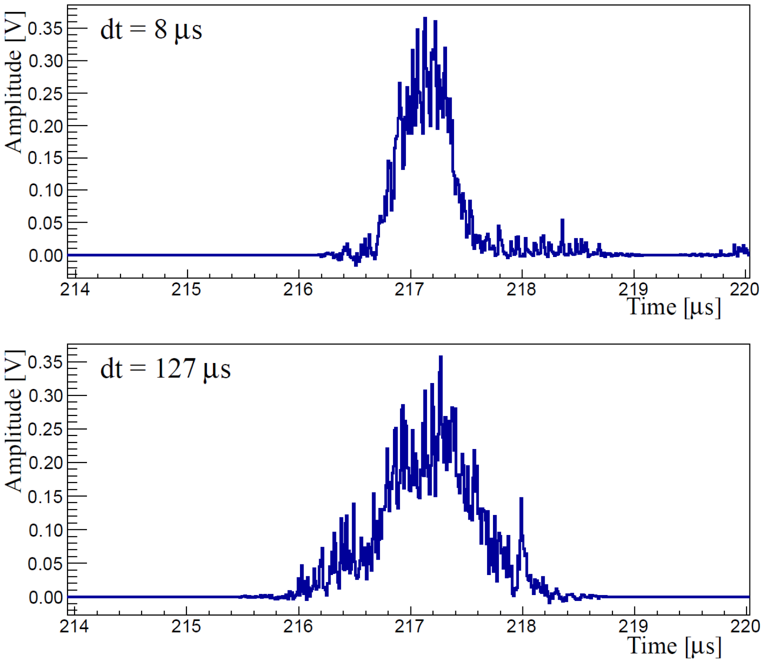

Figure 2.4: S2 pulse width examples for two signals from opposite sites in z of the LXe TPC. (top) S2 event from close to the anode at $t_d = 8\,\mu\text{s}$. (bottom) S2 event from close to the cathode at $t_d = 127\,\mu\text{s}$. Figure taken from [55].

the ER/NR discrimination parameter S2/S1 will become smaller, i.e. more NR-like (see next section), since the S1 contains the sum of two separate interactions. Such events can be (partly) removed by comparing the hit pattern of the primary scintillation light S1 with to one expected for an event of same S1 and position. The third of the consistency cuts compares the pulse width of the S2 with the expectation derived from its drift time t_d in the LXe. Diffusive broadening of the electron cloud increases the S2 pulse width with increasing t_d. An event close to the anode will have an S2 width of about 1 µs while the number almost doubles for events from the bottom of the TPC close to the cathode (see FIG. 2.4 for illustration). The cut on the S2 pulse width was tailored and optimized in this work for the detector conditions during the science run 10 and remarks a fundamental piece of the analysis of the 225 live days publications [21, 27]. Section 2.2, 2.3 and 2.6 are devoted to this topic.

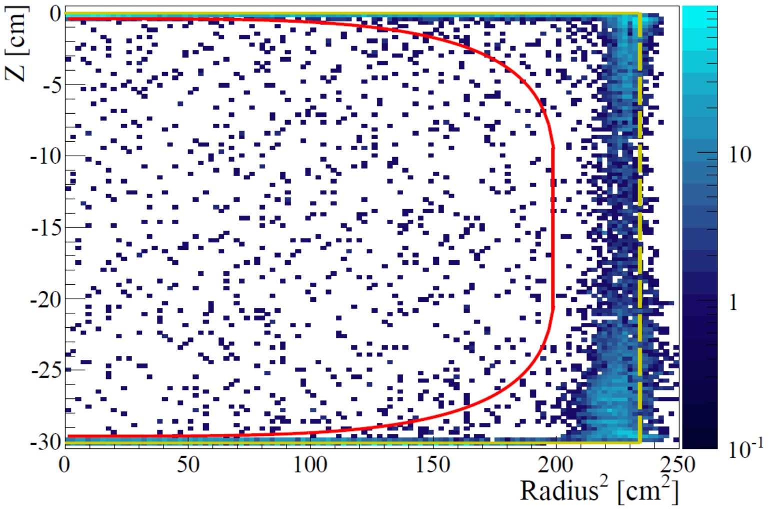

Figure 2.5: Event distribution collected in the 100 live days data set for the energy range from 8.4 keV$_{\mathrm{nr}}$ to 44.6 keV$_{\mathrm{nr}}$ [28]. In red the 48 kg fiducial volume cut is indicated. In yellow the TPC boarders are indicated. Events falling outside the boarders are due to the finite resolution of the position reconstruction algorithms. The flat distribution of events inside the fiducial volume is due to ^{85}Kr disintegrations (see also chapter 3). Figure taken from [55].

Fiducial volume cut and signal/background discrimination

The ability of the XENON100 detector to reconstruct the vertex in all three spatial dimensions allows to select events from an inner region of the detector only. This exploits the high self shielding capability of LXe removing the majority of gamma ray induced background events from disintegrations of radioactive impurities sitting e.g. in the PMTs. FIG. 2.5 shows the spatial distribution (z versus r^2) inside the LXe TPC of all events surviving above explained data cuts in the energy range from 8.4 keV$_{\mathrm{nr}}$ to 44.6 keV$_{\mathrm{nr}}$ as observed in the 100 live days data set [28]. The applied fiducial volume cut is indicated in red confining the target mass to 48 kg. FIG. 2.5 was chosen to be shown as it nicely illustrates the uniformly distributed events inside the inner TPC that are introduced by ^{85}Kr disintegrations homogeneously mixed in the xenon. Chapter 3 will discuss in great detail this background.

In section 1.2.1 we introduced already the advantageous fact of electronic recoils leading to a different ionization density than nuclear recoils. The recombination probability of electrons and ions is a function of this ionization density and results in different ratios S2/S1 for the two interaction types, with the ionization signal S2 being suppressed for WIMP like nuclear recoils. FIG. 2.6 shows the two distributions of electronic (top) and

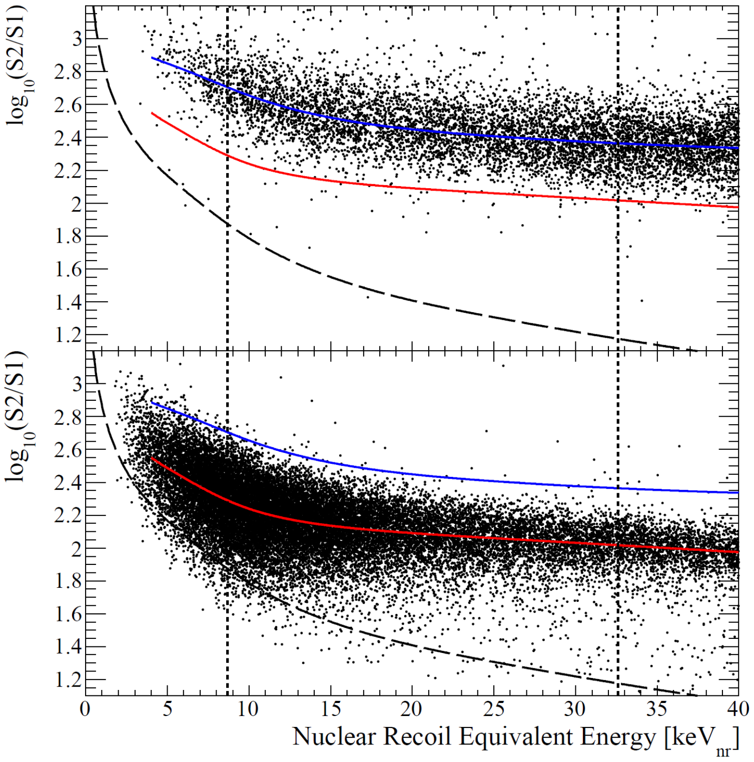

Figure 2.6: Discrimination parameter space $\log_{10}(S2/S1)$ versus the nuclear recoil equivalent energy (E_{nr}) estimated from $S1$. Electronic (top) and nuclear (bottom) recoil bands form calibration data (^{60}Co and ^{241}AmBe respectively) are shown together with their colored medians. Figure taken from [45].

nuclear (bottom) recoils in this particular S2/S1 discrimination space. The electronic recoil band, shown with its corresponding blue median, was calibrated by a ^{60}Co source. The nuclear recoil band (red median) is calibrated by the ^{241}AmBe neutron source [45]. Blue and red medians are obviously separated. Accepting the lower $\sim 50\,\%$ of the nuclear recoils, $\sim 99.5\,\%$ of the electronic recoils are rejected.

2.2 The secondary scintillation light S2 and its pulse width

In Xenon100 free electrons, that are created inside the TPC by ionizing radiation, are drifted upwards in the electric field of $E_d = 0.53\,\text{kV/cm}$ [34]. When passing the gate grid (see FIG. 2.7) the electrons are extracted from the liquid to the gas phase by an about ten times higher electric field at an extraction efficiency close to 100 % [34]. Electroluminescence describes the mechanism of electrons gaining kinetic energy in an external field above the scintillation ($\sim 1\,\mathrm{kV/(cm\,bar)}$) but below the ionization ($\sim 5\,\mathrm{kV/(cm\,bar)}$) threshold [64]. In this regime the amount of light produced per electron drift length is proportional to the electric field and the electron drift length [31]. In the XENON experiment the electric field in the gas gap, that has a fixed width d_g, is set to operate in this regime where the amount of ionization charge, thus, can be determined by the proportional scintillation light S2 seen by the PMTs.

The signals from the PMTs are digitized (see section 2.1.1) at a rate of 10 ns. The peak area is integrated for each PMT by the raw data processor for each identified peak. The resulting parameter S2 (converted to PE) is then a direct measure for the ionization electrons initially produced. The relative arrival time of the secondary scintillation photons, which are produced by the extracted electrons drifting in the electrical field of the gas gap, is stored in the ROOT branches (see section 2.1.2) S2sWidth, that is the S2 pulse width at 50 % height (FWHM), and S2sLowWidth, the width of the S2 pulse at 10 % height[1]. The latter is more sensitive to the non-Gaussian tails of the S2 pulses - a feature exploited in the S2 width cut of section 2.6.

2.2.1 Electric field in gas gap

Following the reasoning in [65], the electric field in the gas gap can be computed approximating gate and anode grids as parallel plates, i.e. ignoring their wire structure. The plates form a capacitor filled with a dielectric fluid (liquid xenon) and a dielectric gas (gaseous xenon).

As there are no free charges except on the capacitor, following Gauss's law, we find the electrical field E to be perpendicular to the grids and the electric displacement field D constant along the liquid-gas interface ($D = D_g = D_l$). In a linear, homogeneous, isotropic dielectric (xenon can be treated as such) both fields are related by the dielectric's permittivity, ϵ, via $D = \epsilon E$, and thus the following relation holds ath the liquid-gas interface:

$$\epsilon_g E_g = \epsilon_l E_l \,. \tag{2.2}$$

For this simple capacitor the equations $U = U_g + U_l$ and $E = U/d$ hold and we find:

$$\frac{U}{d} = E_g \left[\frac{d_g}{d} + \frac{\epsilon_g}{\epsilon_l} (1 - \frac{d_g}{d}) \right] \,, \tag{2.3}$$

---

[1] In the remainder of this work we will at times refer to these quantities as $\Gamma_{50\%}$ and $\Gamma_{10\%}$, respectively.

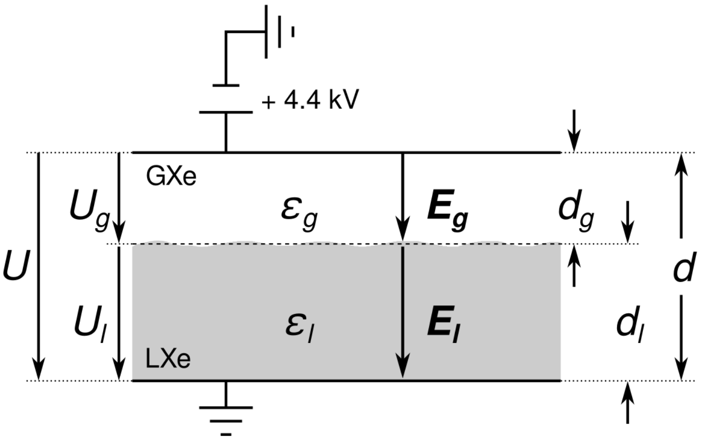

Figure 2.7: The figure illustrates the distances and electric fields between the gate grid, the liquid-gas interface (dashed line) and the anode grid. The indicated voltages supplied to gate and anode correspond to the settings used during the data taking for the XENON100 225 life days publication [27]

or

$$E_g = \frac{U}{\frac{\epsilon_g}{\epsilon_l} \cdot d + (1 - \frac{\epsilon_g}{\epsilon_l}) \cdot d_g}$$

$$E_l = \frac{U}{d + (\frac{\epsilon_g}{\epsilon_l} - 1) \cdot d_g} \tag{2.4}$$

The ratio of the permittivity of gaseous and liquid xenon can be approximated to be 0.5[2] and Equations 2.4 simplify to

$$\frac{\epsilon_g}{\epsilon_l} \approx 0.5 \quad \Rightarrow \quad \begin{aligned} E_g &\approx 2 \cdot (1 + d_g/d)^{-1} \cdot U/d \\ E_l &\approx (1 + d_g/d)^{-1} \cdot U/d \end{aligned} \quad \Rightarrow \quad E_g \approx 2 \cdot E_l \tag{2.5}$$

In the XENON100 experiment we have $d = 5\,\mathrm{mm}$ [34]. At the high voltage of $U = 4.4\,\mathrm{kV}$ (corresponding to the conditions during science run 10) we compute a value for $U/d = 8.8\,\mathrm{kV/cm}$ and find the field in the gas gap to range from $8.8\,\mathrm{kV/cm}$ to $17.6\,\mathrm{kV/cm}$ depending on the liquid level (see equation 2.5).

---

[2] $\epsilon_r(GXe) = 1.00127$ and $\epsilon_r(LXe) = 1.880$ [66]

2.2.2 Electron mobility and electron drift velocity in gaseous xenon

The electron drift velocity $v_{\mathrm{d,\,GXe}}$ in the GXe gas gap is given by the electron mobility μ times the electrical field E. We can express the latter in terms of the reduced field E/N (expressed in units of Townsend $1\,\mathrm{Td} = 10^{-17}\,\mathrm{V\,cm^2}$ [67]) and write

$$v_{\mathrm{d,\,GXe}} = \mu N \cdot E/N\,, \tag{2.6}$$

where N is the number density of xenon particles. At XENON100's operation conditions of about 2.2 bar and −90 °C we compute the number density of xenon to be about $N = 9 \times 10^{19}/\mathrm{cm}^3$ [68], thus we are interested in the electron drift velocity for a range of the reduced field from 10 Td to 20 Td.

A collection of experimental and simulated data of the parameter μN in gaseous xenon can be found in [69]. In the range of interest (10 Td to 20 Td), we can linearly approximate μN as a function of the reduced field:

$$\mu N = p_0 + p_1 \cdot E/N\,, \tag{2.7}$$

and find $p_0 = (0.567 \pm 0.013)\,\mathrm{mm/\mu s/Td}$ and $p_1 = (0.0033 \pm 0.0014)\,\mathrm{mm/\mu s/Td^2}$ reading from FIG. 17 in [69]. To a good approximation we can further neglect parameter p_1, find the electron mobility in the range of interest constant and, hence, the electron drift velocity proportional to the electrical drift field applied. In numbers, the electron drift velocity ranges from 6 mm/µs to 13 mm/µs depending on the liquid level for the high voltage settings in XENON100.

2.2.3 The S2 pulse width and its xy-dependence

The S2 pulse width Γ consists of the following components:

Γ_a: Intrinsic width of the electron cloud due to the interaction. It depends on the type of interaction and the amount of deposited energy. For the energy range of interest its contribution can be neglected [70].

Γ_b: Spread of the electron cloud due to diffusive broadening in the LXe phase. It depends on the drift time t_d in LXe, i.e. on the z coordinate of the interaction. This property is exploited to enhance the data quality by defining a consistency condition. See section 2.2.4 and 2.6.

Γ_c: Spread of the electron cloud due to the finite probability of extracting an electron from the liquid to the gas phase in a given time interval (cross-phase emission probability – see [71] and references therein). It depends on the electrical fields at the liquid-gas interface and, hence, on the width of the gas gap d_g, the distance d between gate and anode grids and the high voltage U_{HV} supplied to the anode.

Γ_d: Spread in time a single electron produces secondary scintillation light along its trajectory from the liquid-gas interface to the anode. Once the electrons are in equilibrium with the electric field, the electrons drift at a constant velocity $v_{\mathrm{d,\ GXe}}$. The spread in time the secondary scintillation light is produced, can be approximated by a boxcar function f_0 of size σ_0 that is directly related to the size of the gas gap d_g. See section 2.2.5 for more details on the drift time dependence of the S2 pulse width.

Assuming all four components to be Gaussian distributed, the S2 pulse width can be expressed as:

$$\begin{aligned}\Gamma &= \sqrt{\Gamma_a^2 + \Gamma_b^2 + \Gamma_c^2 + \Gamma_d^2} \\ &= \sqrt{\Gamma_a^2(S2, \text{interaction}) + \Gamma_b^2(t_d) + \Gamma_c^2(U_{HV}, d_g, d) + \Gamma_d^2(U_{HV}, d_g, d)}\end{aligned} \tag{2.8}$$

The components Γ_c and Γ_d depend on the same quantities and are experimentally difficult to separate, thus they are absorbed into $\Gamma_e^2 \equiv \Gamma_c^2 + \Gamma_d^2$. In XENON100 the radial symmetry is broken due to slightly warped grids (mesh warping), and the distances d and d_g themselves are dependent on the xy position.

For fixed high voltage U_{HV} and liquid level d_g we can split Γ_e into a constant pedestal plus a small xy deviation ϵ_{xy}:

$$\Gamma_e = \hat{\Gamma}_e + \epsilon_{xy} \, ,$$

For a fixed xy position equation 2.8 simplifies to:

$$\begin{aligned}\Gamma(xy) &= \sqrt{\Gamma_a^2 + \Gamma_b^2 + (\hat{\Gamma}_e + \epsilon_{xy})^2} \\ &= \sqrt{\Gamma_a^2 + \Gamma_b^2 + \hat{\Gamma}_e^2 \left(1 + \frac{\epsilon_{xy}}{\hat{\Gamma}_e}\right)^2} \\ &\approx \Gamma_0 + \frac{\hat{\Gamma}_e}{\Gamma_0} \cdot \epsilon_{xy} \, ,\end{aligned} \tag{2.9}$$

where $\Gamma_0 = \sqrt{\Gamma_a^2 + \Gamma_b^2 + \hat{\Gamma}_e^2}$ and using the smallness of $\epsilon_{xy}/\hat{\Gamma}_e$ to approximate the equation in the last step neglecting higher order terms in $\epsilon_{xy}/\hat{\Gamma}_e$.

The result of equation (2.9) can be understood in the following way: For given detector settings (liquid level, high voltage, grid positions), a fixed energy deposition and a defined interaction type (electronic or nuclear) the time spread of the signal produced by the electron cloud (S2 pulse width) depends on the drift length in the detector *plus* a correction factor. This correction factor depends not only on the xy position of the interaction (ϵ_{xy}) but again on the z coordinate (t_d), the interaction type (interaction) and the energy deposition ($S2$): $\hat{\Gamma}_e/\Gamma_0 = \hat{\Gamma}_e/\Gamma_0(t_d, S2, \text{interaction})$.

$$\frac{\hat{\Gamma}_e}{\Gamma_0} = \frac{\hat{\Gamma}_e}{\sqrt{\Gamma_a^2 + \Gamma_b^2 + \hat{\Gamma}_e^2}} = \frac{1}{\sqrt{1 + \frac{\Gamma_a^2 + \Gamma_b^2}{\hat{\Gamma}_e^2}}} \tag{2.10}$$

$$\Rightarrow 0 < \frac{\hat{\Gamma}_e}{\Gamma_0} < 1$$

From equation 2.10 it becomes obvious that the width correction has to be maximal for the minimal drift time, i.e. it should decrease with t_d. Refer to FIG. 2.12 as proof of this statement.

2.2.4 Mesh warping and gas gap determination

XENON100 is sensitive to the total S2 pulse width, i.e. to the z component of the convolution of (a) the intrinsic width of the electron cloud, (b) the electron cloud broadening due to diffusion in the LXe, (c) broadening at the liquid-gas interface, and finally (d) duration of a single electron passing the GXe gap from the liquid-gas interface to the anode. First, we are interested in the mesh warping, that is the xy dependence of the distances d and d_g (see FIG. 2.7). It effects the drift time and drift velocity in the gas gap, but also the transition from liquid to gas phase. A priori we do not know the relative sizes of the contributions and, hence, cannot relate variations in the S2 pulse width to an absolute mesh warping. However, we can make the following assumptions:

1. $\Gamma_a^2 + \Gamma_c^2 \ll \Gamma_b^2 + \Gamma_d^2$,
2. $\Gamma_b = 0$ for interactions at the top of the TPC ($t_d \to 0$),

and, hence, assume for the S2 pulse width from interactions at the top most LXe layer $\Gamma_0 \approx \Gamma_d$. That is to say, the S2 pulse width is solely determined by the duration a single electron drifts in the gas gap and produces secondary scintillation light. The first assumption is supposed to hold as the spacial extent of the electron cloud produced by a recoiling nucleus is $< 0.1\,\mu\text{m}$ [70] and the effect of delayed emission is highly disfavoured in data looking at single electron signals [57]. Under these assumptions equation 2.9 simplifies to

$$\Gamma(xy) \approx \hat{\Gamma}_d + \epsilon_{xy}\,. \tag{2.11}$$

Our assumption states that the spread of an electron cloud from an interaction at the top most LXe layer is negligible and that all electrons are extracted simultaneous to the gas phase. Along their trajectory, starting from the liquid-gas interface until the anode, the electrons will produce secondary scintillation light. We have seen in section 2.2.2 that the drift velocity of electrons is constant inside the gas gap. The time duration the secondary scintillation light is recorded, i.e. the S2 pulse width, thus is simply given by:

$$\hat{\Gamma}_d = \langle d_g\rangle / v_d(U_{HV}, \langle d_g\rangle, \langle d\rangle)\,. \tag{2.12}$$

Equation 2.12 in principle can be exploited to determine d_g. However, we face a technical problem when measuring $\Gamma(xy)$. The data processor used in XENON100 applies a digital filter to the entire waveform to smooth out high frequency components. The filter is a raised cosine low-pass filter with a cut-off frequency at 3 MHz (see FIG. 2.8 and [23]). Only afterwards the S2 pulse width is computed as the width at 50 % ($\Gamma_{50\%}$) and 10 % ($\Gamma_{10\%}$) of the S2 pulse's full height. Doing so, the physical relation between $\Gamma(xy)$, that is the boxcar like arrival time of the secondary scintillation light of width σ_0 (see section 2.2.3), and the parameters accessible ($\Gamma_{50\%}$ and $\Gamma_{10\%}$) is lost (see FIG. 2.8 illustrating this). The relation between the physical width $\Gamma(xy)$ and the width determined by the data processor after having filtered the data ($\Gamma_{10\%}$ or $\Gamma_{50\%}$), to a first approximation they are related by a constant $\Gamma(xy) = \Gamma_{10\%} \times a_{10\%} = \Gamma_{50\%} \times a_{50\%}$, can be studied investigating the S2 pulse width of e.g. single electrons. Their S2 pulse width is only determined by the duration in which the electron produces secondary scintillation light while drifting in the gas gap towards the anode and, thus, present a clean dataset to evaluate equation 2.12 and determine $\langle d_g\rangle$ or even $d_g(xy)$.

However, we can eliminate this unknown relation and extract informations about the mesh warping. Looking at the relative difference between the S2 pulse width at a certain position in xy, i.e. $\Gamma(xy)$, and its average $\hat{\Gamma}_d$, we find:

$$\begin{aligned}\frac{\epsilon_{xy}}{\hat{\Gamma}_d} &\overset{(2.11)}{=} \frac{\Gamma(xy) - \hat{\Gamma}_d}{\hat{\Gamma}_d} = \frac{\Gamma(xy)}{\hat{\Gamma}_d} - 1 = \frac{\Gamma_{10\%}(xy)}{\hat{\Gamma}_{d,\,10\%}} - 1 \\ &\overset{(2.12)}{=} \frac{\langle d_g\rangle + \epsilon}{\langle d_g\rangle} \cdot \frac{v_d(U_{HV}, \langle d_g\rangle, \langle d\rangle)}{v_d(U_{HV}, \langle d_g\rangle + \epsilon, \langle d\rangle + \epsilon + \delta)} - 1\,,\end{aligned} \tag{2.13}$$

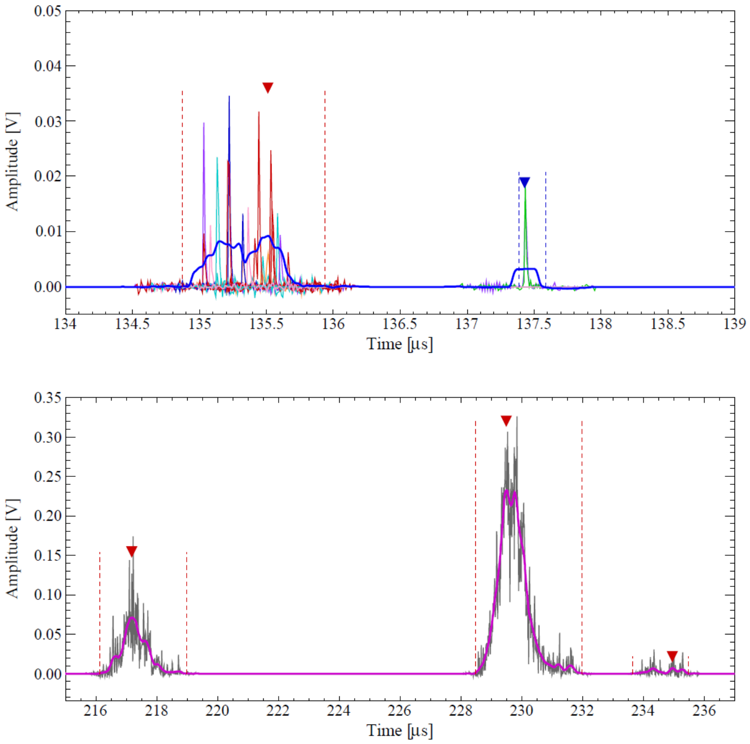

Figure 2.8: Summed PMT waveforms from events seen by the XENON100 detector and processed by the raw data processor. (top) Single electron S2 pulse (red marker) and S1 pulse (blue marker). In blue the corresponding filtered signal is shown. (bottom) S2 pulses (red markers) from multi-electron events. In magenta the filtered waveform is shown. The more electrons are producing secondary scintillation light for one single event (S2 pulse) the better the pulse is described by a Gaussian. Figure from G. Plante [23].

where we used the assumption made in equation 2.11, introduced a local warping of both anode grid ($\langle d_g \rangle \to \langle d_g \rangle + \epsilon$) and gate grid ($\langle d \rangle \to \langle d \rangle + \epsilon + \delta$) and applied equation 2.12 in the last step. In the following we want to denote the average distances (gate to anode and liquid level to anode) simply by d and d_g, respectively, neglecting the mathematical symbols for the average.

In our range of interest from 10 Td to 20 Td, μN is approximately constant and the electron drift velocity proportional to the drift field ($v_{\mathrm{d,\,GXe}} \propto E_g$, see equation 2.6). Hence, the proportionality factor cancels and equation 2.13 simplifies to:

$$\begin{aligned}\frac{\epsilon_{xy}}{\hat{\Gamma}_d} &= (1 + \frac{\epsilon}{d_g}) \cdot (1 + \frac{\epsilon + \epsilon + \delta}{d + d_g}) - 1 \\ &= \frac{\epsilon}{d_g} + \frac{2\epsilon + \delta}{d + d_g}\,,\end{aligned} \tag{2.14}$$

where we made use of $E_g = 2 \cdot U_{HV}/(d + d_g)$ (see equation 2.5) and neglected higher order terms in ϵ and δ. Assuming the mesh warping to be approximately the same for gate and anode grids ($\epsilon \approx \delta$), we can compare the warping which only one grid ($\delta = 0$ or $\epsilon = 0$ in equation 2.14) would have on the relative S2 pulse width variations across the xy plane. We find warping of the gate grid only ($\epsilon = 0$) to be suppressed in the quantity $\epsilon_{xy}/\hat{\Gamma}_d$ by at least a factor of four (this is the case for $d_g = d$). The smaller the ratio d_g/d gets, the more the warping effect by the gate grid will be suppressed in comparison to the effect by warping of the anode (keeping the absolute size of $\epsilon \approx \delta$ constant). Under the assumption $\epsilon \approx \delta$ we can also solve equation 2.14 for the relative anode warping (ϵ/d_g):

$$\frac{\epsilon}{d_g} = \frac{d + d_g}{d + 4d_g} \cdot \frac{\epsilon_{xy}}{\hat{\Gamma}_d}\,. \tag{2.15}$$

In section 2.3 we will see that the quantity $\epsilon_{xy}/\hat{\Gamma}_d$ is accessible in data and we can exploit equation 2.15 to determine the amount to which the anode grid in XENON100 is warped.

2.2.5 S2 pulse width dependence on drift time in LXe

An electron cloud drifting in the electrical field of 0.53 kV/cm needs 176 µs to travel through the full TPC height of 30.6 cm. This translates into a drift velocity in the liquid xenon of $v_{d,\,\mathrm{LXe}} = 0.174\,\mathrm{cm/\mu s}$ – in good agreement with the measurements of [72] at the corresponding electrical field. Following the suggestion made in [73] we treat the initial distribution of n_0 electrons as point like (the spacial extent of the electron cloud produced by a recoiling nucleus is $< 0.1\,\mu\mathrm{m}$ [70]), neglect its transverse motion (a measurement thereof can be found in [74]) and write the distribution (in co-moving coordinates) at time t_d relative to its point like creation at $t_d = 0$ (Brownian motion):

$$n(t_d) = \frac{n_0}{\sqrt{4\pi D_L t_d}} \cdot \exp\left(\frac{-z^2}{4D_L t_d}\right), \tag{2.16}$$

with the mean square displacement $\langle z^2 \rangle$ of this (normal) distribution found to be:

$$\sigma_z^2 \equiv \langle z^2 \rangle = 2D_L t_d\,. \tag{2.17}$$

Therein D_L denotes the diffusion coefficient in longitudinal direction, i.e. along the electrical field lines.

We denoted above the z component of the electron cloud by the S2 pulse width component Γ_b (see section 2.2.3). This component can be related to the mean square displacement σ_z by the drift velocity $v_{d,\,\mathrm{LXe}}$ of the electrons in the liquid xenon. At this point we have to be careful with our nomenclature: Γ_b denotes the drift time dependent S2 pulse width without specification of how this width is measured. Contrary to this, σ_z is well defined as 1/2 of the width of a Gaussian shaped pulse at $\sqrt{1/e}$ of its full height. Let us introduce the corresponding quantities σ_e and σ_{dt} following [73]. The former characterizes the full S2 pulse width, the latter only the drift time dependent component thereof. Assuming the S2 pulse width to be Gaussian, we can directly relate σ_e to the available quantities used in XENON100 (see section 2.1.2): $\sigma_e = \Gamma_{10\%} \cdot (8\ln(10))^{-1/2} = \Gamma_{50\%} \cdot (8\ln(2))^{-1/2}$. Neglecting again both the initial intrinsic width of the electron cloud due to the interaction (Γ_a) and the width contribution (Γ_c) of the finite cross-phase emission probability, we can write:

$$\sigma_e^2 \approx \sigma_{td}^2 + \sigma_0^2\,, \tag{2.18}$$

where, as done in section 2.2.3, the average proportional scintillation distribution f_0 from a single electron is modeled by a boxcar function with standard deviation σ_0.

The approximation of equation 2.18 holds as long as σ_{dt} and σ_0 are similar within 20 % [73] and is exact (we have made this assumption earlier in equation 2.8) in case f_0 is Gaussian with standard deviation σ_0.

In this framework we can access the diffusion coefficient D_L by fitting equation 2.19, a combination of equation 2.16 and 2.18, to the data fixing the drift velocity $v_{d,\,\mathrm{LXe}}$ of the electrons to the value given above and leaving σ_0 and D_L free to float. The outcome

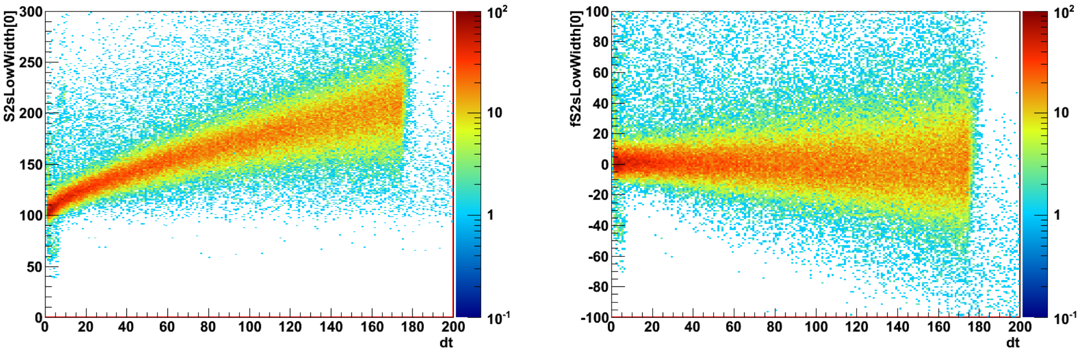

Figure 2.9: Comparison between the S2 pulse width (S2sLowWidth, left) and the flattened (fS2sLowWidth, right) version thereof. The drift time (t_d) is in units of µs, the S2 pulse width in units of 10 ns.

of fits to the data thereby of Xenon100 is presented in FIG. 2.14 and section 2.4.

$$\sigma_e = \sqrt{\frac{2D_L t_d}{v^2_{d,\,\mathrm{LXe}}} + \sigma_0^2} \tag{2.19}$$

2.3 Correcting the S2 pulse width

To determine the S2 pulse width correction map (ϵ_{xy}) we fit an effective version of equation 2.9 of the form:

$$f\Gamma(x,y) = \epsilon_{xy} \cdot \exp(m \cdot t_d)\,, \tag{2.20}$$

where $f\Gamma(x,y) = \Gamma(x,y,t_d) - \Gamma_0(S2,t_d)$ is the drift time flattened version of the S2 pulse width and the more complicated functional behavior of $\hat{\Gamma}_e/\Gamma_0$ of equation 2.9 is approached by an exponential ($\hat{\Gamma}_e/\Gamma_0 \approx \exp(m \cdot t_d)$). That is, to first order the t_d dependence is removed by subtracting the distributions mean for each slice in t_d (see FIG. 2.9).

Γ_0 is extracted from data by cutting on small radii where the xy dependence is weak (this we will see in the following). ϵ_{xy} in equation 2.20 becomes the xy correction map for the flattened S2 width, i.e. we can use ϵ_{xy} and $\exp(m \cdot t_d)$ to correct the data and define the three variables[3]:

$$\begin{aligned} f\Gamma &\equiv \Gamma - \Gamma_0(S2, t_d) \\ c\Gamma &\equiv \Gamma - \epsilon_{x,y} \cdot f(t_d) \\ cf\Gamma &\equiv \Gamma - \epsilon_{x,y} \cdot f(t_d) - \Gamma_0(S2, t_d)\,, \end{aligned} \tag{2.21}$$

where $f\Gamma$ the flattened, $c\Gamma$ is the corrected and $cf\Gamma$ the corrected and flattened S2 pulse width. As mentioned above, the data raw processor makes available both the S2 pulse width at 50 % and at 10 % of the S2 pulse height. In the following we will give details on the S2 pulse width correction map for the width defined at 10 % of the S2 pulse height. However, for both definitions the maps have been made and are (besides statistical fluctuations) identical.

2.3.1 Data Selection

We want to define a correction map (ϵ_{xy}) on the S2 pulse width that is valid for nuclear recoils off xenon atoms, i.e. the type of physical interactions investigated by the standard WIMP analysis. ^{241}AmBe neutron calibration data is available for such studies. FIG. 2.10 shows the available statistics (number of events is color coded) of physical single scatter events in the S2 energy range from 150 PE (lower threshold used in the analysis of the 225 live days data set [21, 27]) to 5000 PE (roughly equivalent to 85 keV$_{\mathrm{nr}}$ [47, 62] where the exponentially falling spectrum from WIMP interactions is negligible) for different physical depths (slices in drift time t_d) that was taken during the relevant period of the 225 live days publication. The data is drawn against the uncorrected horizontal position. We have to use the spacial coordinates that are *not* corrected for the drift field distortions (see section 2.1.2), because we are interested in the position the secondary scintillation light is produced at and not the position of the physical interaction inside the TPC. Inhomogeneities in the electrical drift field in the LXe force electrons from interactions at larger radii in the bottom part of the TPC to trajectories that are directed inwards to smaller radii. A binning of $(20 \times 20)\mathrm{mm}^2$ was chosen to avoid being limited by statistics. The cuts introduced in section 2.1.5 are used to grant data quality and select single scatter events.

---

[3] In the ROOT framework of XENON100 the corresponding branches are labeled S2sLowWidth[0] (Γ), fS2sLowWidth[0] ($f\Gamma$), cS2sLowWidth[0] ($c\Gamma$), cfS2sLowWidth[0] ($cf\Gamma$), S2sTot[0] (S2), S2sPosNn[0][0] (x) and S2sPosNn[0][1] (y).

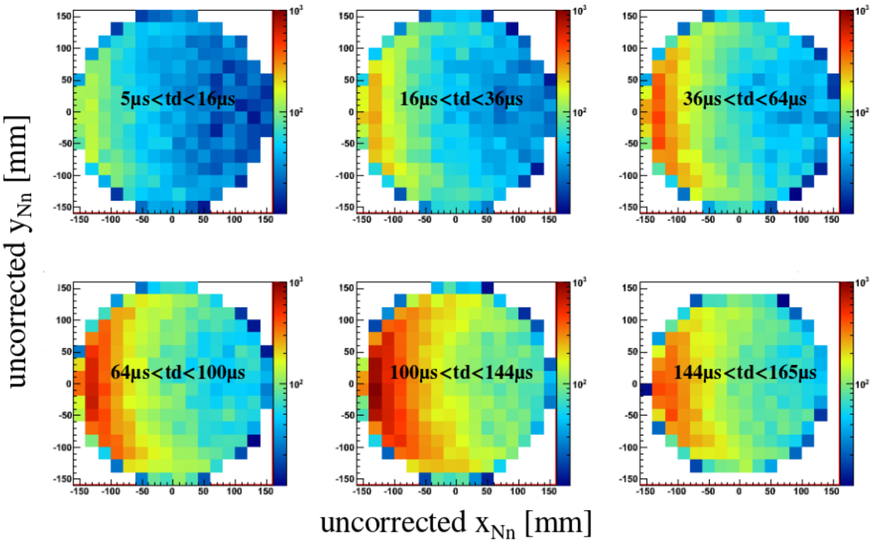

Figure 2.10: Horizontal distribution of ^{241}AmBe neutron interactions (number of events color coded) that were collected during four consecutive days in February, 2011, during the data taking period of the 225 live days [27]. Shown are the xy positions (in mm) where the secondary scintillation light is produced at in the gas gap.

2.3.2 Fitting energy and drift time dependence of the S2 pulse width

The drift time dependence of the S2 pulse width, Γ_0 (for definition see equation 2.20), is determined from the ^{241}AmBe neutron calibration data cutting on events with the secondary scintillation light produced in the horizontal center of the TPC, i.e. within a radius $< 50\,\mathrm{mm}$. The median of individual energy slices (in this study the energy is estimated by the area of the S2 pulse) is fitted using the following effective function:

$$\Gamma_0(S2, t_d) = p_0 + p_1 \cdot \sqrt{t_d} + p_2(S2) \cdot t_d\,. \tag{2.22}$$

For small drift times ($t_d < 40\,\mu\mathrm{s}$) this function describes the drift time dependence of the S2 pulse width in greater detail compared to equation 2.19, where the approximation of the time distribution of secondary scintillation light from a single electron being Gaussian loses accuracy. In the fit to the data, p_0 and p_1 have been fixed to their global optimum ($p_0 = 0.97\,\mu\mathrm{s}$ and $p_1 = 0.05\sqrt{\mu\mathrm{s}}$) while p_2 was free to float in the different S2 slices. Afterwards the S2 dependence of p_2 has been fitted by the following ansatz:

$$p_2(S2) = p_{20} + p_{21} \cdot \ln(S2)\,. \tag{2.23}$$

FIG. 2.11 shows the outcome of these fits. In dotted black the median of the individual S2 width distributions as a function of the drift time t_d is shown. The solid black lines indicate the individual fits to these medians. Finally, in solid green the functional behavior given by equation 2.22 and 2.23 is evaluate for the central value of the individual S2 slice. The solid black and green lines nicely match, hence, validating the chosen parameterization for $p_2(S2)$. Comparing the distributions of the different S2 slices, we observe the spread of each distribution to decrease with increasing number of ionization electrons that are proportional to the S2 pulse. Small signals, consisting of a few electrons only, have a much larger fluctuation around their median. The latter itself is quite independent on the size of the S2 signal.

2.3.3 Fitting the S2 pulse width correction map and its drift time behavior

FIG. 2.12 shows the mean (color coded in units of 10 ns) of the flattened S2 pulse width $f\Gamma$ as a function of the (uncorrected) xy position for six different drift time slices. For each t_d slice this mean is computed from all single scatter events in the S2 range from 150 PE to 5000 PE horizontally binned in the xy position (tiles of $400\,\mathrm{mm}^2$ area). A 3-fold symmetry for small drift times is visible being smeared out with increasing t_d. This symmetry can be correlated to the position of screws fixing the grids to the TPC. The grids were chemically etched from stainless steel foils and spot-welded onto rings as well from stainless steel. Warping was minimized by stretching the meshes before welding. The equipped stainless steel rings in turn were mounted by screws to the TPC structure [34]. These screws likely cause shear forces that are responsible for the observed warping.

The strongest variations seen for small drift times are on the order of 100 ns, i.e. about 10 % of the average S2 pulse width at these drift times.

Equation 2.20 is fitted to the data, visualized in FIG. 2.12, by minimizing the function

$$\chi^2 = \sum_{x,y} \sum_{i} \left(\frac{f\Gamma^i_{xy} - \epsilon_{xy} \exp(m\, t^i_d)}{\sigma^i_{xy}} \right)^2 . \tag{2.24}$$

Therein t^i_d is the center value of the drift time slice i. $f\Gamma^i_{xy}$ and σ^i_{xy} are the above described mean value of the flattened S2 pulse width in the respective drift time slice t^i_d and horizontal xy bin and its uncertainty. The minimization procedure results in $m = -7.4 \times 10^5\,\mathrm{s}^{-1}$, the parameter that effectively describes the t_d dependence, and the S2 pulse width correction map ϵ_{xy} at $t_d = 0$ that is shown in FIG. 2.13 (left). The same correction map but interpolated between the single xy bins is shown in FIG. 2.13 (center). Shown right in the same figure is the xy dependence of the data after having

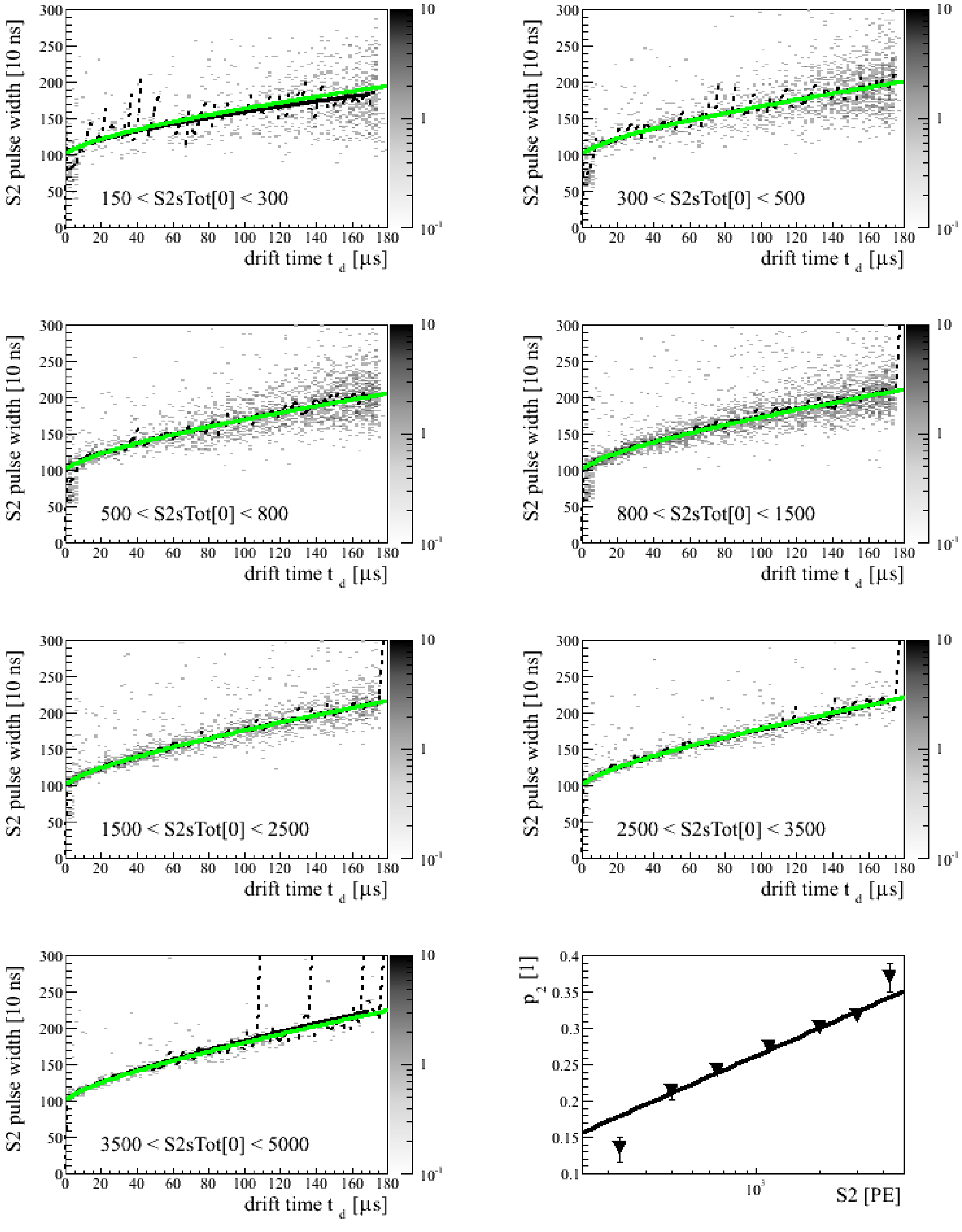

Figure 2.11: S2 pulse width distribution as a function of drift time for several interval regions (slices) of S2. Median of the S2 pulse width (dotted black line), fit to the individual medians (solid black line) and evaluation of equation 2.22 and 2.23 at each S2 slice's mean (green line). The latter covers the fit in most cases, thus, validating the used parametrization of $p_2(S2)$. This is again validated by the bottom right graph showing the S2 dependence of p_2 that is fitted using equation 2.23.

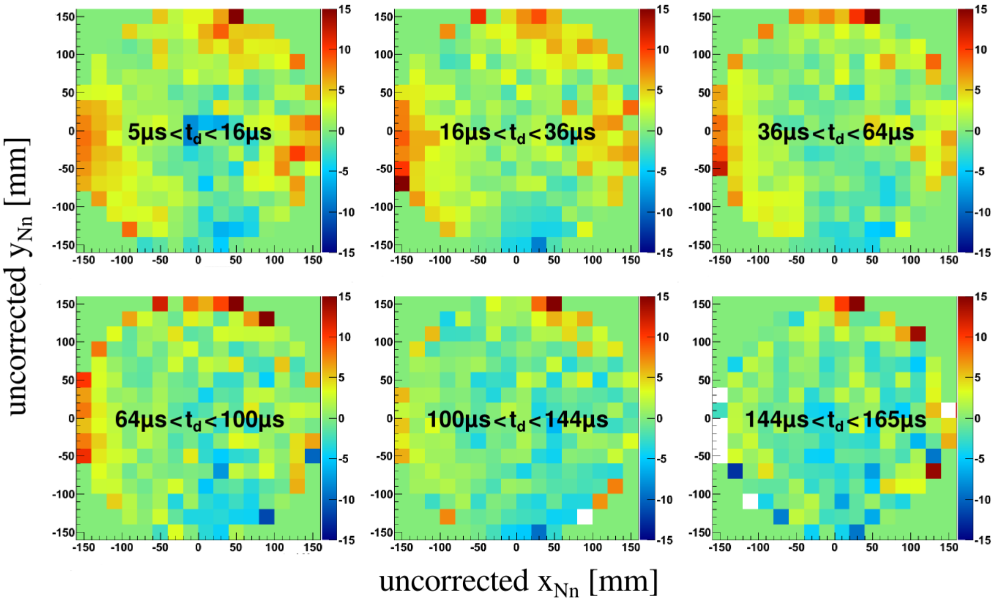

Figure 2.12: Mean of flattened S2 pulse width $f\Gamma$ (see equation 2.21; color coded in units of 10 ns) for different drift time slices as observed by the PMTs at the position of the secondary scintillation light (binned in tiles of 400 mm^2 area). The 3-fold symmetry obvious for small drift times is smeared out with increasing t_d.

applied the correction on the event by event basis. Except for the largest radii, the dependence across xy is successfully removed.

2.4 Longitudinal diffusion coefficient of electrons in LXe

Before we continue to define a consistency condition that relates the longitudinal electron diffusion (S2 pulse width) in liquid xenon to the z coordinate of the interaction vertex, we want to determine the dependence of the longitudinal diffusion coefficient on the applied electric drift field. FIG. 2.14 shows the distribution of $\sigma_e \equiv \Gamma_{50\%} \cdot (8 \ln 2)^{-1/2}$ [4] versus drift time t_d for the ^{241}AmBe calibration data. In this analysis $\Gamma_{50\%}$ was chosen over $\Gamma_{10\%}$ as it is more robust against non-Gaussian tails, thus improving the conversion to σ_e. The energy (S2) was confined to the range from 500 PE to 2500 PE. The median of this distribution, i.e. the 50 % quantile of the 1-dimensional distributions obtained by considering single t_d slices of 1.8 µs width, is indicated by the dotted black curve. The longitudinal diffusion constant D_L is obtained from a fit of equation 2.19 to this

---

[4] $\Gamma_{50\%}$ denotes the S2 pulse width at 50 % pulse height that is stored in the analysis framework of the XENON collaboration in the ROOT branch S2sWidth.

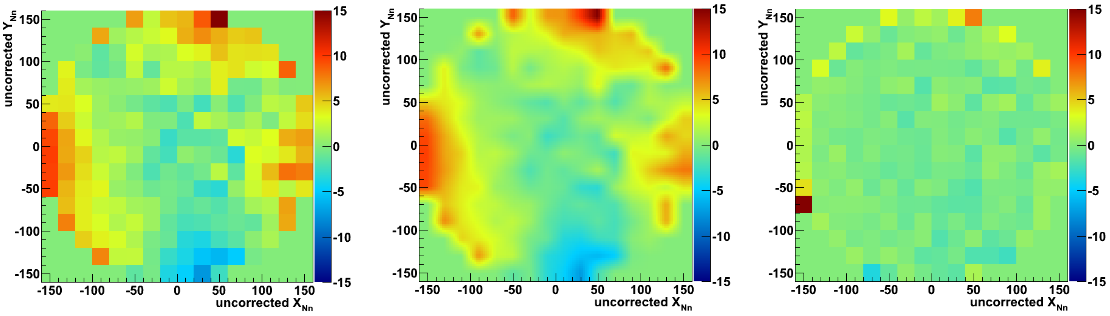

Figure 2.13: Correction map used in the analysis of the 225 live days publication [27] to remove the xy dependence of the S2 pulse width. (left) ϵ_{xy} as determined by minimizing equation 2.24, (middle) interpolated version thereof. (right) Map of $cf\Gamma$ showing ^{241}AmBe calibration data corrected on the event by event basis. Except largest radii, the xy dependence is removed in the corrected data ($cf\Gamma$). The color coded z axis is in units of 10 ns, i.e. the maximal correction to be made is on the order of 0.1 µs.

median, holding fix the electron drift velocity to $v_{d,\,\mathrm{LXe}} = 0.174\,\mathrm{cm/\mu s}$ (530 V/cm) and 0.168 cm/µs (400 V/cm), respectively, but leaving D_L and σ_0 free to float. The fit range was confined to drift times from 40 µs to 160 µs in order to avoid limitations from the approximation made in equation 2.18. Combining the values found for D_L for different anode settings (the electron drift field in the liquid should not be affected by the anode voltage) and the ones of σ_0 for different cathode settings (in turn the pedestal σ_0 is supposed to be dominated by effects in the gas gap independent on the drift field in the liquid), we find:

$$D_L(530\,\mathrm{V/cm}) = 10.74(15)\,\mathrm{cm^2/s} \qquad D_L(400\,\mathrm{V/cm}) = 11.7(5)\,\mathrm{cm^2/s}$$

$$\sigma_0(4.4\,\mathrm{kV}) = 0.281(3)\,\mathrm{\mu s} \qquad \sigma_0(4.25\,\mathrm{kV}) = 0.271(11)\,\mathrm{\mu s} \qquad \sigma_0(4.0\,\mathrm{kV}) = 0.305(2)\,\mathrm{\mu s}\,.$$

As expected the pedestal σ_0 increases with decreasing anode voltage. Within its larger uncertainty, that is due to the small statistics available at this anode setting, the value at 4.25 kV is consistent with this conclusion. The longitudinal diffusion constant D_L seems to increase with the applied drift field in the liquid xenon. This is in agreement with the observation made in [73]. However, there is still a 3.3 % probability for both values to be consistent within statistical uncertainties.

The absolute numbers are in conflict with the ones published in [73]. Therein a value of 12 cm^2/s for a drift field of 730 V/cm and 16 cm^2/s for a drift field of 530 V/cm is found. Informations about the respective uncertainties are missing. From the references

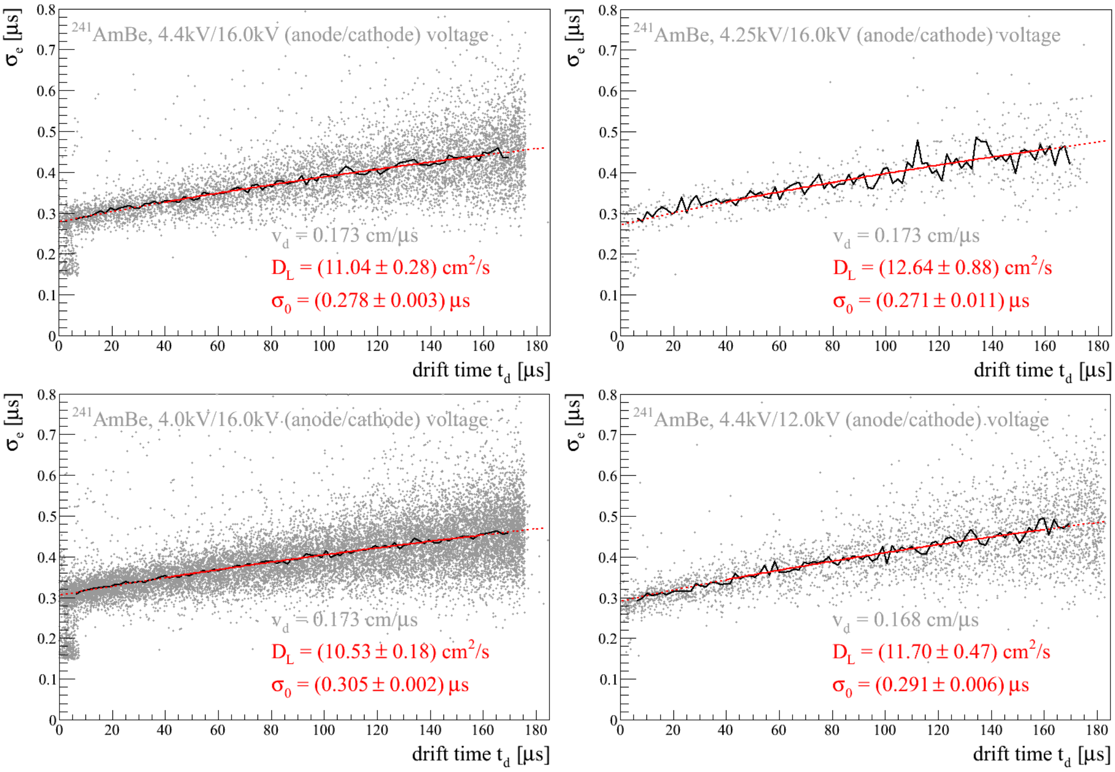

Figure 2.14: S2 pulse width σ_e as function of the drift time t_d for different high voltage settings of anode and cathode. The black curve marks the distribution median. The red curve is a fit to the median in the range from 40 µs to 160 µs. D_L is the longitudinal diffusion constant of electrons in LXe at the respective electrical field of 530 V/cm (16 kV cathode voltage) and 400 V/cm (12 kV cathode voltage). The pedestal σ_0 is dominated by the time a single electron needs to drift through the gas gap and, hence, changes with the anode voltage.

given in [73] it seems that the author extracts information from a talk on XENON100 given by E. Aprile (Wonder 2010 seminar[5]). The accuracy of such an approach seems to be limited and the discrepancy with our result reconcilable.

2.5 Quantification of horizontal gas gap width dependence

Neglecting the suppressed effect of gate grid warping, we can use equation 2.15 to determine the anode warping ϵ relative to the absolute size of the gas gap d_g. The input needed is the relative variation ϵ_{xy} in comparison to the mean value $\hat{\Gamma}_d$ of the S2 pulse width at zero drift length. Both quantities have been determined in section 2.3. From FIG. 2.13 we read the maximal variations to be on the order of 0.1 µs at an total offset of 0.97 µs (parameter p_0 in equation 2.22). XENON100 exploits capacitive level meters to determine the liquid level d_g [34]. Their absolute alignment dominates their uncertainty estimated to be 1 mm [57]. During the ^{241}AmBe calibration (as well as the whole science run 10), that is at the time of our measurement of $\epsilon_{xy}/\hat{\Gamma}_d$, the liquid level is found to be $d_g = (3.5 \pm 1.0)\,\mathrm{mm}$. As mentioned earlier, the distance between gate and anode is $d = 5\,\mathrm{mm}$, hence, we compute $d \cdot (d + d_g)/(d + 4\,d_g) = (1.6 \pm 0.3)\,\mathrm{mm}$ (see equation 2.15) and find the maximal anode grid warping to be

$$\epsilon_{xy}^{\max} = (0.16 \pm 0.03)\,\mathrm{mm}\,. \tag{2.25}$$

The uncertainty of this result is dominated by the systematic uncertainty of the liquid level measurement. However, we can conclude that the anode is properly aligned to a very high precision recalling the diameter of about 30 cm, that is spanned by the mesh.

2.6 Definition of a consistency cut on the S2 pulse width

In section 2.1.5 we sketched the event selection used in the XENON100 analyses [21, 27, 28, 46] and introduced the consistency cut on the S2 pulse width. The z position of an event is inferred from the drift time t_d delay between the prompt S1 and delayed S2 pulse. Knowing the longitudinal diffusion of electrons in LXe at the applied drift field (see section 2.4), we anticipate a S2 pulse width of certain width. Events failing this criteria are rejected.

Gas events are a prominent class of events removed by the S2 pulse width cut. These events are produced in the gas gap or top most LXe layer, e.g. induced by gammas from

---

[5] http://wonder.lngs.infn.it/

the top PMT array. The actual S1 of gas events is hidden by the promptly following S2. As a consequence, the data processor assigns the most prominent but random S1-like signal to the S2 from the gas event. The random time difference t_d between the S2 and the picked up S1 results in a reconstructed z position not reflecting the real interaction vertex of the gas event. However, these events will have a short S2 pulse width and are consequently removed by the S2 width cut.

In section 2.3 we defined the corrected values $c\Gamma$ and $cf\Gamma$ where we removed the xy dependence of the S2 pulse width on event-by-event basis. In $cf\Gamma$ the drift time dependence is removed resulting in valid events scattered around zero. The consistency cut on the S2 pulse width will be defined on this quantity.

The fluctuation of the S2 pulse width depends on the energy estimator S2 of the event. This can be seen in FIG. 2.15. Shown are the distributions of $cf\Gamma$ versus the drift time t_d for different energy (S2) ranges. For each of the shown distributions, the dotted black line indicates the median and the solid black lines represent the $\pm 1\sigma$ and $\pm 2\sigma$ quantiles. The absolute distance of those quantiles from the median decreases with energy (S2), i.e. the fluctuation of the S2 pulse width distribution decreases. In solid green the computed $\pm 2\sigma \equiv 2 \times \pm 1\sigma$ bands are drawn, where we assumed the distribution to be Gaussian. This is approximately true for the lower part of the distributions ($cf\Gamma < 0$, here green and black lines are almost identical), while the distributions' upper part has stronger non-Gaussian tails causing the $+2\sigma$ band (black) being at a greater distance than its computed ($2 \times +1\sigma$) counterpart (green).

The quantile level used to define the cut threshold (finally the computed $\pm 2\sigma$ quantiles showed to perform best) was defined in two separate studies. The rejection power of the cut condition for different quantile levels was investigated on two non-physical event classes: events from ^{60}Co ER calibration data falling below the 99.5 % quantile and ^{241}AmBe neutron calibration data with a drift length greater than the physical dimension of the TPC. The computed $\pm 2\sigma$ definition was found to perform best at a reasonable acceptance for NR events as determined from ^{241}AmBe neutron calibration (see blow).

As a consequence of the above stated, a cut on the S2 width has to be a function of the drift time t_d and the energy estimator S2. To implement this, the cut is defined for different S2 ranges independently. For each range a first order polynomial ($\mathrm{Pol1}_{\pm 2\sigma}$) is fitted to the computed $\pm 2\sigma$ contours:

$$\begin{aligned} \mathrm{Pol1}_{+2\sigma}(S2, t_d) &\equiv p_{0+}(S2) + p_{1+}(S2) \cdot t_d \\ \mathrm{Pol1}_{-2\sigma}(S2, t_d) &\equiv p_{0-}(S2) + p_{1-}(S2) \cdot t_d \,. \end{aligned} \tag{2.26}$$

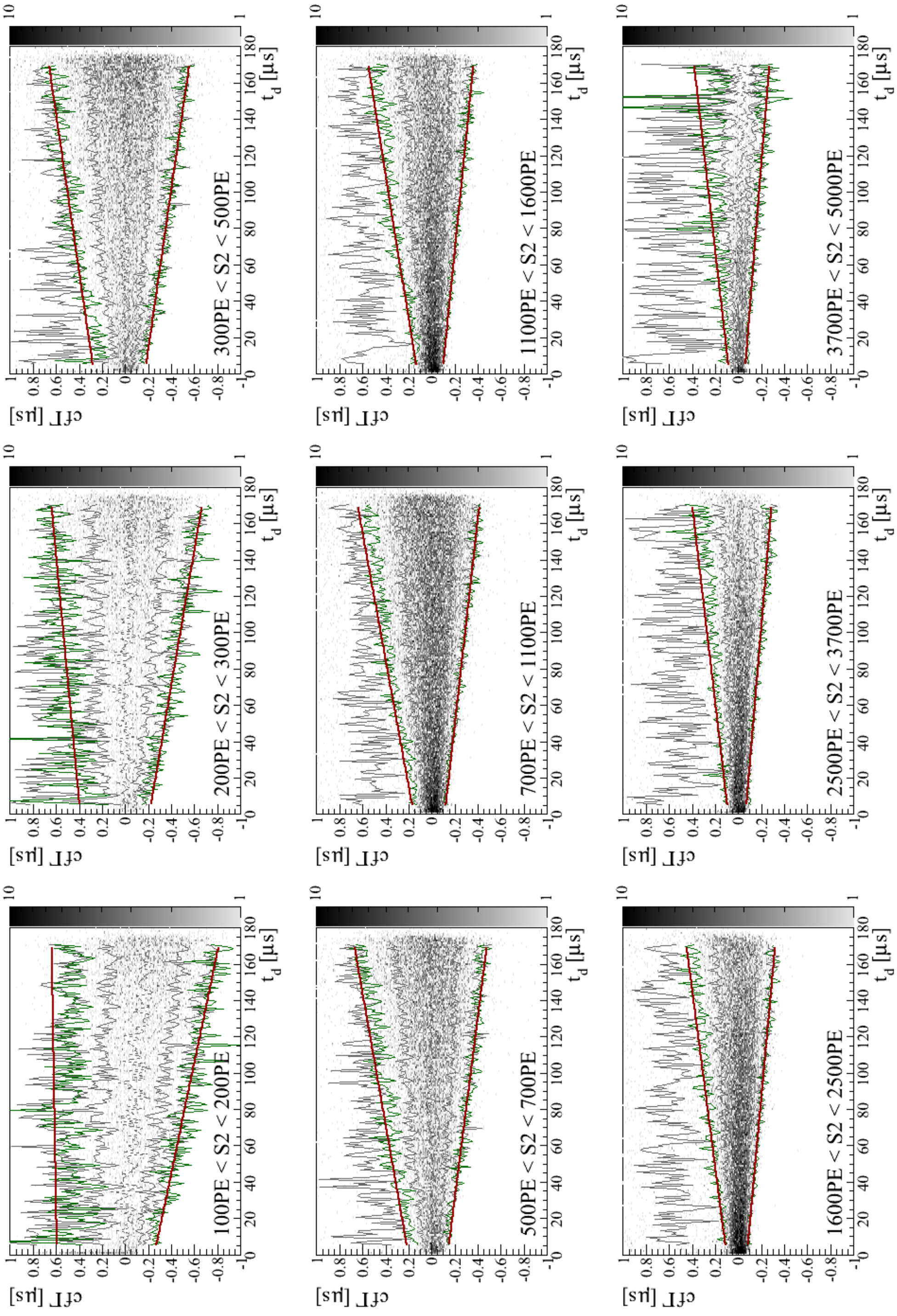

Figure 2.15: Energy (S2) dependent definition of the cut on the (corrected and flattened) S2 pulse width ($cf\Gamma$ in units of 1 µs). Shown in red are the thresholds implemented in the cut. For more informations see text.

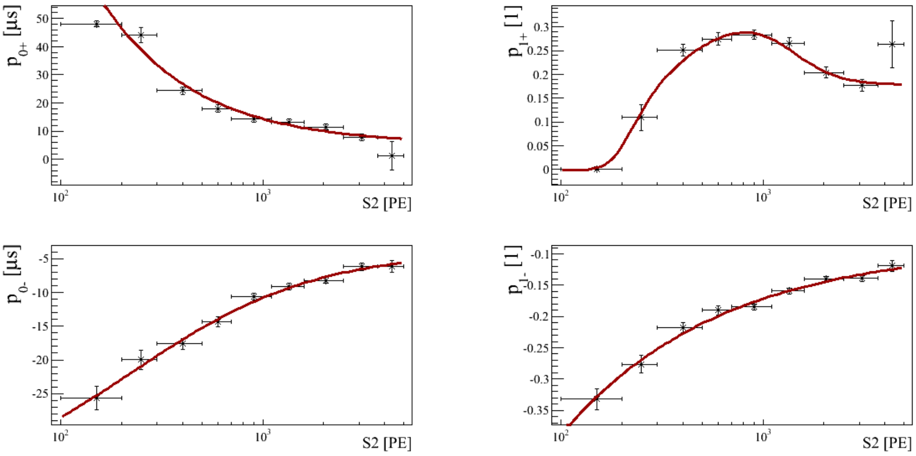

Figure 2.16: S2 dependence of the parameters describing the upper and lower 2σ contour of the corrected and flattened S2 pulse width ($cf\Gamma$). In red their individual S2 dependence is modelled.

These polynomials serve as upper and lower thresholds to formulate the cut on the S2 pulse width:

$$\mathrm{Pol1}_{-2\sigma}(S2, t_d) < cf\Gamma < \mathrm{Pol1}_{+2\sigma}(S2, t_d)\,, \tag{2.27}$$

where good events have to have a (corrected and flattened) S2 pulse width $cf\Gamma$ that fulfills above criteria and are otherwise rejected. In FIG. 2.15 these criteria are illustrated by red lines. Good events (shaded in gray are events from the ^{241}AmBe calibration) are confined between both. Events having a $cf\Gamma$ greater than the upper or less than the lower threshold are rejected.

FIG. 2.16 shows the S2 dependence of the resulting fit parameters $p_{0+}, \ldots, p_{1-}$ of equation 2.26. In turn, their individual S2 dependence is modelled by functions (shown in red) of the form:

$$p_{0+}, \ldots, p_{1-} = a_0 + \frac{a_1 - a_0}{1 + \exp\left(a_3(\log(S2) - a_2)\right)} \tag{2.28}$$

Therein, a_0 and a_1 determine the asymptotic behavior (S2 $\to 0, \infty$) while a_2 and a_3 define the point of inflection and its slope. All parameters a_0, $\ldots$, a_3 are constant except a_0 in p_{1+}, where the following parameterization is used:

$$a_0^{p1+} = q_0 + q_1 \left(\log(S2) - a_2^{p1+}\right)^2 . \tag{2.29}$$

In FIG. 2.17 (top) the resulting cut is shown on the aforementioned ^{241}AmBe calibration data in the parameter space of the corrected S2 pulse width $c\Gamma$ (not flattened) versus the drift time. Highlighted in black are the events removed. Events accepted follow the square root behavior expected from the diffusive broadening of the electron cloud drifting in the electrical field from the interaction vertex to the liquid-gas interface. In FIG. 2.17 (bottom) the acceptance, i.e. the ratio of events not removed by the cut criterion with respect to the full dataset[6], for nuclear recoils (determined as well on the ^{241}AmBe calibration data) within the S1 benchmark region from 3 PE to 30 PE is shown. The cut has an average acceptance of 91.6 % without applying any fiducial volume. The acceptance of the cut slightly decreases for small drift times ($t_d < 20\,\mu\text{s}$) partly rejected depending on the specific fiducial volume cut. The average acceptance for the 34 kg fiducial volume of the 225 live days analyses was $\sim 92\,\%$ [21, 27].

2.6.1 Impact of the S2 pulse width cut on the 225 live days analysis

FIG. 2.18 shows the event distribution (black dots) of all events passing the predefined cuts (see section 2.1 or [55]) after unblinding the 225 live days dark matter data set [27]. Without applying the consistency cut on the S2 pulse width, a few additional events appear that are shown as red dots. As expected, in the electronic recoil band their number is small in comparison to the number of events. However, their abundance dominates below the 99.75 % quantile (red dashed line) of the ER band where "Gaussian leakage" of electronic recoils is largely suppressed. There are four additional events close to the 3 PE threshold in S1, three of them scarcely missing the predefined WIMP benchmark region (gray shaded area). One event is falling inside the benchmark region increasing the number of events from two to three. Another three events appear well below the lower 97 % quantile of the nuclear recoil band (blue dashed line). This confirms that the consistency cut on the S2 pulse width removes events being falsely reconstructed. All six events (black dots) below a value of -0.3 in the flattened discrimination space of FIG. 2.18 passing the consistency cut on the S2 pulse width, the two falling inside the WIMP benchmark region included, have a (corrected and flattened) S2 pulse width well inside the threshold limits ($\text{Pol1}_{\pm 2\sigma}$ of equation 2.26) defined for the cut. On the other hand, the events rejected (red dots) by the consistency condition on the S2 pulse width significantly fail the condition. Before unblinding the dark matter dataset a

---

[6] This is a conservative definition of acceptance. Ideally, we used a clean dataset consisting of WIMP interactions only. No such dataset was available, though. The dataset employed instead, might as well include events inherently different from WIMP interactions. Removing such events should not affect the acceptance.

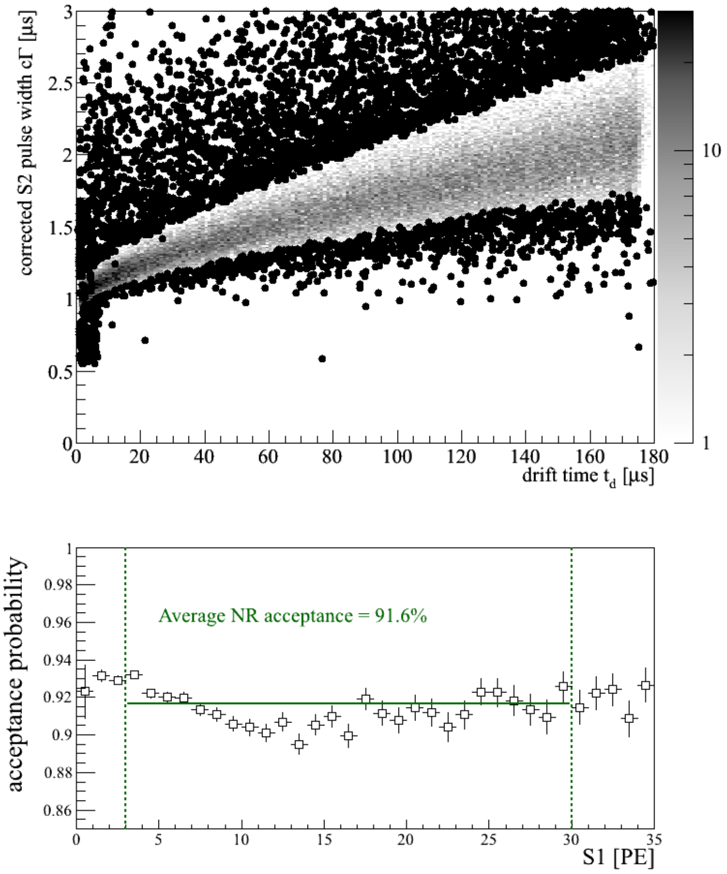

Figure 2.17: (top) Illustration of the defined consistency cut on the S2 pulse width. Marked black are ^{241}AmBe events failing the cut. (bottom) Acceptance of the cut for nuclear recoils (NR) within the S1 benchmark region from 3 PE to 30 PE.

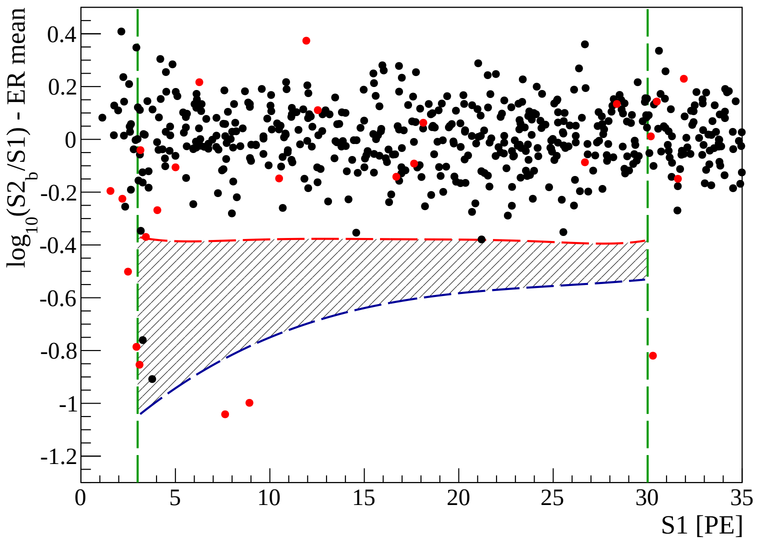

Figure 2.18: Observed event distribution (black dots) in the flattened discrimination space after unblinding the 225 live days dark matter data set [27]. Without applying the consistency cut on the S2 pulse width, additional events appear (red data points). The gray shaded area indicates the predefined WIMP benchmark region for the dark matter analysis.

total background of (1.0 ± 0.2) events in the benchmark region was expected [27]. The two observed events are in good agreement with this prediction. Rejecting the signal hypothesis, the most stringent limit on the elastic spin-independent WIMP-nucleus cross-section was placed for WIMP masses above 8 GeV/c^2 [27].

Chapter 3

Krypton in XENON

This chapter is devoted to the development and application of two analytic techniques based on a chromatographic separation of krypton traces from xenon gas. The more sensitive one, the Rare Gas Mass Spectrometer (RGMS), was proven to reach a detection limit of 8 parts per quadrillion (ppq). This is an improvement by about two orders of magnitude in comparison to what has been achieved so far by other groups. A dedicated publication was prepared on this benchmarking technique covering parts of this chapter. A preprint is available [75]. The RGMS will be discussed in detail in section 3.2. During this work the RGMS was designed, constructed, thoroughly characterized and a variety of samples has been measured that were drawn in the context of XENON100 and XENON1T. The less sensitive but fully automated and customized gas-chromatograph (COMGC), with trace analysis of electronegative impurities being its primary scientific goal, reaches ppb sensitivity for krypton traces in xenon and is discussed in section 3.3. Finally, krypton in xenon assay results obtained with RGMS and COMGC are summarized in section 3.4.

3.1 Introduction

The inert gas krypton with its beta-decaying isotope ^{85}Kr is one of the most serious internal backgrounds for the XENON100 and XENON1T detectors. Their target material xenon is commercially produced by extraction from the atmosphere where the relative abundances of krypton and xenon are 1.14 parts per million by volume (ppmv) and 0.09 ppmv, respectively. In particular, the atmosphere contains about a factor of 10 more krypton than xenon. The separation from atmospheric constituents in this extraction process has limited efficiency resulting in traces of krypton at the level of parts per million (ppm) and, for high purity xenon, parts per billion (ppb).

The activity of the man-made isotope ^{85}Kr in the atmosphere, produced in sizable quantities by nuclear fission and released to the air by nuclear-fuel reprocessing plants and nuclear weapons, has been steadily increasing until a present-day activity concentration of $1.4\,\mathrm{Bq/m^3}$ [76, 77]. This translates into an estimate for the current value of the ^{85}Kr/$^{\mathrm{nat}}$Kr ratio of 2×10^{-11} mol/mol [78]. In section 3.1.2 a direct measurement of ambient air from the same laboratory XENON100 is located in is presented. It confirms the validity of this ratio in the context of XENON100.

^{85}Kr disintegrates by β^- emission mainly (99.56 %) to the ^{85}Rb ground state level. The end-point energy of this decay is 687 keV. In 0.44 % of all ^{85}Kr disintegrations the prompt β^- is followed by a delayed γ emission. The γ is produced in the de-excitation of ^{85}Rb ($J\pi = 9/2+$) with a relaxation time of $1.015\,\mu$s [79]. The two-phase TPC design of the XENON detectors allows to discriminate electronic recoils against nuclear recoils at the level of about 99.5 % (see section 2.1 for more details). While in XENON100 a krypton level of ~ 20 parts per trillion (ppt) was sufficiently low, simulations show the need of a krypton concentration in the xenon target below 100 ppq for XENON1T (see also [29]).

This value can easily be understood by a simple back-on-the-envelope calculation: XENON1T is designed to reach its physical goal after collecting ~ 5 years of statistics. For our simple estimate we want to tolerate 0.1 events per year in the region of interest caused by ^{85}Kr disintegrations. The detector's discrimination capability for electronic recoils of about 99.5 % allows for a maximum limit of 20 events in the energy region of interest for the WIMP search. This region spans over about 30 photoelectrons (PE) in S1 corresponding roughly to 10 keV assuming a light yield of ~ 3 PE/keV for electronic recoils observed in XENON100 (e.g. [27]), thus very roughly another reduction factor of $687\,\mathrm{keV}/10\,\mathrm{keV} \sim 70$ is obtained. Therefore, we can tolerate about 1400 ^{85}Kr decays inside the fiducial volume per year equivalent to 22000 ^{85}Kr atoms. Using the above mentioned value for the ratio of ^{85}Kr/$^{\mathrm{nat}}$Kr this corresponds to 1.1×10^{15} krypton atoms in total or 1.9×10^{-9} moles of krypton. The fiducial volume of XENON1T will be about 1000 kg of liquid xenon, roughly equivalent to 7600 moles. This calculation yields 300 ppq as acceptable for the background requirements of XENON1T.

While purification techniques are already established to remove krypton from xenon to the ppt level based on adsorption, distillation or even by means of centrifuges [44, 80, 81], measurement techniques so far available seem to level off at these concentrations [44, 82–84]. As discussed in section 1.2.2 the XENON collaboration follows the distillation approach and we will present the outstanding purity achieved. The krypton assay of this work provides the proof-of-principle of the distillation technique – one of the key requirements for the upcoming experiment XENON1T.

3.1.1 Krypton analytics

Profound knowledge of the krypton concentration in the XENON detector target is mandatory: We have shown above the contribution of ^{85}Kr disintegrations to the overall background indistinguishable from WIMPs scattering off xenon nuclei. Krypton/xenon concentrations < 100 ppq are needed already for XENON1T as shown above. The XENON detectors have only limited capability to determine the level of ^{85}Kr impurities. They are sensitive to ^{85}Kr disintegrations only, this makes them practically insensitive to the desired low concentrations within a reasonable exposure time. Seeking for ^{85}Kr in the data of XENON100, one follows one of the two approaches: spectral shape and delayed coincidences analyses.

Spectral shape The spectral shape of the low energy background can be fitted using all known background sources convoluted by the energy resolution of the detector and including the distinct β-spectrum of ^{85}Kr with its well known end-point energy. In comparison to the delayed coincidence method (see below), this technique has the advantage to make use of almost all ^{85}Kr events. That is to say, the statistics is as good as it can be, but this technique is limited to cases where the low energy electromagnetic background is dominated by ^{85}Kr. During the 100 live days science run [28], a temporary air leak introduced krypton (see timeline of FIG. 1.7). Hence, in that data the low energy background region is dominated by events from the ^{85}Kr beta decay. A fit of the ^{85}Kr spectrum to the data results in a precise determination of the krypton level. Preparing for the subsequent science run, the krypton level was significantly reduced by cryogenic distillation (see section 1.2.2) while external backgrounds and the internal radon concentration (the role of radon and its progenitors will be discussed in detail in section 4) practically stayed unchanged [47]. This time a spectral fit of ^{85}Kr to the low energy background only provides a limit on the maximal amount of krypton. The degeneracy of other contributions prevents from a more precise determination of the impurity level, as obvious from FIG. 3.1 (left). In the same figure (right) the difference in the electromagnetic backgrounds of both datasets, normalized to the individual lifetimes, is shown. The resulting spectrum is nicely be fitted with ^{85}Kr, confirming the above stated.

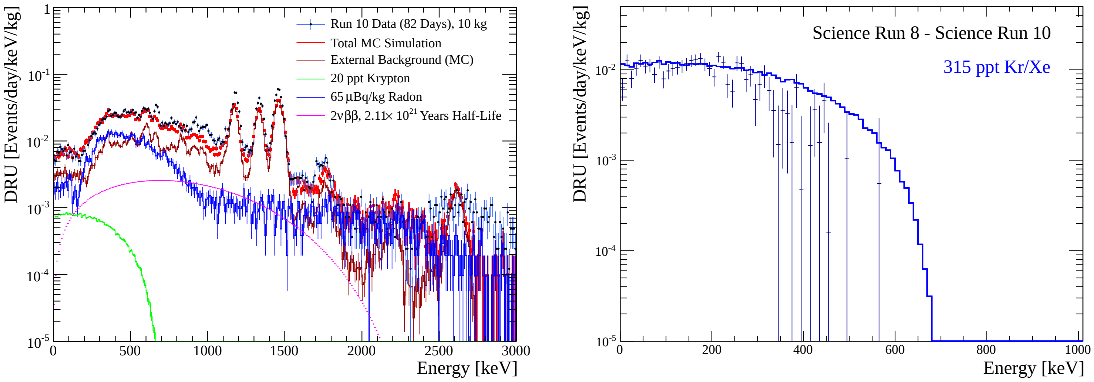

Figure 3.1: Spectral shape analyses of XENON100's electromagnetic background. (left) Single scatter ER background spectrum (black histogram) in 10 kg fiducial volume. Shown in green is the simulated contribution of 20 ppt krypton. Its actual level can not be determined from this study. (right) Difference in single scatter ER background between the science data of the 100 live days (science run 8) and 225 live days (science run 10) publications. The residual is perfectly described by the ^{85}Kr spectrum that is fitted in blue. In between both runs krypton has been removed from the xenon target by cryogenic fractional distillation. Figures provided by K. Lung and A. Behrens (courtesy of XENON100).

Delayed coincidence method In 0.43 % of all decays, ^{85}Kr disintegrates via prompt β emission with end-point energy of 173.4 keV and a subsequent 514 keV γ, delayed by 1.015 µs. In standard Dark Matter data taking conditions (400 µs recorded time window), the acceptance for this delayed coincidence of the XENON100 detector was estimated to be about 80 %. Although this specific event pattern is quite unique, it was found that the ^{212}Bi (β) – ^{212}Po (α) decay coincidence (half-life of the latter isotope is about 0.3 µs) as part of the primordial ^{232}Th decay chain (thorium series) mimics the ^{85}Kr pattern especially at the outer rim of the sensitive volume where energy information is insufficient [85]. Another drawback of the delayed coincidence method is its tiny branching ratio. Only $\sim 0.35\,\%$ of all ^{85}Kr decays will be detected, leading to month-scale exposure times to reach sufficient statistics: In a 60 kg active xenon target with 20 ppt krypton level (these are roughly the conditions during the 225 live days science run) we have to collect about 130 days of data to observe 10 delayed coincidence events from krypton.

External analytics Above drawbacks of internal krypton analytics make an external assay desirable. Preferably, such a method is sensitive to the background creating isotope ^{85}Kr itself. This, however, is not feasible: Assuming a 1 l gaseous xenon (GXe) sample at standard temperature and pressure (STP)[1] with a krypton/xenon concentration of 1 ppt, we face the challenge of providing evidence for 0.5 ^{85}Kr particles in the full xenon sample that contains roughly 3×10^{22} atoms. To our knowledge no such technique exists.

However, the ratio of ^{85}Kr/$^{\mathrm{nat}}$Kr is accessible by low level counting (LLC) methods [76, 87]. Skipping the idea of counting directly the ^{85}Kr particles but using a technique to quantify the total amount of krypton ($^{\mathrm{nat}}$Kr), we gain the mentioned factor of $^{85}\mathrm{Kr}/^{\mathrm{nat}}\mathrm{Kr} = 2 \times 10^{-11}$ (see also 3.1.2) in the number of particles. Returning to our example of 1 liter gaseous xenon, 1 ppt of krypton translates to 3×10^{10} krypton particles to be detected.

3.1.2 The ^{85}Kr/$^{\mathrm{nat}}$Kr ratio

An estimate on the abundance of ^{85}Kr in natural krypton as of the year 2003 is given in [78] to be $^{85}\mathrm{Kr}/^{\mathrm{nat}}\mathrm{Kr} \approx 2 \times 10^{-11}$ mol/mol. ^{85}Kr is purely man-made and produced in sizeable quantities by nuclear fission. Nuclear bomb tests and nuclear-fuel reprocessing plants, the two dominating mechanisms releasing ^{85}Kr into the atmosphere, have been steadily increasing its atmospheric activity concentration until a present-day average of 1.4 Bq/m^3 [76, 77]. FIG. 3.2 shows the atmospheric ^{85}Kr activity concentration at the sampling site Mount Schauinsland, Germany. The figure illustrates, however, that variations of up to a factor 3 on short time scales may occur. The authors of FIG. 3.2 and [77] traced back these "shortly enhanced ^{85}Kr levels" to operation cycles of nuclear reprocessing plants in the last years. There are two operational facilities in Europe, La Hague, France, and Sellafield, Great Britain. The former is at a distance of about 750 km, the latter of about 1050 km from the sampling site Mount Schauinsland. While the geographic situation is known to support a relatively fast and direct air exchange between La Hague and Mount Schauinsland, the Alps might effectively smooth out the spiked ^{85}Kr levels in FIG. 3.2 in Italy and we expect a more or less flat plateau of ~ 1.5 Bq/m^3. To our knowledge, however, there is no monitoring station for ^{85}Kr in Italy available to experimentally validate this assumption.

The dominating krypton background in XENON100 from December 2009 until August 2010 (see the timeline in FIG. 1.7) was introduced through an air leak in December 2009. By chance, around this time we measured the ^{85}Kr atmospheric activity concentration of air from the laboratory (LNGS) XENON100 is located in. This sample was drawn on the 1st of October, 2009, and resulted in (1.3 ± 0.2) Bq/m^3 [87]. Using the volume fraction

---

[1] Throughout this work gaseous quantities are expressed in terms of their volume at STP conditions, where the International Union of Pure and Applied Chemistry (IUPAC) recommendation of 0 °C and 100 kPa [86] is used.

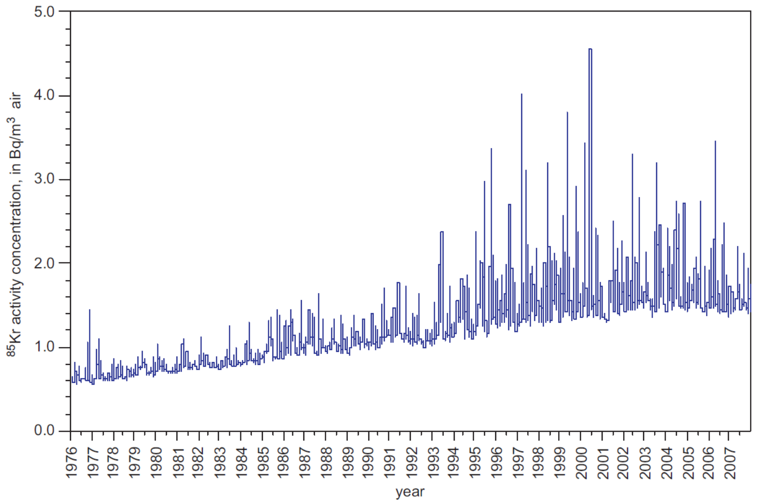

Figure 3.2: ^{85}Kr atmospheric activity concentration at sampling site Mount Schauinsland, Germany. Figure from [77].

of krypton in air (1.14 ppm [66]), krypton's molecular mass (83.79 u = 83.79 g/mol [88]) and its density at STP (3.75 kg/m^3 [68]), one calculates the number of krypton atoms in 1 m^3 air, ϱ_{Kr}, to be:

$$\varrho_{\mathrm{Kr}} = 5.10 \times 10^{-5}\,\mathrm{mol/m^3}\,. \tag{3.1}$$

The measured ^{85}Kr activity (A_{Kr85}) is related to the absolute number of ^{85}Kr atoms (N_{Kr85}) by the decay constant ($\lambda_{\mathrm{Kr85}} = ln(2)/T_{1/2}$) of its β decay:

$$N_{\mathrm{Kr85}}/A_{\mathrm{Kr85}} = 8.12 \times 10^{-16}\,\mathrm{mol/Bq}\,, \tag{3.2}$$

where we used the Avogadro constant $N_A = 6.022 \times 10^{23}\,\mathrm{mol^{-1}}$ [89] and ^{85}Kr's decay constant of $\lambda_{\mathrm{Kr85}} = 2.044 \times 10^{-9}\,\mathrm{s^{-1}}$ [90]. Thus, we find

$$\begin{aligned}\frac{^{85}\mathrm{Kr}}{^{\mathrm{nat}}\mathrm{Kr}} &= \frac{N_{\mathrm{Kr85}}/A_{\mathrm{Kr85}}}{\varrho_{\mathrm{Kr}}} \times \left(\frac{A_{\mathrm{Kr85}}}{\mathrm{Bq/m^3}}\right)\frac{\mathrm{mol}}{\mathrm{mol}} \\ &= 1.59 \times 10^{-11} \times \left(\frac{A_{\mathrm{Kr85}}}{\mathrm{Bq/m^3}}\right)\frac{\mathrm{mol}}{\mathrm{mol}}\,.\end{aligned} \tag{3.3}$$

The aforementioned assay of Hall A, LNGS, air then can be used to compute the ^{85}Kr/$^{\mathrm{nat}}$Kr ratio to be $(2.1 \pm 0.3) \times 10^{-11}$ mol/mol. The values shown in FIG. 3.2 correspond to a much wider range from roughly 1×10^{-11} mol/mol to 6×10^{-11} mol/mol. The fact that the krypton impurities were introduced to XENON100 only within a few

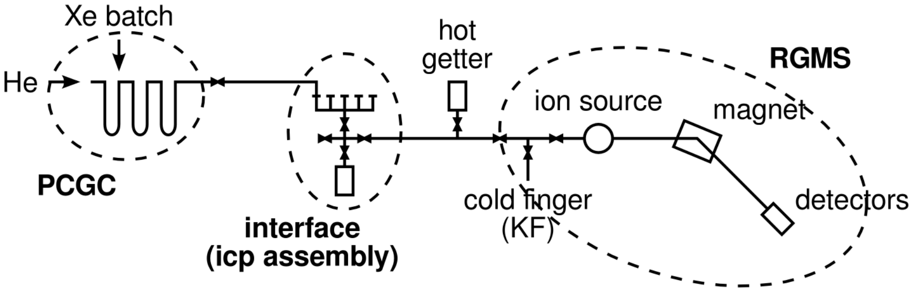

Figure 3.3: Simplified scheme of the connections between ion source, mass analyzer and detectors (RGMS) and the sample preparation (PCGC) as well as the interface where the independent calibration pipette (ICP, see section 3.2.3) has been assembled.

days close to the ambient air assay in the same laboratory, suggests to favor the former ratio of 2×10^{-11} mol/mol.

3.2 The sector field mass spectrometer

In this work a mass spectroscopic technique is developed to quantify the abundance of natural krypton in given xenon gas batches down to the ppq regime. The setup can be divided into four parts: sample preparation, ion source, mass analyzer and detector. Ion source, mass analyzer and detector belong to a customized sector field mass spectrometer (Vacuum Generators model VG 3600) that is described in section 3.2.1 and is referred to as rare gas mass spectrometer (RGMS). The sample preparation, based upon cryogenic gas chromatography, is the essential new development and will be discussed in section 3.2.2. We will refer to this setup as prepended cryogenic gas chromatograph (PCGC) in the following. See FIG. 3.3 for a simplified scheme of the single components, that will be individually discussed in the following sections.

Starting point always is some larger quantity of xenon to be examined, e.g. the liquid xenon target of the XENON100 detector or xenon in a pressurized gas cylinder. To determine the krypton level of this xenon we will not process the full amount of gas but will draw small *sample*s (see section 3.4.1). These samples then are transfered to the PCGC. One sample can be divided in several *batch*es. Each batch then is analyzed individually in the PCGC+RGMS process.

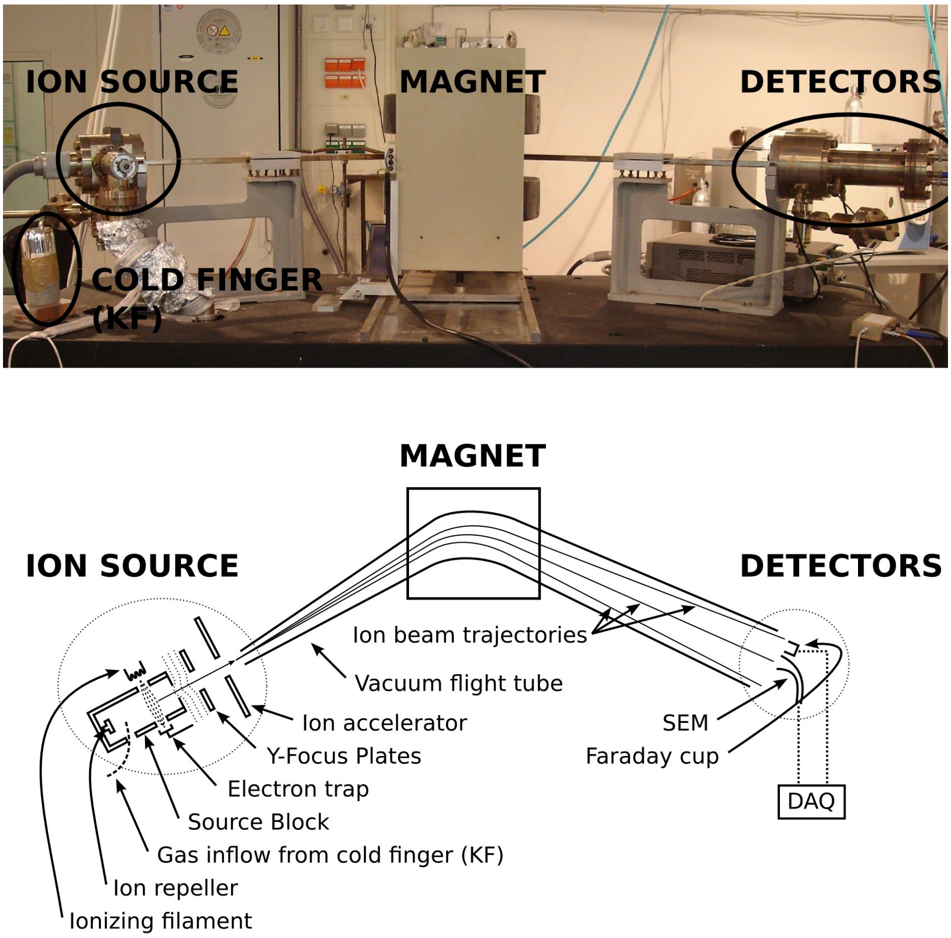

Figure 3.4: (top) Picture of the RGMS (VG 3600) mass spectrometer applied to quantify krypton traces of even 1×10^{-13} cm^3. (bottom) Working principle of the RGMS.

3.2.1 The mass spectrometer

The mass spectrometer is a customized version of a VG 3600 (Fig. 3.4), being utilized intensely for Earth and planetary science applications in the past and capable of quantifying an amount of natural krypton of less than $10^{-13}\,\mathrm{cm}^3$ [91]. The VG 3600's main purpose is the analytics of the isotopic composition of chemically inert (*rare*).

The batch is collected by cryogenic pumping on a cold finger installed between sample preparation part and ion source. Warming up the cold finger, the gas distributes in the entire volume of ion source, mass analyzer and detectors. Ionization, acceleration and focusing take place in the ion source of the mass spectrometer. Electrons are emitted from a hot filament and ionize the batch. The produced ions are accelerated and focused

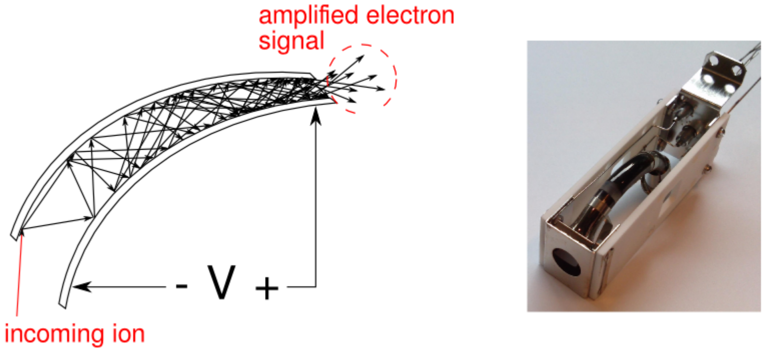

Figure 3.5: Secondary electron multiplier (SEM): a continuous dynode particle (ion) multiplier detector.

in electric fields. Their mass separation is achieved by a variable magnetic dipole-field. The ions are detected by a continuous dynode amplifier (*SEM* = secondary electron multiplier) in case of a small signal ($< 10^5$ ions/sec) or alternatively by a *Faraday cup* in case of stronger signals. A SEM is a vacuum tube structure that multiplies incoming particles. It is coated by a secondary emissive material where the incoming particle induces emission of several (1 to 3) electrons. Each electron is accelerated by the electric potential inside the SEM and induces further secondary emission of electrons when hitting the continuous dynode (see FIG. 3.5). The resulting shower of electrons is collected by a metal anode where the amplified signal is finally measured. A Faraday cup can be seen as part of a circuit in which ions serve as moving charge carriers in vacuum. The number of ions (assumed to be single charged) is accessed by measuring the electrical current the ions generate. To achieve a high sensitivity, batch sizes on the order of $1\,\mathrm{cm}^3$ xenon gas are needed. However, this amount of xenon gas would result in a pressure much above the critical pressure of $10^{-6}\,\mathrm{mbar}$ [92] in the spectrometer and collisions between ions and sample gas make a measurement not possible. As a consequence, the krypton must be separated from the bulk xenon before it is fed into the spectrometer. This separation is achieved in the gas chromatography system. It will be described in more detail in the next section.

3.2.2 The gas chromatography system

The krypton/xenon separation is performed via gas chromatography in the setup sketched in Fig. 3.6. The amount of helium carrier gas used in this process exceeds the size of the xenon batch by more than a factor of 50. Therefore, the purity specifications in terms of krypton inside the helium gas are strict. To reach sub-ppt sensitivity,

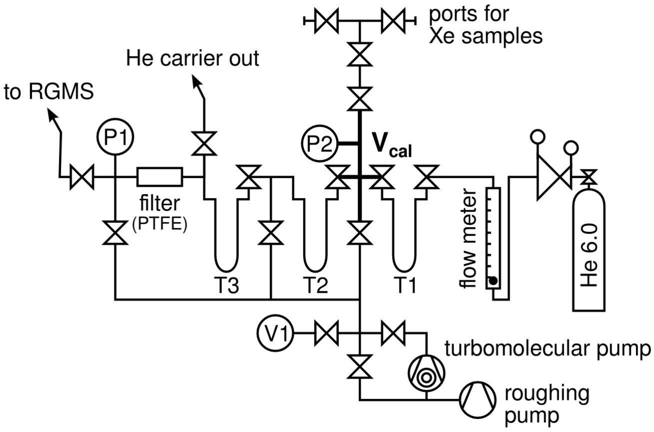

Figure 3.6: Schematic of the gas chromatography system. The system is equipped with an analog membrane pressure gauge (P1), a capacitive pressure gauge (P2) and a combined Pirani/cold cathode vacuum gauge (V1).

the krypton concentration in the helium has to be at or below the ppq level. In this work grade 6.0 helium is purified using an adsorbent filled packed column T1 (10 mm inner diameter, 8.18 g Carbosieve S-III by Supelco Analytical) immersed in a liquid nitrogen bath. Pushed forward by the helium carrier, the gas mixture passes another adsorbent filled column T2 (6 mm inner diameter, 0.64 g Chromosorb 102 by Johns Manville) immersed in a coolant liquid (ethanol). Differences in the interaction strength of each constituent with the adsorbent lead to a macroscopic separation of both. Adjusting the flow of the carrier gas, the pressure gradients and the temperature result in a clear separation of krypton from xenon as shown in Fig. 3.7. The temperature of the ethanol coolant and the helium gas flow for the separation in this work were fixed to −80 °C and 7 standard cubic centimetre per minute (sccm).

The separated krypton is trapped on a third adsorbent filled packed column T3, identical to T2. By heating up T3 after the chromatographic process the krypton is released and can be transfered to the mass spectrometer by cryogenic pumping to the cold finger mounted next to the ion source of the mass spectrometer.

The ultra-high vacuum (UHV) system is, except the three adsorbent filled traps, fully constructed in stainless steel with all flanges being copper sealed (ConFlat flanges). The adsorbent filled traps are made from borosilicate glass with special glass to metal seals well suited for the high purity demands. To avoid dust from the adsorbent entering the mass spectrometer a PTFE nano particle filter is installed. The stainless steel and glass part of the system is bakeable to above 300 °C, however, adsorbent materials and PTFE

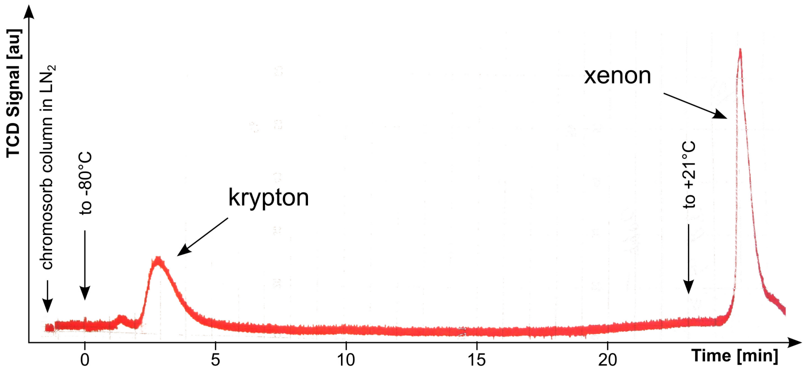

Figure 3.7: Signal of a thermal conductivity detector versus time for a krypton/xenon separation (0.5 cm^3 krypton, 1.0 cm^3 xenon) via cryogenic gas chromatography using an adsorbent filled packed column identical to T2 of the gas chromatographic system.

filter withstand only temperatures up to 150 °C and 120 °C, respectively, setting the upper limit on the temperature during bakeout. The system provides a turbomolecular pump backed up by a dry and oil free piston vacuum pump. The latter one is important to avoid hydrocarbons entering the system and altering the performance of the adsorbents. The used valves are fully metal sealed bellow type 3/4 inch valves with a leak rate specification of $< 5 \times 10^{-11}$ mbar/(l s). A precise capacitance manometer from Edwards (Barocel 600 series, 0.15 % accuracy, labelled P2 in Fig. 3.6) is installed to determine the initial gas amount of the xenon batch. The system is further characterized by an analog, fully metal sealed pressure gauge (P1) and a combinded Pirani/cold cathode vacuum gauge (V1) that can be separated from the sample by a valve.

3.2.3 Calibration and data analysis

A gas standard is available to calibrate the mass spectrometer and to determine the acceptance of the full gas chromatographic process. The gas standard is composed of the noble gases argon, krypton and xenon that are filled to a metal sealed container of a few liters volume. Connected to this container is a second, much smaller volume ($\sim 0.2\,\text{cm}^3$) that is separated from the latter by a fully metal sealed valve. This volume is used to extract a constant fraction of the gas standard (standard pipette). The amount of krypton in one standard pipette was calibrated using a sample of commercially available helium containing a well-known admixture of krypton. This calibration defines the amount of krypton in our standard pipette to be $3.9 \times 10^{-11}\,\text{cm}^3$ ($\pm 16.5\,\%$). The precise procedure is described in the following section. The argon and xenon abundances

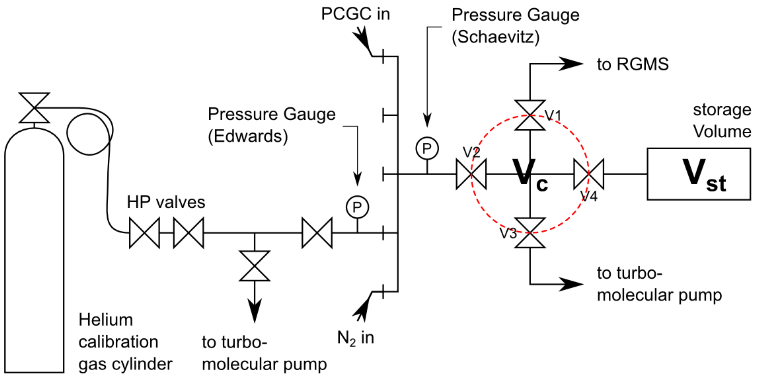

Figure 3.8: In between the RGMS and the PCGC there is an electro-polished, fully metal-sealed interface unit hosting five CF16 sealed ports, two of which permanently occupied by a nitrogen inlet and the connection to the PCGC. Four valves enclose a small volume $V_c = (47 \pm 6)\,\text{cm}^3$. Further, the unit facilitates a pump (combination turbomolecular and roughing pumps) and a second volume $V_{st} = (26.5 \pm 0.7) \times V_c$. A precise pressure gauge (Schaevitz) completes the unit. Also shown in the sketch is the tubing done for ICP assembly (see text).

in the standard pipette were not re-evaluated in this work. However, their amount is estimated to be $40 \times 10^{-9}\,\text{cm}^3$ and $50 \times 10^{-12}\,\text{cm}^3$, respectively [93].

Independent calibration pipette

Certified calibration gas cylinders were purchased from Air Liquide[2] for measurements with the COMGC, a customized tool for analyzing impurities in gases at the low ppb level (see section 3.3). These calibration gases are based on helium with impurities on the 10 ppm level. From one of those calibration gases a cylinder was taken with a certified krypton level of $f_{\text{Kr}} = (11.13 \pm 0.22)$ ppm and connected to one of the ports shown in FIG. 3.8. For purity reasons the gas cylinder was installed without a pressure regulator but two high pressure valves to extract some of the gas. Connected to the high pressure valves by a stainless steel tube a T-fitting with fully metal sealed valves at the remaining two ends was mounted. One of the valves was connected to the port where also a precise pressure gauge (Edwards; Barocel 600 series, 0.15 % accuracy) was added, the other valve was connected to a combination of turbomolecular and roughing pumps. The tubes from the helium calibration gas cylinder to the valve in front of the Edwards pressure gauge were cleaned by flushing calibration gas from the helium cylinder followed by evacuating the tubes. Then the valve at the calibration gas cylinder was closed and the tubes were

---

[2] http://www.airliquide.com/

evacuated to a pressure $< 10^{-7}$ mbar for more than 12 hours. During these operations the valve at Edwards pressure gauge was kept close. The permanently installed part of the interface unit connecting PCGC and RGMS was cleaned by baking and pumping with the turbomolecular pump to $< 10^{-7}$ mbar for again more than 12 hours.

After proving the volumes $\mathrm{V_{st}}$ and $\mathrm{V_c}$ (see FIG. 3.8) to be clean by measuring their individual outgassing of krypton with the RGMS, $\mathrm{V_c}$ was filled at a pressure of $p_{ed} = (0.41 \pm 0.02)\,\mathrm{mbar}$ (determined by the Edwards pressure gauge). This amount of gas (G_0) was then expanded into $\mathrm{V_{st}}$ that was closed afterwards. The remaining gas in $\mathrm{V_c}$, I_0, is a fixed fraction thereof:

$$\begin{aligned} I_0 &= \alpha \cdot G_0 \\ &= \alpha \cdot p_{ed} \cdot \mathrm{V_c} \cdot \frac{T_0}{T_{\mathrm{Vc}}} \cdot f_{\mathrm{Kr}}\,, \end{aligned} \tag{3.4}$$

where T_0 and T_{Vc} are the temperatures (in Kelvin) at standard conditions ($T_0 = 273.15\,\mathrm{K}$) and in $\mathrm{V_c}$, respectively, at the moment when the calibration gas was filled and the pressure p_{ed} was noted. f_{Kr} marks the fraction of natural krypton in the helium calibration gas. The ratio $\alpha = \mathrm{V_c}/(\mathrm{V_c} + \mathrm{V_{st}})$ can be computed knowing the absolute volumes $\mathrm{V_c}$ and $\mathrm{V_{st}}$, or experimentally determined by the pressure decrease after expanding the amount of gas (p_i) from $\mathrm{V_c}$ to $\mathrm{V_{st}}$ (p_f). Then we simply find $\alpha = p_f/p_i$. In this work the latter approach was followed because, due to technical limitations, the relative error on determining $\mathrm{V_{st}}$ is much larger than the one of α.

To I_0, or generally I_n, we refer in the following as independent calibration pipette (ICP) and the amount of krypton it contains is:

$$I_0 = (7.2 \pm 1.1) \times 10^{-9}\,\mathrm{cm}^3\,. \tag{3.5}$$

Hereby, we have inserted $\mathrm{V_c} = (47 \pm 6)\,\mathrm{cm}^3$, $T_{\mathrm{Vc}} = (296.2 \pm 0.5)\,\mathrm{K}$ and $\alpha^{-1} = (26.5 \pm 0.7)$ to equation 3.4.

For every new ICP measurement the remaining gas stored in $\mathrm{V_{st}}$ is expanded to $\mathrm{V_c}$. Thus, the amount of gas extracted is smaller by the factor α compared to the previous extraction. For the n^{th} extraction we find:

$$\begin{aligned} I_n &= \alpha \cdot G_n \\ &= G_0 \cdot \alpha \cdot (1-\alpha)^n\,. \end{aligned} \tag{3.6}$$

The amount of helium in every ICP is by about a factor 10^5 greater than the other components. To reduce it, the ICP is frozen to the cold finger for 40 minutes, as it is done with all batches in the standard procedure. Afterwards the helium is evacuated while the cold finger is still immersed in liquid nitrogen. This procedure is tested to not effect the amount of krypton.

Following above outlined procedure we are able to transfer a well-known amount of krypton from the commercial calibration gas cylinder to the mass spectrometer. The response of the RGMS to this calibrated amount of krypton can be compared to the response generated by the standard pipette. In so doing, the krypton amount of the standard pipette (std_{nat}) is determined to be:

$$std_{\mathrm{nat}} = (3.9 \pm 0.6) \times 10^{-11}\,\mathrm{cm}^3\,. \tag{3.7}$$

Magnetic field calibration

The magnetic field f in our mass analyzer is empirically parameterized by a forth order polynomial in $m^{1/2}$, where m is the ion mass reaching the detector for the given field:

$$f(m) = d + c \cdot m^{1/2} + b \cdot m + a \cdot m^{3/2}\,. \tag{3.8}$$

The parameters $a, \ldots, d$ have to be determined from time to time and are validated subsequent to the measurement of a xenon batch by scanning at least over the masses of the investigated krypton isotopes. The magnetic field is set by a field controller adjusting the current through an electro-magnet's coils of up to 4 A and reading (feedback control) the output of a Hall probe installed inside the magnetic field next to the flight tube. The parameters $a, \ldots, d$ are determined fitting equation 3.8 to the field values corresponding to masses of the various argon, krypton and xenon isotopes present in the standard pipette (see FIG. 3.9).

Batch transfer to mass spectrometer

The batch is transfered to the cold finger by cryogenic pumping for 40 min, while the valve between cold finger and ion source is closed. During this time the main spectrometer parts (ion source, flight tube and detectors) are evacuated. Then the volume around the cold finger is closed and warmed up to room temperature. At the same time evacuation of ion source, flight tube and detectors is stopped and data taking starts. For about 20 minutes, while the sample in the cold finger warms up, the time dependence of the closed spectrometer's background is monitored and stored to disc. At time

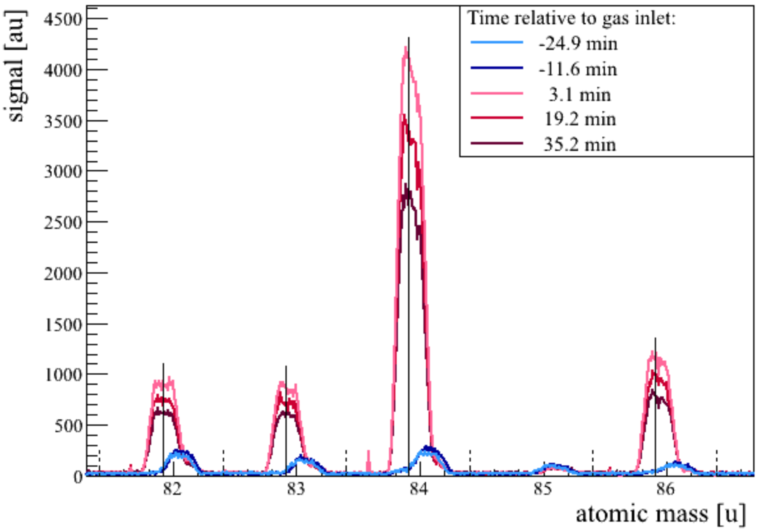

Figure 3.9: SEM signal, scanning the magnetic field over the most abundant krypton isotopes, taken within 1 hour before (blue) and after (red) a krypton sample from the standard pipette is introduced to the spectrometer.

zero (t_0) the valve between cold finger and main spectrometer is opened and the gas distributes in the spectrometer. FIG. 3.9 shows the time dependence of the ^{84}Kr SEM signal from the standard pipette. Outgassing from the walls (increasing background) and implanting to the walls (decreasing signal) explain the shown behavior. A slowly increasing and slightly shifted to higher masses background from (eventually multiply ionized) hydrocarbons is apparent before the krypton sample is introduced (blue curves). The center of mass of these background peaks is shifted compared to krypton because of the proton-neutron asymmetry of stable isotopes. While the krypton peaks are slightly shifted below their respective mass numbers, hydrocarbons are somewhat located above. After introducing the krypton batch a much higher but decreasing signal (red curves) is observed that originates from the standard pipette's krypton. Indicated with solid lines are the literature values of the atomic masses of ^{82}Kr, ^{83}Kr, ^{84}Kr and ^{86}Kr (see Table 3.1 or [88]). The dotted lines mark the offset positions the continuous background is measured at. The shape of the peaks is a convolution of the Maxwellian velocity distribution of the isotopes superimposed by the directed acceleration of the ions in the electric field of the ion source and the slit in front of the detectors that is enhancing the resolution at the expense of signal strength.

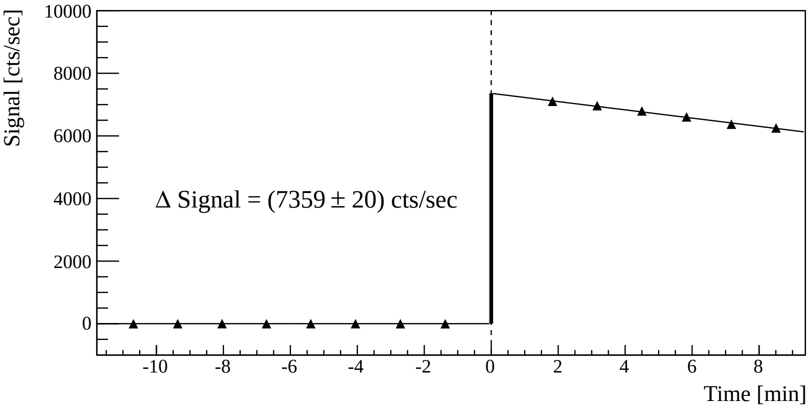

Figure 3.10: Typical time evolution of the ^{84}Kr signal strength from the standard pipette. At time zero ($t_0 = 0$) the gas is expanded from the cold finger into the ion source and adjacent volumes (vacuum flight tube, detectors).

SEM response

The response of the mass spectrometer to the amount of one standard pipette is determined at least once before the measurement of a batch. In the analysis we are interested in the amount of gas initially transfered to the cold finger, that is at time zero (t_0), before other processes (like implanting accelerated ions into the walls of the mass spectrometer's vacuum tube) start to change its amount. The time-dependence of the count rate of background and signal are fitted and extrapolated to t_0 where the size of the pedestal, as seen in Fig. 3.10, is a measure of the amount of gas from the respective isotope in the batch.

Data acquisition

In the standard case the magnetic field is set to the investigated mass (see equation 3.8), is kept constant (depending on previous field settings for 3 s to 10 s) until the signal is stable and the signal strength is measured. Concerning the continuous dynode amplifier (SEM), which is operated in avalanche counting mode, one data point counts pulses (avalanches) above a predefined threshold for 1 s. To improve statistics 8 to 12 data points are acquired without changing the field. Afterwards the continuous background in form of one data point each to the left and to the right of the peak (dotted lines in FIG. 3.9) is recorded by adjusting the magnetic field accordingly. In the off-line analysis the data points taken at the literature mass of the isotope (TAB. 3.1) are averaged

Table 3.1: Atomic masses and mole fractions (relative abundances) of the stable isotopes from argon, krypton and xenon [88, 94–97].

Isotope	atomic mass [u]	mole fraction
^{36}Ar	35.967 546 26(27)	0.003 365(30)
^{38}Ar	37.962 732 2(5)	0.000 632(5)
^{40}Ar	39.962 383 124(5)	0.996 003(30)
^{78}Kr	77.920 388(7)	0.003 55(3)
^{80}Kr	79.916 379(4)	0.022 86(10)
^{82}Kr	81.913 485 0(28)	0.115 93(31)
^{83}Kr	82.914 137(4)	0.115 00(19)
^{84}Kr	83.911 508(3)	0.569 87(15)
^{86}Kr	85.910 615(5)	0.172 79(41)
^{124}Xe	123.905 895 4(21)	0.000 952(3)
^{126}Xe	125.904 268(7)	0.000 890(2)
^{128}Xe	127.903 530 5(15)	0.019 102(8)
^{129}Xe	128.904 779 9(9)	0.264 006(82)
^{130}Xe	129.903 508 9(11)	0.040 710(13)
^{131}Xe	130.905 082 8(18)	0.212 324(30)
^{132}Xe	131.904 154 6(15)	0.269 086(33)
^{134}Xe	133.905 394 5(9)	0.104 357(21)
^{136}Xe	135.907 220(8)	0.088 573(44)

and the baseline average is subtracted. The baseline-corrected value marks the signal strength for the respective isotope at the time of measurement. Usually, in one measurement cycle for each element two or more isotopes are considered. The measurement procedure foresees a loop over the investigated masses lasting approximately one minutes for each pass, following the above explained procedure for each single mass.

Off-line analysis

In standard data taking mode a loop over the isotopes ^{36}Ar, ^{40}Ar, ^{84}Kr, ^{86}Kr and ^{132}Xe is recorded. The measured ratios ^{40}Ar/^{36}Ar and ^{84}Kr/^{86}Kr have to match their natural abundances (mole fractions) and are used as quality parameters. To get a final number on the amount of krypton measured by the mass spectrometer the amount of gas at time zero is determined for ^{84}Kr and ^{86}Kr independently as described above. From both isotopes the amount of natural krypton is computed using the respective relative abundance. The numbers are combined using both an arithmetic average and an average quadratically weighting the respective errors. To be conservative, between both the one having the bigger error is chosen for the further analysis.

Krypton acceptance

A small amount of krypton and xenon from the standard pipette is used to determine the acceptance of the gas chromatographic (PCGC) process for krypton. The calibrated mixture of krypton and xenon is transferred by cryogenic pumping to the adsorbent trap T2 (immersed in liquid nitrogen) used for the krypton/xenon separation. Then the full chromatographic procedure is performed – identical to the standard procedure for a normal xenon batch – and the spectrometer's response to the krypton isotopes is compared to its response without the chromatographic separation process. This calibration procedure yields a krypton acceptance of $\epsilon_a = (0.97 \pm 0.02)$.

However, the procedure uses microscopic krypton and xenon gas samples on the order of a few $10^{-12}\,\mathrm{cm}^3$, while the standard procedure foresees xenon batches of up to several cm^3 containing only traces of krypton. Adding the amount of $3.9 \times 10^{-11}\,\mathrm{cm}^3$ of $^{\mathrm{nat}}$Kr from the standard pipette to roughly $1.2\,\mathrm{cm}^3$ of xenon from sample RDF ((1.8 ± 0.4) ppt intrinsic krypton, see section 3.4.2), we measure $(3.2 \pm 0.7) \times 10^{-11}\,\mathrm{cm}^3$ $^{\mathrm{nat}}$Kr. Reevaluating the acceptance for krypton, we find $\epsilon_a = (0.79 \pm 0.18)$ in agreement with above result. The larger uncertainty in this value is dominated by the uncertainty in the intrinsic krypton level of the bulk xenon and the sample standard deviation of a single measurement (see below). The weighted average of both, $\epsilon_a = (0.97 \pm 0.02)$, will be used throughout this work.

Computation of krypton impurity level

The krypton impurity level for a given batch is the ratio of the amount of krypton gas measured by the mass spectrometer and the initial batch size determined by its pressure in the calibrated volume. We can write:

$$\frac{^{\mathrm{nat}}\mathrm{Kr}}{^{\mathrm{nat}}\mathrm{Xe}} = \frac{\left\langle (\mathrm{Kr}_i - B_i) \cdot f_m(i)^{-1} \right\rangle_i \cdot \epsilon_a^{-1}}{^{\mathrm{nat}}\mathrm{Xe}}\,, \tag{3.9}$$

where i labels the individual isotope, $f_m(i)$ is the mole fraction of the respective isotope, $\langle \dots \rangle_i$ denotes the average over the isotopes i and ϵ_a is the acceptance of the full chromatographic process for krypton. Kr_i is the quantitative measurement of the krypton isotope i with the spectrometer. It is computed from the abundance of the krypton isotope i in the standard pipette (std_i) and from the ratio of the pedestals of the batch (s_i^{batch}) and the standard pipette (s_i^{std}):

$$\mathrm{Kr}_i = \frac{s_i^{\mathrm{batch}}}{s_i^{\mathrm{std}}} \cdot std_i \,. \tag{3.10}$$

Finally, B_i is the procedure blank of the full process for the isotope i, as will be explained below, and can be written similar to (3.10) substituting s_i^{batch} by s_i^B.

Knowing the pressure p at temperature T of the xenon gas in the volume $\mathrm{V}_{\mathrm{cal}}$, the initial size of the xenon batch ($^{\mathrm{nat}}\mathrm{Xe}$) computes to:

$$^{\mathrm{nat}}\mathrm{Xe} = p \cdot \mathrm{V}_{\mathrm{cal}} \cdot T_0/T \,, \tag{3.11}$$

where T_0 is the standard temperature in Kelvin.

Uncertainty budget estimation

Systematic effects common to all measurements are the uncertainty of the standard pipette (Δstd_i), the uncertainty in determining the initial xenon batch size and the uncertainty of the chromatographic acceptance for krypton ($\Delta\epsilon_a$). The uncertainty in the xenon batch size itself results from the systematic uncertainty of the capacitive pressure gauge (Δp), of the absolute size of the calibrated volume ($\Delta\mathrm{V}_{\mathrm{cal}}$) and the temperature reading (ΔT).

Strictly speaking, the uncertainty of the capacitance manometer does have a systematic component that depends on the absolute pressure. Consequently, its uncertainty differs in each measurement. The company specifies for our capacitance manometer (Barocel 600 series) an increasing relative uncertainty with decreasing pressure:

$$p_{\mathrm{err}}[\mathrm{mbar}] = 0.0015 \cdot p[\mathrm{mbar}] + 0.0133 \,, \tag{3.12}$$

where p is the pressure reading of the capacitance manometer and p_{err} its associated uncertainty. The pressure measurement is done as a difference ($p_{\mathrm{corr}} = p - p_{\mathrm{zero}}$) between the final reading p of the manometer with sample and the initial reading p_{zero} while evacuating the volumes around it ($p_{\mathrm{real}} < 10^{-3}$ mbar). That is to say, both values p and p_{zero} actually have different uncertainties. Anticipating the fact that the initial pressure readings for all measurements of this work were in the range $-0.1\,\mathrm{mbar} < p_{\mathrm{zero}} <$

0.1 mbar, we compute the relative uncertainty to be smaller than 3.3 % for pressures $p_{\text{corr}} > 0.6$ mbar as of this work. The uncertainty on the calibration volume V_{cal} is below 0.5 % and can safely be neglected.

Summing quadratically all systematic effects, we end up with a relative uncertainty of 17.0 % dominated by the uncertainty of the standard pipette.

Statistical fluctuations of the number of ions detected by the SEM, variations in performing the chromatographic separation and variations in the electrical fields of the ion optics due to high voltage drifts individually affect single measurements. The sum of these effects is estimated (for each sample individually) from the fluctuations of the measurement of several batches around their mean. The resulting uncertainty estimator is added quadratically to the aforementioned systematic uncertainties. In those cases, where only a single batch was measured, we estimate its uncertainty by averaging the sample standard deviations of all measurements so far done with this setup. We find 13.5 % to be a single measurement's standard deviation. Combining this number with the systematic uncertainty by summing them quadratically, we find the total relative uncertainty of a single batch to be 21.7 %. If more than one single batch is measured, the relative uncertainty decreases being limited to the systematic uncertainty of 17 %.

Sensitivity – procedure blank and detection limit

The sensitivity is limited by the traces of krypton which are collected during the full PCGC+RGMS process and increase the signal in the mass spectrometer. Sources for this type of krypton are potential leaks allowing external krypton to enter the system, outgassing of the surfaces involved in the measurement and krypton introduced by the helium carrier gas.

The amount of these krypton traces is accessed by performing the full procedure, identical to a normal measurement, but without a xenon batch introduced (procedure blank). A value of $(1.00 \pm 0.04) \times 10^{-12}\,\text{cm}^3$ is found averaging the measurements done between October 2012 and January 2013 (see FIG. 3.11) and represents the background condition for most of the presented results in section 3.4.2.

Fluctuations in the high voltage supply of the ion optics caused pronounced variations in the procedure blank until the end of 2012. The first maintenance of the RGMS solved this problem. However, a tiny leak opened in the sample preparation part causing the blank to be stable at an increased value. After a recent upgrade from February 2013 until June 2013 of the system (refurbished high voltage control of ion optics and identification and removal of tiny air leak in the sample preparation part) the new procedure blank was

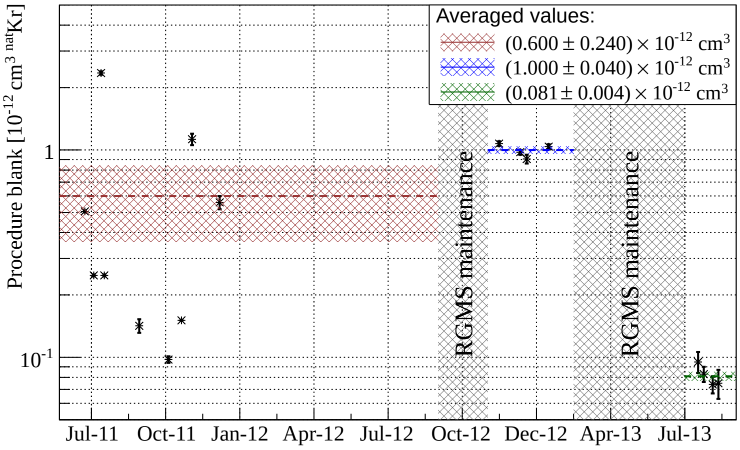

Figure 3.11: Blank of the full PCGC+RGMS procedure. A change in the background level (procedure blank) is observed after both maintenance periods (indicated in gray).

measured to be $(0.081 \pm 0.004) \times 10^{-12}\,\mathrm{cm}^3$. This is a reduction by more than a factor ten with respect to the value mentioned above. The first xenon sample measured at this significantly reduced background level is in excellent agreement with earlier results at the higher background level (see again section 3.4.2).

In the error budget of the procedure blank the systematic uncertainty of the calibration is neglected as all measurements are corrected for this procedure blank before the counting result is converted to an amount of gas using the absolute calibration (see equation 3.9).

The computation of decision threshold and detection limit is illustrated in FIG. 3.12. The dotted black curve shows the probability density function (PDF) for a measurement of a batch containing no krypton. I.e. its variation is identical to the one determined by the procedure blank measurements. The decision threshold (dotted black line) marks the point where the probability is more than 90 % for the outcome of a measurement of a krypton-free sample being smaller than the decision threshold. The solid red curve marks the probability distribution of the smallest possible amount of krypton processed by the full PCGC + RGMS procedure which has a 90 % chance to result in a value higher than the decision threshold, i.e. the detection limit at 90 % confidence level (marked by the dotted red line).

The decision threshold (DT) and detection limit (DL), computed at 90 % confidence level, result in $0.005 \times 10^{-12}\,\mathrm{cm}^3$ and $0.011 \times 10^{-12}\,\mathrm{cm}^3$ ($^{\mathrm{nat}}\mathrm{Kr}$), respectively, assuming a 21.7 % uncertainty of the outcome of a single measurement for the computation of the

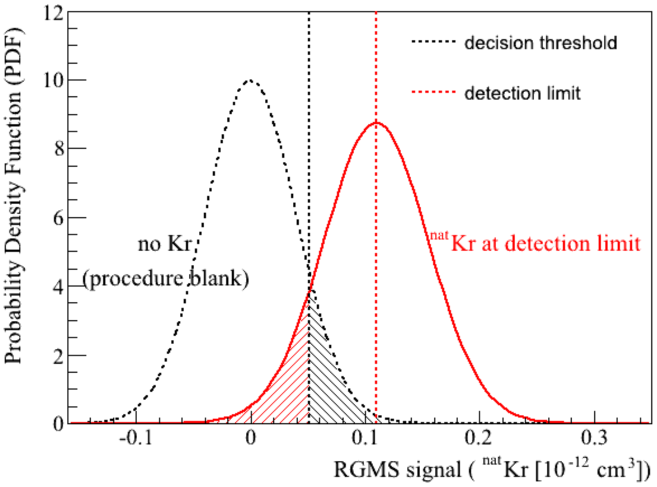

Figure 3.12: Sketch illustrating both decision threshold and detection limit [98] at the 90 % confidence level for the PCGC+RGMS Kr/Xe assay assuming a procedure blank of $(1.00 \pm 0.04)\,\mathrm{cm}^3$ $^{\mathrm{nat}}$Kr and a systematic uncertainty of 21.7 % for a single measurement.

DL. The procedure blank limits the minimal amount of $^{\mathrm{nat}}$Kr that is detectable by the mass spectrometer. The maximal size of the xenon batch that can be processed by the gas chromatographic separation determines the performance of the system. Up to now the largest xenon batch was $1.9\,\mathrm{cm}^3$ and we find at 90 % confidence level:

$$\mathrm{DL} = \frac{(^{\mathrm{nat}}\mathrm{Kr})_{\mathrm{min}}}{(^{\mathrm{nat}}\mathrm{Xe})_{\mathrm{max}}} = 6\,\mathrm{ppq}\,. \tag{3.13}$$

Note that likely larger xenon batches can be processed by the chromatographic process. The upper threshold for acceptable batch sizes was not determined yet. Consequently, the detection limit of currently 6 ppq may still be lowered in the future. This value, to our best knowledge, so far is unprecedented and, of even greater importance, more than sufficient for the krypton assay at the level of 100 ppq crucial for the successful operation of XENON1T (see section 3.1).

3.3 Commercial gas chromatograph

During this work a fully automated gas chromatograph (COMGC in the following) was purchased from S + H Analytic GmbH on the basis of a standard gas chromatograph

(Trace GC Ultra from Thermo Scientific[3]). The COMGC was asked to be set up in a multi-purpose way to be adaptable to a wide range of analytical problems. A version employing five six-port and one ten-port high purity diaphragm switching valves (see FIG. 3.13) placed in two valve ovens with adjustable temperatures of up to 150 °C was required. In the first specified layout four packed columns of 2-3 meters length each were used for the separation process of impurities from a xenon sample - the first analytical task of the COMGC. The packed columns are either hosted in one of the isothermal valve ovens or in the programmable and temperature-controlled cryogenic oven, allowing for temperatures in the wide range from $-99\,^{\circ}\mathrm{C}$ to $300\,^{\circ}\mathrm{C}$. Changing the temperature during a single analytical run, that is in most cases increasing it with time, has the advantage to be able to separate the fast eluting gases N_2, O_2, Ar, H_2, Kr, CH_4 as well as to limit the time gases like Xe, CO_2, H_2O, that interact stronger with the adsorbent, need to pass the packed columns. The gases eluting from the last column are fed to a pulsed discharge detector (see next section) with a universal response to all gases (except for neon) and a detection limit of few ppb.

3.3.1 Pulsed discharge detector

The working principle of a pulsed discharge detector, first described in 1992 [99, 100], is based on pulsed helium discharge photo-ionization (He-PDPI). Gases eluting from the column and fed to the detector are ionized by high energetic photons from the Hopfield emission, that is, the transition from diatomic helium He_2 to the dissociative 2He ground state. In the PDD the Hopfiled emission is created in a pulsed high voltage discharge between platinum electrodes in pure helium gas inside the discharge region (see FIG. 3.14). The Hopfield photons from the He_2 continuum have energies ranging from 13.5 eV to 17.5 eV [101], enough to ionize all elements but neon and helium itself. The ionization current, focussed by two bias electrode rings, is measured on the collector electrode and constitutes the signal. Discharge region and ionization region are locally separated to ensure a clean helium environment at the discharge electrodes minimizing the possibility of contamination of the latter. The response of He-PDPI detectors (in the following only PDD) are linear for most compounds over a range of five orders of magnitude [102], allowing the calibration at the ppm and trace-analysis at the low ppb level.

---

[3] http://www.thermoscientific.com/

PDD	Pulsed Discharge Detector	PRV	Pressure Regulator Valve
PC1	Packed Column (1/4") (2m Hayesep in Valve-Oven)	PC2	Packed Column (1/4") (3m MS5Å in Cryo-Oven)
V1	Diaphragm Switching Valve	V2	Diaphragm Switching Valve

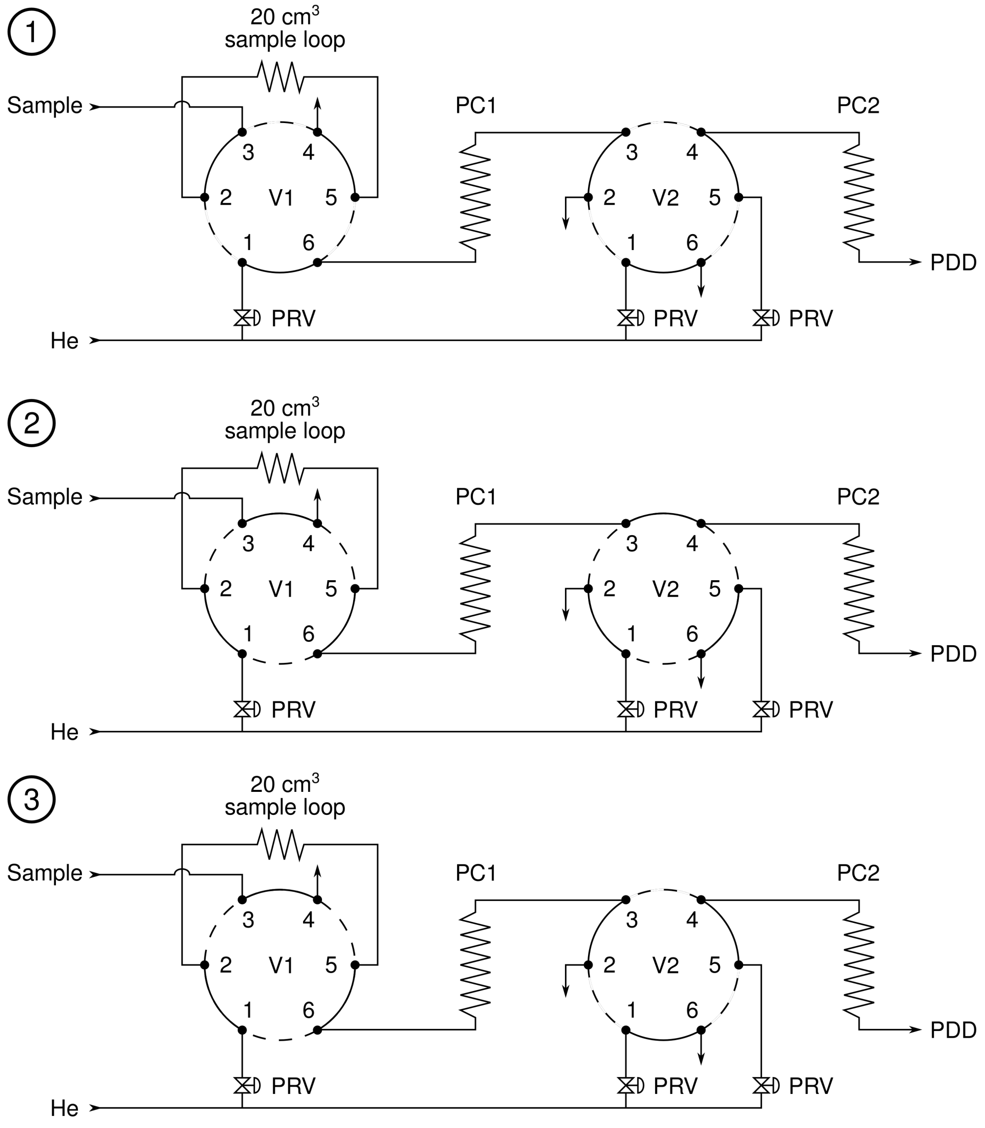

Figure 3.13: Simplified flow chart of the COMGC to measure krypton traces in a xenon sample. Labelled ① – ③ are the flow conditions for the three different valve settings of V1 and V2. See text for a detailed description of the procedure.

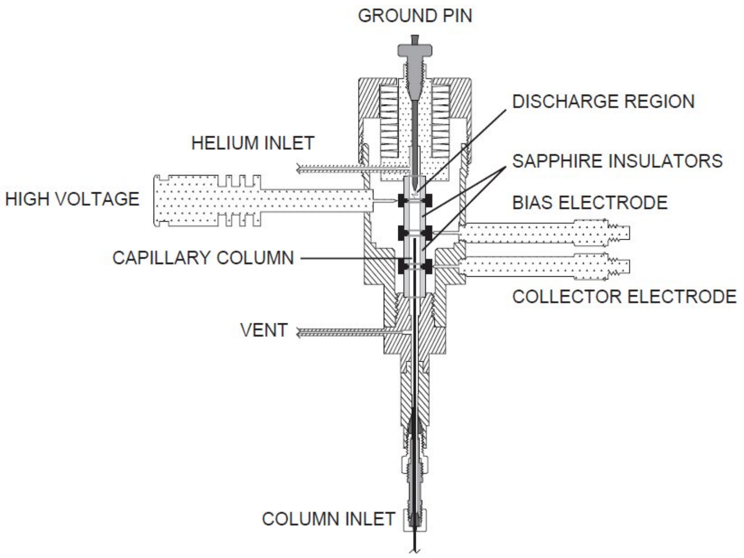

Figure 3.14: Cutaway view of a pulsed discharge detector (PDD) in the so-called helium discharge photoionization configuration (He-PDPID). Reprinted from the VICI (Valco Instruments Co. Inc.) Pulsed Discharge Detector Models D-4-I-TQ-R and D-4-I-TQI-R Instruction Manual. See text and [99–101] for further informations.

3.3.2 Customized setup

FIG. 3.13 shows a simplified flow chart of the COMGC set up to measure krypton traces in a xenon gas sample according to the following procedure:

① The sample loop is flushed by the xenon sample, while the two packed columns PC1 and PC2 are cleaned by a purified (hot getter) helium gas stream.

② V1 and V2 are switched compared to ①. Thus, the sample stored in the 20 cm^3 sample loop is transfered by the helium carrier to PC1. At an isothermal temperature of 60 °C the xenon matrix is slowed down compared to the krypton traces by PC1 in the Valve Oven. Krypton elutes after some time from PC1 together with the other air specific impurities like N_2, O_2 and Ar.

③ V2 is switched back after krypton passed PC1 but before the xenon matrix gas starts to elute. PC2, placed in the Cryo Oven, is initially cooled to -25 °C, followed by a temperature increase to 40 °C. This results in a clear separation of those impurities, that elute before xenon from PC1 with a detection limit of about 5 ppb.

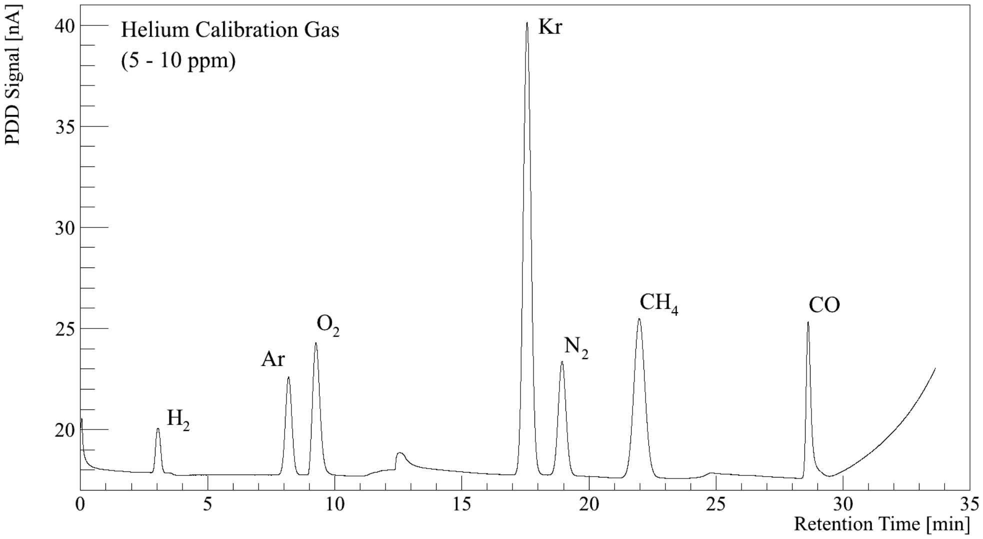

Figure 3.15: Calibration of COMGC using a helium based calibration gas with impurities at the 5 to 10 ppm level. A good separation of the single components is visible. Krypton, the impurity of interest in this work, has a retention time of about 17.5 minutes. Its concentration in the calibration gas is (10.98 ± 0.22) ppm.

3.3.3 Calibration and data analysis

The COMGC is calibrated by a commercially available He gas cylinder with certified amounts of trace impurities in the low (5 to 10) ppm regime. The sample loop is flushed with the helium calibration gas for sufficient time[4]. Then the fully automated procedure is started. Gases elute after a fixed time (retention time) from the columns. The ordering in time of different components has to be determined by spiking with the respective single component and is in first approximation the same as the order of the boiling points of these components. See FIG. 3.15 for the PDD response to $20\,\mathrm{cm}^3$ calibration gas processed by the COMGC.

The area below a peak – subtracting the baseline by a linear extrapolation of the background to the left and to the right of the peak[5] – is proportional to the amount of gas. Thus, for each component i the signal (area) a_i^{cal} corresponding to the concentration $cal(i)$ of the component i in the calibration gas is assessed:

$$c_i \equiv a_i^{cal}/cal(i)\,. \tag{3.14}$$

---

[4] Remaining traces from previous measurements or ambient air has to be removed. This has to be experimentally validated.

[5] This is only a good approximation as long as there are no other peaks in between.

The background, coming from the helium carrier gas and other possible sources like tiny leaks, can be accessed by two means: First, by neglecting the first step in the procedure (3.3.2), i.e. not switching V1 to the sample loop, and second, by flushing the sample loop with purified helium. If the system works correctly, either of both methods give the same result. Usually the background signal is much lower than the calibration signal and can safely be neglected in the computation of c_i. The impurity level (IL_i) of the component i in a sample is then computed by the product

$$\mathrm{IL}_i = c_i \cdot (a_i - a_i^{bg}), \tag{3.15}$$

where a_i is the signal area of the peak corresponding to component i and a_i^{bg} is the area of the same peak found in a background measurement.

3.3.4 Sensitivity

In the measurements of the krypton concentration in a xenon sample, that will be presented in the following, a_i^{bg} (black curve in FIG. 3.16) is difficult to be distinguished from random baseline variations. Those baseline variations are predominantly produced by the PDD, but also impurities entering the system continuously through tiny (diffusive) leaks result in untypical retention times and hence a fluctuating baseline. However, by repeating the background and sample measurements several times the random contributions cancel out. By integrating the region of interest – as determined from calibration measurements as shown in FIG. 3.15 – we find $a_{\mathrm{Kr}}^{bg} = (4.1 \pm 1.1)\,\mathrm{ppb}$. This translates (see also section 3.2.3) to a detection limit of

$$\mathrm{DL}_{\mathrm{COMGC}} = 2.8\,\mathrm{ppb} \tag{3.16}$$

at 90 % confidence level. The achieved detection limit for krypton in xenon is extraordinary recalling the simplicity of the employed PDD detector and convenience of the fully automated device. Comparing it to the sensitivity of the PCGC+RGMS technique of 6 ppq (see 3.13), i.e. a detection limit lower by more than 5 orders of magnitude, however approves the impressive achievements made with the mass spectroscopic setup.

3.4 Krypton assay

In this section we want to present the results obtained with the previously introduced devices that were developed to measure the krypton impurity level in a given xenon

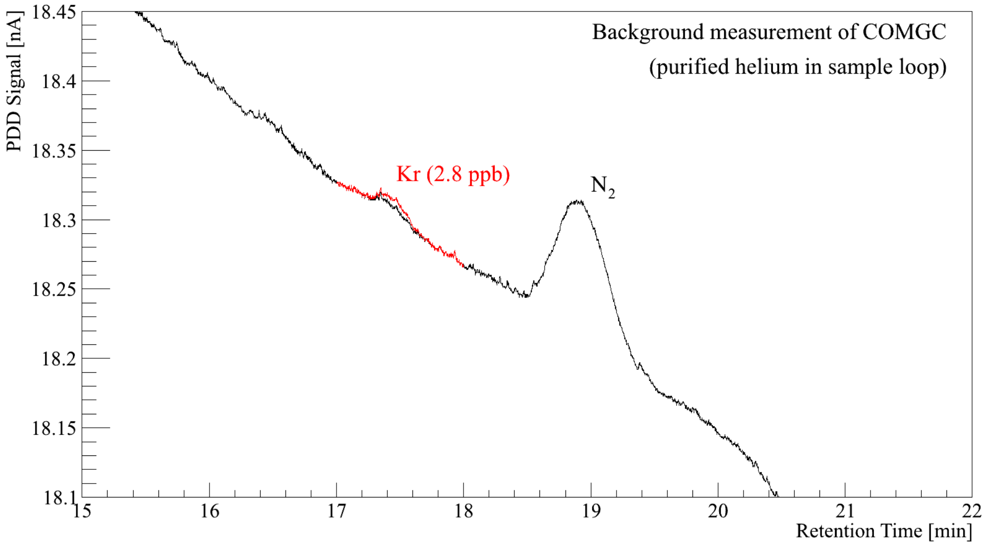

Figure 3.16: Region of interest for the krypton and nitrogen peaks of a background measurement of the COMGC. The sample loop was flushed with purified He and switched according to the procedure of FIG. 3.13. In red a signal of 2.8 ppb krypton is artificially added to the fluctuating baseline of this background measurement to show the effect we would observe at our detection limit.

sample. Prior to that, we will present the methods of drawing samples and transferring them into one of these highly sensitive devices RGMS and COMGC.

3.4.1 Drawing xenon samples

In terms of sampling, two different tasks have to be accomplished: First, the assay of xenon in systems not free to move and, second, the assay of xenon in movable storage containers, e.g. xenon gas cylinders. While the latter type of samples can be shipped to the laboratory and mounted directly at the device, the sampling of the former requires the use of an intermediate transport vessel.

Sampling from gas cylinders The PCGC facilitates two ports where bottles can be connected to either directly or via a pressure regulator (see FIG. 3.6). The former has the advantage of having less volumes potentially contaminated, but has the drawback to reduce the pressure from xenon gas cylinders filled with pressures up to 65 bar. This was achieved by installing two high pressure valves (see FIG. 3.8) enclosing a small volume compared to the volume of the tubing from there on to the port of the PCGC. The volumes enclosed by the two high pressure valves is then filled with a xenon sample

Figure 3.17: Employed vessels (xenon sampling device) for xenon samples. The four (fully metal sealed) valves enclose three volumes of $\sim 10\,\mathrm{cm}^3$ size. The port to the left is used to connect the xenon sampling device to the PCGC, while the two flanges to the left are used to connect the xenon sampling device to the vessel that contains the xenon and to install a vacuum system during preparation.

at the pressure of the gas cylinder and, afterwards, only this small amount of gas is expanded to the PCGC resulting in a strongly reduced pressure.

Sampling with the xenon sampling device Initially developed for a similar purpose in the framework of the Borexino experiment but with focus on gaseous nitrogen samples [103], four half inch fully metal sealed valves were welded together in series enclosing three volumes of $\sim 10\,\mathrm{cm}^3$ size to be filled with pressures up to 70 bar. An example of such a xenon sampling device is shown in FIG. 3.17. The central volume is shielded by the two adjacent volumes from ambient air that might penetrate the sample through tiny leaks.

The initial preparation of the xenon sampling device consists of baking ($\sim 100\,^\circ\mathrm{C}$) and evacuating the three volumes, that will hold the samples, to a pressure below 10^{-7} mbar for several days. Then the sample volumes are sealed, left under vacuum for several days and finally checked for remaining krypton background using the mass spectrometer. Only if the latter is sufficiently low the device qualifies for taking xenon samples.

The preparation on site consists of mounting the xenon sampling device to a port of the setup that contains the xenon and setting up a vacuum system. Next, the parts that have been in contact with air, that is between the setup's port and the first valve of the xenon sampling device, are baked and evacuated to a pressure below 10^{-7} mbar. To remove possible impurities from the surfaces and to avoid effects of different impurity compositions in the xenon gas that might be present close to the port, a small amount of xenon is flushed from the setup to the vacuum system. Then the valve to the vacuum system is closed and the samples are drawn by expanding the xenon into the prepared volumes of the xenon sampling device.

Table 3.2: RGMS krypton assay summary for samples involving xenon sampling device. These samples were drawn in the context of the Xenon100 experiment. In FIG. 1.7 they are placed into the timeline of important events characterizing the status of the Xenon100 experiment.

Sample	Date	Kr/Xe [ppt]
SR8	02 Jun 2010	340 ± 60
SR10	16 Dec 2011	14.0 ± 2.0
SR12	14 Dec 2012	0.95 ± 0.16
KC	21 Sep 2012	0.97 ± 0.19
RDF	29 Oct 2012	1.8 ± 0.4
B2B	04 Nov 2012	7.0 ± 1.7

3.4.2 Krypton assay results

Tables 3.2 and 3.3 give summaries of the krypton assay results of the different samples that have been measured during this work. For readability the different samples are labelled with a short identifier (see also section 1.2.2 and FIG. 1.7). Table 3.4 lists the results of the individual measurements together with the amount of processed xenon gas and the date of measurement. In the following section we want to focus on four different entities useful to draw conclusions on the performance of the analysis devices described in this chapter. Two of them (IB and AL) are xenon gas cylinders with krypton concentrations at the low ppb and high ppt level, i.e. sufficient to be measured with more common devices for cross checks. The third (RDF) and forth (KC) samples were drawn in the context of the Xenon100 experiment (see FIG. 1.7). The low krypton level of the RDF sample enabled for the first time the direct verification with a macroscopic xenon sample of the krypton acceptance (ϵ_a) of the developed procedure by measuring this sample without and with admixing krypton from the standard pipette. The KC sample is one of the purest xenon samples so far measured with the PCGC+RGMS technique and gives an idea of its potential.

Assay results characterizing krypton trace analysis tools

IB This sample was drawn from a carbon steel gas cylinder containing high purity xenon depleted in the isotope ^{136}Xe from the gas supplier Iceblick (IB). Combining the four measurements and adding the systematic uncertainty as described in 3.2.3, we find a krypton level of (7.3 ± 1.3) ppb. This level in the low ppb regime made possible a

Table 3.3: RGMS krypton assay summary for samples directly drawn from gas cylinders, (†) measured with the COMGC, (‡) measured by our colleges from Münster [83].

Sample	Date	Kr/Xe [ppb]
IB	22 Jun 2011	7.3 ± 1.3
	04 Oct 2011	$6.3 \pm 1.3^{\dagger}$
AL1	08 Dec 2011	2.8 ± 0.5
AL2	11 Apr 2012	0.29 ± 0.05
	20 Dec 2012	$0.33 \pm 0.20^{\ddagger}$
SG	01 Jun 2012	14 ± 3

completely independent measurement using the COMGC as described in 3.3. This measurement yielded a krypton concentration of (6.3 ± 1.3) ppb in very good agreement with the RGMS value.

AL2 This sample was drawn from a carbon steel gas cylinder containing ultra-pure xenon from the supplier Air Liquide (AL2). The xenon was purchased by a collaborating group from the University of Münster and measured also by their device combining a cold-trap with a quadrupole mass-spectrometer. The three measurements done with the RGMS are combined for a final value of (0.29 ± 0.05) ppb. This is again in good agreement with the completely independent analysis from our Münster colleagues who found a krypton concentration of (0.33 ± 0.20) ppb in this very same gas sample [83].

RDF Sample drawn from the XENON100 gas system during a maintenance period after the 225 live days science run (see FIG. 1.7). The maintenance became inevitable after a rupture disk failed (RDF) subsequent to an electrical power outage. Taking into account the systematic uncertainty, we end up with a value of (1.8 ± 0.4) ppt for the one measurement done on this sample.

KC This sample was directly drawn from the output of the XENON100 cryogenic distillation column (KC: krypton column; see also section 1.2.2) optimized to remove krypton from xenon gas. Again, for the transport of the sample the xenon sampling device was used. Combining the two measurements done, we find a value of (0.97 ± 0.19) ppt for this sample. While the first xenon batch had a size of about $0.7\,\mathrm{cm}^3$ giving a signal well above the detection limit, the second xenon batch was by a factor four smaller.

Still the central value is in very good agreement with the first measurement proving the linearity of the spectrometer for such small signals. Comparing the size of this second xenon batch with the second one from SR12 (Table 3.4) we see that the amount of xenon can be increased by a factor of ten giving sensitivity to krypton concentrations below 100 ppq as suggested by the detection limit (see equation 3.13).

Conclusions By comparing our assay results of two xenon gas samples at the low ppb and high ppt level with results obtained by two independent devices, we confirmed the thorough understanding of the absolute calibration and linearity of the instrument. We presented the assay results of a xenon sample with a krypton concentration below 1 ppt and showed, by comparing to the successful measurement of a 10 times larger xenon batch, the potential of the system to quantify krypton concentrations below 100 ppq.

Assay results from XENON100 science run samples

In the following we will present measurements of three samples taken from the XENON100 detector during the 100 live days science run (SR8: science run 8), during the 225 live days science run (SR10: science run 10) and ongoing (to the time of writing) science run 12 (SR12). All three presented results were drawn at one of the available ports at the XENON100 gas purification-recirculation system. See section 1.2.2 for details on the XENON100 gas system.

SR8 This sample was drawn from the XENON100 gas system into the xenon sampling device No. 4 on June 20, 2010 during science data taking that resulted in the 100 live days publication [28]. At that time the RGMS was not ready for any measurement and the sample was stored in the lab in Heidelberg. Only on October 6, 2011, more than a year later, the measurements started. In total there are four measurements with a final result of (340 ± 60) ppt. In [28] a krypton/xenon level of (700 ± 100) ppt is given based on a spectral fit to ^{85}Kr. This result was obtained assuming a $^{85}\mathrm{Kr}/^{\mathrm{nat}}\mathrm{Kr}$ ratio of 1×10^{-11}. Using the better motivated number of 2×10^{-11} (see section 3.1.2 or [27, 78]), the modified value of (350 ± 50) ppt agrees with the result obtained in this work.

SR10 On December 16, 2011, during science data taking for the 225 live days publication [27] another sample was drawn from the XENON100 gas system into the xenon sampling device No. 3. In total four measurements were performed resulting in (14 ± 2) ppt. Note the different value of (19 ± 4) ppt reported in [27], that was evaluated in advance of the precise calibration of our system reported in this work. The correct number of

Table 3.4: Details on the individual measurements presented in this work. The column Kr/Xe lists the krypton concentration specifying statistical and systematic uncertainties. The final numbers combining multiple measurements (if available) are found in TAB. 3.2 and 3.3.

Name	Date	$^{\mathrm{nat}}\mathrm{Xe}$ [$10^{-3}\,\mathrm{cm}^3$]	Kr/Xe [ppt]
IB	22 Jun 2011	452 ± 13	$(7.83 \pm 0.24^{\mathrm{stat}} \pm 1.33^{\mathrm{sys}}) \times 10^3$
	27 Jun 2011	96 ± 4	$(7.37 \pm 0.27^{\mathrm{stat}} \pm 1.25^{\mathrm{sys}}) \times 10^3$
	19 Jun 2011	1710 ± 50	$(6.59 \pm 0.20^{\mathrm{stat}} \pm 1.12^{\mathrm{sys}}) \times 10^3$
	22 Sep 2011	158 ± 5	$(7.72 \pm 0.25^{\mathrm{stat}} \pm 1.31^{\mathrm{sys}}) \times 10^3$
AL1	08 Dec 2011	890 ± 30	$(2.97 \pm 0.09^{\mathrm{stat}} \pm 0.50^{\mathrm{sys}}) \times 10^3$
	12 Dec 2011	82 ± 3	$(2.54 \pm 0.10^{\mathrm{stat}} \pm 0.43^{\mathrm{sys}}) \times 10^3$
AL2	11 Apr 2012	1240 ± 40	$294 \pm 9^{\mathrm{stat}} \pm 50^{\mathrm{sys}}$
	13 Apr 2012	1810 ± 50	$310 \pm 9^{\mathrm{stat}} \pm 53^{\mathrm{sys}}$
	03 May 2012	108 ± 4	$277 \pm 10^{\mathrm{stat}} \pm 47^{\mathrm{sys}}$
SG	01 Jun 2012	3390 ± 100	$(13.9 \pm 0.5^{\mathrm{stat}} \pm 2.4^{\mathrm{sys}}) \times 10^3$
B2B	06 Dec 2012	340 ± 10	$8.2 \pm 0.3^{\mathrm{stat}} \pm 1.4^{\mathrm{sys}}$
	17 Dec 2012	414 ± 12	$5.8 \pm 0.2^{\mathrm{stat}} \pm 1.0^{\mathrm{sys}}$
SR8	06 Oct 2011	603 ± 17	$353 \pm 11^{\mathrm{stat}} \pm 60^{\mathrm{sys}}$
	10 Oct 2011	669 ± 19	$369 \pm 11^{\mathrm{stat}} \pm 63^{\mathrm{sys}}$
	12 Oct 2011	599 ± 17	$279 \pm 8^{\mathrm{stat}} \pm 47^{\mathrm{sys}}$
	20 Oct 2011	586 ± 17	$359 \pm 10^{\mathrm{stat}} \pm 61^{\mathrm{sys}}$
SR10	16 Dec 2011	830 ± 20	$14.5 \pm 0.5^{\mathrm{stat}} \pm 2.5^{\mathrm{sys}}$
	19 Dec 2011	191 ± 6	$13.1 \pm 1.4^{\mathrm{stat}} \pm 2.2^{\mathrm{sys}}$
	21 Dec 2011	692 ± 20	$13.5 \pm 0.6^{\mathrm{stat}} \pm 2.3^{\mathrm{sys}}$
	18 Jan 2012	615 ± 18	$13.9 \pm 0.6^{\mathrm{stat}} \pm 2.4^{\mathrm{sys}}$
RDF	28 Nov 2012	398 ± 12	$1.80 \pm 0.14^{\mathrm{stat}} \pm 0.31^{\mathrm{sys}}$
KC	16 Nov 2012	700 ± 20	$0.97 \pm 0.09^{\mathrm{stat}} \pm 0.16^{\mathrm{sys}}$
	19 Nov 2012	170 ± 5	$1.0 \pm 0.4^{\mathrm{stat}} \pm 0.2^{\mathrm{sys}}$
SR12	21 Jan 2012	262 ± 8	$0.71 \pm 0.18^{\mathrm{stat}} \pm 0.12^{\mathrm{sys}}$
	14 Aug 2013	1950 ± 60	$0.96 \pm 0.03^{\mathrm{stat}} \pm 0.16^{\mathrm{sys}}$

(14 ± 2) ppt is in agreement with the value of (18 ± 8) ppt obtained from counting the number of delayed $\beta - \gamma$ coincidences associated with the ^{85}Kr beta decay [27]. Here the ^{85}Kr/$^{\mathrm{nat}}$Kr ratio of 2×10^{-11} is used.

SR12 On December 14, 2012, and January 9, 2013, two further samples were drawn from the XENON100 detector. A single measurement of the first sample resulted in (0.71 ± 0.24) ppt. At the significantly improved background conditions of our system the second sample was measured to contain (0.96 ± 0.22) ppt. Combining both results we find a krypton concentration in the XENON100 detector of (0.95 ± 0.16) ppt. To our knowledge, this is the lowest krypton/xenon concentration so far measured and the purest xenon target ever present in a LXe particle detector.

Conclusions The krypton/xenon assay results of the samples SR8 and SR10 serve as further proof of principle of the RGMS instrument by comparing them with the in-situ measurements of XENON100 that well match within errors. Historically seen however, there was a discrepancy between RGMS and in-situ measurements. The RGMS results presented in this work resulted in an update of the ^{85}Kr/$^{\mathrm{nat}}$Kr so far employed by the XENON collaboration. In time the xenon target was further purified by cryogenic fractional distillation and the spectral fit analysis turned out to be insensitive to the significantly lowered krypton level during the 225 live days science data. Discrepancies between RGMS and delayed coincidence method arose that triggered further data analysis. The so-far neglected background source ^{220}Rn was incorporated in the data analysis that solved the tension between both methods.

Assay results from XENON100 and XENON1T related samples

In this work we want to present three further samples that were studied in the context of XENON100 and in view of the next phase detector XENON1T. AL1 is a sample drawn from a gas cylinder as purchased from the supplier Air Liquide to verify the low krypton concentration specified. At a later stage the xenon gas from this gas cylinder was processed by the XENON100 distillation column in a single pass and a sample was drawn at the output of the distillation column (B2B: bottle-to-bottle distillation). By comparing the two measured levels the purification yield of the XENON100 distillation column could be quantified for the first time. Finally, SG is a sample drawn from a gas cylinder that was used at the XENON100 experiment to store distilled xenon not feed to the detector but that was believed to be pure in krypton. The RGMS assay of this sample proved this assumption wrong and spoiling the high purity of SR12 by admixing this xenon was avoided in turn.

AL1 On December 8, 2011, the high purity xenon gas cylinder (B50 Carbon steel, 50 l, ID 8673497) purchased by the gas supplier Air Liquide was mounted to the chromatographic system of the RGMS. In total two measurements were done that combine to the final krypton concentration of (2.8 ± 0.5) ppb. This value fulfills the specifications of Air Liquide stating the krypton concentration to be < 10 ppb.

B2B On November 4, 2012, a sample was drawn from the output of the XENON100 distillation column into the xenon sampling device No. 5. Fed into the distillation column was xenon from the above mentioned gas cylinder ID 8673497 (AL1) with an initial krypton concentration of (2.8 ± 0.5) ppb. Two measurements were done on the distilled xenon (single pass) that resulted in a krypton concentration of (7.0 ± 1.7) ppt. The purification yield (y_p) of the distillation column thus computes to $y_p = (390 \pm 120)$. In [44] the XMASS collaboration describes a cryogenic distillation column similar (but not the same) to the one used by the XENON100 collaboration. Therein the authors find the krypton reduction to be $y_p \sim 1000$. Such a strong reduction was albeit not observed with the XENON100 distillation column.

SG On June 1, 2012, a single measurement of xenon stored in a gas cylinder from Spectral Gas (SG) was done. This gas cylinder was employed to store xenon processed by the cryogenic distillation column but not filled to the XENON100 detector. The xenon gas it contained was supposed to be very pure in krypton. However, the measurement resulted in (14 ± 3) ppb – well above any expectation. Gas from this cylinder was foreseen to compensate the losses occurred after the rupture disk failure (see timeline of events in FIG. 1.7). Due to the outcome of the measurement it was avoided to spoil the still high purity of the xenon target present in the XENON100 detector (see sample RDF drawn after the failure).

3.5 Summary and outlook

We have presented our new approach of assaying krypton concentrations in xenon below the 1 ppt level using a gas chromatographic krypton/xenon separation followed by a mass spectroscopic krypton measurement. We explained the data analysis and absolute calibration of our device and discussed in detail its uncertainties. By comparing our assay results of two xenon gas samples at the low ppb and high ppt level with the results obtained by two independent devices, we confirmed the thorough understanding of the absolute calibration and linearity of the instrument. We presented the assay results of a xenon sample with a krypton concentration below 1 ppt and showed, by comparing to the successful measurement of a 10 times larger xenon batch, the potential of the system to quantify krypton concentrations below 100 ppq.

Recently the electronics of the spectrometer ion optics has been refurbished and a tiny leak was removed in the sample preparation part of the spectrometer. Consequently, the procedure blank and its stability were significantly improved resulting in a detection limit of 6 ppq at 90 % confidence level. At these conditions a single sample was measured that is in excellent agreement with the results obtained at the higher background.

We showed our system to be very useful both for the ongoing XENON100 experiment as well as for the upcoming XENON1T detector. Employing our off-line analysis technique, it was possible for the first time to quantify the purification yield of the XENON100 distillation column. A reduction by a factor of (390 ± 120) was found starting from a level of roughly 3 ppb. The achieved krypton purity renders the intrinsic background source ^{85}Kr insignificant for XENON100. Still, the krypton concentration in XENON1T has to be lowered by about a factor 10 to reach its scientific goal. Projecting the so-far accomplished, though, we are confident that the improved cryogenic distillation column currently under construction will succeed in doing so.

Hence, we suppose the role of the intrinsic background ^{85}Kr to be minor in XENON1T. The reduced threat posed by ^{85}Kr, however, is accompanied by an increasing importance of the second intrinsic background source, ^{222}Rn. The background induced by this source will be investigated in the next chapter where we outline possible ways to circumvent the peril it poses.

Chapter 4

Radon in XENON

The inert gas radon is a serious source of internal background in the XENON100 detector [27, 47] and is likely to become the dominant one in the next phase detector XENON1T. The four radioactive radon isotopes in traces abundant in nature ^{218}Rn, ^{219}Rn, ^{220}Rn and ^{222}Rn are produced in the primordial decay chains of the long lived isotopes ^{235}U (actinium series), ^{232}Th (thorium series) and ^{238}U (radium series). Traces thereof are present in almost every material – so they are in the construction material used for the XENON detectors. Due to the chemically inertness of radon and resulting (comparably) high diffusion length in many materials, the continually produced isotopes are able to leave the point of their creation. This process is called radon emanation. Eventually they enter the liquid xenon directly or the gaseous xenon purification-recirculation stream (see section 1.2.2), and are transported into the fiducial volume of the XENON detectors by means of convection and diffusion.

Due to the short half-life of less than a minute[1], ^{220}Rn was shown not to penetrate the fiducial volume of XENON100 but being closely confined to the PTFE which encloses the TPC [47]. As ^{219}Rn and ^{218}Rn have even shorter half-lifes on the timescale of seconds and below, they are believed to behave similar and do not contribute to the intrinsic background inside a fiducial volume at some distance to the surrounding materials.

In the XENON100 detector, however, ^{222}Rn has been shown to penetrate any fiducial volume [47]. Of special importance are the beta decaying ^{222}Rn daughters ^{214}Pb and ^{214}Bi that create low energetic events with a topology mistakable for a WIMP interaction [49] (see also the corresponding krypton section 3.1). ^{222}Rn is produced in the radium series that ends on the stable lead isotope ^{206}Pb. The 22 years half-life of ^{210}Pb, however, usually breaks the secular equilibrium and subsequent decays are suppressed [38] or even enhanced [105].

---

[1] If not marked different, the quoted nuclear data is collected from the recommended database provided by the Laboratoire National Henri Becquerel [104].

Detailed Monte Carlo (MC) studies assuming a homogeneous distribution of radon and its successors until ^{210}Pb in the LXe target of XENON100 have been carried out. They result in a linear relation between the activity concentration of ^{222}Rn and the resulting background index stating $1\,\mathrm{mDRU} = 35\,\mu\mathrm{Bq/kg}$ [38] (see also equation 1.9). The maximum number of events in the region of interest caused by ^{222}Rn and subsequent disintegrations can be predicted assuming this MC study to be meaningful also in the context of the XENON1T detector. This assumption is reasonable as the dominant part of the radon background in the energy region of interest for WIMPs is produced by the low energetic part of the beta spectrum of ^{214}Pb and ^{214}Bi [49] that is not influenced much by detector specific parameters like light yield. Requiring at maximum 0.1 events per year in a 1 ton fiducial volume in the WIMP region of interest ($10\,\mathrm{keV_{ee}}$ width assumed) and assuming XENON1T's rejection power for electronic recoils to be similar to XENON100 ($\sim 99.5\,\%$) we end up with a radon background of $< 5.5 \times 10^{-3}\,\mathrm{mDRU}$. This translates to $< 0.19\,\mu\mathrm{Bq/kg}$ or $< 0.58\,\mathrm{mBq}$ total radon emanation of the XENON1T detector homogeneously distributed in the LXe – a reduction by a factor 300 per kilogram or 20 in total emanation rate in comparison to the radon level in XENON100.

4.1 ^{222}Rn assay of the XENON100 detector

A dedicated measurement campaign was initiated after the science data taking period of the 225 live days publication [27] (see FIG. 1.7 for a detailed time-line of XENON100) in order to investigate the radon level observed in the XENON100 data. To conduct these measurements the detector was emptied, its xenon stored in gas cylinders and ^{222}Rn emanation measurements performed. The principle of these emanation measurements is in a more general context discussed in section 4.5. Basically the detector is sealed while ^{222}Rn atoms emanate that are afterwards extracted and detected by their disintegrations. While the detector is sealed, the constant emanation source term will increase the ^{222}Rn level until decay and source terms compensate (saturation activity). All emanation activities given in this work are extrapolated to this equilibrium limit. The extractions of the radon atoms were done after sealing the detector for less than one week and the radon atoms filled to miniaturized proportional counters [54]. These devices are sensitive to the alpha particles produced in the ^{222}Rn decay used to determine the emanation activity.

The volumes, during normal operation in contact with xenon, were separated in two parts (gas purification system and cryostat; see FIG. 1.5) in order to be sensitive to their individual contribution to the overall emanation. During the first three science runs [27, 28, 45] the xenon flow in the purification system was maintained by a diaphragm pump (KNF[2]). In view of XENON1T, where three metal sealed piston type pumps (QDrive[3]) are supposed to replace the KNF diaphragm pump, a QDrive was temporarily connected to the XENON100 gas purification system replacing the KNF. In both configurations, KNF and QDrive, the gas system's ^{222}Rn emanation was measured.

4.1.1 ^{222}Rn assay of the XENON100 cryostat

For the emanation measurements the cryostat was filled with boil-off nitrogen (~ 1.5 bar) purified by activated carbon (AC) traps that were cooled by immersing them in liquid argon (LAr). Both procedures, the preparation of ^{222}Rn free and the extractions of ^{222}Rn enriched nitrogen, were done with the Mobile Radon Extraction (MoREx) unit [106]. As PMTs would be damaged if helium is used, nitrogen was chosen as carrier gas. Helium diffuses into the PMTs, worsens the vacuum and increases the rate of so-called after-pulses that are due to helium ions formed inside the PMTs. The rate of such events has to be minimized for the WIMP Dark Matter search where a low energy threshold is essential and only achieved by a loose coincidence condition between several PMTs.

After recuperating the LXe target to the storage gas cylinders the residual xenon gas present in the detector was pumped only at room temperature as the PMTs are not specified for temperatures above 50 °C. As a consequence, the xenon outgassing of the cryostat throughout all emanation measurements was significant. The initial outgassing was estimated to be on the order of 10^{-3} mbar l/s and several liters of xenon were found mixed with the emanated radon atoms in the nitrogen gas of the first extraction. The similar physical properties of xenon and radon presented difficulties in separating the emanated radon atoms from the residual xenon. However, this was necessary in order to fill the ^{222}Rn atoms to the proportional counters with a physical volume of only about 1 cm^3. The separation was performed via gas chromatography in the underground counter filling lab at LNGS using the counter filling line (see sketch of FIG. 4.17). Due to the finite size of the packed column (Chromosorb 102 by Johns Manville) available for chromatography, the maximal amount of xenon to be separated is limited to roughly 50 cm^3. Hence, the cryostat was pumped and several times flushed with boil-off nitrogen for about four weeks until the outgassing was reduced by more than a factor of ten. Further, the time the cryostat was sealed and radon atoms were emanating was limited

---

[2] Stainless steel housed double diaphragm pump type N143SN.12E from KNF Neuberger (http://www.knf.com/).

[3] Customized version of a Pressure Wave Generator model 2S132W from the company QDrive part of Chart Industries (http://www.qdrive.com/).

Table 4.1: ^{222}Rn emanation measurements of the individual components of XENON100.

XENON100 sample	Date of filling sample to proportional counter	Activity [mBq]
cryostat	04 August 2012	10.8 ± 0.8
	06 August 2012	8.5 ± 0.7
	09 August 2012	10.9 ± 1.0
	24 August 2012	7.1 ± 0.9
gas-system + KNF	11 June 2012	3.0 ± 0.3
	26 June 2012	2.1 ± 0.3
gas-system + QDrive	25 August 2012	5.8 ± 0.6
	27 August 2012	6.1 ± 0.6
	29 August 2012	5.8 ± 0.8

to less than 48 hours. Finally, only a well defined fraction (20 % to 50 %) was filled to the proportional counters using the outgassed xenon itself as counting gas adding 10 % CH_4 quenching gas. These additional steps compared to the procedure described in section 4.5 increase the systematic uncertainty on the individual measurements resulting in a bigger overall error. In total four measurements were done. Averaging them (weighted mean), we end up with the final result of (9.3 ± 1.0) mBq. The individual results are listed in TAB. 4.1.

4.1.2 ^{222}Rn assay of the XENON100 gas system

In contrast to the XENON100 cryostat, the radon emanation measurements of the gas system did not require any special operations compared to standard emanation measurements. The xenon from the gas system was recuperated to the storage gas cylinder together with the xenon from the cryostat, flushed and finally filled with about 1.5 bar absolute ^{222}Rn free helium from grade 5.5 gas cylinders, that were additionally purified by AC traps (MoREx) immersed in LN_2. The hot getter (SAES[4] type PS4-MT15-R-1, see FIG. 1.5) was operational and, by opening all internal valves, i.e. not the ones going to air, detector, storage or pumping port, the operating pump (KNF or QDrive) maintained an internal helium flow of about 10 slpm. All preparations and radon extractions were performed using the MoREx unit. Nitrogen, used for the emanation measurements

---

[4] http://www.saesgetters.com/

of the XENON100 cryostat, could not be used as carrier gas because of the hot getter not being specified for its use.

In total two measurements were done on the gas system operating the KNF diaphragm pump and another three on the gas system operating the QDrive piston pump. Averaging the results for the individual systems we find (2.6 ± 0.5) mBq for the KNF gas system and (5.9 ± 0.4) mBq for the QDrive gas system. The results of the individual measurements can be found in TAB. 4.1.

4.1.3 Conclusions on the ^{222}Rn assay of XENON100

Analyzing XENON100 data and focussing on the 5.5 MeV line from the ^{222}Rn alpha decay, an average activity of (62.9 ± 0.8) mBq/kg was found homogeneously distributed inside a ~ 46.7 kg volume of the TPC during the 225 live days science data taking [47]. Assuming the ^{222}Rn activity to be homogeneously distributed in the full 161 kg xenon target of XENON100, we expect a total ^{222}Rn emanation of (10.13 ± 0.13) mBq. The ^{222}Rn assay of the XENON100 cryostat at room temperature plus gas system operating the KNF diaphragm pump resulted in a total emanation of (11.9 ± 1.1) mBq. This is in already good agreement with the α-particle counting technique.

Possible explanations for the slightly enhanced ^{222}Rn emanation activity found in this work, are the higher temperature during emanation and the remote production site with respect to the fiducial volume of at least part of the ^{222}Rn atoms. The diffusion driven part of the ^{222}Rn emanation has a strong temperature dependence and, thus, the overall emanation rate might be higher at room temperature compared to the cryogenic temperature conditions during data taking mode of XENON100.

^{222}Rn atoms emanated by the KNF pump, the hot getter or elsewhere in the gas system, have to be transported into the sensitive volume of the TPC to be seen in XENON100 data. This process takes time – at XENON100's recirculation speed of 5 standard liter per minute (slpm) the full xenon target is exchanged about once in 3.8 days – and we actually expect some deviations from a homogeneously distributed ^{222}Rn activity concentration due to the ^{222}Rn decay during the time of mixing. At this point we want to refer also to section 1.2.2 where we compare two methods, $^{\mathrm{nat}}$Kr and ^{222}Rn α-particle counting, that give an estimate on the amount of air that entered the detector in December 2009. The observed discrepancies when assuming a homogeneous admixture of radon, support the existence of a gradient in the ^{222}Rn distribution inside the detector – assuming an inhomogeneous distribution of ^{222}Rn sources. However, the gas is mixed within roughly one half-live of ^{222}Rn and, consequently, the gradient should not exceed a relative factor of two within the sensitive volume of the TPC.

The ^{222}Rn emanation of the hot getter, known to be a radon source due to zirconium present in the metal alloy, and the KNF diaphragm pump, supposedly the two main sources for the radon emanation of the gas system, already contribute more than 20 % to the overall ^{222}Rn emanation (cryostat at ambient temperature). Remarkably, the ^{222}Rn emanation of the QDrive driven gas system is more than doubled compared to the KNF gas system and would contribute almost 40 % of the overall ^{222}Rn emanation.

4.2 ^{222}Rn in XENON1T

> The XENON1T instrument can be realized by essentially scaling up the existing XENON100 detector by about a factor of 10 and reducing the background by a factor of 100. This was successfully achieved in going from XENON10 to XENON100. (Elena Aprile in [29])

In section 1.2.3 we have already introduced the XENON1T detector following up XENON100. XENON1T is designed to allow for a $\sim 1\,\mathrm{t}$ fiducial volume [29] employing about 3 t of xenon in total. Scaling up the volume ($V \sim d^3$, $S \sim d^2$), the surface to volume ratio scales with $S/V \sim V^{-1/3}$. Hence, a factor of 10 in volume improves the surface to volume ratio by about a factor of 2. As a consequence, the surface dominated part of the ^{222}Rn emanation is relaxed by this number in XENON1T.

The high purity demands on electronegative impurities in the LXe target, essential to reach the desired meter scale drift length of electrons in the TPC, require the recirculation flow in the gas purification loop to be on the order of 100 slpm. Guided by the experience with XENON100 and dedicated experiments in various laboratories, the current design foresees the parallel operation of three hot getters and pumps to maintain this high flow at maximal purification efficiency. At the time of writing, for long term stability and noise pollution reasons, the QDrive piston type pumps are favored to replace the XENON100 KNF diaphragm pump. The type of hot getter is supposed to be unchanged.

4.2.1 Estimations on radon background of XENON1T

We want to draw a conservative picture of XENON1T's radon emanation – improvements enabled by a careful material screening and selection (see section 4.5 and the promising results therein) will consequently improve the physical reach of XENON1T.

Linearly extrapolation from the measured ^{222}Rn emanation rate of XENON100's gas system, and recalling its increased complexity in XENON1T (three units, consisting of recirculation pump and high temperature getter, are considered to be employed; see section 1.2.3), we conservatively estimate the gas purification-recirculation system to emanate three times the rate found for the corresponding QDrive system in XENON100. That is to say, we project the gas system to emanate 18 mBq of ^{222}Rn.

Note that we have not included any knowledge on screening results of the various components. In section 4.5 we put forward promising measurements of the high temperature getter (SAES type PS4-MT50-R2) to be employed in XENON1T and present the screening progress to reduce the emanation of the QDrive. These results make us believe that 18 mBq are too conservative by at least a factor of two. Still we want to neglect this additional information for the time being and keep in mind the projection to be conservative. In the remainder of this chapter we will realize the ^{222}Rn emanation rate to be too high, regardless of a factor of two. As a direct consequence, a radon mitigation system will be introduced that, in turn, renders emanation in the gas system (almost) insignificant.

The number of PMTs including their bases, cabling, holders, vacuum feedthroughs and suchlike is approximately the same as in XENON100. These parts are supposed to dominate the ^{222}Rn emanation of the cryostat. The surfaces S of the cryostat itself and of the light reflecting TPC walls, that scale with the volume V like $S \sim V^{2/3}$ and, thus, are about a factor 5 larger than the corresponding ones in XENON100, are made from stainless steel and PTFE, respectively. Both materials have typically a low ^{222}Rn emanation rate and upscaling their amount by a factor of 5 should not change the overall emanation by much. Being conservative and neglecting the possibility of finding materials with a reduced ^{222}Rn emanation compared to the ones used in XENON100, we estimate the XENON1T cryostat to emanate 20 mBq, i.e. by a factor of two increased in comparison to XENON100.

Summing up the ^{222}Rn emanation of the XENON1T cryostat and gas purification-recirculation system, we find 38 mBq in our conservative estimation. Comparing this number to the requirement for XENON1T of < 0.58 mBq, that we have estimated in the introductory part of this section (see 4), we find ourselves off by a factor of ~ 65. This means, we will observe on average 6.5 events, indistinguishable from a WIMP interaction, per year in a 1 t fiducial volume that result from disintegrations of continually emanated ^{222}Rn and subsequent decays. Therein, we assumed the ^{222}Rn daughters ^{214}Pb and

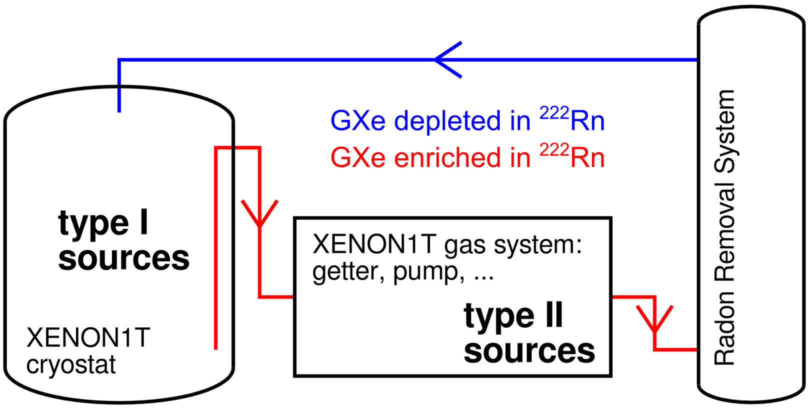

Figure 4.1: Simplified sketch of the XENON1T purification loop. Radon emanated from materials inside the cryostat (type I source) directly contributes to the electromagnetic background while radon produced outside the cryostat in the gas system (type II source) has to pass the radon removal system first.

^{214}Bi to be homogeneously distributed in the LXe target and a total ^{222}Rn emanation of 38 mBq.

4.2.2 Impact of radon removal system

In the previous section we have determined the amount of ^{222}Rn present in the XENON100 detector due to emanation and discussed the dominant role this continuously produced internal source has for the electromagnetic background of XENON1T. We find the ^{222}Rn background by a factor ~ 65 too high, if we construct XENON1T as a simple upscaled version of XENON100. In the following, we want to investigate possibilities to break the homogeneous distribution of ^{222}Rn in the xenon target to achieve a reduction of the latter in the fiducial target. We want to generally refer to concepts allowing for such a depletion as *(online) radon removal system.* In this section, the radon removal system is mathematically modelled. In section 4.3 one realization of such a system is discussed while in section 4.4 alternative approaches are introduced. Finally, in section 4.5 a dedicated material screening effort is presented to reduce the ^{222}Rn emanation in the first place.

Mathematical model of an online radon removal system in Xenon1T

Placed last in the gas purification loop (see FIG. 4.1), a radon removal system takes out the ^{222}Rn atoms from the gaseous xenon recirculation-purification flow and puts back to the detector xenon with a diminished ^{222}Rn concentration. Such a system is able to lower the number of ^{222}Rn atoms in the sensitive detector region while increasing their number inside the removal system at the same time.

To significantly minimize the ^{222}Rn background in the fiducial volume of the detector, it is important both to reduce the radon concentration in the purification loop, and to flush out the radon atoms from the fiducial volume at a reasonable speed. Both parameters, radon reduction of the removal system and recirculation speed, are strongly coupled in the computation of the overall reduction.

Assuming a homogeneous radon concentration in the liquid xenon target of XENON1T (our standard assumption), the number of ^{222}Rn atoms flushed out per unit time is given by the total number N of ^{222}Rn atoms in the detector times f, defined as the recirculation flow $\mathcal{F}$ divided by the total xenon mass M_{tot} inside the detector ($f = \mathcal{F}/M_{\text{tot}}$). Therein the recirculation flow $\mathcal{F}$ is the xenon mass flow per unit time. In the following, we are only interested in the equilibrium reached when the XENON1T detector is operated continuously and the spatial radon concentrations do not vary with time. In this case, the performance of the radon removal system can mathematically be described by the removal system's reduction factor ($\mathcal{R} = c_{\text{in}}/c_{\text{out}}$) constant in time, comparing the number of ^{222}Rn atoms entering (concentration at inlet c_{in}) and leaving (concentration at outlet c_{out}) the radon removal system[5]. We distinguish type I from type II ^{222}Rn sources (see FIG. 4.1). They are defined by the advantageous fact that type II sources have to pass the radon removal system once before entering the sensitive detector volumes. Type I sources, on the contrary, emanate to the LXe in the cryostat. Only the aforementioned fraction f of type I radon is per unit time evaporated from the cryostat and transferred to the removal system.

FIG. 4.2 illustrates the four different source terms of differential equation 4.1 for the number of ^{222}Rn atoms inside the detector. Therein $-\lambda N$ accounts for the ^{222}Rn disintegrations, $-fN$ gives the number of ^{222}Rn atoms flushed out to the recirculation-

---

[5] Time dependent features, e.g. when turning on the radon removal system, are not modelled by this approach. In the strict sense there is no causal connection between the radon concentration at the inlet of the radon removal system and at its outlet *at the same time.* Only in the limit of equilibrium both concentrations can be linked by a factor constant in time.

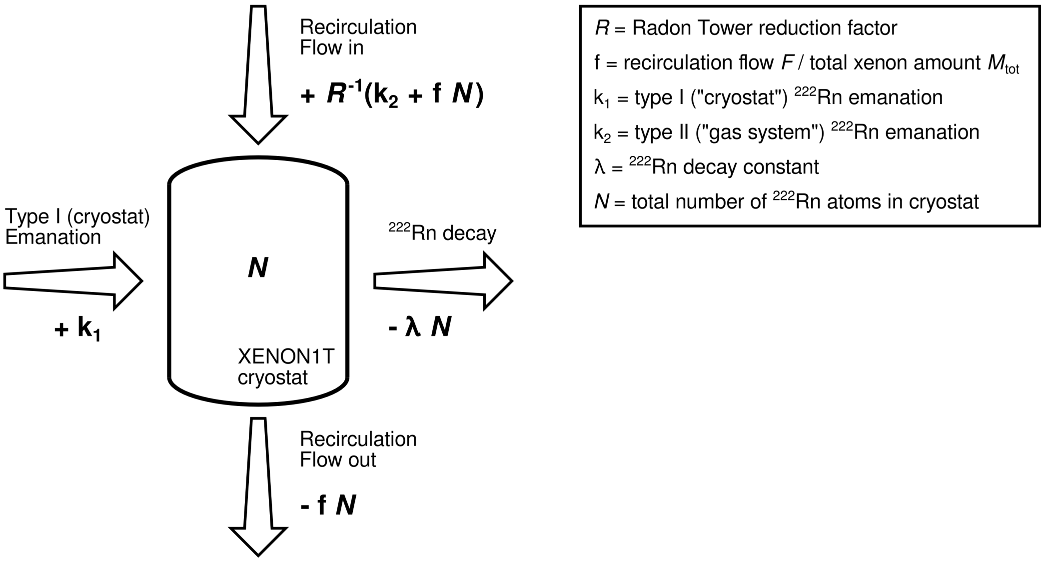

Figure 4.2: Scheme illustrating the single contributions to the differential equation (4.1) modelling the impact of a radon removal system on the ^{222}Rn budget of XENON1T.

purification system and $+k_1$ is the constant type I source term added. Finally, the amount of ^{222}Rn atoms evaporated to the gas purification-recirculation system $(+fN)$ plus the constant type II source term $+k_2$ are passed through the radon removal system, where their amount is diminished by the factor $\mathcal{R}^{-1}$, before being re-introduced to the detector. Hence, this last source term reads $+(k_2 + fN)/\mathcal{R}$ and we find:

$$\begin{aligned}\frac{\partial N}{\partial t} &= -\lambda N - fN + k_1 + (k_2 + fN)/\mathcal{R} \\ &= -\underbrace{(\lambda + f(1-\mathcal{R}^{-1}))}_{\Lambda}N + \underbrace{(k_1 + k_2/\mathcal{R})}_{K} \\ &= -\Lambda N + K\,,\end{aligned} \tag{4.1}$$

with the known solution:

$$N(t) = const \cdot e^{-\Lambda t} + \frac{K}{\Lambda}\,. \tag{4.2}$$

Therein, the constant *const* has to be matched to the initial conditions. We are only interested in the equilibrium $t \to \infty$, i.e. running continuously the radon removal system in XENON1T, and equation 4.2 simplifies to:

$$N(t \to \infty) = \frac{K}{\Lambda} = \frac{k_1 + k_2/\mathcal{R}}{\lambda + f(1 - \mathcal{R}^{-1})} \,. \tag{4.3}$$

In order to get a better understanding of the static solution 4.3 to our differential equation 4.1, we want to look at its behavior in the two limits $\mathcal{R} = 1$ and $\mathcal{R} \to \infty$ before studying the generic case:

Inoperative radon removal system In the limit $\mathcal{R} = 1$, i.e. for an inoperative radon removal system, equation 4.3 for the number of ^{222}Rn atoms in the detector simplifies to $N^{\mathcal{R}=1} = (k_1 + k_2)/\lambda$. This is the well known relation between the number of atoms and the corresponding activity ($N = A/\lambda$).

Maximum efficient radon removal system Assuming the radon removal system to remove all radon from the gaseous xenon recirculation loop, $\mathcal{R} \to \infty$ applies, and equation 4.3 reads $N^{\mathcal{R}\to\infty} = k_1/\lambda \cdot (1 + f/\lambda)^{-1}$. In this limit, type II sources are inconsequential and the final number of radon atoms in the detector inversely depends on the recirculation flow.

Realistic radon removal system In general, the radon removal system has some rejection power $\mathcal{R}$ for ^{222}Rn atoms from the finite gaseous xenon recirculation flow $\mathcal{F}$. We have already seen in the limit of $\mathcal{R} \to \infty$ that the recirculation flow $\mathcal{F}$ is the limiting factor. We define the relative ^{222}Rn removal $\mathcal{D}$ as the fraction of the ^{222}Rn activity inside the fiducial volume without and with a radon removal system. This fraction can easily be computed from equation 4.3 to be:

$$\mathcal{D} = \frac{k_1 + k_2}{k_1 + k_2/\mathcal{R}} \cdot \left(1 + \frac{f}{\lambda} \cdot (1 - \mathcal{R}^{-1})\right) \,. \tag{4.4}$$

Looking at the effect of a radon removal system on type I and type II sources individually, we can artificially set type I or type II sources to zero in equation 4.4 and find the relative reductions that are *independent* on the actual amount of type I and type II sources:

$$\mathcal{D}_{\mathrm{I}} \overset{k_2=0}{=} 1 + \frac{f}{\lambda} \cdot (1 - \mathcal{R}^{-1}) \qquad \mathcal{D}_{\mathrm{II}} \overset{k_1=0}{=} \mathcal{R} \cdot \left(1 + \frac{f}{\lambda} \cdot (1 - \mathcal{R}^{-1})\right) \,. \tag{4.5}$$

TAB. 4.2 lists the relative ^{222}Rn removals $\mathcal{D}$, $\mathcal{D}_{\mathrm{I}}$ and $\mathcal{D}_{\mathrm{II}}$ for different reduction fac-

Table 4.2: Impact of the radon removal system on XENON1T assuming the conservative forecast made in this work of 20 mBq type I and 18 mBq type II ^{222}Rn emanation. The numbers illustrate the dependence of the relative ^{222}Rn removal ($\mathcal{D}$, $\mathcal{D}_\mathrm{I}$ and $\mathcal{D}_\mathrm{II}$) on the recirculation flow $\mathcal{F}$ and the reduction factor $\mathcal{R}$ of the radon removal system.

	$\mathcal{D}$ $\mathcal{D}_\mathrm{I}$, $\mathcal{D}_\mathrm{II}$	Recirculation Flow $\mathcal{F}$ [slpm]				
		10.0	30.0	50.0	100.0	300.0
$\mathcal{R}$	2	1.41 1.08, 2.2e+00	1.61 1.23, 2.5e+00	1.82 1.39, 2.8e+00	2.32 1.77, 3.5e+00	4.34 3.31, 6.6e+00
	5	1.81 1.12, 5.6e+00	2.21 1.37, 6.8e+00	2.60 1.62, 8.1e+00	3.60 2.23, 1.1e+01	7.57 4.70, 2.3e+01
	10	1.98 1.14, 1.1e+01	2.47 1.42, 1.4e+01	2.95 1.69, 1.7e+01	4.16 2.39, 2.4e+01	9.00 5.16, 5.2e+01
	50	2.15 1.15, 5.8e+01	2.71 1.45, 7.3e+01	3.28 1.76, 8.8e+01	4.69 2.51, 1.3e+02	10.33 5.53, 2.8e+02
	100	2.17 1.15, 1.2e+02	2.75 1.46, 1.5e+02	3.32 1.76, 1.8e+02	4.76 2.53, 2.5e+02	10.50 5.58, 5.6e+02
	500	2.19 1.15, 5.8e+02	2.77 1.46, 7.3e+02	3.36 1.77, 8.8e+02	4.81 2.54, 1.3e+03	10.65 5.62, 2.8e+03
	1000	2.19 1.15, 1.2e+03	2.78 1.46, 1.5e+03	3.36 1.77, 1.8e+03	4.82 2.54, 2.5e+03	10.67 5.62, 5.6e+03
	5000	2.19 1.15, 5.8e+03	2.78 1.46, 7.3e+03	3.36 1.77, 8.9e+03	4.83 2.54, 1.3e+04	10.68 5.62, 2.8e+04
	10000	2.19 1.15, 1.2e+04	2.78 1.46, 1.5e+04	3.36 1.77, 1.8e+04	4.83 2.54, 2.5e+04	10.68 5.62, 5.6e+04

tors $\mathcal{R}$ and recirculation flows $\mathcal{F}$ in the case of the conservative forecast we made for XENON1T. Obviously, even in the unrealistic scenario of a recirculation flow of 300 slpm and a radon reduction factor of 10000, XENON1T will not reach its scientific goal if amount and distribution of the ^{222}Rn sources happen to fulfill the conservative projection we made above.

However, there is something we can learn from TAB. 4.2. At XENON1T's estimated recirculation flow of 100 slpm a reduction factor of 50 is already sufficient to reduce type II sources by more than two orders of magnitude – satisfactory to render type II sources unimportant even in our conservative forecast. Improving the reduction factor further does not change the picture much. Type II sources remain unimportant while the flow of 100 slpm is not sufficient to extract type I ^{222}Rn atoms in time from the liquid and transport them to the removal system. As a consequence, we level off at a reduction factor of 2.5 for type I sources. This factor of 2.5 for type I sources is completely independent on the ^{222}Rn emanation of both the cryostat and the gas system we estimated above.

Two important conclusions can be drawn from this: First of all, there is no need for any radon removal system to perform significantly better than $\mathcal{R} = 50$, and, second, type I sources have to be reduced to:

$$\begin{aligned} k_1 &< \mathcal{D}_{\mathrm{I}}(\mathcal{R}=50) \cdot \left(0.58\,\mathrm{mBq} - \frac{k_2}{\mathcal{D}_{\mathrm{II}}(\mathcal{R}=50)}\right) \\ &\lesssim 1.1\,\mathrm{mBq}\,. \end{aligned} \tag{4.6}$$

A total ^{222}Rn emanation rate of type I sources at the level of 1 mBq might be achieved both by a thorough ^{222}Rn screening campaign, as described in section 4.5, and by transforming type I into type II sources. One approach of realizing the latter, that already is foreseen in the design of the XENON1T cryogenic system, is to split up the recirculation gas stream into several parallelized ones that are combined again in the gas system. The main part of the gas flow still is going to be evaporated from the LXe (as done in XENON100, see FIG. 1.5) to effectively remove electronegative impurities from the liquid phase, but in addition further GXe flows will be maintained pushing out the gas blanket formed above the LXe phase and inside the tubes connecting the cryostat with the gas system and the electronics outside the water tank. This blanket is supposed to be enriched in ^{222}Rn as it houses large parts of the electronic cabling as well as feedthroughs and suchlike.

4.3 Single column adsorption

In the single column adsorption system the ^{222}Rn enriched xenon gas from XENON1T's purification loop is passed through a packed column filled with a for the radon/xenon separation task adapted adsorbent. We aim for sufficiently retaining the radon atoms in the system with respect to xenon such that the reduction is achieved by the disintegration of ^{222}Rn inside the removal system. The radon successors bismuth (Bi), polonium (Po) and lead (Pb) are chemically bound much stronger to the adsorbent than the inert gases xenon and radon and, hence, are supposed to persist in the packed column.

In [107] the XMASS collaboration published results on "*radon removal from gaseous xenon with activated carbon*" following the above outlined idea. Therein they introduced the linear relationship between the mean propagation velocity v_{Rn} of radon and v_{Xe} of xenon in the packed column trap and found for their choice of adsorbent (activated carbon Shirasagi $\mathrm{G_{2x}}$ 4/6 from JEChem) $v_{\mathrm{Rn}}/v_{\mathrm{Xe}} = (0.96 \pm 0.10) \times 10^{-3}$ at $-85\,^{\circ}\mathrm{C}$.

In section 4.3.1, we want to relate the empirical ratio $v_{\mathrm{Rn}}/v_{\mathrm{Xe}}$ to the Henry's constant H of the adsorbent, a quantity more common in literature that is introduced to describe the linear regime of single component adsorption. In section 4.3.3 we introduce an experimental setup designed to study the radon adsorption in the presence of xenon gas for different adsorbents, temperatures and xenon gas pressures. Section 4.3.4 deals with an experimental setup similar to the one described in [107] to dynamically assay radon adsorption properties in presence of a xenon gas carrier. Section 4.3.5 is devoted to the problem of the xenon consumption of such a single column radon removal system. Finally, we will conclude on the single column adsorption radon removal system in section 4.3.6 and give an estimate on the physical reach of this approach.

4.3.1 Henry's law and retention time predictions

Classically, Henry's law describes the regime where single component adsorption can be linearly approximated by

$$n_{\mathrm{ad}} = H \cdot m \cdot p\,, \tag{4.7}$$

where n_{ad} is the number of adsorbed particles, p the pressure created by the free, i.e. not adsorbed particles, m the amount of adsorbent used and, finally, Henry's constant in units $[H] = \mathrm{mol/(kg\,Pa)}$. We want to adopt equation 4.7 in a form more adequate to use in our context where the amount of ^{222}Rn atoms is not determined by their partial pressure but activity, that is their total number n. Using the ideal gas law we write:

$$n_{\text{ad}} = H \cdot m \cdot \frac{n_{\text{free}} \cdot R \cdot T}{V}\,, \tag{4.8}$$

with n_{free} the number of particles not adsorbed, V the available volume the adsorption process takes place, R the ideal gas constant and T the temperature of the system. In presence of xenon as a second and in its total amount dominating gas component, the adsorption of radon is strongly influenced by competitive adsorption of xenon. Still a similar linear relationship is found in our two component system [49] with a diminished constant that we want to call two component Henry's constant $\widetilde{H}$ (this wording will be justified in section 4.3.3).

For the following consideration we want to investigate a system composed of an adsorbent filled column that is looped (similar to XENON1T) by a gaseous xenon stream. Spiking this GXe at the inlet of the adsorbent column with some ^{222}Rn, we will observe the ^{222}Rn concentration at the output of the column to rise after the retention time t_{Rn}. FIG. 4.3 sketches this setup as well as the spatial distribution of the ^{222}Rn concentration for a set of different times.

Assuming the adsorbent in equilibrium with the gaseous xenon flow and a step-like incoming ^{222}Rn concentration, outside the adsorbent this ^{222}Rn concentration peak will move at the velocity of xenon ($v_{\text{Rn}} = v_{\text{Xe}}$) given by the xenon flow ϕ_{Xe}. For a column of length l and cross-section A ($V_{\text{col}} = A \times l$), xenon velocity and flow are related by $\phi_{\text{Xe}} = A \times v_{\text{Xe}}$. The retention time t_{Xe} of xenon, that is the time xenon needs to pass the adsorbent once, then is given by the relation:

$$\phi_{\text{Xe}} = \frac{V_{\text{col}}}{t_{\text{Xe}}}\,. \tag{4.9}$$

In analogy to equation 4.9 we define the radon flow inside the column:

$$\phi_{\text{Rn}} = \frac{V_{\text{col}}}{t_{\text{Rn}}}\,. \tag{4.10}$$

Starting to loop (dotted line in FIG 4.3), we will observe an oscillating ^{222}Rn concentration outside the column. The amplitude of this oscillation will be dumped in time due to all kind of broadening and smearing mechanisms effecting the concentration peak (mainly diffusive broadening but also channeling inside the column and non-laminar flow conditions). At some point (t_n) a static spatial distribution of the ^{222}Rn concentra-

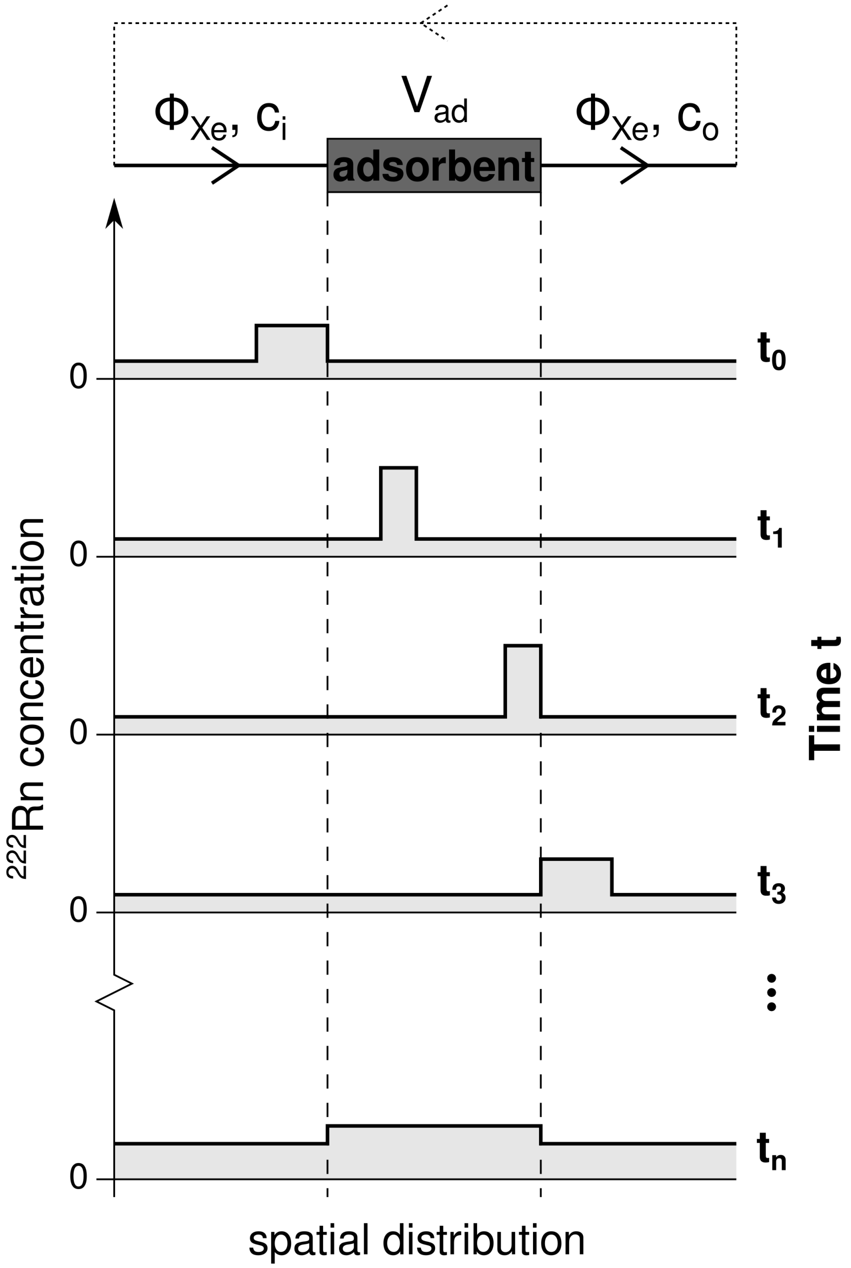

Figure 4.3: Spatial distribution of the ^{222}Rn concentration c for fixed times t_i. The sketch illustrates how a peaked ^{222}Rn concentration in a gaseous xenon stream ϕ_{Xe} moves with time through an adsorbent filled packed column. All effects broadening or smearing the peak in space or time are neglected for the times t_0 to t_3. Starting to loop (dotted line), from time t_n on these effects cause a static spatial distribution of the ^{222}Rn concentration (ignoring the exponential overall decrease due to disintegrations).

tion forms. Despite an overall exponential decrease due to the disintegration of ^{222}Rn, this distribution does not change with time and we find outside the adsorbent a ^{222}Rn activity concentration c_l. The spatial integral of the concentration (corrected for the exponential decay) is conserved (gray area in FIG 4.3). If we could "turn off" the radon adsorption (practically this can be achieved by baking the adsorbent to temperatures above $\sim 150\,°\mathrm{C}$ – however, also xenon will desorb in turn), the ^{222}Rn concentration was flat in FIG 4.3 at a level we will refer to as c_u.

In the following we want to ignore the presence of xenon insofar as we express the ^{222}Rn concentration as number of ^{222}Rn atoms per physical volume. That is to say, increasing the amount of xenon in the system does not change the radon concentration as both the system's physical volume and the number of ^{222}Rn atoms stay the same. Calling V_{out} the system's outer volume, i.e. the volume that does not belong to the adsorbent column, the total number of ^{222}Rn atoms (n_{tot}) reads:

$$n_{\text{tot}} = c_u \cdot (V_{\text{out}} + V_{\text{col}})\,. \tag{4.11}$$

We can compute the concentration decrease when "turning on" the adsorbent using the two component version of Henry's law (equation 4.8) relating the amount of free and adsorbed particles ($n_{\text{tot}} = n_{\text{free}} + n_{\text{ad}}$):

$$\begin{aligned} \frac{c_u}{c_l} &= \frac{n_{\text{tot}}/(V_{\text{out}} + V_{\text{col}})}{n_{\text{free}}/(V_{\text{out}} + V_{\text{col}})} = 1 + \frac{n_{\text{ad}}}{n_{\text{free}}} \\ &= 1 + \widetilde{H} \cdot \frac{m \cdot R \cdot T}{V_{\text{out}} + V_{\text{col}}}\,, \end{aligned} \tag{4.12}$$

or, solving for Henry's constant and introducing the total volume $V_{\text{tot}} = V_{\text{out}} + V_{\text{col}}$:

$$\widetilde{H} = \left(\frac{c_u}{c_l} - 1\right) \cdot \frac{V_{\text{tot}}}{m \cdot R \cdot T}\,. \tag{4.13}$$

We now can relate also the relative velocities $v_{\text{Xe}}/v_{\text{Rn}}$ to the system's two component Henry's constant $\widetilde{H}$ by introducing the concept of a virtual volume V_{virt}. This volume is made such that the ^{222}Rn (volume) concentration is the same outside and inside V_{virt}. Turning off the adsorption, virtual volume V_{virt} and physical volume V_{col} of the adsorbent column are identical. Turning on the adsorption, we find $V_{\text{virt}} > V_{\text{col}}$ leading to a reduced number of radon atoms outside the adsorbent column and hence a reduced concentration:

$$c_l \equiv \frac{n_{\text{tot}}}{V_{\text{out}} + V_{\text{virt}}}\,. \tag{4.14}$$

Combining equations 4.11 and 4.14 we find:

$$\frac{c_u}{c_l} = \frac{V_{\text{out}} + V_{\text{virt}}}{V_{\text{out}} + V_{\text{col}}} \,. \tag{4.15}$$

The enlarged virtual volume effects also the retention time of radon atoms in the adsorbent column. Looping radon at the speed given by the xenon flow ϕ_{Xe} with the adsorbent turned off, will result in a retention time given by equation 4.9 of $t_{\text{Rn}} = t_{\text{Xe}} = V_{\text{col}}/\phi_{\text{Xe}}$. Turning on the adsorbent, increases this time by the ratio $V_{\text{virt}}/V_{\text{col}}$ and we write:

$$\frac{t_{\text{Rn}}}{t_{\text{Xe}}} = \frac{V_{\text{virt}}}{V_{\text{col}}} \,. \tag{4.16}$$

Solving equation 4.16 for V_{virt} and inserting into equation 4.15, we find:

$$\frac{c_u}{c_l} = \frac{1}{V_{\text{tot}}} \left(V_{\text{out}} + V_{\text{col}} \cdot \frac{t_{\text{Rn}}}{t_{\text{Xe}}} \right) \,. \tag{4.17}$$

Combining equations 4.17 and 4.12, the relation between the two component Henry's constant of the adsorbent $\widetilde{H}$ and the relative retention times $t_{\text{Rn}}/t_{\text{Xe}}$ in an adsorbent filled packed column is:

$$\frac{v_{\text{Xe}}}{v_{\text{Rn}}} = \frac{t_{\text{Rn}}}{t_{\text{Xe}}} = 1 + \frac{m \cdot R \cdot T}{V_{\text{col}}} \cdot \widetilde{H} \,, \tag{4.18}$$

were we made use of the simple relation $v_{\text{Xe}} \cdot t_{\text{Xe}} = l = v_{\text{Rn}} \cdot t_{\text{Rn}}$. Using equation 4.18, substituting the xenon retention time $t_{\text{Xe}} = V_{\text{col}}/\phi_{\text{Xe}}$ and introducing the adsorbent's density $\rho_{\text{ad}} = m/V_{\text{col}}$, we write for the retention time of radon:

$$t_{\text{Rn}} = \frac{m}{\phi_{Xe}} \left(\rho_{\text{ad}}^{-1} + R \cdot T \cdot \widetilde{H} \right) \,, \tag{4.19}$$

and find for the radon removal factor $\mathcal{R}$ of our single column adsorption radon removal system:

$$\begin{aligned} \mathcal{R} &= c_{\text{in}}/c_{\text{out}} = c_{\text{in}}/(c_{\text{in}} \exp(-\lambda t_{\text{Rn}})) \\ &= \exp\left[\frac{\lambda \cdot m}{\phi_{\text{Xe}}} \cdot \left(\rho_{\text{ad}}^{-1} + R \cdot T \cdot \widetilde{H} \right) \right] \,. \end{aligned} \tag{4.20}$$

In section 4.3.4 we will present a setup measuring the oscillation period of a peaked ^{222}Rn concentration being looped in a system containing an adsorbent filled packed column. This system operates a ^{222}Rn detector and is sensitive to the time $t_{\text{Rn}}^{\text{osc}}$ of ^{222}Rn atoms passing the entire system. This is the sum of the time radon needs to pass the adsorbent t_{Rn} plus the time it takes to pass the remaining system at the speed of the gaseous xenon ϕ_{Xe}. We compute:

$$\frac{t_{\mathrm{Rn}}^{\mathrm{osc}}}{t_{\mathrm{Xe}}^{\mathrm{osc}}} \quad \equiv \quad \frac{(V_{\mathrm{out}} + V_{\mathrm{virt}})/\phi_{\mathrm{Xe}}}{(V_{\mathrm{out}} + V_{\mathrm{col}})/\phi_{\mathrm{Xe}}} \quad \overset{(4.15)}{=} \quad \frac{c_u}{c_l}\,. \tag{4.21}$$

Exploiting equation 4.13, we express Henry's constant in terms of the (experimentally accessible) time for one single pass through the system:

$$\begin{aligned} \widetilde{H} &= \left(\frac{t_{\mathrm{Rn}}^{\mathrm{osc}}}{t_{\mathrm{Xe}}^{\mathrm{osc}}} - 1\right) \cdot \frac{V_{\mathrm{tot}}}{m \cdot R \cdot T} \\ &= \frac{t_{\mathrm{Rn}}^{\mathrm{osc}} \phi_{\mathrm{Xe}} - V_{\mathrm{tot}}}{m \cdot R \cdot T}\,. \end{aligned} \tag{4.22}$$

4.3.2 Intrinsic radon emanation of single column radon removal system

One of the most critical points, inherent to all adsorbent based radon removal systems, is the ^{222}Rn emanation of the adsorbent itself. In section 4.3.3 and 4.3.4 we will see that large quantities of adsorbent material will be needed to achieve a reasonable purification efficacy of the single column removal system. However, the adsorbent material itself has intrinsic ^{226}Ra impurities and contributes to the overall ^{222}Rn emanation rate. If we assume the intrinsic ^{222}Rn emanation sources of the adsorbent to be homogeneously distributed throughout the adsorbent, i.e. their amount scales with the adsorbent's mass m and sums to a total emanation k_3, the mass element $d\mu$ emanates $\epsilon_{k3} = k_3/m$. The radon removal factor $\mathcal{R}(\mu)$ of the single column radon removal system, achieved by the ^{222}Rn decay inside the column, exponentially depends on the mass μ of adsorbent to be passed (see equation 4.20):

$$\mathcal{R}(\mu) = \exp(\lambda \cdot t_{\mathrm{Rn}}) = \exp(\ln(\mathcal{R}) \cdot \mu/m)\,, \tag{4.23}$$

where $\mathcal{R}$ is the in section 4.2.2 introduced radon removal factor for the entire ($\mu = m$) single column radon removal system. The fraction of the adsorbent's intrinsic emanation that is *not* retained in the removal system but directly adds to the type I sources inside the cryostat, we want to call type I *equivalent*. The type I equivalent contribution of a given mass element's intrinsic ^{222}Rn emanation therefore depends on its position inside the adsorbent, that is on the adsorbent mass μ still to be passed. The total type I equivalent contribution $\widetilde{k}_3$ generated by the intrinsic ^{222}Rn emanation (k_3) of the

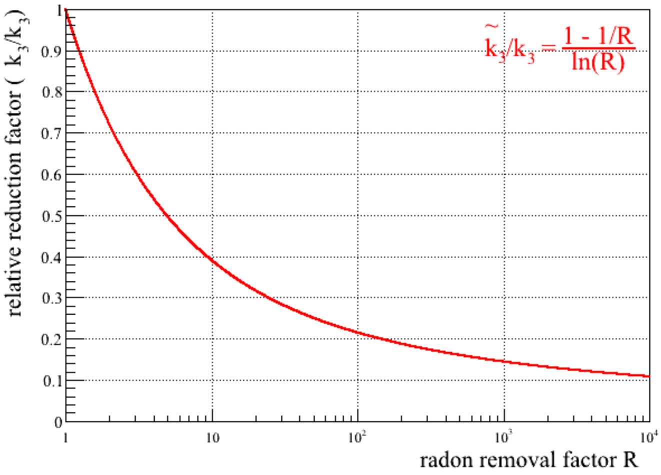

Figure 4.4: Relative effect ($\widetilde{k}_3/k_3$) of the single column adsorption radon removal system on its intrinsic ^{222}Rn emanation.

adsorbent, thus, can be written summing over all mass elements $d\mu$:

$$\begin{aligned}\widetilde{k}_3 &= \int_0^m \epsilon_{k3}/\mathcal{R}(\mu)\, d\mu \\ &= \frac{k_3}{m}\int_0^m \exp\left(-\ln(\mathcal{R})\cdot\mu/m\right)\, d\mu \\ &= \frac{1-1/\mathcal{R}}{\ln(\mathcal{R})}\cdot k_3\end{aligned} \tag{4.24}$$

The efficacy of the single column radon removal system, expressed in the radon removal factor $\mathcal{R}$, impacts the type I equivalent contribution of the adsorbent's intrinsic ^{222}Rn emanation. FIG. 4.4 shows the (relative) effect $\mathcal{R}$ has on the type I equivalent contribution. We find that, even for unrealistically high values of $\mathcal{R}$, still more than 10 % of the adsorbent's emanation rate contributes to XENON1T's type I budged.

4.3.3 Static adsorbent selection

We have to select a proper adsorbent for radon in the presence of xenon in order to maximise the radon removal factor $\mathcal{R}$ at a minimum amount of employed adsorbent mass (see equation 4.20). For our purposes, the contribution of ρ_{ad}^{-1} can safely be neglected in equation 4.20, and the logarithm of the radon removal factor is proportional to the two

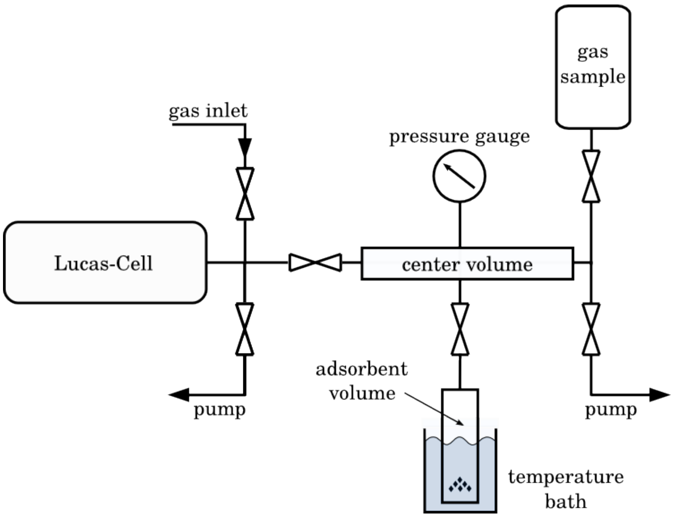

Figure 4.5: Experimental setup to quantify the radon adsorption in the presence of a second, substantially more abundant gas such as xenon. Figure courtesy of Stefan Bruenner.

component Henry's constant: $\ln(R) \propto \widetilde{H}$.

During this work an experimental setup was designed to measure the adsorption of ^{222}Rn in the presence of a second, by orders of magnitude more abundant (carrier) gas, e.g. xenon. FIG. 4.5 shows a schematic drawing of this setup. The amount of ^{222}Rn particles is quantified by means of their alpha decays *before* and *after* the adsorbent removes a distinctive fraction of the particles. A Lucas-Cell scintillation detector [108], using ZnS(Ag) as scintillation material, is used for the activity measurement, while a capacitive pressure gauge quantifies the amount of the non-adsorbed (free) carrier gas particles.

The setup was characterized and employed to determine a large variety of adsorbent's characteristics of different adsorbents such as activated carbons (AC), a metal-organic framework (MOF) and zeolites in two bachelor [109, 110] and one diploma [49] theses and a dedicated publication is in preparation. Therefore, we do not want to go into much detail about the setup itself, but want to focus on results relevant for this work.

In section 4.3.1 we introduced the linear approximated relationship (Henry's Law) between the amount of adsorbed particles and the partial pressure the free particles create above the adsorbent in presence of a second gas component. A validation of this linear approximation for different ^{222}Rn activities, i.e. different partial pressures of ^{222}Rn, is found in TAB. 4.3 for both helium and xenon as second gas components.

Table 4.3: Henry's constant for radon adsorption on activated carbon at room temperature (294 K) for different ^{222}Rn activities in the presence of the second gas components helium and xenon.

second gas component and used adsorbent	^{222}Rn activity [Bq]	$\widetilde{H}\,[10^{-4}\,\mathrm{mol/(Pa\,kg)}]$
helium on	65	27.7 ± 0.7
Blücher 100050	580	28.0 ± 0.9
	670	29.0 ± 2.0
xenon on	46	4.3 ± 0.2
Blücher 100878	242	4.4 ± 0.2
	369	4.4 ± 0.2

Three activated carbon samples, two of them produced by the German company Blücher (100050, 100878) and one from the Japanese company JEChem (SHIRASAGI G_{2x} 4/6), have been investigated in [49], two zeolites (MS5Å and MS10Å from the German company Roth) and one metal-organic framework ($Cu_3(BTC)_2$) were studied in [110]. Details on the different adsorbent samples and measurements are provided in the corresponding works. TAB. 4.4 lists the two component Henry's constants found for the different adsorbents at the investigated xenon pressure of 264 mbar and 294 K.

We find the sample Blücher 100878 to perform best with a Henry's constant of $\widetilde{H} = (4.52 \pm 0.14) \times 10^{-4}\,\mathrm{mol/(Pa\,kg)}$ in the presence of 264 mbar xenon at 294 K. This is an important result, however, we have to keep in mind that the two component Henry's constant itself is a function of both temperature and partial xenon pressure. The competitive adsorption behavior of xenon is best illustrated at the example of the adsorbent sample Blücher 100050 from TAB. 4.3 and 4.4. While the presence of helium, in good approximation being not adsorbed on activated carbon [111], does not alter the adsorption of radon, 264 mbar of xenon reduce its adsorption by more than a factor of six. If realized, the single column adsorption radon removal system is operated roughly at the operation pressure of XENON1T, that is at about 2 bar. The higher xenon pressure will reduce the capability of the adsorbent to retain radon. Any quantification of this effect by theoretical models is difficult and accompanied by significant uncertainties. However, a decrease of $\widetilde{H}$ by about one order of magnitude has to be assumed (see for example [112] for the dependence on the xenon pressure of krypton adsorption).

Table 4.4: Summary of ^{222}Rn adsorption on different adsorbents in the presence of xenon at room temperature 294 K. $\mathrm{Ad}_{\mathrm{Xe}}$ gives the amount of adsorbed xenon. Data courtesy of Stefan Bruenner [49] and Simon Stemmle [110].

adsorbents	Xe pressure [mbar]	$\mathrm{Ad}_{\mathrm{Xe}}$ [mol/kg]	$\widetilde{H}$ [10^{-4} mol/(Pa kg)]	$\widetilde{H}/\mathrm{Ad}_{\mathrm{Xe}}$ [10^{-4}/Pa]
Blücher 100050	264	2.04 ± 0.04	3.5 ± 0.2	1.72 ± 0.10
Blücher 100878	264	2.35 ± 0.04	4.4 ± 0.2	1.87 ± 0.09
JEChem G_{2x} 4/6	264	2.22 ± 0.03	3.9 ± 0.2	1.76 ± 0.09
$Cu_3(BTC)_2$ MOF	264	1.41 ± 0.08	2.03 ± 0.07	1.44 ± 0.10
Roth MS5Å	255	0.81 ± 0.04	1.32 ± 0.03	1.63 ± 0.09
Roth MS10Å	255	0.79 ± 0.03	1.31 ± 0.04	1.66 ± 0.08

As stated above, $\widetilde{H}$ is not only a function of the pressure of the competing gas but also of the adsorbent's temperature. Going from ambient to cryogenic temperatures will improve the ^{222}Rn adsorption at the expense of an increase in the amount of adsorbed xenon. In section 4.3.4 we will introduce a dynamic setup to determine radon adsorption properties following the example given in [107]. In section 4.3.5 we present data on the xenon adsorption at cryogenic temperatures for the pressure range of interest for XENON1T to get an estimate on the xenon consumption of a single column adsorption radon removal system.

4.3.4 Dynamic adsorbent selection

FIG. 4.6 shows a schematic drawing of the gas system used to determine the ^{222}Rn adsorption properties in presence of xenon gas. The setup was assembled and tested during the bachelor thesis of G. Marschmann [113] who collected data for the activated carbon Blücher 100050 already characterized by the static adsorbent setup from section 4.3.3.

A measurement with this setup follows subsequent procedure: residual ^{222}Rn is removed evacuating the entire system while baking the adsorbent at $\sim 200\,^{\circ}$C. A radon sample of ~ 1 kBq is extracted from an aqueous ^{226}Ra source using a gaseous xenon carrier, stored in a small (~ 50 ml) glass vessel and connected to the system (see FIG. 4.6). Then, the adsorbent is immersed in a coolant liquid of adjustable temperature and the system is filled with xenon gas. Once the desired xenon pressure is reached (already a sizable amount of xenon is adsorbed), the adsorbent column is closed and the xenon gas is looped by-passing the adsorbent by means of the diaphragm pump. At this point,

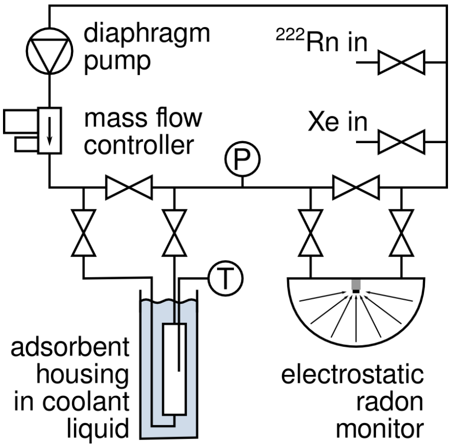

Figure 4.6: Gas system schematics of the experimental setup to quantify the radon adsorption in the presence of a second, much more abundant gas such as xenon. (P) is a capacitance pressure gauge, (T) a PT100 temperature sensor mounted inside the adsorbent housing. The volume of the adsorbent housing is about 50 ml. The ^{222}Rn activity is measured by an electrostatic ion-collection chamber of ~ 1.1 l volume focussing the electrically charged daughters of the ^{222}Rn decay chain to an alpha sensitive silicon PIN diode. This detector operates after the principle published in [114].

a high voltage of -1.8 kV is supplied to the electrostatic radon monitor and the xenon based ^{222}Rn sample is introduced. In time the ^{222}Rn atoms distribute homogeneously in the system and the activity concentration (c_u) is measured by the radon monitor. The monitor needs several hours to stabilize. Data is collected for about 10 hours. Finally, the adsorbent column is opened and the bypass closed. The recirculation pump forces the ^{222}Rn to pass the adsorbent, where it is retained compared to the xenon gas. Consequently, the activity concentration observed by the radon monitor drops. After the retention time of radon in the adsorbent column the activity in the radon monitor's volume (~ 1.1 l) ascents again. A now started periodic behavior is dumped by diffusive broadening of the radon in the adsorbent and inefficient flushing out of the radon monitor's volume. Finally a constant lower concentration level (c_l) forms, exponentially decreasing with the decay constant of ^{222}Rn. FIG. 4.7 (top) shows the ^{218}Po count rate seen by the radon monitor as an illustrative example of the above described measurement procedure.

The two component Henry's constant $\widetilde{H}$ can be evaluated by both, the observed periodic activity in the radon monitor (equation 4.22), and the different ^{222}Rn activity concentrations (c_u and c_l) observed while bypassing and when passing through the adsorbents (equation 4.13). Evaluating the latter, we have to reduce the activity con-

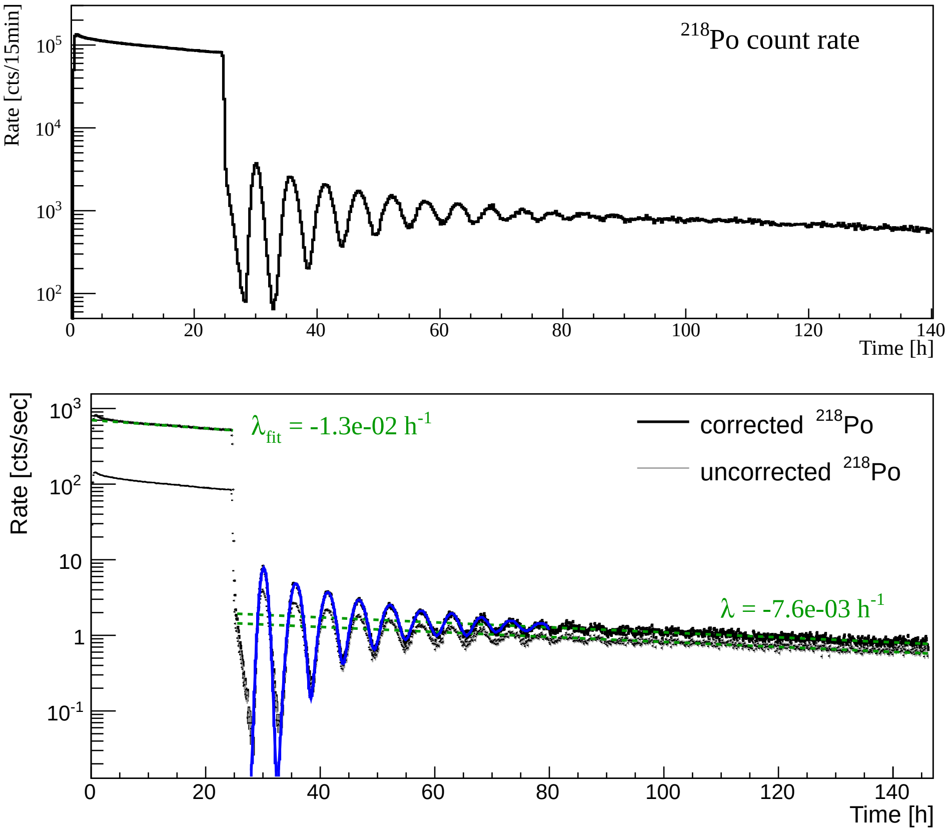

Figure 4.7: (top) Retention of ^{222}Rn atoms in (25.2 ± 0.5) g of activated carbon (Blücher 100050) at (-71.1 ± 0.5) °C. GXe at a pressure of $p_{\mathrm{Xe}} = (200.4 \pm 0.4)$ mbar is looped at $\phi_{\mathrm{Xe}} = (0.25 \pm 0.03)$ slpm. The black curve shows the ^{218}Po count rate measured by the radon monitor. A clear periodic behavior is visible for about 50 hours. (bottom) In gray the data from above measurement are redrawn. For the black curve the corrections discussed in the text are shown. In solid blue a series of Gaussian is fitted describing very well the periodic part. Fits to the upper and lower concentration levels are shown in dotted green.

centration c_u by the factor $(V_{\text{tot}} - V_{\text{col}})/V_{\text{tot}}$ to compensate for the slightly smaller total volume when the adsorbent column is bypassed. Summarizing the above, we can evaluate the two component Henry's constant by the observed periodicity ($\widetilde{H}_\omega$) and by the reduction in the activity concentration ($\widetilde{H}_{\text{c}}$):

$$\begin{aligned} \widetilde{H}_\omega &= \frac{t_{\text{Rn}}^{\text{osc}} \phi_{\text{Xe}} - V_{\text{tot}}}{m \cdot R \cdot T} \\ \widetilde{H}_{\text{c}} &= \frac{(V_{\text{tot}} - V_{\text{col}}) c_u / c_l - V_{\text{tot}}}{m \cdot R \cdot T} \end{aligned} \tag{4.25}$$

The electrostatic ion-collection chamber as ^{222}Rn detector

A reverse biased (30 V) silicon PIN photodiode[6] is used in the electrostatic chamber of (1.14 ± 0.04) l volume, similar to the one described in [114], to count α-particles produced in the decays subsequent to ^{222}Rn from ^{218}Po and ^{214}Po. The detector has a good energy resolution of about 50 keV at the energies of the two polonium α-particles of 6.00 MeV and 7.69 MeV and, thus, is well suited to distinguish between both. FIG. 4.8 shows a typical energy spectrum measured with this device obtained form aforementioned ^{222}Rn sample. ^{218}Po ions produced in the disintegration of ^{222}Rn in the xenon gas are focused by an electrical field onto the silicon PIN diode. The electrical field is created between the stainless steel walls of the detector vessel at ground and the silicon PIN diode at a high-voltage of -1.8 kV. The created ^{218}Po ions have a finite lifetime due to neutralization on electronegative impurities, like H_2O, and might get discharged before being focused to the PIN diode [114]. This, however, was not observed in the high purity xenon gas used in this work.

The peaks in FIG. 4.8 are tailing to lower energies due to partial energy depositions of the α-particles in the PIN diode. An electronic cut-off around channel 125 causes the spectrum to fall off for smaller energies. The α-particles from ^{222}Rn, which is homogeneously distributed in the xenon gas above the diode, have energies only slightly above the ones from ^{210}Po but loose part of their energy in the xenon gas. These α-particles cause the flat plateau for energies below the ^{210}Po peak.

After the disintegration of ^{218}Po the created ions have again the chance to be collected and subsequently detected through the alpha decay of ^{214}Po. In this work, we focus on ^{218}Po disintegrations being a more precise marker for ^{222}Rn due to their relatively short half-life of 3.1 min.

$t_{\text{Rn}}^{\text{osc}}$, the time radon atoms need for one turn in the loop, is determined by fitting a

---

[6] Hamamatsu large active area Si PIN photodiode model S3204-09.

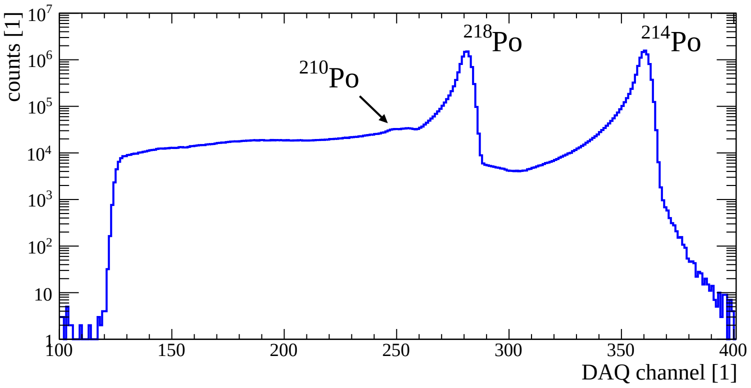

Figure 4.8: Energy resolution of PIN-detector. The two dominant alpha peaks from the ^{222}Rn decay chain of ^{218}Po and ^{214}Po as well as the longer lived ^{210}Po are visible. The flat plateau is caused by ^{222}Rn in the xenon gas. Around channel 125 an electronic cut-off causes the spectrum to steeply fall off.

series of Gaussians to the periodic behavior of observed ^{218}Po disintegrations keeping their relative position fixed to multiples of $t_{\mathrm{Rn}}^{\mathrm{osc}}$. Effects like diffusive broadening inside the adsorbent (see also section 4.3.1), cause the observed dumping and smears the shape of the peaked ^{222}Rn concentration that is looped in the system. The Gaussian approach, thus, is observed to reproduce the data quite well. This is shown by the blue curve in FIG. 4.7 (bottom). The concentration levels c_u and c_l are accessed fitting the exponential decay of ^{222}Rn ($\lambda_{\mathrm{Rn}} = 7.6 \times 10^{-3}\,\mathrm{h}^{-1}$) in the regions not affected by the periodic variations and extrapolating to the time the radon was passed through the adsorbent column (dotted green in FIG. 4.7 (bottom)). While the lower concentration is accurately fitted by fixing λ_{Rn} to its literature value, the upper level is observed to decay with an effective time constant smaller than that of ^{222}Rn ($|\lambda_{\mathrm{fit}}| > |\lambda_{\mathrm{Rn}}|$).

The radon monitor's efficiency, however, was observed to be strongly effected by alpha activities above $\sim 0.1\,\mathrm{Bq}$ (see FIG. 4.9). The ions, that are already collected on the PIN diode but are not neutralized yet, are thought to compensate the electrical field inside the electrostatic chamber (sketched in FIG. 4.10). In the following we will estimate the size of this effect assuming the electrostatic chamber to be a simple parallel-plate capacitor. The PIN diode of FIG. 4.10 has a surface of $S = (18 \times 18)\mathrm{mm}^2$. Facing upwards, the p-type layer is at $-1.8\,\mathrm{kV}$ with respect to the stainless steel housing of the electrostatic chamber at ground. The PIN diode's surface, however, was measured to be highly resistive. This is most likely caused by a $\mathrm{SiO_2}$ passivation layer. In our simple estimate the thickness of this dielectric layer can safely be neglected. The gaseous xenon

($\epsilon_r(GXe) \approx 1$, see section 2.2.1) filled gap between the silicon diode and the grounded stainless steel surface is about $d = 20\,\mathrm{cm}$ wide. We find the capacity C of our simplified setup to be:

$$C = \epsilon_0 \epsilon_r(GXe) \frac{S}{d} \approx 1.4 \times 10^{-14}\,\mathrm{C/V}\,, \tag{4.26}$$

where we used $\epsilon_0 = 8.85 \times 10^{-12}\,\mathrm{A\,s/(V\,m)}$ [89]. Hence, for our high voltage setting of $-1.8\,\mathrm{kV}$ each parallel plate holds about $2.6 \times 10^{-11}\,\mathrm{C}$ or $1.6 \times 10^{8}\,e$ elementary charges. From the average energy needed to form an electron-ion pair in gaseous xenon of roughly $W_i = 22\,\mathrm{eV}$ [115] and the α-particle's kinetic energy of 5.49 MeV we compute a total of 2.5×10^5 xenon ions produced on average in a ^{222}Rn disintegration. Hence, ~ 650 ^{222}Rn decays are sufficient to completely compensate the charges present on the PIN diode. This estimate suffers from many assumptions and unknown parameters. The thickness of the highly resistive passivation layer is small and, when getting charged by positive xenon ions, a parallel-plate capacitor with orders of magnitude higher capacitance forms due to the greatly reduced distance d.

A second effect, inherent to all data, is present we refer to as "turn on" effect. This effect manifests itself within the first $\sim 50\,\mathrm{h}$ in FIG. 4.9 (top) and, as a consequence, in the derived efficiency curve of FIG. 4.9 (bottom) for rates $> 50\,\mathrm{Bq}$. While the relative difference between the expected exponential decay of ^{222}Rn (blue curve) and observed rate (black markers) in FIG. 4.9 (top) is well described by the blue function in FIG. 4.9 (bottom) this is not the case for the first $\sim 50\,\mathrm{h}$. This "turn on" effect so far is unexplained. Electric charging of the PTFE and ceramics holder has been observed in similar setups [116]. These parts are high-impedant isolators, thus electric charging of the latter might be on the needed timescales causing stray fields responsible for the observed.

Assuming a 100 % collection and detection efficiency for late times $> 50\,\mathrm{d}$ in FIG. 4.9 (top), the blue curve in FIG. 4.9 (bottom) gives the collection efficiency as a function of the ^{222}Rn activity. Due to the 2π geometry, half of the α-particles from the ^{218}Po decay are emitted opposite to the PIN diode, the actual ^{222}Rn activity is at least a factor of two higher.

Reevaluation of dynamic adsorbent selection data from [113]

To (re)evaluate $\widetilde{H}_c$ (see equation 4.25) from the concentration levels found before (c_u) and after (c_l) passing the ^{222}Rn atoms in the GXe stream through the adsorbent, the rate dependent efficiency has to be taken into account. In principle this can be done using the blue curve in FIG. 4.9 (bottom). However, during the first $\sim 50\,\mathrm{h}$ the efficiency is dominated by the initial effect of "turning on" the high voltage and also seems to depend

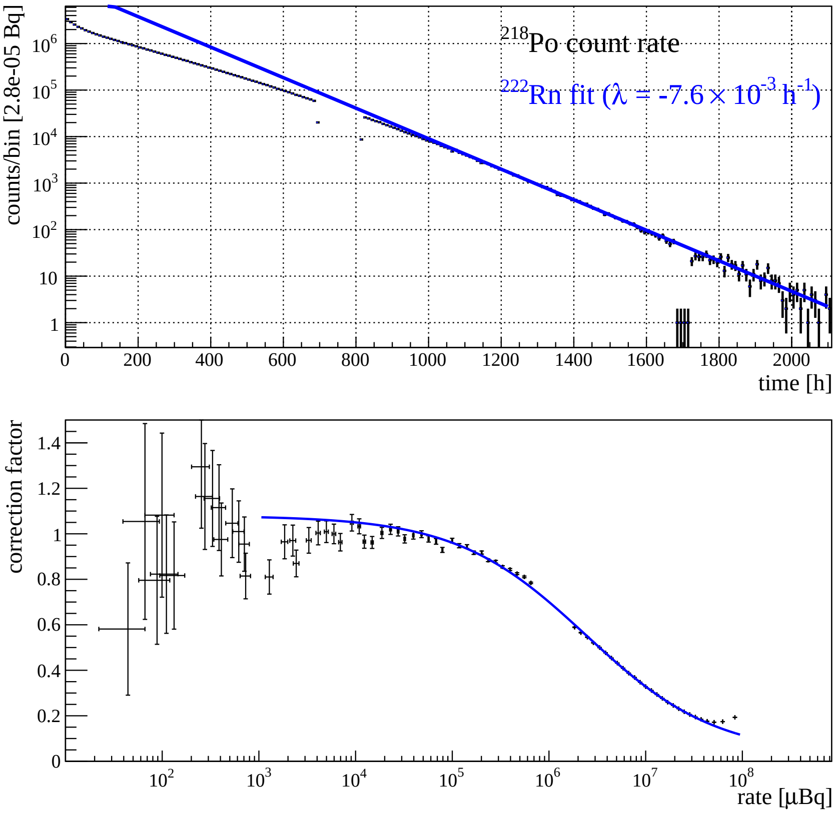

Figure 4.9: (top) ^{218}Po count rate evolving in time (about three months of data) induced by a ^{222}Rn source of about 1 kBq detected by the electrostatic ion-collection chamber of this section. (bottom) Efficiency correction as function of the observed ^{218}Po rate. See text for details.

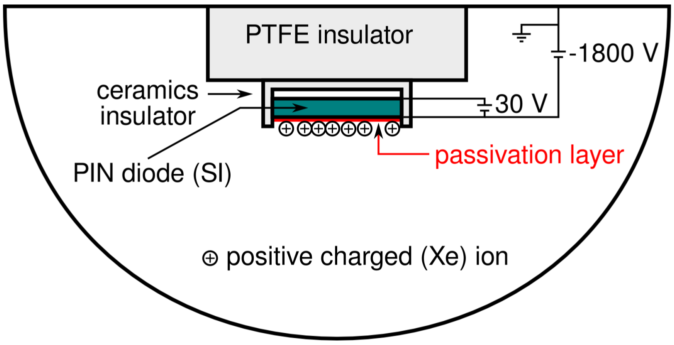

Figure 4.10: Sketch showing the silicon pin diode in its ceramics frame mounted on top of a PTFE holder. Indicated are the electric potentials as well as the collection of positively charged xenon ions produced in the ionization track of α-particles from the ^{222}Rn disintegrations.

Table 4.5: Reevaluation of data from [113] using the updated xenon flow of $\phi_{\mathrm{Xe}} = (0.25 \pm 0.03)\,\mathrm{l/min}$ and the additional knowledge about the radon monitor's rate dependent efficiency for the activated carbon Blücher 100050.

Temperature [°C]	Xe pressure [mbar]	$\widetilde{H}_\omega$ [$10^{-4}\,\mathrm{mol/(Pa\,kg)}$]	$\widetilde{H}_c^{\mathrm{est}}$
-71.1 ± 0.5	204 ± 4	19.4 ± 2.4	25.7 ± 1.0
-40.5 ± 0.4	206 ± 4	5.9 ± 0.8	7.4 ± 0.3
-39.7 ± 0.6	201 ± 4	6.9 ± 0.9	8.9 ± 0.4
-40.2 ± 0.4	197 ± 4	7.7 ± 1.0	29.2 ± 1.1

on the diodes history (amount of electronegative components in the gas discharging the collected ions, ...). This effect is not accounted for appropriately with the shown correction function. In FIG. 4.7 (bottom) a fit to the upper concentration level c_u to the corrected ^{218}Po rate is shown (green curve), leaving λ_{fit} free to float. The best fit value for the ^{222}Rn decay constant is $\lambda_{\mathrm{fit}} = -1.3 \times 10^{-2}/\mathrm{h}$; a factor two off compared to the literature value.

Assuming the "turn on" effect to dominate the efficiency loss at the very beginning, we can estimate the upper concentration level c_u by the highest measured activity right after inserting the ^{222}Rn source into the system and supplying the high voltage. From that point on, the efficiency was observed to decrease. For the lower concentration level c_l the "turn on" effect plays a minor role and the corrected rate is accurately fitted by an exponential decay of ^{222}Rn. Extrapolating both levels to the time of opening to the adsorbent trap, we compute the estimated two component Henry's constant $\widetilde{H}_c^{\mathrm{est}}$.

Despite the aforementioned efficiency drop with increasing alpha decay rate, the calibration of the mass flow controller made in [113] was found to be off roughly by a factor of two due to a wrong setting made at the controller. The correct flow was measured in a dedicated test, looping xenon at the investigated pressure of 200 mbar with the setup's diaphragm pump through a 39 m long tube of (1018 ± 4) ml volume, spiking nitrogen and observing this spike for several turns through the tube with a thermal conductivity detector (TCD). The periodicity and the knowledge of the tubes volume then were compared to the reading of the mass flow controller.

TAB. 4.5 lists the reevaluated numbers of the measurements done in [113]. The two component Henry's constant determined from the concentration level measurement $\widetilde{H}_c^{\mathrm{est}}$, due to its hard to quantify systematic uncertainty, is assumed to represent a cross-check only. Still its values, neglecting the outlier at −40.2 °C, are compatible with the Henry's constants found from the oscillation measurements. Averaging the values $\widetilde{H}_\omega$ measured at −40 °C, we find for the two components Henry's constant of radon in presence of xenon:

$$\begin{aligned} &(-40\,^\circ\mathrm{C}, 200\,\mathrm{mbar\,GXe}): && \widetilde{H} = (0.67 \pm 0.05) \times 10^{-3}\,\mathrm{mol/(Pa\,kg)} \\ &(-70\,^\circ\mathrm{C}, 200\,\mathrm{mbar\,GXe}): && \widetilde{H} = (1.94 \pm 0.24) \times 10^{-3}\,\mathrm{mol/(Pa\,kg)} \end{aligned} \tag{4.27}$$

To conclude on the dynamic adsorbent selection section, we note that the ion collection efficiency, changing with rate and history, significantly increases the uncertainties in determining the two component Henry's constant by the change in activity concentrations. This problem could be best avoided by introducing a known ^{222}Rn activity to the system. The measurement of the initial activity concentration then is nonessential. Further, we want to point out the reduction in count rate observed. Looking again at FIG. 4.7, we observe an activity decrease by more than 3 orders of magnitude (neglecting rate dependent effects) when passing the ^{222}Rn through the adsorbent column at −70 °C. We conclude, that an adsorbent column has the best reduction efficacy for ^{222}Rn as long as it is used for a time shorter than the retention time t_{Rn} of radon (*chromatography mode*). We will exploit this fact in the *swing system* introduced in section 4.4.1. Finally, we can compare the velocity ratio of xenon and radon in the adsorbent column given in [107] of $v_{\mathrm{Rn}}/v_{\mathrm{Xe}} = (0.96 \pm 0.10) \times 10^{-3}$ with the value we compute (equation 4.18) from our data of $v_{\mathrm{Rn}}/v_{\mathrm{Xe}} = (0.65 \pm 0.11) \times 10^{-3}$. That is to say, the radon velocity relative to xenon is reduced by another factor of ~ 1.5 in the activated carbon adsorbent from Bluecher that was investigated in the laboratory in Heidelberg with respect to the adsorbent Shirasagi G_{2x} 4/6 studied in [107]. We attribute this difference partially to enhanced adsorbent characteristics of the activated carbon from Bluecher. However, while our data was collected at 200 mbar, in [107] no information on the xenon pressure is specified. Differences in the gas pressure of xenon, being a strongly competitive component in the radon adsorption process, are expected to be a more likely reason for the observed differences.

4.3.5 Xenon adsorption

The total amount of xenon needed for the XENON1T experiment is affected by the amount of xenon adsorbed in the single column adsorption system. A small experimental setup, as shown in FIG. 4.11, was assembled in order to determine the xenon adsorption per amount of adsorbent.

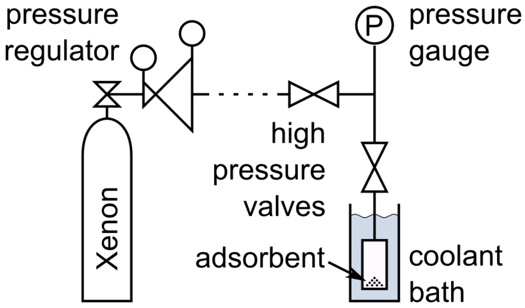

Figure 4.11: Schematic drawing of the experimental setup to measure the xenon adsorption at the projected XENON1T conditions on activated carbon.

Gaseous xenon is filled from a pressurized gas cylinder into a calibrated volume equipped with a capacitive pressure gauge to quantify its amount. Expanding the xenon gas into the volume housing the adsorbent, that itself is immersed in an adjustable temperature bath, the observed pressure drop is a measure for the amount of xenon adsorbed. By repeating the measurement without any adsorbent, the effect of the increased volume and of the temperature gradients on the pressure reading are accessed and compensated subsequently in the analysis of the data. In FIG. 4.12 the measurements done in [110] on the activated carbon adsorbent Blücher 100050 at $-80\,^{\circ}\mathrm{C}$ are shown as function of the xenon pressure above the adsorbent after the adsorption equilibrium for xenon is reached. The xenon adsorption saturates for pressures $\gtrsim 1.5\,\mathrm{bar}$ at a value of $1.4\,\mathrm{g/g}$ xenon per adsorbent mass. In [110] we find the same measurements done at $-40\,^{\circ}\mathrm{C}$ where the adsorbed amount of xenon levels around $1.2\,\mathrm{g/g}$ xenon per adsorbent mass. For the XENON1T relevant pressure of 2 bar saturation is reached.

4.3.6 Conclusions on single column adsorption radon removal system

In the previous sections we introduced the single column adsorption radon removal system to mitigate the threat of the ^{222}Rn emanation on the scientific goal of XENON1T. We found a reduction factor of $\mathcal{R} \approx 50$ to be needed to reduce type II sources (^{222}Rn emanation from the gas system) by a factor 100 [7]; enough to render type II sources inconsequential. At XENON1T's projected recirculation flow of 100 slpm, type I sources (^{222}Rn emanation inside the cryostat to the LXe) are not transported in time to the radon removal system and a maximal reduction factor of ~ 2.5 is achievable. Equation 4.20

---

[7] A factor of 50 is reached by the first pass through the removal system. The remaining factor of two is achieved by the recirculation flow allowing a fraction of the radon atoms to pass the removal system a second time. See section 4.2.2 for more details.

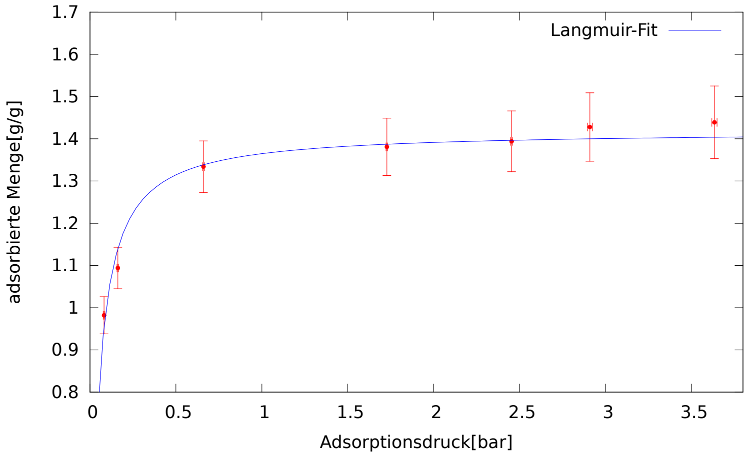

Figure 4.12: Adsorption of xenon on the activated carbon adsorbent Blücher 100050 as function of the xenon pressure created by the xenon gas above the adsorbent. The temperature is fixed to −80 °C. Figure courtesy of Simon Stemmle [110].

relates the properties of the single column adsorption like mass, Henry's constant and temperature to the radon removal factor $\mathcal{R}$. Solving for the required amount of adsorbent at a temperature of −70 °C and employing the two component Henry's constant $\widetilde{H}$ measured in section 4.3.4, we compute a mass of 900 kg. Unfortunately, this still is an optimistic assumption, as $\widetilde{H}$ was measured at 200 mbar and is supposed to decrease with increasing xenon pressure. At −70 °C the 900 kg of activated carbon adsorb ∼ 1.3 tons of xenon – more than a third of XENON1T's total xenon mass.

Considering further the projection of the activated carbon's intrinsic ^{222}Rn emanation of ∼ 1 mBq/kg (see section 4.5.3 or [107]), i.e. assuming the ^{222}Rn emanation to be the same at cryogenic (∼ −70 °C) temperatures as measured at 200 °C, a 900 kg activated carbon column with a removal factor of $\mathcal{R} = 50$ increases the type I budged by 225 mBq (see equation 4.24) – irreconcilable with XENON1T's scientific goal.

Turning the argument, in section 4.2.2 we found 1.1 mBq to be the acceptable upper limit on type I (and type I equivalent) ^{222}Rn emanation sources at the projected 100 slpm gaseous xenon recirculation flow setting the removal factor to be $\mathcal{R} = 50$. If we evaded all type I sources from the cryostat itself and were left with type II sources to mitigate, the type I equivalent ^{222}Rn emanation of the activated carbon adsorbent would be limited to above-mentioned 1.1 mBq. At the intrinsic ^{222}Rn emanation of the adsorbent of ∼ 1 mBq/kg we exploit equation 4.24 ($\widetilde{k_3}/k_3(\mathcal{R} = 50) = 0.25$) and find the maximum possible adsorbent mass to be 4.4 kg.

The adsorbent's two components Henry's constant, required to accomplish $\mathcal{R} = 50$ at

4.4 kg mass, is directly given by the mass ratio $900/4.4 \approx 200$ times the value found in section 4.3.4 (see equation 4.20). Recalling the results presented in sections 4.3.3 and 4.3.4 an increase by a factor of 10 already seems to be unlikely. An improvement by a factor 200, therfore, seems at the present unfeasible.

4.4 Alternatives to single column adsorption

The large quantity of adsorbent, that is needed to sufficiently retain radon in the single column adsorption setup at the required GXe recirculation flow, poses two serious problems: it adsorbs a significant fraction of XENON1T's totally available xenon target and might increase the total ^{222}Rn budged above the allowed maximum. At this point we want to outline two alternative ideas for a realization of a radon removal system. The first one – we refer to as temperature swing adsorption – is based on the different adsorption properties of xenon and radon as well and, hence, it still suffers from the problematic type I equivalent ^{222}Rn emanation that limits the amount of adsorbent drastically. The second approach differs from what was discussed so far as it is based on cryogenic distillation. Theoretical models forecast extraordinary performances. However, to our knowledge so far there exists no experimental validation and further research and development is needed to objectively judge its potential.

4.4.1 Temperature swing adsorption

We mentioned already at the end of section 4.3.4 the impressive purification efficacy of an adsorbent column that is used in "chromatography mode" instead of the so far discussed "static concentrations mode" of the single column adsorption. By the term chromatography mode we stress the fact that the ^{222}Rn concentration at a certain position inside the adsorbent column *does* change with time; in contrast to the static concentration mode of the single column adsorption.

Consider looping radon free xenon gas through an adsorbent column. We want to spike the xenon gas with a peaked radon concentration that enters the adsorbent column at time zero as shown in FIG. 4.3. In time, this concentration peak will broaden inside the adsorbent column while its center of mass approaches at velocity v_{Rn} (see equation 4.18) the end of the adsorbent column. There is a period of time where neither the concentration distribution's center of mass nor its tails have passed the adsorbent column. If the adsorbent retains radon with respect to xenon, and we have shown in the previous sections how to select an appropriate adsorbent doing so, during this period of time the adsorbent column will provide gaseous xenon depleted in radon.

Neglecting channeling effects and intrinsic ^{222}Rn emanation of the adsorbent for the time being, in our simplified model radon is removed completely from the out-streaming xenon. If operated properly, the TSA system seems to radon atoms to be of infinite length. Hence, they can never pass the column. A purification, thus, would have been achieved, even if radon did not decay inside the adsorption column – the working principle of the single column adsorption setup responsible for its large size.

In the following we want to construct a system that makes use of this high purification efficacy in chromatography mode, that runs continuously and, furthermore, that does not discard any xenon. Systems working after this principle – however rejecting a certain fraction of their initial feed – are well known as (pressure or temperature) *swing* systems in industrial air separation processes [117, 118]. To relinquish the need of exhausting radon-enriched xenon is, in principle, conceivable due to radon disintegrating in time. FIG. 4.13 shows a series of schematic drawings that illustrate a system working after above-sketched principle. The minimal system consists of three adsorbent filled columns (AC1 to AC3). At any given time only one column is purifying the GXe in XENON1T's recirculation loop *plus* some additional xenon employed to prepare the other two adsorbent columns. This column we want call active. At every time we have a gaseous volatile phase inside the adsorbent columns. That is to say, we are not purifying a liquid xenon stream. In the following the single steps sketched in FIG. 4.13 are described:

① AC1 is active, i.e. it is radon free and maximally loaded with xenon at its operation conditions (cryogenic temperature and pressure of XENON1T's purification loop). AC1 purifies (in chromatography mode) the full GXe in the XENON1T purification loop plus an additional amount of gas used to purge AC2. AC2 is hot and at the purification loop's operation pressure. However, AC2 is still (partially) loaded with radon. The ^{222}Rn-free GXe supplied by AC1 is used to flush out the radon abundant in AC2. AC3 is bypassed and at cryogenic temperature with the maximum amount of xenon and radon being adsorbed.

② AC1 is still active. AC2 is fully purged, that is all radon is removed. Purified xenon from AC1 is fed into AC2 to compensate the xenon adsorption while cooling down AC2. The additional xenon needed to fill up AC2 is supplied by (radon loaded) xenon desorbing in AC3 being heated at the same time.

③ Once AC3 is at the nominal baking temperature and AC2 cooled to the cryogenic temperature, AC1 is switched to bypass mode and AC2 is becoming active pro-

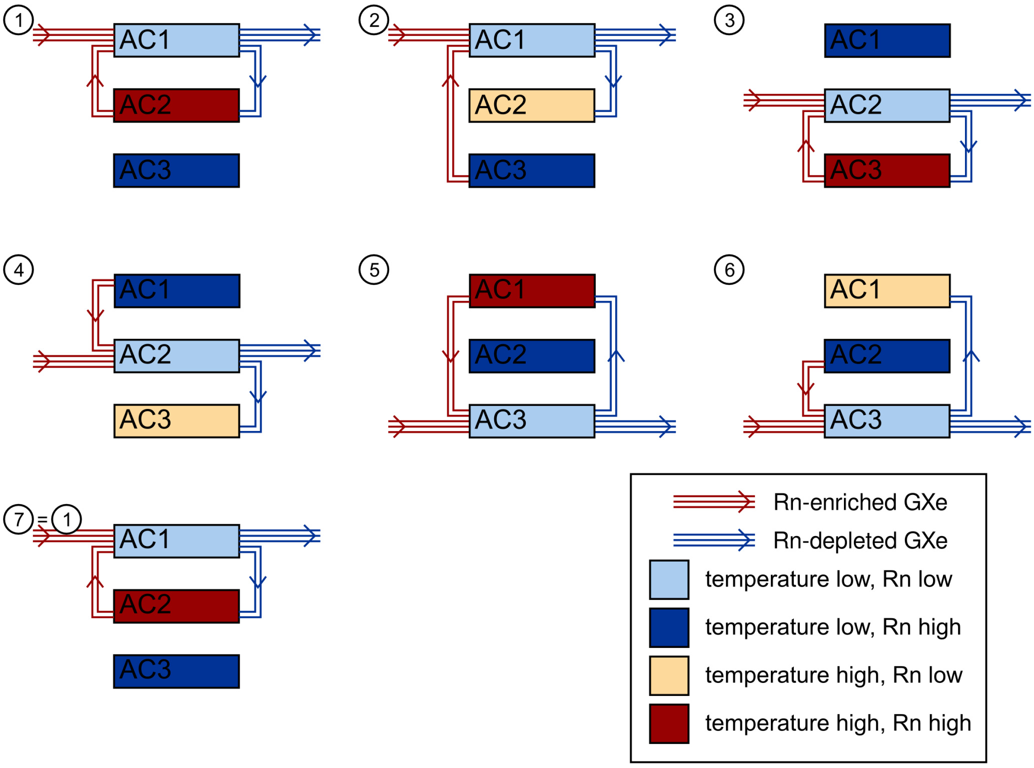

Figure 4.13: Illustration of the six different steps necessary to run the three column adsorption temperature swing system presented in the text continuously in chromatography mode without rejecting any xenon. AC1 to AC3 are three identical adsorbent filled packed columns that can be cooled or baked to alter the adsorption properties of radon inside.

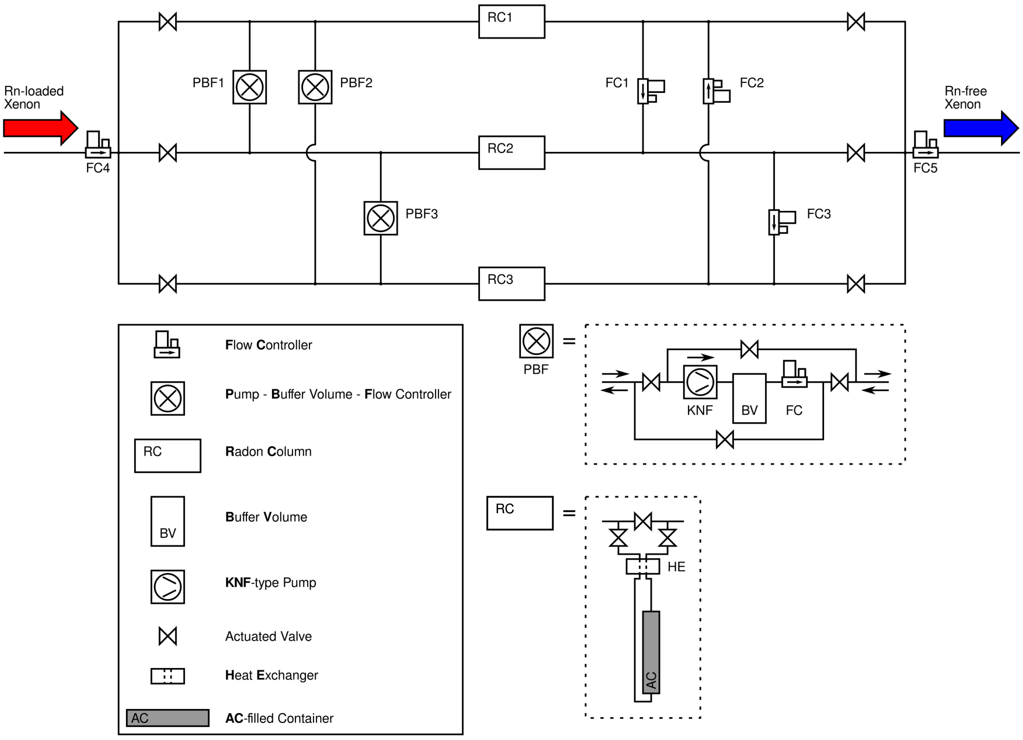

Figure 4.14: Flow chart scheme realizing the conceptual drawing of FIG. 4.13.

cessing the full GXe from the purification loop plus the additional amount of gas to purge AC3.

④ – ⑥ Permutations of the above stated. After six steps the initial starting position is reached again.

In FIG. 4.14 a flow chart is sketched realizing the above depicted concept. To achieve zero xenon waste, additional pumps are deployed that are mandatory to maintain the pressure gradients. As these pumps are supposed to be ^{222}Rn emanation sources as well, they have to be placed at FIG. 4.14's left side. That is, xenon passing a pump is purified by the active adsorption column before being fed into the XENON1T detector again.

A technically delicate aspect is to exactly control the temperature gradients of the columns being heated or cooled. The amount of desorbed xenon from the column being heated has to exactly compensate the xenon adsorbed by the column being cooled down. This has to be achieved while granting stable conditions in XENON1T's purification loop. In total eight mass flow controllers and three buffer volumes are supposed to smoothen remaining pressure variations and ensure stable flow conditions.

While the proposed system is well suited to remove externally produced ^{222}Rn from the GXe purification loop, it suffers from its own ^{222}Rn emanation. Intrinsically produced (emanated) ^{222}Rn propagates the adsorbent in the same way as it does in the single column adsorption setup, and equation 4.24 holds. To be more precise, for small masses and the measured two component Henry's constant, $\mathcal{R} \xrightarrow{m\to 0} 0$ holds and equation 4.24 reads $\widetilde{k}_3 = k_3$. That is, the full intrinsic ^{222}Rn emanation of the adsorbent has to be treated as a type I source fully entering the detector[8]. As discussed above, we are limited to 1.1 mBq type I ^{222}Rn emanation looping at 100 slpm recirculation flow, equivalent to ~ 1.1 kg adsorbent mass. Thus, every single column contains only ~ 350 g of adsorbent. The resulting retention time of radon is $t_{\mathrm{Rn}} \approx 10$ min at a GXe flow through the column of 120 slpm for the measured Henry's constant of 2×10^{-3} mol/(Pa kg). This calculation considers the radon distribution's center of mass only. Tails of the ^{222}Rn distribution preceding the center of mass might result in even shorter time intervals a single adsorption column effectively can be employed.

The additional 20 slpm are used to purify and prepare the other two columns. Warming up 350 g of xenon loaded adsorbent, i.e. about 490 g of xenon (see section 4.3.5), at the set GXe flow of 20 slpm, takes about 4.5 min. The remaining time is available for purging. In order to effectively remove radon, the purged adsorbent needs to be at temperatures around 150 °C or above [107].

Microwave supported TSA

To achieve temperature changes of about 300 K on the timescale of several minutes for an adsorbent mass of 350 g, technically is greatly challenging. The cooling power might be achieved by pre-cooling the xenon gas inflow augmented by an efficiently coupled temperature bath. To introduce the energy exactly at the location needed to desorb radon, i.e. into the adsorbent itself, while minimizing the heat introduced to the surrounding vessel, a microwave supported temperature swing adsorption setup was proposed. The idea of alternative energy transfers has attracted attention during the last decade in order to make temperature swing adsorption a competitive technique. Amongst them is indirect heating/cooling [119], heat generated inside the adsorbent by passing an electric current through the adsorbent itself [120] and the mentioned microwave heating technique [121, 122]. Preliminary laboratory tests using a domestic microwave oven cavity

---

[8] This assumption is somewhat conservative as there is only one of the three columns active at a time. The radon (also the emanated in the column itself) of the other two columns is purged before the next column becomes active (see FIG. 4.13 ①). However, during filling xenon and cooling down the column becoming active next (②), emanated radon acquires that is not purged out. Once this column becomes active (③) the additional radon enters the detector.

(2.45 GHz at a wavelength of 122 mm) showed the activated carbon adsorbent Blücher 100050 almost opaque for the microwaves: within seconds temperatures far above 100 °C were reached in a small glass vessel of 2 cm diameter and 5 cm height. Dedicated tests have to follow examining the potential of this technique in presence of xenon as well as investigating the homogeneity of the heat transfered to the adsorbent.

The fast temperature changes, that are needed in our conservative forecast of ~ 1 mBq/kg intrinsic ^{222}Rn emanation rate, are technically demanding. We are confident, though, that above outlined techniques can be successfully employed to achieve the desired fast cooling cycles. We will present in section 4.5 screening results of the activated carbons from Bluecher 100050 and Shirasagi G_{2x} 4/6 that hint at lower intrinsic emanation rate than assumed for the Bluecher adsorbent in such a system. Measuring this intrinsic emanation is very challenging at cryogenic temperatures due to the strong adsorption of xenon and radon itself. However, first ideas exist to provide evidence for a reduced intrinsic emanation rate in presence of xenon when decreasing the temperature from 200 °C to 100 °C. Proving the intrinsic emanation to be lower by only a factor of ~ 3, allows to increase its mass employed by the same factor and significantly smooths the temperature gradients that have to be achieved. This, in turn, makes the TSA approach even more promising.

4.4.2 Cryogenic fractional distillation

Cryogenic fractional distillation exploits the difference in volatility of the constituents in a multi-component liquid mixture. It is a well understood technique [42, 43] finding application both in commercial gas separation plants [117] and scientific basic research [34, 44, 123]. The XENON collaboration itself already extensively uses cryogenic distillation to purify xenon from traces of krypton (see section 1.2.2). The idea is to use a similar cryogenic distillation column to the one that will purify XENON1T's xenon target from krypton. This column is supposed to continuously remove radon distilling the expected 100 slpm GXe of the purification loop. The vapor pressure of radon is at 178 K about 15 mbar [124], while the one of xenon is at the same temperature already ~ 2 bar – greater by more than two orders of magnitude. This large difference should result in a separation efficacy comparable to the one of the binary system of krypton and xenon[9] assuming the classically employed MacCabe-Thiele method [125] to be valid

---

[9] Actually we assume the radon/xenon separation by cryogenic fractional distillation to be superior to the krypton/xenon separation. The ratios of the vapor pressures P_i at the operation temperature is more than an order of magnitude higher for the radon/xenon separation ($P_{\mathrm{Xe}}/P_{\mathrm{Rn}} > 100$, $P_{\mathrm{Kr}}/P_{\mathrm{Xe}} = 10.4$ [44]) and the crucial parameter characterizing distillation.

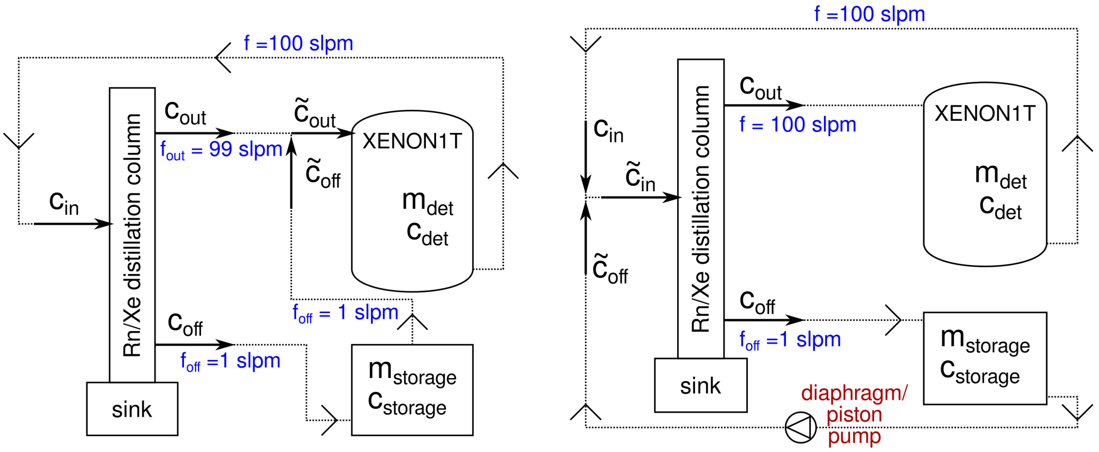

Figure 4.15: Sketch illustrating the working principle of a radon removal system based on cryogenic fractional distillation in continuous loop mode. (left) Straight forward modification starting from a batch mode distillation system. The off-gas is retained in a storage vessel before being fed back to the detector (right) Slightly modified version of left figure: retained off-gas is put back into the distillation column. Additionally a pump is needed to compensate the pressure gradients.

for the extremely low radon concentrations (20 mBq ^{222}Rn correspond to only $\sim 1 \times 10^4$ atoms).

For a simple back-of-the-envelope calculation we assume the following scenario: the radon/xenon online distillation column reaches the same reduction factor as determined for the krypton/xenon distillation column of XENON100 (see section 1.2.2). In chapter 3 this reduction was evaluated to be $y_p = c_{\text{in}}/c_{\text{out}} = 390 \pm 120$ at 1 % off-gas xenon. While the krypton/xenon distillation is performed in batch mode and the off-gas can be stored separately, we have to come up with a different idea for the online radon/xenon distillation. The straight forward solution is to retain the off-gas in a separate container (V_{storage}), putting it back to the detector only when its ^{222}Rn activity is sufficiently reduced. FIG. 4.15 (left) sketches such a simple system. For our estimate we assume 1 % off-gas (f_{off}) equivalent to 1 slpm gaseous xenon at a total of $f = 100$ slpm recirculation flow. Consequently we find $f_{\text{out}} = 99$ slpm ^{222}Rn-free distilled xenon at the outlet of the distillation column.

We want to neglect any effect by ^{222}Rn disintegrating in the columns sink. In equilibrium, ^{222}Rn particle conservation reads:

$$f \cdot c_{\text{in}} = f_{\text{out}} \cdot c_{\text{out}} + f_{\text{off}} \cdot c_{\text{off}} \,. \tag{4.28}$$

The ^{222}Rn concentrations c_{in} and c_{out} are related by the above-mentioned reduction factor of the distillation column of $y_p = \sim 390$, and we find for the concentration in the off-gas:

$$c_{\text{off}} = \frac{f - f/y_p + f_{\text{off}}/y_p}{f_{\text{off}}} \cdot c_{\text{in}} \tag{4.29}$$

$\widetilde{c}_{\text{out}}$, the concentration put back to the XENON1T detector, has to be reduced by a factor of $\mathcal{D}_{\text{II}} = \widetilde{c}_{\text{out}}/c_{\text{in}} = 50$ as we argued in section 4.2.2. Particle conservation at the input into the XENON1T detector gives:

$$f \cdot \widetilde{c}_{\text{out}} = f_{\text{out}} \cdot c_{\text{out}} + f_{\text{off}} \cdot \widetilde{c}_{\text{off}} \,. \tag{4.30}$$

Solving equation 4.30 for $\widetilde{c}_{\text{off}}$ as function of c_{in} we find:

$$\widetilde{c}_{\text{off}} = \frac{f/\mathcal{D}_{\text{II}} - f/y_p + f_{\text{off}}/y_p}{f_{\text{off}}} \cdot c_{\text{in}} \,, \tag{4.31}$$

and compute for the required ^{222}Rn reduction inside the storage volume combining equation 4.29 and 4.31:

$$\frac{\widetilde{c}_{\text{off}}}{c_{\text{off}}} = \frac{y_p/\mathcal{D}_{\text{II}} - (1 - f_{\text{off}}/f)}{y_p - (1 - f_{\text{off}}/f)} \approx \mathcal{D}_{\text{II}}^{-1} \,. \tag{4.32}$$

Again, this reduction has to be achieved by retaining the ^{222}Rn in the storage volume where it disintegrates. To compute the required amount of xenon in the storage volume (m_{storage}), we assume the radon introduced to be instantaneously mixed and, thus, the concentration in the storage volume (c_{storage}) being constant and identical to the concentration of the xenon taken out of the storage vessel ($\widetilde{c}_{\text{off}}$). We find the amount of ^{222}Rn atoms N present in the storage volume (neglecting any intrinsic emanation of the latter) to be described by the following differential equation:

$$\frac{dN}{dt} = c_{\text{off}}\, f_{\text{off}} - \widetilde{c}_{\text{off}}\, f_{\text{off}} - \lambda\, N \,. \tag{4.33}$$

The absolute number of ^{222}Rn atoms in the storage vessel is computed from the xenon mass and its ^{222}Rn concentration: $N = \widetilde{c}_{\text{off}} \cdot m_{\text{storage}}$. We are interested in the equilibrium, i.e. $dN/dt = 0$ in equation 4.33 and, hence, can solve for the xenon mass:

$$m_{\text{storage}} = \left(\frac{c_{\text{off}}}{\widetilde{c}_{\text{off}}} - 1\right) \frac{f_{\text{off}}}{\lambda} \tag{4.34}$$

$$\approx \mathcal{D}_{\text{II}} \cdot f_{\text{off}}/\lambda \,. \tag{4.35}$$

Inserting the decay constant of ^{222}Rn ($\lambda = \ln(2)/3.8\,\text{d} = 0.182\,\text{d}^{-1}$) and translating the off-gas flow of 1 slpm into the mass-flow of 8.38 kg/d, we compute the stored amount of xenon to be $\sim 2.6\,\text{t}$, still asking a radon removal of $\mathcal{D}_{\text{II}} = 50$.

Having a total of 3 t xenon available for XENON1T, this is clearly not feasible. However, we can slightly modify the flowchart (FIG. 4.15 right) and reinsert the xenon from the storage back to the distillation column instead of feeding it directly to the detector. To maintain the desired flow conditions and overcome the pressure gradient between the outlet of the storage vessel and the input of the distillation column we will need an additional pump. Following above reasoning, we can write the ^{222}Rn particle conservation in the modified setup of FIG. 4.15 (right) to be:

$$(f + f_{\text{off}}) \cdot \widetilde{c}_{\text{in}} = f \cdot c_{\text{in}} + f_{\text{off}} \cdot \widetilde{c}_{\text{off}} \tag{4.36}$$

$$(f + f_{\text{off}}) \cdot \widetilde{c}_{\text{in}} = f \cdot c_{\text{out}} + f_{\text{off}} \cdot c_{\text{off}} \tag{4.37}$$

Therein, we neglected again the decay of ^{222}Rn inside the distillation column. Solving for the ratio of the concentrations put into and taken off the storage vessel, we find:

$$\frac{\widetilde{c}_{\text{off}}}{c_{\text{off}}} = \frac{y_p\,(1 + f_{\text{off}}/f) - \mathcal{D}_{\text{II}}}{y_p\,(1 + f_{\text{off}}/f) - 1} \approx 1 - \frac{\mathcal{D}_{\text{II}}}{y_p\,(1 + f_{\text{off}}/f)} \tag{4.38}$$

Here we made use of the assumed purification yield of the distillation column and its effective radon removal factor, that read in our model $y_p = \widetilde{c}_{\text{in}}/c_{\text{out}}$ and $\mathcal{D}_{\text{II}} = c_{\text{in}}/c_{\text{out}}$, respectively (see FIG. 4.15 (right)). Employing equation 4.34 and inserting above values for purification yield and radon removal ($y_p = 390$, $\mathcal{D}_{\text{II}} = 50$), we compute a required amount of xenon to be stored of $m_{\text{storage}} \sim 7\,\text{kg}$.

We have seen that it is not feasible to store the off-gas xenon in a separate vessel before reinserting it directly back to the detector. The required amount of xenon stored simply is too large. However, feeding the off-gas back to the inlet of the distillation column, after retaining it for some time in the storage vessel, reduces the amount of additionally demanded xenon drastically. A mere 7 kg are needed to meet the specification of a radon removal factor of $\mathcal{D}_{\mathrm{II}} = 50$, that we showed to be sufficient in section 4.2.2.

The above mentioned two orders of magnitude difference in the relative vapor pressures of $P_{\mathrm{Rn}}/P_{\mathrm{Xe}}$ in comparison to $P_{\mathrm{Xe}}/P_{\mathrm{Kr}}$ are promising to be able to construct a radon/xenon distillation column with similar purification yield as demonstrated for the krypton/xenon separation. The greatest uncertainty remains in the feasibility of single atoms distillation. Compared to krypton the amount of ^{222}Rn atoms in the xenon gas is suppressed by about 12 orders of magnitude, assuming krypton/xenon ~ 1 ppt. Besides ^{222}Rn, emanation of ^{220}Rn might slightly enhance the greatly suppressed number of radon atoms, however, the general picture is not supposed to change.

If few-atoms radon/xenon distillation will be successfully demonstrated, the technically ambitious task persists to cope with the high xenon mass flow of 100 slpm. To overcome only the heat of evaporation when liquefying the mass flow of ~ 840 kg/d (equivalent to 100 slpm), roughly 1 kW are needed. The pulse tube refrigerators (PTR) employed in XENON100 (see section 1.2.2) are limited to about 0.2 kW. The krypton/xenon distillation columns of both XMASS and XENON100 [34, 44] are processing a xenon gas flow of only 14.4 kg/d. In other words about a factor of 50 less than required for a distillation based radon removal system. Yet, both systems operate each two PTRs. Extrapolating this technology results in $\gtrsim 10$ PTRs to be employed. This illustrates the technically ambitious task of maintaining a recirculation loop of 100 slpm including a distillation process.

4.5 Radon emanation assay studies

^{222}Rn is a serious source of intrinsic background for both XENON100 and XENON1T as we pointed out in the introductory part of this chapter. Once a detector is assembled, a constant rate of emanating ^{222}Rn is observed due to its long-lived predecessor ^{226}Ra. If we assumed a maximum efficient ^{222}Rn removal system implemented last in the purification-recirculation system, the ^{222}Rn background suppression still would have been limited due to the finite recirculation speed. In section 4.2.2 we showed the reduction of type I sources at 100 slpm to be limited to a factor of only 2.5 (see $\mathcal{D}_{\mathrm{I}}$ in TAB. 4.2). A thorough material screening in advance of the detector's construction to avoid any ^{222}Rn emanation is the mandatory consequence. Gamma-ray screening for ^{226}Ra might not be sufficient as surface and not bulk contaminations can dominate the emanation properties. Hence, the materials have to be screened with a dedicated technique for their ^{222}Rn emanation.

4.5.1 Principle of ^{222}Rn emanation measurements

Commonly there exist two different approaches to quantify a ^{222}Rn emanation rate. Alpha-particle detectors are used to count both the ^{222}Rn disintegrations directly as well as the two α-particles produced in the subsequent decay chain (see section 4.3.4). Alternatively, detectors sensitive as well to beta decays can make use of a characteristic delayed coincidence signature present in the ^{222}Rn decay chain. The disintegration of the beta-decaying ^{214}Bi is shortly followed by the alpha decay of ^{214}Po ($T_{1/2}(^{214}\mathrm{Po}) = 162.3\,\mu\mathrm{s}$). This for the ^{222}Rn chain characteristic coincidence is commonly referred to as BiPo. While the latter type of detection principle discriminates all kind of backgrounds due to its unique coincidence feature, the former technique requires a good energy resolution or high radiopurity to reach the desired sensitivities. The advantages of the former techniques, however, are a higher statistics and, usually, lower demands on the data acquisition systems.

In this work miniaturized proportional counters were employed to detect the α-particles of the ^{222}Rn decay chain. These devices, originally developed at the Max-Planck-Institut für Kernphysik (Heidelberg, Germany) in the context of the GALLEX/GNO solar neutrino experiments [54], are optimized to detect ionizing particles with energy depositions as low as 300 eV [87, 126]. Alpha particles, that are fully adsorbed in the sensitive volumes of the devices, cause the amplifiers to saturate and any energy resolution is lost. However, below the energy range of interest $\lesssim 50\,\mathrm{keV}$ the devices efficiently reject gammas, betas and muons that compose the dominant part of background in an unshielded laboratory above ground. The remaining part of the background is dominated by intrinsic alpha decays. Typical backgrounds in the region of interest of these devices are 0.5 cpd to 1.0 cpd (cpd = counts per day).

The housing of the miniaturized proportional counters is entirely made of synthetic quartz glass. The sensitive volume is confined by a cylindrical cathode made from iron or silicon where the negative high voltage is applied. A thin tungsten anode wire (13 µm) at ground in the center of the sensitive volume is used to collect primary and secondary electrons initially produced by an ionizing particle in the sensitive volume. The size of the active volume is about $1\,\mathrm{cm}^3$ and contains the gas sample at pressures close to 1 bar absolute. The gas sample is confined to the proportional counter by sealing the inflow with liquid mercury. A stop cock keeps the mercury itself in place. FIG. 4.16 shows a picture of such a device.

Filling emanated ^{222}Rn atoms to such a proportional counter is non-trivial. The screened material is put into a leak tight container (*emanation container*) filled with

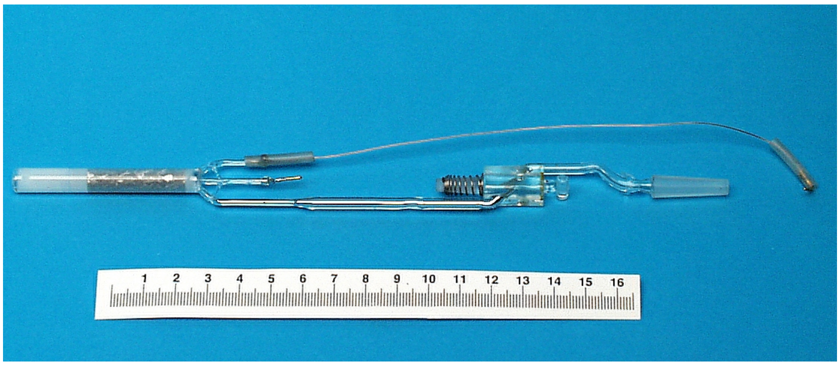

Figure 4.16: Miniaturized ultra-low background proportional counter. The shown scale is in units of centimetre.

^{222}Rn free gas (*carrier gas*) that is usually helium purified by an activated carbon adsorbent at LN_2 temperature. In time the ^{222}Rn activity inside the emanation container saturates (*saturation activity*) due to a constant emanation source term and the exponential decay of the ^{222}Rn atoms. The amount of carrier gas inside the emanation container exceeds in almost all cases the volume of the miniaturized proportional counters by orders of magnitude and a separation of the emanated radon atoms is mandatory. Moreover, radioactive components like ^{85}Kr and ^{39}Ar as well as gases diminishing the performance of the proportional counters like O_2, CO_2 and H_2O must be removed. Finally, operating the proportional counters using an argon-methane or xenon-methane counting gas mixture is desirable as those mixtures exhibit a good energy resolution, require reasonable high voltages ($\sim 1\,\mathrm{kV}$) and appropriate calibration sources (^{55}Fe, cerium X-rays [87, 127, 128]) exist. For the mentioned objectives a gas handling, sample purification and counter filling line (see FIG. 4.17) is used. Basic principle is the separation of the different gases by means of chromatography and the subsequent removal of remaining impurities other than noble gases by a hot getter. For this purpose several U-shaped traps are available filled with different adsorbents that can individually be used or bypassed at various temperatures.

In the standard procedure the emanated ^{222}Rn atoms present inside an emanation container are purged by means of purified helium ($\sim 0.3\,\mathrm{slpm}$) at a pressure slightly above 1 bar absolute. The ^{222}Rn atoms in the helium gas pass a glass wool filled trap immersed in a temperature bath at $-25\,^{\circ}\mathrm{C}$. Therein water vapor and organic compounds are supposed to freeze out. The ^{222}Rn atoms in the dried helium gas are subsequently directed through an activated carbon (alternatively Chromosorb 102) filled adsorbent trap at LN_2. Here the radon atoms adsorb while the helium gas almost unaffectedly

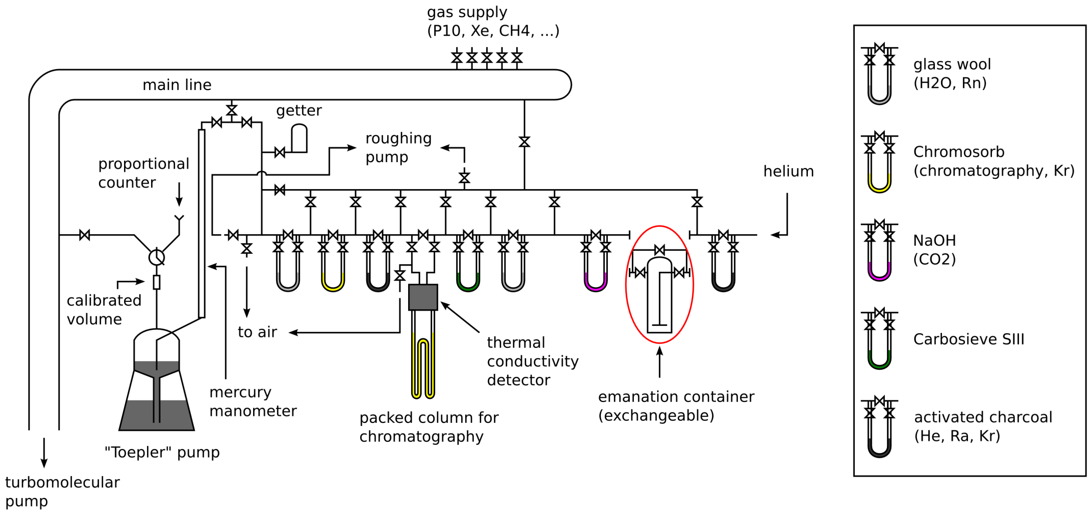

Figure 4.17: Sketch of counter filling line available at MPIK and LNGS.

passes. For the employed emanation container flushing an amount of helium gas of about ten times their volume is sufficient to collect the emanated radon completely on the adsorbent trap. The remaining helium gas is evacuated by a roughing pump. Once the helium is removed, the ^{222}Rn atoms and the remaining impurities desorb by heating the adsorbent trap to about 180 °C. A hot getter can be used to further purify the desorbed gas from hydrocarbons eventually abundant. By means of a calibrated volume, the "Toepler" pump and a mercury manometer (see FIG. 4.17) a defined amount of counting gas is assembled and mixed with the desorbed ^{222}Rn atoms from the sample. Employing again the "Toepler" pump, the ^{222}Rn atoms mixed with the counting gas are transfered to the proportional counter pushed forward by the liquid mercury sealant.

Once the ^{222}Rn atoms are mixed with counting gas and filled to a miniaturized proportional counter, the counter is disconnected from the counter filling line and connected to the data acquisition system. A lead housing that is fitted to the special shape of the proportional counter shields ambient γ rays. The housing additionally incorporates amplifiers for the signals induced to the anode wire. The amplified signal is fed to a Flash ADC module (Struck model SIS3300) with a sampling rate of up to 105 MHz for the individual channel and 12-bit resolution. The events are online compressed in time and shaped by a moving window deconvolution algorithm. The filtered pulse height and its time stamp are stored to disk. Events above a threshold of $\sim 47\,\mathrm{keV}$ are accepted to be valid ^{222}Rn induced events. Before starting a measurement the negative high voltage supplied to the cathode of about $-0.8\,\mathrm{kV}$ is adjusted by means of a calibration source.

In most cases the counters are calibrated using the K_α transitions of ^{55}Mn (~ 5.9 keV) that are subsequent to the electron capture disintegration of ^{55}Fe. The region of interest for ^{222}Rn events is set 8 times above the induced calibration peak, i.e. at about 47 keV.

4.5.2 General formula to evaluate ^{222}Rn emanation measurements

We have shown throughout this chapter the mandatory need to select radio-pure materials for constructing the XENON1T detector. A thorough ^{222}Rn emanation assay of all construction materials in contact with the gaseous or liquid xenon target is one centerpiece of this effort. In order to make the best use of the available ^{222}Rn emanation data a database was implemented (based on PostgreSQL[10]) incorporating a web interface. This database is aimed to consistently collect emanation data and to facilitate search functions for the growing wealth of information collected during the last decade of ^{222}Rn emanation measurements. Furthermore, the database implements the necessary algorithms to evaluate the data provided by the data acquisition system. The latter not only is convenient for the user and efficiently quickens daily work, but is invaluable in cases where additional information is gained for example on the blank contribution of an emanation container or an altered background of a proportional counter and data has to be reevaluated. In such cases the database facilitates algorithms to consistently and reliably update affected data.

In the following we want to present the mathematical algorithm implemented in the database to evaluate the ^{222}Rn measurement data. FIG. 4.18 illustrates this computation in the simplified case of additional four source terms (three emanation container plus the blank of the gas filling line). Shaded in gray is the time interval $[t_6, t_7]$ actual ^{222}Rn decays are detected and the activity A is inferred from. During the time intervals $[t_i', t_{i+1}]$ the various emanation containers contribute (violet curves) to the overall ^{222}Rn emanation. The black curve shows the development of the ^{222}Rn activity with time, however, simplified by the approach to add the effect (Δ_{i-1}) of further radon sources (blanks of emanation containers, blank of gas filling line) only at the very last moment t_{i+1} of their contribution (violet vertical lines). Separating both processes, exponential decay of the initial radon and limited growth of the additional radon sources, mathematically is possible due to the linear nature of the underlying differential equation and significantly simplifies the computation. Marked with black dots are the activities along the line of computation. Once the activity A is computed from the number of recorded

---

[10] http://www.postgresql.org/

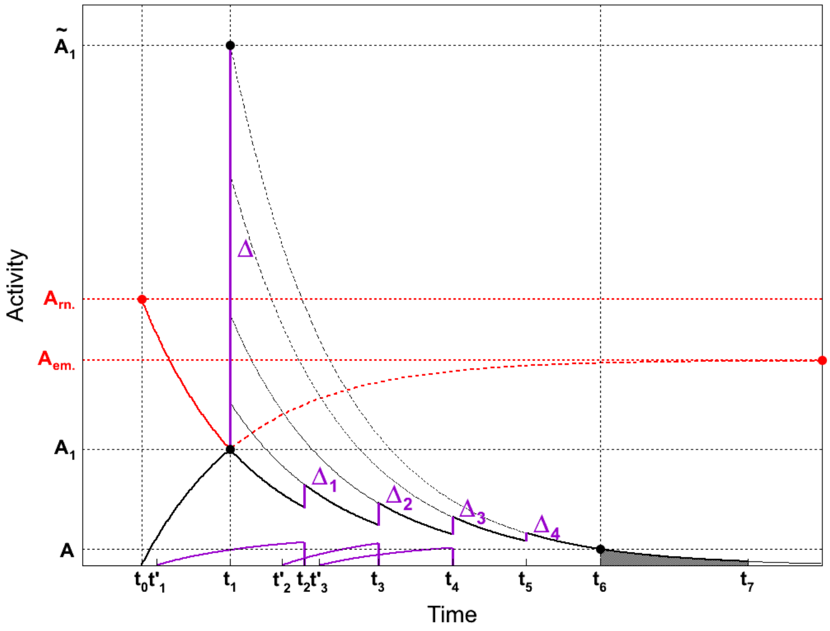

Figure 4.18: Sketch illustrating the various parameters (times and activities) that appear in equations 4.39 to 4.47 describing the evaluation of radon emanation measurements implemented in the database.

events in the region of interest, this activity is interpolated back to the moment the emanation period of the sample stopped (t_1) to the activities before ($\widetilde{A}_1$) and after the blanks of the emanation containers are subtracted ($A_1 = \widetilde{A}_1 - \Delta$). Continuing from this activity, the results $A_{rn.}$ and $A_{em.}$ can be computed, assuming an amount of radon that is continuously decaying since t_0 or, respectively, that is increasing with time starting from zero since t_0 due to a permanent radon source term.

In the time interval $[t_6, t_7]$ ^{222}Rn decays are detected in one of the proportional counters and recorded by the data acquisition system in one or more data runs. From the number of recorded counts N, the summed lifetimes of the data runs t_{data}, the background of the used proportional counter N_{bg}, the decay-constant λ_{Rn} of ^{222}Rn atoms, as well as the efficiencies (ϵ_{fill}, $\epsilon_{counter}$ and ϵ_{yield}), the activity at time t_6 is computed by:

$$A = \frac{(N - N_{bg} \cdot t_{data}) \cdot \lambda_{Rn}}{\epsilon_{fill} \cdot \epsilon_{counter} \cdot \epsilon_{yield}} \,. \tag{4.39}$$

Therein, the efficiencies ϵ_{fill} and $\epsilon_{counter}$ correct the loss of sample when filling the proportional counter and, respectively, the fact that each ^{222}Rn atom on average induces

$\sim$ 1.5 counts above threshold in the proportional counter due to its progenies. The efficiency ϵ_{yield} corrects for the finite lifetime of the data runs and computes to:

$$\epsilon_{yield} = \sum_i \left[exp(-\lambda_{Rn} \cdot t^i_{start}) - exp(-\lambda_{Rn} \cdot t^i_{stop}) \right] \ , \tag{4.40}$$

where we summed over the different data runs i is summed.

The summed lifetime of the data runs t_{data} is readily computed summing the durations $(t^i_{stop} - t^i_{start})$ of the single data runs i:

$$t_{data} = \sum_i \left(t^i_{stop} - t^i_{start} \right) \ . \tag{4.41}$$

The activity A_1 at the time t_1 induced by the sample alone is found to be:

$$A_1 = \widetilde{A}_1 - \Delta = A \cdot exp(\lambda_{Rn} \cdot (t_6 - t_1)) - \Delta \, . \tag{4.42}$$

Here we introduced the summed contribution Δ of n additional radon sources, i.e. blanks of emanation containers. Δ is given by:

$$\begin{aligned} \Delta &= \Delta_1 k_1 + \Delta_2 k_1 k_2 + \Delta_3 k_1 k_2 k_3 + \Delta_4 k_1 k_2 k_3 k_4 + \ldots \\ &= \sum_{i=1}^{n} \left(\Delta_i \cdot \prod_{j=1}^{i} k_j \right) \ , \end{aligned} \tag{4.43}$$

employing the short hand notation of

$$k_i = exp(\lambda_{Rn} \cdot (t_{i+1} - t_i)) \qquad \text{, for } i = 0 \ldots 5. \tag{4.44}$$

Are the blanks B_i (emanation activity in saturation) of the emanation containers known, the Δ_i compute to:

$$\Delta_i = \frac{B_i}{1 - exp(-\lambda_{Rn} \cdot (t_{i+1} - t'_i))} \ . \tag{4.45}$$

At time of writing, the database implemented the contribution of the gas filling line and the counter filling procedure by a fixed contribution. This contribution is allowed to differ for the individual gas filling lines and is added at the time the sample is mixed with counting gas (t_5 in FIG. 4.18). This contribution is readily incorporated by an additional Δ_i added to equation 4.43 (see Δ_4 in FIG. 4.18).

The sample's activity in saturation $A_{em.}$, that is after equilibrium of ^{222}Rn atoms emanating and decaying is reached, is easily extrapolated from the activity A_1 by:

$$\begin{aligned} A_{em.} &= A_1 \cdot \frac{1}{1 - exp(-\lambda_{Rn} \cdot (t_1 - t_0))} \\ &= A_1 \cdot \frac{k_0}{k_0 - 1} \,. \end{aligned} \tag{4.46}$$

If, on the other hand, we are interested in the activity $A_{rn.}$ of a radon sample that is decaying since t_0 without any source term of the sample itself (of course there might be still source terms from the various emanation containers), we get:

$$\begin{aligned} A_{rn.} &= A_1 \cdot exp(\lambda_{Rn} \cdot (t_1 - t_0)) \\ &= A_1 \cdot k_0 \,. \end{aligned} \tag{4.47}$$

4.5.3 Excerpt ^{222}Rn screening results

In the following section we will highlight a handful of XENON1T related samples that were screened for their ^{222}Rn emanation. TAB. 4.6 lists these samples grouped according to their application.

Heat exchanger The investigated heat exchanger (HE) was supplied by our colleagues from Columbia University, New York. HEs of this type are supposed to be used in the recirculation system of XENON1T. The HE employs 60 flat stainless steel plates that form the exchange structure. The stainless steel plates are copper braced together and form two separate volumes of about 3.8 l in total. The HE is manufactured by GEA[11] and is of version FG5X12-60. Details on this HE are found in [52]. Therein a xenon recirculation-purification prototype system for XENON1T is described.

For our ^{222}Rn emanation study the two distinct volumes of the HE were merged by shortcutting inlet and outlet. The metal surfaces of the HE had been degreased by some solvent prior to shipment by the company. Before the first measurements started, the solvent was removed by baking the HE to about 80 °C and flushing helium gas. The ^{222}Rn emanation of the "untreated" HE resulted in (0.49 ± 0.06) mBq. After completing these measurements, the interior of the HE was etched by nitric acid (HNO_3) diluted to 1.8 %. This procedure is commonly assumed to be "soft" leaving the metal almost unaffected but possibly removing ionic surface contaminations. After the nitric acid was

---

[11] http://www.gea-heatexchangers.com/

Table 4.6: Excerpt of ^{222}Rn emanation measurements relevant for XENON1T.

Sample	Description	specific ^{222}Rn emanation rate
HE GEA FG5X12-60	untreated	(0.49 ± 0.06) mBq/pc
HE GEA FG5X12-60	HNO_3 etched	(0.12 ± 0.02) mBq/pc
AC Shirasagi G_{2x} 4/6	141.5 g, 200 °C	(62 ± 4) mBq/kg
AC Bluecher 100050	100.1 g, 200 °C	(2.6 ± 0.3) mBq/kg
KNF N143SN.12E	neoprene diaphragm	(0.38 ± 0.03) mBq/pc
Spare diaphragm 1	neoprene	(0.20 ± 0.03) mBq/pc
Spare diaphragm 2	EPDM	(0.42 ± 0.06) mBq/pc
Getter PS3-MT3-N-2	5 slpm, room temperature	< 43 µBq/pc
Getter PS3-MT3-N-2	5 slpm, hot	(0.34 ± 0.10) mBq/pc
Getter PS4-MT50-R-2	75 slpm, room temperature	(0.60 ± 0.04) mBq/pc
Getter PS4-MT50-R-2	75 slpm, hot	(1.34 ± 0.10) mBq/pc
XENON100 gas system	+ KNF	(2.6 ± 0.5) mBq
XENON100 gas system	+ QDrive	(5.9 ± 0.4) mBq
Resin Dolphon CC-1105	3.6 g, 1 mm thick	(19 ± 5) µBq/g
Magnets	black coating	(61 ± 9) µBq/pc

rinsed and the HE again baked and flushed with helium, the reassessed ^{222}Rn emanation was reduced to (0.12 ± 0.02) mBq.

These results confirm that ^{222}Rn emanation potentially is surface dominated. This renders γ ray screening for ^{226}Ra futile in predicting ^{222}Rn emanation rates. A soft etching by nitric acid reduced the emanation by about a factor of 3. The total emanation of the HE is not completely negligible, however. At least one such module is required in XENON1T to transfer the latent heat from the xenon taken in liquid phase from the detector to the gaseous xenon coming from the purification-recirculation loop [52]. That is, the ^{222}Rn emanating from one of the two separated volumes will not be mitigated by a radon removal system. Assuming the remaining ^{222}Rn emanation after etching of the HE to be equally shared between those two volumes, the HE will add 60 µBq type I radon, that is about 5 % of the totally allowed type I budget (see section 4.2.2).

Activated carbon adsorbent The ^{222}Rn emanation has been investigated for the two activated carbons that have been thoroughly studied in this chapter: Shirasagi G_{2x} 4/6 from JEChem and Bluecher 100050. The measurements were performed according to the procedure sketched at the beginning of this section (see section 4.5). After preparation of the activated carbons, radon accumulated in the emanation vessel for several days. About 15 min before starting the extraction, the adsorbents were baked to 200 °C and kept at this temperature during the full procedure. We find (62 ± 4) mBq/kg and (2.6 ± 0.3) mBq/kg for the activated carbon adsorbents from Shirasagi and Bluecher, respectively. While the Shirasagi adsorbent is produced from coconut husk, the Bluecher adsorbent is synthetically produced and a higher purity was expected [49].

Additional information on the Shirasagi adsorbent is found in a publication from the XMASS collaboration [107]. Therein the ^{222}Rn emanation of the adsorbent Shirasagi G_{2x} 4/6 is determined to be (1.91 ± 0.12) mBq/kg at a baking temperature of 120 °C. This rate is accessed looping gaseous xenon through 5.5 kg of Shirasagi G_{2x} 4/6 adsorbent and counting the ^{218}Pb and ^{214}Pb disintegrations that are part of the ^{222}Rn decay chain. A radon detector consisting of an α sensitive PIN photodiode inside an electrostatic chamber similar to the one described in section 4.3.4 is used.

Two different conclusions can be drawn from the large discrepancy in the determined ^{222}Rn emanation of Shirasagi G_{2x} 4/6 adsorbent: We have seen from the previous sample that surface contaminations can dominate emanation properties. The two investigated samples are of the same type but eventually quite different in their purity. In the context of a radon removal system based on adsorption, a second explanation of the observed discrepancy is more appealing. The presence of xenon and the lower temperature during extraction of the radon atoms, do affect the intrinsic ^{222}Rn emanation of an adsorbent. In our previous argumentation on the limited use of adsorbents due to their intrinsic emanation (see section 4.3.2), we conservatively assumed the intrinsic emanation of an adsorbent to be perfectly unaffected by its temperature. If both emanation results of the Shirasagi adsorbent can be compared, i.e. the discrepancy is not related to the different batches, and if the effect can be transfered also to the Bluecher adsorbent, the intrinsic emanation of a cryogenic radon removal system employing Bluecher 100050 activated charcoal is reduced to (0.080 ± 0.012) mBq/kg. This is lower by more than a factor of 10 than the made assumption for the temperature swing radon removal system (see section 4.4.1). This linearly increases the amount of adsorbent that can be employed in such a system. The time a column is “active” consequently is extended to more than one hour. This in turn significantly relaxes the otherwise challenging task of rapid temperature changes. Future work will investigate on the intrinsic emanation of activated carbon adsorbents at various temperatures in presence of xenon employing the dynamic adsorbent selection system introduced in section 4.3.4.

KNF diaphragm pump Investigated was a stainless steel housed diaphragm pump (KNF Neuberger[12] type N143SN.12E double diaphragm pump) identical to the one employed in the XENON100 gas system during the 100 and 225 live days science runs. The membranes are from neoprene. The total ^{222}Rn emanation resulted in (0.38 ± 0.03) mBq. The company provided us with two spare diaphragms for use with this pump model. One diaphragm was made as well from neoprene, the other from EPDM (ethylene propylene diene monomer) rubber. The emanation assay resulted in (0.20 ± 0.03) mBq and (0.42 ± 0.06) mBq, respectively. Mind, however, that in the fully assembled KNF pump only one side of one membrane is facing the pumps internal volume, while the radon assay of the single diaphragms was probing their full surface. We conclude that about a fourth of the total ^{222}Rn emanation of the KNF diaphragm pump is generated by the neoprene diaphragm. Employing the EPDM spare diaphragm in the gas purification-recirculation loop of XENON100 is supposed to increase the ^{222}Rn emanation by about 0.1 mBq. This, however, is almost negligible ($\sim 4\,\%$) compared to the emanation of the full gas system. If reasons like long term endurance favour EPDM rubber over neoprene, the measured ^{222}Rn emanation does not proscribe its use.

---

[12] http://www.knf.com/

SAES getter We further want to note the ^{222}Rn emanation assay studies made on two SAES[13] getters. Getter 1 is a nitrogen getter type PS3-MT3-N-2. It is specified for a maximum flow of 5 slpm and *does not* remove nitrogen from a gas stream. The second, getter 2, is of type PS4-MT50-R-2. It is meant to purify rare gases like xenon and *is* removing nitrogen from a gas stream. It is specified for flow rates of up to 75 slpm. Both models are high temperature getters, i.e. they are operated well above ambient temperature to reach their specified purification efficacy (internal heaters adjust the temperature in purification mode). We performed ^{222}Rn emanation assays both at ambient temperature and at purification temperature. For both getters a significant increase in emanation is observed in purification mode (hot) compared to ambient temperature. This confirms that ^{222}Rn emanation depends on temperature (see also [48]). The increase with temperature is more pronounced for the nitrogen getter than for the rare gas model. At operation temperature getter 2 emanates about 4 times more ^{222}Rn than the smaller version getter 1. Normalizing to the maximum flow of purified gas, getter 2 emanates (17.9 ± 1.3) µBq/slpm; a factor of about 4 less than getter 1 with (68.9 ± 2.0) µBq/slpm. In XENON1T three modules of getter 2 (PS4-MT50-R-2) are foreseen to be operated in the purification loop. Their emanation seems to be below the one operated in XENON100 (see below) although such a model was not investigated in the laboratory.

Xenon100 gas system We described at the beginning of this chapter the ^{222}Rn emanation assay that was performed of the XENON100 detector and its gas system (see section 4.1). The gas system was found to emanate about a factor of two less radon employing the KNF diaphragm pump (diaphragm made from neoprene) compared to the same system employing the QDrive piston type pump. From the difference in emanation of the XENON100 gas system employing the QDrive and the gas system using the KNF, we conclude the ^{222}Rn emanation of the QDrive to be higher by (3.3 ± 0.6) mBq compared to the KNF. A similar KNF diaphragm pump was later on measured in our laboratory in Heidelberg (see above). Its ^{222}Rn emanation was determined to be (0.38 ± 0.03) mBq. Assuming the diaphragm pump of the XENON100 gas system to emanate an equal amount of radon, we compute the total ^{222}Rn emanation of the QDrive to be (3.7 ± 0.7) mBq. Therein we neglected systematic uncertainties introduced by the strong assumption of both KNF pumps having an identical emanation.

Following the same reasoning, we can estimate the contribution of XENON100's gas system (getter and tubing) without the KNF diaphragm pump. Subtracting the ^{222}Rn

---

[13] http://www.saesgetters.com/

emanation rate of the KNF found in the laboratory from the gas system's emanation we find (2.2 ± 0.5) mBq. Neglecting the tubing (again a strong assumption), we can attribute this full emanation to the getter (SAES type PS4-MT15-R-1) employed in the XENON100. Under these assumptions, PS4-MT15-R-1 has a higher ^{222}Rn emanation than the version PS4-MT50-R-2 XENON1T is going to operate. This confirms our projection on the total ^{222}Rn emanation of XENON1T's gas purification-recirculation system actually to be pessimistic.

QDrive piston type pump Aspects of noise pollution, long term endurance and leak tightness favor the QDrive[14] over the KNF pump. Hence, a screening effort started to determine and eventually remove dominant radon sources. At the time of writing, 3.6 g of resin (Dolphon CC-1105[15]) and small cubic magnets that are present in the interior of the QDrive were screened for their ^{222}Rn emanation. The emanation of the resin is negligible with ~ (68 ± 18) µBq for the full amount of 3.6 g of resin used in the QDrive. The magnets contribute (61 ± 9) µBq per piece. In total there are 8 magnets installed in one QDrive, resulting in a combined contribution of (0.49 ± 0.07) mBq. The magnets are coated with a black paint. In upcoming measurements this coating will be removed, as it is not required for the working principle of the QDrive but suspected to cause the relatively high emanation. Further parts of the QDrive will be investigated. We are optimistic to revise the QDrive in terms of its ^{222}Rn emanation making it a competitive alternative to the KNF diaphragm pump.

4.6 Summary and outlook

At the presence of krypton concentrations above 100 ppt the effect of the ^{222}Rn decay chain on the electronic recoil (ER) background in XENON100 has been negligible. Improvements on the cryogenic fractional distillation column operated by the XENON collaboration pushed the krypton concentration far below this level. The low energetic single-scatter ER background, induced mainly by the ^{222}Rn progeny ^{214}Pb, turned out to be responsible for almost 50 % of ER background in the WIMP search region in the 225 live days science data [27, 47]. Going from XENON100 to the next phase detector XENON1T, additional shielding will diminish the background induced by external radiation in the fiducial volume. We concluded in the previous chapter that the internal background source ^{85}Kr most likely will be reduced below critical levels for XENON1T.

---

[14] http://www.qdrive.com/

[15] http://www.dolphs.com/

What we will be left with is an ER background generated from intrinsic disintegrations of ^{222}Rn and progenies.

In this work we confirmed the α-particle counting technique developed in [47] that quantifies the ^{222}Rn concentration inside the TPC of the XENON100 detector. This verification was achieved by a ^{222}Rn emanation assay of the XENON100 detector during a maintenance period in summer 2012. From the consistency of both methods we conclude the emanated ^{222}Rn to be homogeneously mixed in the full xenon target. Some room is left, however, for a slightly enriched ^{222}Rn concentration inside the TPC introduced from the gas purification-recirculation system.

Based on these results, we projected the ^{222}Rn emanation for the next phase detector XENON1T. We estimate a total emanation of cryostat and contained equipment of 20 mBq, and forecast the gas purification-recirculation system to emanate 18 mBq. Comparing those numbers to the activity rate to be achieved of < 0.58 mBq, we found ourselves off by a factor of ~ 65.

In order to mitigate this large discrepancy, a radon removal system has been proposed. This system is supposed to be placed last in the gas purification-recirculation system filtering radon atoms from the gaseous xenon before feeding the xenon back to the detector. We found such a system particularly useful to avoid ^{222}Rn entering the liquid xenon target that is produced in the gas system (type II sources). However, the efficacy of such a system on ^{222}Rn emanated inside the cryostat (type I sources) is limited by the speed of recirculation. At the predicted recirculation speed of 100 standard liters per minute, the full 3 t target is exchanged once every 3.6 d. As a consequence, the reduction of the ^{222}Rn concentration inside the liquid xenon is limited to a factor of 2.5. Still, such a system considerably relaxes the problem. If realized, we are left with the task to reduce type I sources of projected $20\,\mathrm{mBq}/2.5 = 8\,\mathrm{mBq}$. Type II sources are relegated inconsequential.

We investigated three possible implementations of a radon removal system. The technically most elegant solution retains the radon atoms in a packed adsorbent column while xenon passes at its nominal flow of 100 slpm. This solution was shown not to be practical. Main reason is the large mass of adsorbent. This causes both the amount of stored xenon inside the removal system to be large (~ 1 t) and increases the ^{222}Rn budget above the allowed limit due to the intrinsic ^{222}Rn emanation of the adsorbent itself.

Two further solutions have been introduced: A temperature swing solution, that reduces the amount of required adsorbent mass to a mere kg-scale and a system based on cryogenic fractional distillation. Both systems are supposed to fulfill the required mitigation of radon. However, both systems are demanding in terms of their engineering and further research and development has to follow.

An operational radon removal system allows for two further modifications. A significant fraction of all ^{222}Rn sources is supposed to be located in the gaseous xenon phase of the cryostat. Splitting the recirculation loop and using a small gas flow to continually push out the gaseous xenon blanket, this fraction, being originally of type I, is transformed into a type II source; i.e. having almost no impact on the ER background of XENON1T. The second reduction of up to a factor of 2 might be achieved by introducing the purified xenon from the radon removal system directly into the TPC. Comparing estimations provided by $^{\mathrm{nat}}$Kr and ^{222}Rn α-particle counting on the amount of air entering XENON100, the TPC was shown to be particularly sensitive to sources in the gas system that were introduced into the diving bell structure. Exploiting this fact, continually purging the TPC with radon-free xenon should result in a reduction of the ^{222}Rn induced background.

We ended our discourse on ^{222}Rn by introducing the screening efforts conducted at the MPIK, Heidelberg. These efforts aim at a thorough selection of construction materials to avoid any ^{222}Rn emanation in the first place. Emanation screening studies are time consuming and experimentally demanding, but they are of uttermost importance for XENON1T. It turns on the success of these screening efforts, if the radon induced background can be further reduced and ends up being completely negligible. Assuming above techniques are successful, the initially estimated 20 mBq total ^{222}Rn emanation rate from the cryostat is reduced by efficiently purging the TPC with liquid and the formed GXe blanket by gaseous xenon. If we assume that both techniques achieve a reduction by a factor of ~ 2 and recall the factor of 2.5 achieved by the radon removal system, we are left with 2 mBq type I sources. Thorough material selection succeeding a careful screening effort is supposed to achieve the remaining reduction by a factor ~ 3. This will make XENON1T sensitive for the elastic spin-independent WIMP-nucleon scattering with cross-sections as small as $\sigma_{\mathrm{SI}} \approx 2 \times 10^{-47}\,\mathrm{cm}^2$.

Summary and Outlook

The present thesis was prepared in the framework of the XENON Dark matter search project. The current generation detector, XENON100, started taking science data in late 2009. Since then, although not being successful in detection, XENON100 evolved to become the most sensitive instrument for elastic spin-independent WIMP-nucleus scattering at the day of writing. We outlined the blinded data analysis of 225 live days × 34 kg exposure acquired in 13 months during 2011 and 2012, that sets the most stringent limit on this cross section for WIMP masses above $8\,\mathrm{GeV/c^2}$.

In context of this data analysis a consistency condition was defined that relates the longitudinal electron diffusion (S2 pulse width) in liquid xenon to the z coordinate of the particle interaction. This condition was implemented in the final analysis before unblinding. Therein, it proved to remove non-physical events, adding otherwise to the background in the region of interest. Prior to defining the condition, we introduced a new method to correct the S2 pulse width for its position dependence. This dependence is caused by small inhomogeneities of the electric field in the gas gap along the horizontal xy plane. We conclude that these inhomogeneities are generated by small variations in the distance between the field generating grids. These small dislocations are estimated to be at maximum $\sim 150\,\mu\mathrm{m}$.

In the central part of this work, we investigated the two dominant intrinsic background sources ^{85}Kr and ^{222}Rn. Being rare gases, both admix in the liquid xenon target and thus are unaffected by the otherwise powerful discrimination achieved by defining a fiducial volume and exploiting the high self shielding of LXe.

We developed a new method to determine krypton traces in xenon at so far unprecedented low concentrations. This is a mandatory task for the upcoming detector generation XENON1T but also for many near-future low-background particle physics detectors employing a liquid xenon target. Our system is based on a cryogenic gas chromatographic krypton/xenon separation and a subsequent mass spectroscopic krypton quantification. In this work we demonstrated that the system reaches a detection limit of 6 parts per quadrillion (ppq). This is an improvement by two orders of magnitude over conventional techniques. The reliable calibration of the system, its ultra-low detection limit and the procedure developed to draw samples from the XENON100 detector during science data taking, rendered this technique very valuable.

Employing this technique we were able to unambiguously determine the krypton level during the two main science runs of XENON100 and reconcile the discrepancies initially present compared to complementary data analysis methods. In this work the first measurement of a krypton level inside a particle detector below 1 parts per trillion (ppt) was performed. This remarks a proof-of-principle of the distillation technique to achieve the purity level mandatory for XENON1T. Comparing assay results of the krypton level inside the XENON100 target to an α-particle ^{222}Rn counting technique [47], we found evidence that locally introduced ^{222}Rn atoms do not admix homogeneously due to their half-life being on the same timescale as the recirculation speed.

Besides ^{85}Kr, the inert gas ^{222}Rn poses a dangerous threat for the XENON detectors. We performed a ^{222}Rn emanation assay of the XENON100 detector during a maintenance period succeeding the 225 live days science data taking and found a total emanation of $(11.9 \pm 1.1)\,\mathrm{mBq}$. Comparing this result to the corresponding concentration level determined by counting α-particles from the ^{222}Rn decay, we conclude that the emanated ^{222}Rn atoms are homogeneously admixed in XENON100. Combining this information with the above found evidence for locally introduced ^{222}Rn to admix only on the timescale of their half-life, we conclude the radon sources to be distributed rather homogeneously in XENON100.

Based on the ^{222}Rn emanation assay results, we made an estimate for the ^{222}Rn emanation of XENON1T. We concluded that the ER background will be dominated by the decay chain subsequent to ^{222}Rn, if we construct XENON1T with materials having a similar ^{222}Rn emanation rate as the materials used in XENON100. To mitigate the negative impact of ^{222}Rn on the physical reach of XENON1T, we introduced the concept of a radon removal system. After having developed a mathematical model, we conclude it to be particularly useful to remove radon produced in the gas purification-recirculation loop but of limited benefit for sources inside the cryostat. We discussed three possible realizations of such a system, pointed out the difficulties they are faced with and presented two very promising solutions.

Taken the radon removal system alone, it might not sufficiently diminish the ^{222}Rn induced background to make XENON1T become a “zero-background” experiment. We introduced three additional techniques that are supposed to alleviate the remaining discrepancy. Most notably, a thorough material screening campaign for ^{222}Rn emanation was presented. This campaign aims at selecting appropriate materials for construction to minimize the ^{222}Rn emanation rate in the first place. We are confident that these combined efforts will sufficiently reduced the ^{222}Rn induced background allowing XENON1T to successfully probe the parameter space highly interesting for WIMP-like Dark Matter down to cross sections of $\sim 10^{-47}\,\mathrm{cm}^2$ for elastic spin-independent WIMP-nucleon scattering.

Bibliography

[1] J. Einasto, *Dark Matter*, Brazilian Journal of Physics , 1 (2013), arXiv:1308.2534 [astro-ph.CO] .

[2] G. Bertone, D. Hooper, and J. Silk, *Particle dark matter: Evidence, candidates and constraints*, Phys. Rep. **405**, 279 (2005), arXiv:hep-ph/0404175 [hep-ph] .

[3] D. Fixsen, *The Temperature of the Cosmic Microwave Background*, Astrophys. J. **707**, 916 (2009), arXiv:0911.1955 [astro-ph.CO] .

[4] P. Ade *et al.* (Planck), *Planck 2013 results. I. Overview of products and scientific results*, ArXiv e-prints (2013), arXiv:1303.5062 [astro-ph.CO] .

[5] P. Ade *et al.* (Planck), *Planck 2013 results. XVI. Cosmological parameters*, ArXiv e-prints (2013), arXiv:1303.5076 [astro-ph.CO] .

[6] V. C. Rubin, N. Thonnard, and W. K. Ford, Jr., *Extended rotation curves of high-luminosity spiral galaxies. IV - Systematic dynamical properties, SA through SC*, Astrophys. J. **225**, L107 (1978).

[7] A. Bosma, *The distribution and kinematics of neutral hydrogen in spiral galaxies of various morphological types*, Ph.D. thesis, Groningen Univ. (1978).

[8] S. M. Faber and R. E. Jackson, *Velocity dispersions and mass-to-light ratios for elliptical galaxies*, Astrophys. J. **204**, 668 (1976).

[9] D. Clowe, M. Bradac, A. H. Gonzalez, M. Markevitch, S. W. Randall, *et al.*, *A direct empirical proof of the existence of dark matter*, Astrophys. J. **648**, L109 (2006), arXiv:astro-ph/0608407 [astro-ph] .

[10] L. Bergstrom, J. Edsjo, and C. Gunnarsson, *Neutralino gamma-ray signals from accreting halo dark matter*, Phys. Rev. **D63**, 083515 (2001), arXiv:astro-ph/0012346 [astro-ph] .

[11] J. R. Bond, G. Efstathiou, and J. Silk, *Massive Neutrinos and the Large-Scale Structure of the Universe*, Phys. Rev. Lett. **45**, 1980 (1980).

[12] G. Jungman, M. Kamionkowski, and K. Griest, *Supersymmetric dark matter*, Phys. Rev. **267**, 195 (1996), arXiv:hep-ph/9506380 [hep-ph] .

[13] G. Bertone, D. Cumberbatch, R. Ruiz de Austri, and R. Trotta, *Dark Matter Searches: The Nightmare Scenario*, JCAP **1201**, 004 (2012), arXiv:1107.5813 [astro-ph.HE] .

[14] J. Ellis, *Casting Light on Dark Matter*, ArXiv e-prints (2011), arXiv:1106.2923 [hep-ph] .

[15] G. Aad *et al.* (ATLAS), *Search for dark matter candidates and large extra dimensions in events with a photon and missing transverse momentum in pp collision data at $\sqrt{s} = 7$ TeV with the ATLAS detector*, Phys. Rev. Lett. **110**, 011802 (2013), arXiv:1209.4625 [hep-ex] .

[16] J. Liu, B. Shuve, N. Weiner, and I. Yavin, *Looking for new charged states at the LHC: Signatures of Magnetic and Rayleigh Dark Matter*, J. High Ener. Phys. **1307**, 144 (2013), arXiv:1303.4404 [hep-ph] .

[17] A. Drukier and L. Stodolsky, *Principles and applications of a neutral-current detector for neutrino physics and astronomy*, Phys. Rev. D **30**, 2295 (1984).

[18] M. W. Goodman and E. Witten, *Detectability of certain dark-matter candidates*, Phys. Rev. D **31**, 3059 (1985).

[19] I. Wasserman, *Possibility of detecting heavy neutral fermions in the Galaxy*, Phys. Rev. D **33**, 2071 (1986).

[20] L. M. Widrow, B. Pym, and J. Dubinski, *Dynamical Blueprints for Galaxies*, Astrophys. J. **679**, 1239 (2008), arXiv:0801.3414 [astro-ph] .

[21] E. Aprile *et al.* (XENON100), *Limits on spin-dependent WIMP-nucleon cross sections from 225 live days of XENON100 data*, ArXiv e-prints (2013), arXiv:1301.6620 [astro-ph.CO] .

[22] M. C. Smith, G. Ruchti, A. Helmi, R. Wyse, J. Fulbright, *et al.*, *The RAVE Survey: Constraining the Local Galactic Escape Speed*, Mon. Not. Roy. Astron. Soc. **379**, 755 (2007), arXiv:astro-ph/0611671 [astro-ph] .

[23] G. Plante, *The XENON100 Dark Matter Experiment: Design, Construction, Calibration and 2010 Search Results with Improved Measurement of the Scintillation Response of Liquid Xenon to Low-Energy Nuclear Recoils*, Ph.D. thesis, Columbia University (2009).

[24] M. Ambrosio *et al.* (MACRO), *Vertical muon intensity measured with MACRO at the Gran Sasso laboratory*, Phys. Rev. D **52**, 3793 (1995).

[25] J. Angle *et al.* (XENON), *First Results from the XENON10 Dark Matter Experiment at the Gran Sasso National Laboratory*, Phys. Rev. Lett. **100**, 021303 (2008), arXiv:0706.0039 [astro-ph] .

[26] D. S. Akerib *et al.* (CDMS), *Limits on Spin-Independent Interactions of Weakly Interacting Massive Particles with Nucleons from the Two-Tower Run of the Cryogenic Dark Matter Search*, Phys. Rev. Lett. **96**, 011302 (2006).

[27] E. Aprile *et al.* (XENON100), *Dark Matter Results from 225 Live Days of XENON100 Data*, Phys. Rev. Lett. **109**, 181301 (2012), arXiv:1207.5988 [astro-ph.CO] .

[28] E. Aprile *et al.* (XENON100), *Dark Matter Results from 100 Live Days of XENON100 Data*, Phys. Rev. Lett. **107**, 131302 (2011), arXiv:1104.2549 [astro-ph.CO] .

[29] E. Aprile (XENON1T), *The XENON1T Dark Matter Search Experiment*, ArXiv e-prints (2012), arXiv:1206.6288 [astro-ph.IM] .

[30] A. S. Barabash and A. I. Bolozdynya, *How to detect the dark matter of the galaxy if it is made up of weakly interacting neutral particles with masses 1-10 GeV/c^2*, JETP Lett. **49**, 356 (1989).

[31] A. Lansiart, A. Seigneur, J.-L. Moretti, and J.-P. Morucci, *Development research on a highly luminous condensed xenon scintillator*, Nucl. Inst. & Meth. **135**, 47 (1976).

[32] E. Conti *et al.*, *Correlated fluctuations between luminescence and ionization in liquid xenon*, Phys. Rev. B **68**, 054201 (2003).

[33] E. Aprile, C. E. Dahl, L. de Viveiros, R. J. Gaitskell, K. L. Giboni, J. Kwong, P. Majewski, K. Ni, T. Shutt, and M. Yamashita, *Simultaneous Measurement*

of Ionization and Scintillation from Nuclear Recoils in Liquid Xenon for a Dark Matter Experiment, Phys. Rev. Lett. **97**, 081302 (2006).

[34] E. Aprile *et al.* (XENON100), *The XENON100 Dark Matter Experiment*, Astroparticle Phys. **35**, 573 (2012), arXiv:1107.2155 [astro-ph.IM] .

[35] M. Yamashita, T. Doke, K. Kawasaki, J. Kikuchi, and S. Suzuki, *Scintillation response of liquid Xe surrounded by PTFE reflector for gamma rays*, Nucl. Inst. & Meth. in Phys. Res. **A535**, 692 (2004).

[36] E. Aprile *et al.* (XENON100), *The neutron background of the XENON100 dark matter experiment*, ArXiv e-prints (2013), arXiv:1306.2303 [astro-ph.IM] .

[37] E. Aprile *et al.*, *Material screening and selection for XENON100*, Astroparticle Phys. **35**, 43 (2011), arXiv:1103.5831 [physics.ins-det] .

[38] E. Aprile *et al.* (XENON100), *Study of the electromagnetic background in the XENON100 experiment*, Phys. Rev. **D83**, 082001 (2011), arXiv:1101.3866 [astro-ph.IM] .

[39] T. Haruyama, K. Kasami, H. Nishiguchi, S. Mihara, T. Mori, W. Otani, R. Sawada, Y. Maruno, and T. Nishitani, *LN_2-free Operation of the MEG Liquid Xenon Calorimeter by using a High-power Pulse Tube Cryocooler*, AIP Conference Proceedings **823**, 1695 (2006).

[40] A. Baldini *et al.*, *Absorption of scintillation light in a 100 l liquid xenon γ-ray detector and expected detector performance*, Nucl. Inst. & Meth. in Phys. Res. **A545**, 753 (2005).

[41] G. Bakale, U. Sowada, and W. F. Schmidt, *Effect of an electric field on electron attachment to sulfur hexafluoride, nitrous oxide, and molecular oxygen in liquid argon and xenon*, J. Phys. Chem. **80**, 2556 (1976).

[42] A. L. Arey, *Elementary Chemistry for High Schools and Academies* (The MacMillan Company, New York, 1899) p. 204.

[43] W. L. McCabe and J. C. Smith, *Unit Operations of Chemical Engineering* (McGraw-Hill, 1976).

[44] K. Abe *et al.* (XMASS), *Distillation of liquid xenon to remove krypton*, Astroparticle Phys. **31**, 290 (2009), arXiv:0809.4413 [physics.ins-det] .

[45] E. Aprile *et al.* (XENON100), *First Dark Matter Results from the XENON100 Experiment*, Phys. Rev. Lett. **105**, 131302 (2010), arXiv:1005.0380 [astro-ph.CO] .

[46] E. Aprile *et al.* (XENON100), *Implications on Inelastic Dark Matter from 100 Live Days of XENON100 Data*, Phys. Rev. **D84**, 061101 (2011), arXiv:1104.3121 [astro-ph.CO] .

[47] M. Weber, *Gentle Neutron Signals and Noble Background in the XENON100 Dark Matter Search Experiment*, Ph.D. thesis, Universität Heidelberg (2013).

[48] S. Lindemann, H. Simgen, and G. Zuzel, *Behaviour of* ^{222}Rn *at cryogenic temperatures*, AIP Conference Proceedings **1338**, 156 (2011).

[49] S. A. Bruenner, *Study of radon adsorption on activated carbon for a purification system in XENON1T*, Master's thesis, Universität Heidelberg (2013).

[50] E. Aprile *et al.* (XENON100), *Likelihood Approach to the First Dark Matter Results from XENON100*, Phys. Rev. **D84**, 052003 (2011), arXiv:1103.0303 [hep-ex] .

[51] S. Yellin, *Finding an upper limit in the presence of an unknown background*, Phys. Rev. D **66**, 032005 (2002), arXiv:physics/0203002 .

[52] E. Aprile, R. Budnik, B. Choi, H. A. Contreras, K. L. Giboni, L. W. Goetzke, R. F. Lang, K. E. Lim, A. J. Melgarejo, G. Plante, A. Rizzo, and P. Shagin, *Performance of a cryogenic system prototype for the XENON1T detector*, JINST **7**, 10001 (2012), arXiv:1208.2001 [physics.ins-det] .

[53] K. L. Giboni, E. Aprile, B. Choi, T. Haruyama, R. F. Lang, K. E. Lim, A. J. Melgarejo, and G. Plante, *Xenon recirculation-purification with a heat exchanger*, JINST **6**, 3002 (2011), arXiv:1103.0986 [physics.ins-det] .

[54] R. Wink, P. Anselmann, D. Dörflinger, W. Hampel, G. Heusser, T. Kirsten, P. Mögel, E. Pernicka, R. Plaga, and C. Schlosser, *The miniaturized proportional counter HD-2(Fe)/(Si) for the GALLEX solar neutrino experiment*, Nucl. Inst. & Meth. **A329**, 541 (1993).

[55] E. Aprile *et al.* (XENON100), *Analysis of the XENON100 Dark Matter Search Data*, ArXiv e-prints (2012), arXiv:1207.3458 [astro-ph.IM] .

[56] R. Brun and F. Rademakers, *ROOT – An object oriented data analysis framework*, Nucl. Inst. & Meth. in Phys. Res. **A389**, 81 (1997), new Computing Techniques in Physics Research V.

[57] E. Aprile *et al.* (XENON100), "Observation and applications of single-electron charge signals in the XENON100 experiment," (2013), in preparation.

[58] T. Shutt, C. Dahl, J. Kwong, A. Bolozdynya, and P. Brusov, *Performance and fundamental processes at low energy in a two-phase liquid xenon dark matter detector*, Nucl. Inst. & Meth. in Phys. Res. **A579**, 451 (2007), proceedings of the 11th Symposium on Radiation Measurements and Applications.

[59] E. Aprile, K. L. Giboni, P. Majewski, K. Ni, and M. Yamashita, *Observation of anticorrelation between scintillation and ionization for MeV gamma rays in liquid xenon*, Phys. Rev. B **76**, 014115 (2007).

[60] A. Manalaysay, T. Undagoitia, A. Askin, L. Baudis, A. Behrens, *et al.*, *Spatially uniform calibration of a liquid xenon detector at low energies using 83m-Kr*, Rev. Sci. Inst. **81**, 073303 (2010), arXiv:0908.0616 [astro-ph.IM] .

[61] E. Aprile, R. Budnik, B. Choi, H. Contreras, K. Giboni, *et al.*, *Measurement of the Scintillation Yield of Low-Energy Electrons in Liquid Xenon*, Phys. Rev. **D86**, 112004 (2012), arXiv:1209.3658 [astro-ph.IM] .

[62] E. Aprile *et al.* (XENON100), *Response of the XENON100 dark matter detector to nuclear recoils*, Phys. Rev. D **88**, 012006 (2013).

[63] G. Plante, E. Aprile, R. Budnik, B. Choi, K. Giboni, *et al.*, *New Measurement of the Scintillation Efficiency of Low-Energy Nuclear Recoils in Liquid Xenon*, Phys. Rev. **C84**, 045805 (2011), arXiv:1104.2587 [nucl-ex] .

[64] F. Favata, A. Smith, M. Bavdaz, and T. Kowalski, *Light yield as a function of gas pressure and electric field in gas scintillation proportional counters*, Nucl. Inst. & Meth. **A294**, 595 (1990).

[65] Y. Mei, *Direct Dark Matter Search with the XENON100 Experiment*, Ph.D. thesis, Rice University (2011).

[66] D. R. Lide, ed., *CRC Handbook of Chemistry and Physics, 93st Edition (CRC Handbook of Chemistry & Physics)* (CRC Press, 2013).

[67] L. G. H. Huxley, R. W. Crompton, and M. T. Elford, *Use of the parameter E/N*, British Journal of Applied Physics **17**, 1237 (1966).

[68] DIN 1871, "Gaseous fuels and other gases - density and other volumetric quantities," (1999).

[69] T. H. V. T. Dias, F. P. Santos, A. D. Stauffer, and C. A. N. Conde, *Monte Carlo simulation of x-ray absorption and electron drift in gaseous xenon*, Phys. Rev. A **48**, 2887 (1993).

[70] C. E. Dahl, *The Physics of Background Discrimination in Liquid Xenon, and First Results from Xenon10 in the Hunt for WIMP Dark Matter*, Ph.D. thesis, Princeton University (2009).

[71] E. Santos *et al.* (ZEPLIN-III), *Single electron emission in two-phase xenon with application to the detection of coherent neutrino-nucleus scattering*, J. High Ener. Phys. **2011**, 1 (2011).

[72] L. S. Miller, S. Howe, and W. E. Spear, *Charge Transport in Solid and Liquid Ar, Kr, and Xe*, Phys. Rev. **166**, 871 (1968).

[73] P. Sorensen, *Anisotropic diffusion of electrons in liquid xenon with application to improving the sensitivity of direct dark matter searches*, Nucl. Inst. & Meth. , 41 (2011), arXiv:1102.2865 [astro-ph.IM] .

[74] T. Doke, *Recent developments of liquid xenon detectors*, Nucl. Inst. & Meth. in Phys. Res. **196**, 87 (1982).

[75] S. Lindemann and H. Simgen, *Krypton assay in xenon at the ppq level using a gas chromatographic system combined with a mass spectrometer*, ArXiv e-prints (2013), arXiv:1308.4806 [physics.ins-det] .

[76] H. H. Loosli, B. E. Lehmann, and W. M. J. Smethie, in *Environmental Tracers in subsurface Hydrology*, edited by P. Cook and A. L. Herczeg (Kluwer Academic Publishers, 2000) pp. 379 – 397.

[77] J. Bieringer, C. Schlosser, H. Sartorius, and S. Schmid, *Trace analysis of aerosol bound particulates and noble gases at the BfS in Germany*, Appl. Radiat. Isot. **67**, 672 (2009).

[78] X. Du, R. Purtschert, K. Bailey, B. E. Lehmann, R. Lorenzo, Z.-T. Lu, P. Mueller, T. P. O'Connor, N. C. Sturchio, and L. Young, *A new method of measuring* ^{81}*Kr and* ^{85}*Kr abundances in environmental samples*, Geophys. Res. Lett. **30**, 2068 (2003), 10.1029/2003GL018293, arXiv:physics/0311118 .

[79] H. Sievers, *Nuclear data sheets update for A = 85*, Nuclear Data Sheets **62**, 271 (1991).

[80] A. Bolozdynya, P. Brusov, T. Shutt, C. Dahl, and J. Kwong, *A chromatographic system for removal of radioactive 85Kr from xenon*, Nucl. Inst. & Meth. in Phys. Res. **A579**, 50 (2007).

[81] M. Auger *et al.*, *The EXO-200 detector, part I: detector design and construction*, JINST **7**, 5010 (2012), arXiv:1202.2192 [physics.ins-det] .

[82] A. Dobi *et al.*, *Xenon purity analysis for EXO-200 via mass spectrometry*, Nucl. Inst. & Meth. in Phys. Res. , 40 (2012), arXiv:1109.1046 [physics.ins-det] .

[83] E. Brown, S. Rosendahl, C. Huhmann, C. Weinheimer, and H. Kettling, *In situ measurements of krypton in xenon gas with a quadrupole mass spectrometer following a cold-trap at a temporarily reduced pumping speed*, JINST **8**, 2011P (2013), arXiv:1212.5136 [physics.ins-det] .

[84] A. Dobi, C. Davis, C. Hall, T. Langford, S. Slutsky, and Y.-R. Yen, *Detection of krypton in xenon for dark matter applications*, Nucl. Inst. & Meth. in Phys. Res. **A665**, 1 (2011).

[85] A. Rizzo, personal communication (2012).

[86] J. G. Clavert, *Glossary of Atmospheric Chemistry Terms*, Pure Appl. Chem. **62**, 2167 (1990).

[87] S. Lindemann, *Reinigung und Nachweis von Edelgasen mit miniaturisierten Proportionalzählrohren*, Master's thesis, Universität Heidelberg (2009).

[88] J. R. de Laeter, J. K. Boehlke, P. D. Bievre, H. Hidaka, H. S. Peiser, K. J. R. Rosman, and P. D. P. Taylor, *Atomic weights of the elements. Review 2000 (IUPAC Technical Report)*, Pure Appl. Chem. **75**, 683 (2003).

[89] P. J. Mohr, B. N. Taylor, and D. B. Newell, *CODATA recommended values of the fundamental physical constants: 2010*, Rev. Mod. Phys. **84**, 1527 (2012), arXiv:1203.5425 [physics.atom-ph] .

[90] H. Schrader, *Half-life measurements with ionization chambers - A study of systematic effects and results*, Appl. Radiat. Isot. **60**, 317 (2004), proceedings of the 14th International Conference on Radionuclide Metrology and its Applications.

[91] J. Hopp, M. Trieloff, and R. Altherr, *Noble gas compositions of the lithospheric mantle below the Chyulu Hills volcanic field, Kenya*, Earth. Planet. Sci. Lett. **261**, 635 (2007).

[92] E. de Hoffmann and V. Stroobant, *Mass Spectrometry: Principles and Applications* (Wiley-Interscience, 2007).

[93] J. Hopp, (2012), privat communication.

[94] G. Audi and A. Wapstra, *The 1993 atomic mass evaluation: (I) Atomic mass table*, Nucl. Phys. A **565**, 1 (1993).

[95] A. O. Nier, *A Redetermination of the Relative Abundances of the Isotopes of Carbon, Nitrogen, Oxygen, Argon, and Potassium*, Phys. Rev. **77**, 789 (1950).

[96] Y. Aregbe, S. Valkiers, J. Poths, J. Norgaard, H. Kipphardt, P. D. Bievre, and P. Taylor, *A primary isotopic gas standard for krypton with values for isotopic composition and molar mass traceable to the Systeme International d'Unites*, Int. J. Mass spectrom. **206**, 129 (2001).

[97] S. Valkiers, Y. Aregbe, P. Taylor, and P. D. Bievre, *A primary xenon isotopic gas standard with SI traceable values for isotopic composition and molar mass*, Int. J. Mass Spectrom. Ion Processes **173**, 55 (1998).

[98] ISO 11929, "Determination of the characteristic limits (decision threshold, detection limit and limits of the confidence interval) for measurements of ionizing radiation – fundamentals and application," (2010).

[99] W. Wentworth, S. Vasnin, S. Stearns, and C. Meyer, *Pulsed discharge helium ionization detector*, Chromatographia **34**, 219 (1992).

[100] S. Vasnin, W. Wentworth, S. Stearns, and C. Meyer, *Pulsed discharge emission detector Application to analytical spectroscopy of permanent gases*, Chromatographia **34**, 226 (1992).

[101] D. Forsyth, *Pulsed discharge detector: theory and applications*, J. Chromatogr. **1050**, 63 (2004), current State of Element Selective Detection in Chromatography.

[102] J. G. Dojahn, W. Wentworth, S. N. Deming, and S. D. Stearns, *Determination of percent composition of a mixture analyzed by gas chromatography: Comparison of a helium pulsed-discharge photoionization detector with a flame ionization detector*, J. Chromatogr. A **917**, 187 (2001).

[103] G. Zuzel, H. Simgen, and G. Heusser, *Ar and Kr concentrations in nitrogen as a measure of the 39Ar and 85Kr activities in connection with the solar neutrino experiment Borexino*, Appl. Radiat. Isot. **61**, 197 (2004).

[104] L. N. H. Becquere, "Table de radionucleides," (2006).

[105] C. Arpesella *et al.* (Borexino), *First real time detection of Be-7 solar neutrinos by Borexino*, Phys. Lett. **B658**, 101 (2008), arXiv:0708.2251 [astro-ph] .

[106] W. Rau and G. Heusser, *222Rn emanation measurements at extremely low activities*, Appl. Radiat. Isot. **53**, 371 (2000).

[107] K. Abe *et al.* (XMASS), *Radon removal from gaseous xenon with activated charcoal*, Nucl. Inst. & Meth. , 50 (2012).

[108] H. F. Lucas, *Improved Low-Level Alpha-Scintillation Counter for Radon*, Rev. Sci. Inst. **28**, 680 (1957).

[109] J. Schick, *Entwicklung eines Versuchsaufbaus zur Adsorptionsmessung von Radon an Aktivkohle*, Bachelor's thesis, Universität Heidelberg (2011).

[110] S. Stemmle, *Untersuchung der Adsorption von Radon und Xenon an verschiedenen Adsorbensien*, Bachelor's thesis, Universität Heidelberg (2013).

[111] L. Duband, A. Ravex, and J. Chaussy, *Adsorption isotherms of helium on activated charcoal*, Cryogenics **27**, 397 (1987).

[112] K. Munakata, T. Fukumatsu, S. Yamatsuki, K. Tanaka, and M. Nishikawa, *Adsorption Equilibria of Krypton, Xenon, Nitrogen and Their Mixtures on Molecular Sieve 5A and Activated Charcoal*, J. Nucl. Sci. Technol. **36**, 818 (1999).

[113] G. L. Marschmann, *Aufbau und Betrieb eines hochempfindlichen Detektors zum kontinuierlichen Nachweis von Radon in Xenon*, Bachelor's thesis, Universität Heidelberg (2012).

[114] J. Kiko, *Detector for ^{222}Rn measurements in air at the 1 mBq/m^3 level*, Nucl. Inst. & Meth. **A460**, 272 (2001).

[115] F. Santos, T. Dias, A. Stauffer, and C. Conde, *Variation of energy linearity and w value in gaseous xenon radiation detectors for X-rays in the 0.1 to 25 KeV energy range: a Monter Carlo simulation study*, Nucl. Inst. & Meth. in Phys. Res. **A307**, 346 (1991).

[116] J. Schreiner, (2013), private communication.

[117] A. Smith and J. Klosek, *A review of air separation technologies and their integration with energy conversion processes*, Fuel Processing Technology **70**, 115 (2001).

[118] C. A. Grande, *Advances in Pressure Swing Adsorption for Gas Separation*, ISRN Chemical Engineering **2012** (2012), 10.5402/2012/982934.

[119] J. Bonjour, J.-B. Chalfen, and F. Meunier, *Temperature Swing Adsorption Process with Indirect Cooling and Heating*, Industrial & Engineering Chemistry Research **41**, 5802 (2002).

[120] M. Petkovska, D. Tondeur, G. Grevillot, J. Granger, and M. Mitrovi, *Temperature-Swing Gas Separation with Electrothermal Desorption Step*, Separation Science and Technology **26**, 425 (1991).

[121] R. Cherbanski and E. Molga, *Intensification of desorption processes by use of microwaves – An overview of possible applications and industrial perspectives*, Chem. Eng. Process. **48**, 48 (2009).

[122] R. Cherbanski, M. Komorowska-Durka, G. D. Stefanidis, and A. I. Stankiewicz, *Microwave Swing Regeneration vs Temperature Swing RegenerationComparison of Desorption Kinetics*, Industrial & Engineering Chemistry Research **50**, 8632 (2011).

[123] H. Back *et al.* (DarkSide), "First Commissioning of a Cryogenic Distillation Column for Low Radioactivity Underground Argon," (2012), pre-print, arXiv:1204.6061 [astro-ph.IM] .

[124] A. Ferreira and L. Lobo, *On the vapour pressure of radon*, J. Chem. Thermodyn. **39**, 1404 (2007).

[125] W. McCabe and E. Thiele, *Graphical Design of Fractionating Columns*, Ind. Eng. Chem. (1925).

[126] H. Simgen, G. Heusser, and G. Zuzel, *Highly sensitive measurements of radioactive noble gas nuclides in the Borexino solar neutrino experiment*, Appl. Radiat. Isot. **61**, 213 (2004).

[127] M. Altmann *et al.* (GNO), *GNO solar neutrino observations: Results for GNO I*, Phys. Rev. **B490**, 16 (2000), arXiv:hep-ex/0006034 [hep-ex] .

[128] A. Urban, *Analyse von Proportionalzählrohrimpulsen zum Nachweis von solaren Neutrinos*, Ph.D. thesis, Technische Universität München (1989).

Danksagung

Abschließend möchte ich mich bei all jenen bedanken, die zum Gelingen dieser Arbeit beigetragen haben. Zuvorderst will ich an dieser Stelle Prof. Manfred Lindner nennen, der es mir ermöglicht hat in einem so hervorragenden Umfeld zu forschen und Teil eines so spannenden Experiments zu sein.

Weiter muss dem Erstbetreuer meiner Arbeit, Prof. Wolfgang Hampel, Dank gelten, der mich als seinen vermutlich letzten Doktoranden aufnahm und in dieser Arbeit unterstützte.

Bedanken möchte ich mich an dieser Stelle auch bei Prof. Werner Aeschbach-Hertig, der das Zweitgutachten zu dieser Arbeit beisteuerte.

Dr. Hardy Simgen war ohne Zweifel in den letzten Jahren die Person, die ich mit jedwedem Problem belagern konnte. Danke für viele Stunden an Erklärung und aufmunternden Worten, wenn die Arbeit im Labor die Grenze meiner persönlichen Frustrationstoleranz erweiterte.

Für ihre Hilfe mit dem Massenspektrometer, speziell in der ersten Zeit meiner Arbeit, möchte ich mich bei Dr. Grzegorz Zuzel und Dr. Jens Hopp bedanken. Ihre Hilfe war gewiss nicht selbstverständlich und dennoch musste ich nie darauf warten.

Bedanken möchte ich mich ganz besonders bei Dr. Marc Weber. Während den letzten Jahren des gemeinsam bestrittenen Doktorandenlebens stand er mir stets mit viel Geduld und weisem Rat zur Seite. Mit ihm teilte ich nicht nur ein Bett in schwüler, südkanadischer Nacht, und so manches Mal das Zimmer in einem uns wohlbekannten Appartement, auch den Namen haben wir zuweilen gemeinsam tragen dürfen.

Dr. Teresa Marrodán Undagoitia, die sich in der letzten Phase meiner Arbeit unserer Gruppe anschloss, möchte ich für ihre ungemein hilfreiche und zugleich nette Art danken.

Gebührend erwähnt sollen auch Dr. Florian Kaether und Dr. Jochen Schreiner werden, die mir mit ihrem Wissen oft genug helfen konnten.

Besonderer Dank gilt weiter all jenen, die mir in vielen verschiedenen Dingen geholfen haben, aber vor allem gute Kollegen und Freunde waren und so die Arbeit am Institut zu einer großartigen Zeit werden ließen. Hier sind vor allem Stefan Brünner (Dulliöh zurück), Michael Dürr, Dr. Alexander Dück, Julia Haser, Daniel Schmidt, Stefan Wagner, Victoria Wagner, Ludwig Rauch und Dominik Stolzenburger zu nennen. Diese Liste hätte ich noch um viele Namen erweitern können und entschuldige mich bei denen, die ich hier nicht namentlich erwähnte. Auch euch vielen Dank.

Ohne die Unterstützung und Hilfe von XENON100-Kollegen hätte diese Arbeit ebenfalls nicht in dieser Form stattfinden können. Stellvertretend für eine ganze Kollaboration voller netter Menschen will ich namentlich Prof. Elena Aprile und Dr. Alfredo Ferella nennen.

Dank gilt Hannes Richter, der mich viel im Labor unterstützte und lehrte den Tag mit den Ersten zu beginnen. Michael Reißfelder möchte ich danken für seine optimale Unterstützung in der Werkstatt und Benjamin Gramlich für seine Hilfe mit dem Gaschromatographen sowie in allen chemischen Fragen. Erich Borger für seine wundervolle Art und die Kunst mit Glas den Alltag im Labor zu vereinfachen. Erich Burkhart und Reinhard Hofacker für ihre Unterstützung was elektronische Fragen anging.

Zuletzt will ich mich bei meiner Familie bedanken. Meinen Eltern Monika und Jo und meiner Schwester Ann-Marie danke ich dafür, dass sie für mich da sind, wenn ich sie brauche.

Ganz besonders danke ich aber meiner (kleinen) Familie. Ohne die Unterstützung meiner Frau Pina hätte ich diese Arbeit nicht geschrieben. Ihr danke ich, dass sie immer für mich da ist. Ennio will ich für sein Lächeln danken, das mich noch jeden Schreibstress hat sofort vergessen lassen. Ihr beide seid mein größtes Glück.